UNIVERSITÀ
DI TRENTO

DOCTORAL SCHOOL IN MATHEMATICS

Computational modelling of global haemodynamics and its interaction with cerebrospinal fluid and brain dynamics with application to essential hypertension

---

AUTHOR:
Morena CELANT

SUPERVISORS:
Prof. Lucas O. MÜLLER,
Prof. Eleuterio F. TORO

June 19, 2022

Doctoral thesis in **Mathematics**, XXIV cycle.
Department of Mathematics, **University of Trento**
Academic year: 2021/2022
Supervisors: **Prof. Lucas O. Müller, Prof. Eleuterio F. Toro**, *University of Trento, Italy*

External examiner: **Prof. Jordi Alastruey**, Senior Lecturer, *Biomedical Engineering, King's College London*
External examiner: **Prof. Vartan Kurtcuoglu**, Associate Professor, *Institute of Physiology, University of Zürich*

University of Trento
Trento, Italy
April, 2022

Abstract

Two major medical applications have inspired this thesis: firstly, the potential link between the venous circulation and several neurological pathologies, secondly arterial hypertension. The work presented in this thesis consists of a multiscale model of the global, arterio-venous circulation in the entire human body. The present model represents an enhanced version of the original Müller-Toro mathematical model. It includes one-dimensional, nonlinear PDE systems for major blood vessels and zero-dimensional, differential-algebraic systems for the remaining components. Highlights include the viscoelastic, rather than purely elastic, models for all blood vessels, arterial and venous; total control of blood volume, including both the stressed and unstressed components; a physiological distribution of vascular compliance; a nonlinear representation of venous resistances and compliances; myogenic mechanism of cerebral blood regulation; baroreflex control of arterial pressure.

Concerning the first medical topic, we couple the circulation to a refined description of the cerebrospinal fluid (CSF) dynamics in the craniospinal cavity. Two versions of the CSF model are presented; both versions account for deformations and interaction between the cerebral vasculature, brain parenchyma and CSF compartments during the cardiac cycle. The first one includes all major CSF pathways and the brain parenchyma represented by zero-dimensional lumped-parameter models. The linear character of intracranial compliant compartments is considered together with a classical version of the Monro-Kellie hypothesis, which states that intracranial volume inside the skull is constant over time. The second version comprises zero-dimensional lumped-parameter models for the cranial CSF and a one-dimensional co-axial model for the spinal CSF and the spinal cord. The nonlinear behaviour of the pressure-volume curves of the CSF compartments is introduced at the level of the spinal subarachnoid space and into a relaxed version of the Monro-Kellie doctrine which admits almost constant intracranial volume in the cranial space; the exponential-like character of the pressure-volume relationship is tested through an injection of fluid into the cranial subarachnoid space. The coupled models are validated through comparison of computational results against published data and MRI measurements. We present two medical scenarios: (i) transverse sinus stenoses and their relation to Idiopathic Intracranial Hypertension; (ii) extra-cranial venous strictures, their impact in the inner ear circulation and its implications for Ménière's disease. We will computationally show that intracranial pressure is the result of a dynamic interaction between the CSF production, the arterial pulsation, the venous reabsorption of CSF and the ability of the spinal subarachnoid space in accommodating the displaced CSF from the cranial spaces. This interaction is reflected in the intracranial pressure waveform with its physiological landmark peaks, both in healthy and pathological conditions.

The second topic of this thesis concerns a computational study on arterial hypertension in the context of a global model. Such an approach poses the need of controlling the total amount of blood volume in the circulatory system, as well as how it is distributed between different vascular districts by means of vascular compliance and unstressed volumes. To this end, total effective vascular compliance is determined in silico in a healthy subject by performing an infusion test of 500 ml of blood in four minutes. By means of presented computational results, we will show that effective total vascular compliance is the result of the interaction between the assigned constant physical vascular compliance and the capacity of the cardiovascular system to adapt to new situations via regulatory mechanisms. Focusing on arterial hypertension, the global model of the entire circulation is adapted to reproduce alterations in the cardiovascular system that are the cause and/or consequence of the hypertensive state. Adaptation does not only affect large systemic arteries and the heart but also the microcirculation, the pulmonary circulation and the venous system. Using a global closed-loop model allows us to establish the interplay between different blood compartments and their role in the progression of the disease. We will observe that the hypertensive state is mainly determined by the combined effects of increased arterial resistance and reduced venous compliance; the last one plays an essential role in preserving cardiac output and stroke volume in case of left ventricular hypertrophy, as well as in blood volume distribution in the hypertensive subject. Addressing arterial hypertension with a global closed-loop model of such complexity poses the basis for a more comprehensive study of this pathology and opens the way to a wide range of potential applications.

Acknowledgements

First and foremost I am extremely grateful to my supervisors, Prof. Lucas O. Müller and Prof. Eleuterio F. Toro for their invaluable advice, continuous support, and patience during my PhD program. Their knowledge and experience have inspired and encouraged me in all the time of my academic research and daily life. I would also like to thank Dr. Gino I. Montecinos for useful discussion and exchange of ideas.

I would like to offer my special thanks to Beatrice Ghitti for the time spent together during this PhD project. I found a precious friend, her support and encouraging suggestions have been fundamental at many stages of my work.

I would like to thank my friends and colleagues - Luca, Claudia and Giovanni - for stimulating discussions as well as happy distractions to rest my mind outside of my research.

I also thank the University of Trento, and in particular the Department of Mathematics, for providing the financial and academic support to carry out this PhD research project in terms of scholarship and allowances for participating in relevant conferences and advanced courses and workshops.

Finally, I would like to express my gratitude to Matteo, my parents, my brother and the rest of my family. Without their tremendous understanding and encouragement in the past few years, it would be impossible for me to complete my study.

Contents

Abstract iii

Acknowledgements v

Scientific publications xvii

1 Introduction 1
- 1.1 Motivation and goals . . . 1
- 1.2 State of the art . . . 2
  - 1.2.1 Global mathematical models of the human cardiovascular system . . . 2
  - 1.2.2 Mathematical modelling of cerebrospinal fluid dynamics . . . 3
  - 1.2.3 Arterial hypertension modelling . . . 4
- 1.3 Contributions of this thesis . . . 5

2 Computational modelling of global haemodynamics 9
- 2.1 Introduction . . . 9
- 2.2 Mathematical Models . . . 9
  - 2.2.1 Equations for blood flow in major vessels . . . 9
    - Conservation laws and closure conditions . . . 10
    - Variable material properties and augmented equations . . . 11
    - Hyperbolic approximation of a parabolic system . . . 12
  - 2.2.2 Equations for lumped-parameter models . . . 14
    - The microvasculature . . . 14
    - Valves, Starling resistors and stenoses . . . 15
    - Heart and pulmonary circulation . . . 16
    - Venous valves and Starling resistors . . . 17
    - Control system: cerebral autoregulation . . . 18
- 2.3 Numerical Methods . . . 19
  - 2.3.1 Path-conservative scheme . . . 20
  - 2.3.2 The numerical fluctuation . . . 20
  - 2.3.3 The ADER-DET scheme . . . 22
  - 2.3.4 Local time stepping . . . 24
  - 2.3.5 The coupling of vessels . . . 25
  - 2.3.6 Ghost cell for spatial reconstruction . . . 26
  - 2.3.7 1D-0D coupling . . . 27
- 2.4 Parametrization of the model . . . 28
- 2.5 Concluding remarks . . . 33

3 Cerebrospinal fluid dynamics coupled to the global circulation in holistic setting **37**
3.1 Introduction . . . 37
3.2 Mathematical model for cerebrospinal fluid and brain dynamics and its coupling to the blood circulation . . . 39
3.2.1 Equations for cerebrospinal fluid and brain dynamics . . . 39
3.2.2 Numerical treatment of CSF equations and its coupling to the circulation . . . 43
3.2.3 CSF model parametrization . . . 44
3.3 Sample numerical results and validation . . . 45
3.3.1 Validation of systemic haemodynamics . . . 46
3.3.2 Validation of cerebral haemodynamics . . . 47
3.3.3 Validation for CSF and brain dynamics . . . 57
3.4 Applications: impact of head and neck venous strictures on blood and CSF dynamics . . . 60
3.4.1 Idiopathic intracranial hypertension patient with transverse sinus stenoses . . . 62
Problem setup . . . 62
Comparison between healthy and IIH patient . . . 62
3.4.2 Extracranial venous outflow strictures and their implication for Ménière's disease . . . 67
Problem setup . . . 67
Comparison between healthy and pathological patients . . . 67
3.5 Concluding remarks . . . 70

4 A multiscale model for the cerebrospinal fluid coupled to the systemic circulation **73**
4.1 Introduction . . . 73
4.2 Methods . . . 75
4.2.1 A brief overview of the global mathematical model of the circulation . . . 75
4.2.2 Governing equations for the craniospinal CSF model . . . 77
Governing equation for the cranial CSF and brain dynamics . . . 78
Governing equation for the one-dimensional model of the spine . . . 79
4.2.3 Coupling between blood circulation, cranial CSF model, spinal CSF model . . . 83
4.2.4 Assessment of normal and pathological conditions . . . 84
Healthy subject: model setting . . . 84
Sensitivity analysis of the CSF system . . . 85
Analysis of pressure-volume relationship and outflow resistance of the CSF system . . . 85
Pathological condition: effects of transverse sinus stenoses on the blood and CSF systems . . . 86
4.3 Results . . . 86
4.3.1 Baseline condition . . . 86
4.3.2 Sensitivity analysis . . . 89
4.3.3 PVI and outflow resistance estimation . . . 90
4.3.4 Transverse sinus stenoses . . . 92
4.4 Discussion . . . 93
4.4.1 Comparison between computational results and literature data in healthy subjects . . . 93
4.4.2 Sensitivity analysis of the intracranial pressure . . . 96
4.4.3 Pressure-volume relationship and outflow resistance of the CSF system . . . 98
4.4.4 Impact of transverse sinus stenoses on blood and CSF dynamics . . . 100
4.5 Conclusions . . . 101

5 Determination of the Total Effective Vascular Compliance **103**
5.1 Introduction . . . 103
5.2 Methods . . . 106
5.2.1 A global closed-loop model for the human circulation . . . 106
5.2.2 Compliances, unstressed volumes, and total blood volume distribution . . . 109
5.2.3 Nonlinear venous resistances and compliances . . . 110
5.2.4 The baroreflex regulation . . . 111
5.2.5 Determination of total effective compliance . . . 114
5.3 Results & Discussion . . . 114
5.3.1 Control of vascular blood volume . . . 114
5.3.2 Nonlinearities in venous compartments . . . 118
5.3.3 Baroreflex . . . 119
5.4 Conclusions . . . 123

6 Major determinants of essential hypertension **127**
6.1 Introduction . . . 127
6.2 Methods . . . 131
6.2.1 Mathematical model of the cardiovascular system . . . 131
6.2.2 Hypertensive scenario . . . 134
6.3 Results & Discussion . . . 136
6.3.1 Large and small arteries remodelling . . . 136
Computational pressure-area relationship of large arteries . . . 139
Assessment of arterial stiffening by means of pulse wave velocity, augmentation and arterial compliance indexes . . . 140
The arterioles and capillaries compartments . . . 142
Pulsatility and resistive indexes . . . 143
6.3.2 The heart in hypertension . . . 144
Left ventricle hypertrophy and its effect on elastance . . . 144
The right heart and the pulmonary circulation . . . 145
6.3.3 Total blood volume and vascular compliance . . . 146
6.3.4 The venous system in hypertension . . . 149
6.3.5 Analysis of distinctive effects of remodelling . . . 152
Effects on arterial pressure . . . 152
Effects on arterial elastance and left ventricle elastance . . . 154
Effects on cardiac index: the role of reduced venous compliance . . . 156
6.4 Conclusions . . . 158

7 Conclusions **161**
7.1 Achievements . . . 161
7.1.1 Computational modelling of global haemodynamics . . . 161
7.1.2 Mathematical modelling of the cerebrospinal fluid system and its interaction with the blood circulation . . . 162
7.1.3 Mathematical modelling of arterial hypertension . . . 163
7.2 Future works . . . 163

A Geometry of 1D vessels' networks **165**

B Cardiovascular indexes **173**

Bibliography **175**

List of Figures

2.1 Schematic representation of the generic vascular bed model. . . . 15
2.2 Arterial and venous network . . . 29
2.3 Detail of head and neck arteries and veins . . . 30
2.4 Complex vascular beds . . . 31

3.1 Schematic representation of the global model for the full human circulatory system coupled to the craniospinal fluids and brain parenchyma. . . . 38
3.2 Schematic representation of the cerebrospinal fluid compartments. . . . 40
3.3 Schematic representation of the coupling between blood circulation and CSF and brain dynamics models. . . . 44
3.4 Computed blood pressure and blood flow in the aortic tree . . . 48
3.5 Blood flow distribution in selected systemic arteries and veins . . . 49
3.6 Computed blood pressure and blood flow in selected systemic veins . . . 49
3.7 Computed blood pressure and blood flow in selected arteries obtained with viscoelastic and elastic model for vessels wall. . . . 50
3.8 Computed blood pressure and blood flow in selected veins obtained with viscoelastic and elastic model for vessels wall. . . . 51
3.9 Computed pressure values for three vascular beds . . . 52
3.10 Computed pressures and volumes in the heart. . . . 52
3.11 Computed Pressure-Volume loop for the right and left ventricles. . . . 53
3.12 Computed blood pressure and blood flow in the main cerebral and neck arteries . . . 54
3.13 Blood flow in head and neck arteries and veins . . . 55
3.14 Computed autoregulation curve . . . 55
3.15 Computed blood flow and PC-MRI flow quantification in dural sinuses and internal jugular veins . . . 56
3.16 Computed cerebral venous pressure and CSF dynamics. . . . 57
3.17 Variation in time of $V - V_{av}$ of cerebral blood volumes within the cardiac cycle . . . 57
3.18 Pressure in CSF compartments over a cardiac cycle . . . 58
3.19 Cerebrospinal fluid pressure . . . 58
3.20 Cerebrospinal fluid volumes . . . 59
3.21 Time variation of $V - V_{av}$ of cerebral fluid volumes within the cardiac cycle . . . 60
3.22 Time variation of blood and CSF flow within a cardiac cycle. . . . 60
3.23 Cerebral arterial inflow and inflow of spinal subarachnoid space . . . 61
3.24 Computed flow and velocity in the aqueduct of Sylvius. . . . 61
3.25 Location of transverse sinus stenosis and computed flow in healthy control and stenotic case compared with MRI data . . . 64
3.26 Averaged pressure over a cardiac cycle of different dural sinuses: comparison between healthy control and stenotic case . . . 64

3.27 Pressure in CSF compartments over a cardiac cycle: comparison between healthy control and subject with transverse sinuses stenoses . . . 65
3.28 Intracranial pressure waveform and variation in time of flow through the aqueduct of Sylvius: comparison between healthy and stenotic subjects . . . 66
3.29 Computed cardiac-cycle averaged pressures for the healthy control and the CCSVI subjects . 68
3.30 Computed pressure in CSF compartments over a cardiac cycle: comparison between the healthy control and CCSVI subject . . . 69
3.31 Variation in time of flow through the aqueduct of Sylvius for the healthy control and the CCSVI patient with and without collaterals . . . 69

4.1 Schematic representation of the global model coupled to the multiscale model of the cerebrospinal fluid . . . 76
4.2 Schematic representation of the cerebrospinal fluid cranial compartments and spinal models. 77
4.3 Schematic representation of the coupling between blood circulation, cranial CSF and brain dynamics models and spinal CSF dynamic . . . 83
4.4 Pressure in CSF compartments over a cardiac cycle . . . 87
4.5 Cerebrospinal fluid pressure . . . 87
4.6 Computed results compared to measured data . . . 88
4.7 Computed flow and velocity in the aqueduct of Sylvius . . . 88
4.8 Time variation of $V - V_{av}$ of fluid volumes and blood and CSF flow within the cardiac cycle . 89
4.9 Spinal cord motion at the cervical level . . . 90
4.10 Contour plots in space and time of pressure, area and velocity in the cord and in spinal CSF . 91
4.11 Sensitivity analysis of the intracranial pressure waveform . . . 91
4.12 Computational results from CSF bolus injection test . . . 92
4.13 Pressure-volume index and outflow resistance estimation . . . 93
4.14 Pressure in CSF compartments in the case of transverse sinus stenoses . . . 94
4.15 Cerebrospinal fluid pressure waveform in the case of transverse sinus stenoses . . . 95
4.16 Cerebrospinal fluid pressure waveform in subject with transverse sinus stenoses: comparison with previous computational results . . . 101

5.1 Schematic representation of the global model used in this work . . . 107
5.2 Example of a generic complex vascular bed connecting three 1D arteries to multiple 1D veins 111
5.3 Comparison between linear and nonlinear pressure-volume relationship in one venule/vein compartment of the right forearm . . . 112
5.4 Total blood volume distribution . . . 115
5.5 Computed total effective vascular compliance by means of an infusion test of 500 ml of blood in 4 min. . . . 117
5.6 Comparison between linear and nonlinear resistances and compliances of venule compartments . . . 119
5.7 Changes in haemodynamic parameters before and after volume expansion. . . . 120
5.8 Changes in haemodynamic parameters before and after volume expansion: comparison between different baroreceptors systems. . . . 122
5.9 Efferent response of the baroreflex model during the volume expansion . . . 123

6.1 Schematic representation of the global model of the circulation and its adaptation in hypertensive condition. . . . 130

6.2 Computed blood pressure in the aortic tree at different locations in normotensive and in hypertensive states. . . . 138
6.3 Computed diameter-pressure curve in right common carotid artery and in right radial artery in normotensive and hypertensive subjects. . . . 140
6.4 Pressure-area curves and pressure waveforms of two exemplary arteries: the right radial artery and the right common carotid artery. . . . 141
6.5 Computed pressure variations along the vascular system of the right arm in normotensive and hypertensive subjects. . . . 143
6.6 Computed volume-pressure relationship of the left and right cardiac ventricles in normotensive and hypertensive subjects. . . . 146
6.7 Computed total effective vascular compliance and changes in haemodynamic parameters before and after expansion in normotensive and hypertensive subjects. . . . 149
6.8 Computational blood volume distribution in normotensive and hypertensive subject. . . . 150
6.9 Computed blood pressure in selected veins at different locations in normotensive and in hypertensive states. . . . 151
6.10 Blood flow distribution in selected systemic veins and in head and neck veins. . . . 152
6.11 MBP, SBP, DBP and PP: distinctive effects of remodelling . . . 154
6.12 SBP and DBP: combination of two of the most relevant parameters of the hypertensive scenario 155
6.13 MBP and PP: combination of two of the most relevant parameters of the hypertension scenario 155
6.14 SBP, DBP, MBP and PP: combination of three of the most relevant parameters of the hypertensive scenario . . . 156
6.15 CI, E_a, E_{es} and E_a / E_{es}: distinctive effects of remodelling . . . 157
6.16 E_a and CI: combination of two of the most relevant parameters of the hypertensive scenario . 158

List of Tables

2.1 Vascular beds - simple connections . . . 32
2.2 Heart chambers parameters . . . 32
2.3 Cardiac valves parameters. . . . 33
2.4 Parameters for pulmonary circulation. . . . 33
2.5 Location of venous valves. . . . 34
2.6 Baseline values of cerebral haemodynamic variables . . . 34
2.7 Parameters for the autoregulation model . . . 35

3.1 Hydraulic length, area at rest and elastance of each CSF compartment. . . . 45
3.2 Flow resistances of CSF compartments. . . . 45
3.3 Initial pressure conditions for vascular compartments. . . . 46
3.4 Cardiovascular indexes . . . 53
3.5 CSF and blood flow over a cardiac cycle. . . . 61
3.6 Computed averaged volume of blood and CSF over a cardiac cycle in main cerebral compartments . . . 65
3.7 Cerebrospinal fluid exchange $q^{in}_{br,L-R}$ and q^{out}_{br,L_R} and brain porosity . . . 66
3.8 Cerebrospinal fluid exchange and brain porosity: comparison between healthy control and subject with IJV stenoses . . . 70

4.1 Parameters for the spinal one-dimensional model. . . . 85
4.2 CSF and blood flow over a cardiac cycle. . . . 89
4.3 Sensitivity analysis results . . . 92

5.1 Basal value for model parameters of compliance and unstressed volume in the main vascular compartments. . . . 110
5.2 Parameters for the efferent pathways of the baroreceptors and for the arterial and venous gain 114
5.3 Cardiovascular indexes . . . 116

6.1 Cardiovascular indexes: comparison between normo- and hypertensive subject. . . . 137
6.2 Cardiac and pulmonary indexes: comparison between normo- and hypertensive subject. . . . 147

A.1 Geometrical and mechanical parameters of the arterial network. . . . 165
A.2 Geometrical and mechanical parameters of the venous network. . . . 168

Scientific publications

Papers published or submitted during the PhD candidature:

- Eleuterio F. Toro, Andrea Santacá, Gino I. Montecinos, **Morena Celant** & Lucas O. Müller. AENO: a Novel Reconstruction Method in Conjunction with ADER Schemes for Hyperbolic Equations. *Communications on Applied Mathematics and Computation*, 2021.
https://doi.org/10.1007/s42967-021-00147-0

- **Morena Celant**, Eleuterio F. Toro & Lucas O. Müller. Total Effective Vascular Compliance of a Global Mathematical Model for the Cardiovascular System. *Symmetry*, 2021; 13(10):1858.
https://doi.org/10.3390/sym13101858

- Eleuterio F. Toro, **Morena Celant**, Qinghui Zhang, Christian Contarino, Nivedita Agarwal, Andreas Linninger & Lucas O. Müller. Cerebrospinal fluid dynamics coupled to the global circulation in holistic setting: Mathematical models, numerical methods and applications. *International Journal of Numerical Method in Biomedical Engineering*, 2021; e3532.
https://doi.org/10.1002/cnm.3532

- Gino M. Montecinos, Andrea Santacà, **Morena Celant**, Lucas O. Müller & Eleuterio F. Toro. ADER scheme with a simplified solver for the generalized Riemann problem and an average ENO reconstruction procedure. Application to blood flow. *Submitted to Computers and Fluids*, 2022.

- **Morena Celant**, Eleuterio F. Toro, Giulia Bertaglia, Valerio Caleffi, Alessandro Valiani, Pablo J. Blanco & Lucas O. Müller. Major determinants of essential hypertension: a computational study based on a closed-loop model for human circulation. *In preparation*, 2022.

- **Morena Celant**, Eleuterio F. Toro & Lucas O. Müller. A multiscale model for the dynamic of the cerebrospinal fluid coupled to the systemic circulation. *To be submitted to Fluid and Barriers of the CNS*, 2022.

Chapter 1

Introduction

1.1 Motivation and goals

The living human body is a complex biological system, which involves the dynamic interaction of fluids, gases and solids, all mediated through controls, membranes and intricate networks of conduits and barriers. In this broad scenario it is becoming increasingly accepted that bodily fluid systems and their interactive dynamics play a major role in human-body physiology and pathology [298, 152, 113]. Mathematical modelling of these systems has received great attention since it represents a useful tool to better understand the complex physiological mechanisms of different diseases. The most complete mathematical model for the human extracellular bodily fluids should include the complete circulatory system (arteries, veins, microvasculature), interstitial fluid (ISF), the lymphatic system and the cerebrospinal fluid.

This thesis focuses on the modelling of the cardiovascular system and the cerebrospinal fluid system. Two classes of pathological conditions have inspired this work. First, the cerebrospinal fluid (CSF) in the craniospinal cavity is the centre of attention of many specialists concerned with a range of disorders of the central nervous system (CNS), such as hydrocephalus, syringomyelia, spinal cord injury, Chiari malformations and spinal tumours. The work of Zamboni and collaborators [324] on the potential connection of multiple sclerosis to anomalies of the extracranial venous system has stimulated increasing attention to the venous district of the circulatory system and its potential link to several neurological pathologies. It has become established that main venous draining routes may be affected by various types of anomalies, such as stenoses, resulting in impaired draining of venous blood from the central nervous system to the heart. Furthermore, it was observed that venous abnormalities affect cerebrospinal fluid dynamics [177, 326]; impaired venous drainage with consequent venous hypertension at the level of the dural sinuses reduces the bulk flow of cerebrospinal fluid into the superior sagittal sinus from the subarachnoid space.

Second, arterial hypertension is by far one of the most important sources of morbidity and mortality in the world, according to the World Health Organization [226]. It affects approximately 40-45% of the world population aged >25 years (1.13 billion in 2015 [179]) with a global age-standardised prevalence of 24 and 20% in men and women, respectively [179]. Moreover, hypertension becomes progressively more common with advancing age, with a prevalence $>$ 60% in people aged $>$ 60 years. It has been estimated that complications of hypertension account for 9.4 million deaths worldwide every year [226]; examples of hypertension-related diseases are ischaemic heart disease, heart failure, atrial fibrillation, chronic kidney disease, peripheral artery disease, stroke and cognitive decline, to name but a few. The recent COVID-19 pandemic has posed particular attention on possible risks associated with hypertension. The available evidence suggests that hypertension increases the risk of acquiring SARS CoV-2 infection, admission to intensive care units, severe disease and mortality [227]. Despite the evidence of treatment benefit, fewer than half of all hypertensive patients have adequately controlled blood pressure.

Our goal is to provide some insights into the fluid dynamics of the aforementioned diseases in the context of a global closed-loop model for the entire human cardiovascular system. Such a model departs from

the original Müller-Toro model [201, 202]. For the first motivating class of pathologies, the blood circulation will be coupled to cerebrospinal fluid dynamics in order to study their interaction in healthy and pathological situations. For the second disease, we will adapt the global model of the entire cardiovascular system to the mechanical, structural and functional changes that are cause/consequence of arterial hypertension.

1.2 State of the art

1.2.1 Global mathematical models of the human cardiovascular system

The cardiovascular system includes a network of arteries and veins connected through the microcirculation, which comprises arterioles, capillaries, venules, the heart and the pulmonary circulation. In the last decades, mathematical modelling of the cardiovascular system has received great attention due to the increasing impact of cardiovascular diseases worldwide. Early contributions in this field include the seminal work of Otto Frank in 1899 [253], which was primarily concerned with the basic shape of the arterial pulse. This is probably the first application of a mathematical model to successfully describe haemodynamics, especially the exponential decay of the arterial pressure pulse in diastole.

Depending on the clinical application to be addressed, cardiovascular models of different dimensions, from three-dimensional (3D) to zero-dimensional (0D), have been developed. Fluid-Structure Interaction (FSI) models, which involve time-dependent, nonlinear systems of equations for the fluid and the vessel wall mechanics in three space dimensions, have the advantage of addressing local details such as velocity vectors and wall shear stresses. However, due to their complexity and computational cost, at the present time, it is unrealistic to think of deploying FSI models for a full human bodily fluid system, not even for the circulatory system alone. One-dimensional averaged models derived from 3D models represent a trade-off between mathematical simplification of the reality and computational cost. Lumped-parameter, or zero-dimensional, models constitute another option; these are governed by systems of ordinary differential equations in time, subject to algebraic constraints. Due to the complexity of the cardiovascular system, most of the closed-loop models of the entire circulation are exclusively based on lumped-parameter models that incorporate 0D models to simulate flow in the larger arteries, veins, pulmonary and cardiac circulation. Another popular approach for constructing closed-loop models of the entire circulation is represented by geometric multiscale models; in this case, 3D FSI models, 1D averaged models and lumped parameter models, with appropriate matching conditions, are integrated together to create an heterogeneous mathematical model of the entire cardiovascular system. A first example in this line is that of Liang [160]; in this work, the arterial tree is described by 1D models, while the remainder, including the heart, the peripheral circulation, the venous system, and the pulmonary circulation, is represented by lumped parameter models. Another example was proposed by Blanco [33]; this work presents a computational model of the entire cardiovascular system including one-dimensional models for the arterial tree, lumped parameter models for the remainder part of the circulatory system and 3D models for local haemodynamics in specific vessels of interest. The resulting model is an integrated 3D-1D-0D coupled model which forms a closed loop network capable of taking into account the interaction between the global circulation and the local haemodynamics. Another relevant example is represented by the global closed-loop model developed by Müller and Toro in 2014 [201], and then refined in [202]. This model includes a network of arteries and veins, described by one-dimensional models, while the microcirculation, the heart, the pulmonary circulation, venous valves and Starling resistors, and a very simple model for the cerebrospinal fluid are represented by lumped-parameter models. A distinctive novelty of this work is the one-dimensional description of the venous circulation, with emphasis on the neck and head venous system. Another work along these lines is that of Mynard [215], wherein in addition to arterial/venous one-dimensional networks for systemic,

pulmonary and coronary circulations, lumped-parameters models were adopted for peripheral circulation, cardiac chambers and valves.

1.2.2 Mathematical modelling of cerebrospinal fluid dynamics

Cerebrospinal fluid (CSF) is a clear and colourless liquid that protects the brain and spinal cord from chemical and physical injuries. It also carries oxygen, glucose, and other needed chemicals from the blood to neurons and neuroglia [154]. CSF circulation through the cavities of the brain, as well as around the brain and the spinal cord in the subarachnoid space, is a dynamic phenomenon; such movement is responsible for the transport of the choroid plexus secretion products to their site of action, the balance of the electrolytes and the elimination of catabolites. CSF provides homeostatic regulation of the brain's parenchymal interstitial fluid. The dynamics of cerebrospinal fluid flow are directly linked to those of the cardiovascular system [113, 298, 121]. In fact, CSF is produced at the level of the choroid plexuses, that are networks of blood capillaries in the walls of the ventricles where CSF is formed by filtration and secretion from blood plasma. Then, CSF flows from the lateral ventricles to the third ventricle through the intraventricular foramina, and from the third ventricle through the aqueduct of Sylvius into the fourth ventricle. CSF then circulates in the cranial and spinal subarachnoid spaces around the surface of the brain and spinal cord. Finally, it is gradually reabsorbed into the blood, mainly through arachnoid villi of the dural venous sinuses (especially the superior sagittal sinus) or by travelling along cranial or spinal nerve sheaths to reach the peripheral lymphatic drainage [268]. Cerebrospinal fluid pressure is the result of a dynamic equilibrium between CSF secretion, absorption and resistance to flow. It varies with the systolic pulse wave, respiratory cycle, abdominal pressure, jugular venous pressure and posture [68].

There is abundant literature on CSF modelling and its interaction with cerebral haemodynamics and brain tissue dynamics; it ranges from simple lumped-parameter models which provide a circuit-based representation of the fluid dynamics in one or more CSF compartments, to one-dimensional models that are able to capture wave-propagation phenomena in the cerebrospinal fluid, to 3D models of selected cavities containing CSF. Lumped-parameter models of CSF dynamics are represented by balance equations for pulsatile volumetric deformations and compartmental pressures, fluid exchange, and bulk flows to quantify system interactions among CSF flow, blood, and nervous tissue. An early contribution on mathematical modelling of cerebrospinal fluid dynamics was due to Marmarou [181, 182]; in that work, the CSF system was depicted by an equivalent electrical circuit wherein intracranial pressure dynamics was studied in terms of nonlinear intracranial compliance, dural sinus pressure, CSF formation, and resistance to CSF absorption; however, this model did not explicitly incorporate brain vasculature or the porous parenchyma. Ursino et al. [307] proposed a simple mathematical model to simulate the interactions between CSF and cerebral blood flow, which accounted for cerebral venous pressure instability, cerebral blood volume, and autoregulation. This CSF model was included in the global closed-loop model of the circulation by Müller and Toro [202]. Linninger and collaborators [162] introduced a more complete dynamic model consisting of the bi-phasic brain, arteries, arterioles, capillaries, venules, veins, venous sinus, ventricles, subarachnoid space and the spinal canal with clinical relevance in normal and pathological conditions.

One-dimensional models are suitable for representing the spinal CSF compartment, wherein the CSF dynamics are dominated by wave propagation. The spine was generally idealised by a co-axial geometry composed of an inner cylinder for the spinal cord and an outer tube for the dura, with CSF flowing in between. Examples along those lines are the works by Berkouk [26], Carpenter [47], Cirovic [59], Toro [290]. Kim and Cirovic [139] proposed a computational model of the cerebrospinal fluid system incorporating lumped-parameter cranial compartments for arteries and veins, and one-dimensional distributed spinal CSF compartment. Martin et al. [183] coupled the cardiovascular and cerebrospinal fluid systems. Their representation of the cardiovascular system was composed by a 1D network of viscoelastic arteries, linked

to a varying elastance model of the left ventricle and coupled to three-element Windkessel models. The cerebrospinal fluid system was modelled by a tube-like structure which represented the spinal subarachnoid space; this kind of model allowed for studying the axial distribution of flow and pressure along the spinal canal. However, the rest of the cranial space was described by a transfer function that delivers spinal CSF flow from arterial flow curves.

To conclude this short review on cerebrospinal fluid mathematical models, we recall three dimensional models of CSF; attempts along these lines include simulations of CSF flow patterns consistent with biomechanical principles such as the Navier-Stokes equations, porous media flow, and the FSI of fluid flow within distensible boundaries. These models were often focused on partial aspects of CSF spaces, on a single CSF compartment or a small group of CSF districts. Examples along these lines include those by Kurtucuoglu et al. [145] and Gupta et al. [109]. In the first study, cerebrospinal fluid flow was studied in the third ventricle and in the aqueduct of Sylvius, while Gupta et al. focused on the inferior cranial space, the superior spinal subarachnoid space, and the fourth cerebral ventricle; in both cases, magnetic resonance imaging experiments were used to reconstruct the patient-specific domain and its boundary conditions that was then treated by means of a finite-volume computational fluid dynamics approach. Sweetman and Linninger [278] developed a computational model from CINE-MRI that reproduced the three-dimensional flow field in all regions of interest in the entire CSF-filled spaces of the central nervous system.

For a comprehensive review on the state of the art, refer to [165, 144, 255].

1.2.3 Arterial hypertension modelling

Essential, or primary, or idiopathic hypertension is historically defined as a rise in blood pressure of unknown cause that increases risk for cerebral, cardiac, and renal adverse events. Computational models can be a practical approach to better quantifying the haemodynamic effects of cardiovascular properties in this medical condition. An early, seminal contribution in this field is due to Guyton in the early 70s [112], which was concerned with a system analysis of arterial pressure regulation and hypertension. The model consists of several hundred algebraic and ordinary differential equations that incorporate the main ingredients of the vascular system, their interaction with extracellular fluid volume and detailed regulatory mechanisms. Guyton's work challenged the widely accepted view at that time of the primary role of the heart in controlling cardiac output and that of the peripheral resistance in the determination of arterial blood pressure. He explored the linkage between blood pressure and sodium balance and demonstrated an overriding importance of renal salt and water balance in setting the long-term blood pressure level [196]. From the pioneering work by Guyton, several mathematical works about physiological long-term regulation model of the cardiovascular system have been developed, see for example [137, 136, 3].

One-dimensional models of the arterial system have been widely employed to study arterial haemodynamics under various pathophysiological conditions; this kind of models are suitable for studying wave propagation phenomena under hypertensive conditions. Examples on analysis of arterial pressure waveform in ageing and hypertension by means of mathematical models include [317, 157, 230, 10, 53, 91]. Westerhof et al. [317] used a passive linear electrical model of the human systemic arterial tree to study the effects of reduced arterial distensibility in old age hypertension and those of induced vasoconstriction in essential hypertension. In [157], the hypothesis that increased pulse wave reflection and altered backward waveform morphology contribute to increased pulse pressure in subjects with higher pulse pressure was tested with the help of numerical modelling (55-segment 1D arterial network model) to confirm the interpretation of the experimental results. Another example on one-dimensional arterial models for hypertensive studies was due to Blanco et al. [30]. In that work, an Anatomically Detailed Arterial Network (ADAN) model was used to study the role of hypertension in cerebral small vessel disease; model parameters were modified to consider structural changes in arterial vessels in the hypertensive scenario. Pagoulatou and

Stergiopulos [230] studied the major ageing mechanisms in the arterial system and the heart using a mathematical one-dimensional model of the arterial tree, in order to assess the evolution of systolic and pulse pressure during normal ageing. On the same topic, in [53] a one-dimensional computational model was used to provide a complementary approach for research into the arterial pulse waves in healthy ageing and to establish the main cardiovascular determinants of pulse wave indexes. Alfonso et al. [10] considered a different approach than the traditional distributed 1D modelling of arterial segments to assess the main features of the pulse pressure propagation, such as the pulse pressure amplification phenomena. They used only one long tapering artery, composed of constant parameter vessels, placed in a simple cascading order; in each of these segments, the pulse pressure wave dynamics were modelled by a non- linear Korteweg-de Vries equation describing only forward soliton interactions. This type of model was able to reproduce the pressure wave dynamics in an arterial network in healthy and hypertensive subjects, with the useful effect of a reduced computational cost. Still on the pulse pressure amplification, in [91] the authors presented two methods based on the physics of blood flow for estimating central pulse pressure from non-invasive measurements of aortic flow and peripheral blood pressure; three blood flow models with decreasing level of mathematical complexity were employed in this study: a full 116-artery one-dimensional model, a reduced 15-artery model containing the aortic-brachial arterial path of the full model and a single-vessel model of the brachial artery. They tested these models on in silico data for different age groups and in vivo data for normotensive and hypertensive subjects. However, all these studies focused only on the arterial tree in ageing and hypertension. A first attempt towards a more global view of hypertension was due to Mynard et al. [214], who studied the influence of hypertension on coronary conduit arterial and microcirculatory flow patterns by means of a multiscale model of the human coronary circulation situated in a closed-loop cardiovascular model. Such a model was adapted to the systemic hypertension scenario modifying the systemic arterial resistance and compliance of vascular beds, systemic arteries wave speed and proximal area and pulmonary venous reference pressure. However, this study mainly focused on effects of hypertension on coronary circulation, hence it did not consider other aspects that commonly influence arterial pressure, such as total blood volume. As pointed out by Liang [158], mechanical, structural and functional changes may occur in the entire cardiovascular system as a cause or consequence of hypertension. In this framework, Liang et al. [158] proposed a multiscale model which integrates the main cardiovascular components prone to alterations in hypertension (such as the heart, large arteries, distal arteries and arterioles) into a unique computational framework that enables to explore the determinant cardiovascular factors for haemodynamic variables of concern in the treatment of hypertension. Both the global multiscale model proposed by Mynard et al. [214] and Liang et al. [158] did not focus on the adaptation of the venous system in hypertension; the venous circulation was represented by one- or zero-dimensional compartment and it was included to close the cardiovascular system. However, the venous system is not only a passageway for flow of blood to the heart, but it also contributes in regulating cardiac output and it serves as blood reservoir for the circulation, which in turn plays a role in arterial blood pressure regulation. Hence, in a closed system like the circulatory system, changes to the venous part of the circulation have an impact on the heart function and on the arterial system and vice versa. As we will show in this thesis, accounting for venous system adaptation to hypertension can have significant consequences on the characterization of the major determinants of arterial blood pressure.

1.3 Contributions of this thesis

The work presented in this thesis can be divided into two main parts: 1) development in computational modelling of global haemodynamics and its interaction with cerebrospinal fluid and brain dynamics, 2) mathematical modelling for arterial hypertension. The common link to both parts is a global approach

to cardiovascular modelling. Concerning the first part, previous works on the interaction between blood and cerebrospinal fluid were performed using lumped-parameter models [307, 162], or multiscale models for the circulation and lumped-parameters model for the cerebrospinal fluid in the craniospinal cavity [202] or models which included only some compartments for the cerebrospinal fluid [183]. The work presented in this thesis aims to couple a global multiscale model of the circulation and a detailed model of the cerebrospinal fluid, which includes all the cranial and spinal spaces containing cerebrospinal fluid; such a model has allowed to study the effects of impaired venous drainage, such as venous stenoses, to the cerebrospinal fluid dynamics and its interaction with the cerebral circulation. Regarding the second part, arterial hypertension was previously treated in the context of global closed-loop models, even if the adaptation of the cardiovascular system to this pathology was only partially modelled, without considering the venous system. In this thesis we look at hypertension remodelling including also the contribution of the venous circulation, as well as total blood volume and vascular compliance; these aspects influence arterial pressure and need to be considered when a global closed-loop model of the circulatory system is used. This work has allowed a more comprehensive view of the effects of hypertension remodelling and to computationally establish which factors contribute more significantly to the elevation of arterial pressure. Here, we briefly discuss the work performed in these fields and the structure of the thesis.

Computational modelling of global haemodynamics and its interaction with cerebrospinal fluid and brain dynamics

In [292], we substantially improved the original Müller-Toro mathematical model [201, 202] for the global systemic and pulmonary circulations in the entire human body. The improvements concern physiological aspects, underlying mathematical models, as well as the associated computational methods. On the physiological aspects, we included the adoption of a viscoelastic tube law, not just for the arterial tree as in [7, 241], but also for the venous circulation. The heart model was modified with respect to the original global model [201, 202]; the cardiac valves are represented through a model based on [216]. Other additions include the parametrization of the vascular beds and the introduction of the brainstem and cerebellar vessels' network, which together with the cerebral autoregulation model, is relevant when studying anatomical malformations of the cerebral circulation. The physiology modelling improvements have resulted in new mathematical problems to be solved, notably, the viscoelastic nature of all major blood vessels. The associated parabolic system of equations has been approximated by a hyperbolic system with stiff source terms following a relaxation approach [295, 197, 199]. The resulting stiff system is solved numerically with the same high-order ADER-type numerical scheme [294, 76], as in the original model [201, 202]. An additional numerical improvement is the adoption of the local time stepping technique [78], first introduced for blood flow in [204] for solving a simplified one-dimensional vessel network. This technique results in significant computational savings, which are more evident when coupling the blood circulation to the CSF and brain dynamics, as these two systems have different temporal scales and the computational time needed to reach periodicity of the solution is considerably larger than the time scale of a cardiac cycle. An overview of the global multiscale mathematical model of human circulation and the numerical methods can be found in Chapter 2 of this thesis.

The main novelty of Chapter 3 is the coupling of the blood circulation to a refined mathematical description of the cerebrospinal fluid dynamics in the craniospinal cavity [162]. The CSF model includes all major CSF pathways and it is described by nine zero-dimensional compartments representing the cerebral ventricles, the aqueduct of Sylvius, the cranial and spinal subarachnoid spaces and the bi-phasic brain parenchyma. This model accounts for deformations and interaction between the cerebral vasculature, brain parenchyma and cerebrospinal fluid compartments during the cardiac cycle. The full model is validated through comparison of computational results against published data and bespoke MRI measurements. The

applicability of our model is illustrated in two classes of fluid-dynamics related pathologies that involve the close dynamical interaction of all major fluid compartments in the craniospinal space. The first class of pathologies concerns transverse sinus stenoses and its relation to Idiopathic Intracranial Hypertension (IIH) [20, 194, 4]. The second class of fluid-related pathologies concerns the altered haemodynamics of the inner ear circulation resulting from extra-cranial venous outflow strictures, and its implications for Ménière's disease [96, 13, 40, 297]. This work can be found in Chapter 3 of this thesis.

In a successive paper [50], a revised version of the previous global model was presented. The main improvement of the model proposed in [50] with respect to a previous version of the model (see [292]) regards the introduction of a multiscale model of the cerebrospinal fluid and brain dynamics. Such a model comprises zero-dimensional lumped-parameter models for the cranial CSF and brain dynamics based on [162, 292] and a one-dimensional co-axial model for the spinal CSF and the spinal cord, based on [59, 290, 259]. Non-linear pressure-volume relationships for the cranial and spinal CSF were included in order to reproduce the exponential-like behaviour and to well capture deviations from baseline condition. The model was validated for a setup corresponding to a healthy subject, including a sensitivity analysis of the intracranial pressure waveform to main model parameters. We determined the pressure-volume index and the outflow resistance to CSF absorption through an injection of fluid into the cranial subarachnoid space. As an example of the applicability of the model, we tested the effects of transverse sinus stenoses and their relation to Idiopathic Intracranial Hypertension. Computational results are compared to published data and MRI measurements, as well with computational results obtained with the previous version of the model [292]. On the physiological aspects of the present work [50], two improvements deserve attention. The first one regards the introduction of a spatially-resolved model for the spinal subarachnoid space that is able to capture the wave propagation along the spine. The advantage of using this kind of model becomes evident in the computed intracranial pressure waveform that is characterised by three physiological peaks. While average intracranial pressure is mainly determined by the production and absorption processes, its waveform mainly depends on the spinal properties. The second consists in the introduction of nonlinearity in pressure-volume relationships for both cranial and spinal cerebrospinal fluid systems. This is necessary when large deviations from the baseline model state are introduced. As fluid is injected into the craniospinal CSF system, intracranial pressure increases, as well as its pulse pressure. Obstructions in the drainage pathway caused by transverse sinus stenoses lead to increased intracranial pressure, which displays a progressive elevation of the second peak, a landmark of decreased intracranial compliance. The one-dimensional model for the spine, along with the numerical method to solve it and its coupling to the cranial cerebrospinal fluid model and the blood circulation, are included in Chapter 4.

Mathematical modelling for arterial hypertension

This part of the thesis is devoted to characterise the major determinants of essential hypertension by means of a computational study based on a closed-loop model for the human circulation.

Since total effective compliance and total blood volume are the main determinants of arterial pressure, we determined in silico the effective total vascular compliance of a global closed-loop model for the cardiovascular system. To this end, in [51], we reproduced the experiment of London et al. [171] which consists of an infusion test of 500 ml of blood in four minutes. Changes in blood volume and changes in central venous pressure were recorded during the infusion. We enriched the global mathematical model described in Chapter 2 to better capture the main physiological processes involved in the infusion test as well as to update modelling assumptions that needed to be improved in order to consider a deviation from the baseline state. Main improvements regarded: 1) a physiologically sound parametrization of the mathematical model in the baseline pre-infusion status, which includes a physiological distribution of vascular compliance and total blood volume; 2) the introduction of nonlinear resistances and compliances in the venous 0D

compartments to take into account the distension of the vasculature during volume expansion; 3) the coupling to a model for short-term regulation of pressure that considers the activity of high- and low-pressure baroreceptors. By means of a presented in silico experiment, we showed that effective total vascular compliance is the result of the interaction between the assigned constant physical vascular compliance and the capacity of the cardiovascular system to adapt to new situations via regulatory mechanisms. The computational results presented in [51] should contribute to raise awareness about the difference between effective and physical parameters, as well as about the need to enrich the set of physiological processes included in our model, especially if large deviations from the baseline model state are to be described. This piece of work is presented in Chapter 5.

Finally, we adapted the global closed-loop multiscale model for the human circulation to reproduce computationally the alterations in the cardiovascular system that are cause and/or consequence of the hypertensive state and to assess the role played by different components of the model in the determination of elevated diastolic and systolic arterial pressure [52]. There is clinical evidence showing that adaptation in the hypertensive condition does not only affect large systemic arteries and the heart but also the microcirculation, the pulmonary circulation and the venous system. Model predictions in normotensive and hypertensive conditions were validated and discussed with respect to clinical measurements reported in the literature; moreover, we studied the distinctive effects of remodelling in different cardiovascular districts to better quantify their impact on the determination of arterial pressure. Using a global closed-loop model allows us to establish the interplay between different blood compartments and their role in the progression of the disease. We observed that the hypertensive state is mainly determined by the combined effects of increased arterial resistance and reduced venous compliance; the last one plays an essential role in preserving cardiac output and stroke volume in case of left ventricular hypertrophy, as well as in blood volume distribution in the hypertensive subject. Details on this topic can be found in Chapter 6.

Chapter 2

Computational modelling of global haemodynamics: mathematical models and numerical methods

2.1 Introduction

In this chapter, we present the mathematical models for describing the human circulatory system. As already pointed out, the present global closed-loop model emerges from [201] and [202], with some significant improvements. For the one-dimensional representation of the blood vessels we include viscoelasticity of the vessel wall [7, 199]. The resulting partial differential equation system is solved numerically using the high-order Arbitrary DERivative Riemann problem (ADER) framework [294] with a solver that allows for local time stepping [207]. The microcirculation and heart models are also partially modified with respect to [201]. Representation of pulmonary circulation follows the same models as in [201] and [202] wherein a simple three-compartment (arteries, capillaries, veins) description for systemic microcirculation based on the work by Sun et al. [276] is adopted. Venous valves and Starling resistors are modelled following [216].

Since in this thesis we are particularly interested in the cerebral dynamics, we incorporate into our model one of the most important physiological control systems, the cerebral autoregulation. This process aims at maintaining adequate and stable cerebral blood flow during changes in blood pressure working on dilatation or contraction of arterioles and capillaries [319]. The model used to account for this phenomenon is based on [305] and [234].

The chapter proceeds as follows. Section 2.2 presents the mathematical models for major arterial and venous blood vessels, consisting of systems of partial differential equations (2.2.1) and the compartmental, or 0-dimensional (0D), models consisting of systems of ordinary differential equations, for other districts of the circulation (2.2.2). Section 2.3 introduces the numerical schemes for one-dimensional blood in viscoelastic vessels coupled to the local time stepping solver. Moreover, the coupling between 1D-0D models is presented. Section 2.4 describes all the parameters needed for the implementation of the global closed-loop model.

2.2 Mathematical Models

2.2.1 Equations for blood flow in major vessels

In this section we review the partial differential equations representing blood flow in major vessels, along with closure laws and reformulations.

Conservation laws and closure conditions

The flow of blood in major arteries and veins is represented through one-dimensional (1D) cross-sectional averaged models resulting in time-dependent systems of partial differential equations. We start from the classical laws of conservation of mass and of balance of momentum

$$\begin{cases} \partial_t A + \partial_x q = 0 \,, \\ \partial_t q + \partial_x \left(\hat{\alpha} \frac{q^2}{A} \right) + \frac{A}{\rho} \partial_x p = -f \,, \end{cases} \tag{2.1}$$

where x is the axial coordinate along the longitudinal axis of the vessel and t is time. For details on the derivation of (2.1) see [94], for example. The 2×2 system (2.1) contains three unknowns, namely $A(x,t)$, the cross-sectional area of the vessel lumen; $q(x,t)$, the blood flow rate and $p(x,t)$, the cross-sectionally averaged internal pressure. Parameters in the equations include $\hat{\alpha}$, the Coriolis coefficient, ρ the blood density, assumed constant, and f the friction force per unit length of the tube. The Coriolis coefficient depends on the assumed velocity profile; here we take $\hat{\alpha} = 1$, which corresponds to a flat velocity profile.

The system of differential equations (2.1) has more unknowns than equations; hence, one extra closure condition is required. Such extra condition, usually called tube law, attempts to couple the internal blood flow distribution with the mechanical properties of the solid moving vessel wall. A comparative analysis of various mathematical descriptions of elastic properties of vessel walls in modern one-dimensional models of hemodynamics can be found in [311]. In the existing versions of our model [201, 202] we used elastic tube laws for both arteries and veins. In the present thesis we improved upon this by adopting viscoelastic tube laws for both arteries and veins in the entire circulation. To this end we follow recent works concerned with approximating time-dependent parabolic systems with hyperbolic balance laws with stiff source terms [295, 197]. The approach was applied in [199] to a simplified arterial network. In the present work we deploy the framework to the full human circulatory system, major arteries and veins. Following [199], the following pressure-area relation (tube law) is adopted

$$p(x,t) = \psi(A(x,t); A_0(x), K(x), P_0) + \varphi(A(x,t); A_0(x)) \partial_t A + p_{ext}(x,t) \,. \tag{2.2}$$

Here, the first term $\psi(A(x,t); A_0(x), K(x), P_0)$ is the elastic part of the tube law, which in turn depends on the reference pressure P_0 and the parameters $A_0(x)$ and $K(x)$ and can be written as

$$\psi(A(x,t); A_0(x), K(x), P_0) = K(x) \Phi(A(x,t), A_0(x)) + P_0 \,, \tag{2.3}$$

with

$$\Phi(A(x,t); A_0(x)) = \left(\left(\frac{A(x,t)}{A_0(x)} \right)^m - \left(\frac{A(x,t)}{A_0(x)} \right)^n \right) . \tag{2.4}$$

The term $\varphi(A(x,t); A_0(x)) \partial_t A$ represents the viscoelastic part of the tube law; here we adopt a Voigt-type viscoelastic model. $p_{ext}(x,t)$ denotes the external pressure. As usual, the transmural pressure is defined as

$$p_{transm} \equiv p(x,t) - p_{ext}(x,t) = K(x) \Phi(A(x,t), A_0(x)) + P_0 + \varphi(A(x,t); A_0(x)) \partial_t A \,. \tag{2.5}$$

We now define geometric and mechanical parameters in the tube law. $A_0(x)$ defines the vessel cross-sectional area at equilibrium; $K(x)$ represents the vessel wall stiffness, while m and n are two real numbers, to be specified. Note that $A_0(x)$ and $K(x)$ are variable parameters, they depend on the spatial coordinate x. Throughout this work, we adopt $m = 0.5$ and $n = 0$ for arteries, as was usually done in the literature; the values of these parameters were derived from a mechanical model for the vessel-wall displacement, considering a generalized string model [93]. For veins, we use $m = 10$ and $n = -1.5$; these parameter values are related to veins collapse and stiffening [90, 38]. Moreover, $K(x)$ is a positive function that was obtained from the reference wave speed c_0 assumed for each vessel, distinguishing arteries, veins and dural sinuses.

The viscoelastic term of the tube law depends on the time partial derivative of the cross-sectional area of the vessel and is defined as

$$\varphi(A(x,t);A_0(x))\partial_t A = \frac{\Gamma}{A_0\sqrt{A}}\partial_t A\,. \tag{2.6}$$

Γ is related to the viscous properties of the vessel wall, which following [7] is chosen as

$$\Gamma = \frac{2}{3}\sqrt{\pi}\gamma h_0\,, \tag{2.7}$$

where γ is the wall viscosity. The wall viscosity is evaluated as the product of the viscoelastic parameter K_M and the volume fraction of smooth muscle. K_M is chosen such that hysteresis behaviour of pressure-area plots in peripheral arteries and veins lies within the physiological range. For arteries we take $K_M = 3\times 10^5$ $dyn\ s\ /cm^2$ and a percentage of smooth muscle of 10% [31]. For veins we take $K_M = 5\times 10^4$ $dyn\ s\ /cm^2$ and a smooth muscle fraction of 8%. Concerning the wall thickness h_0 we follow [31] and express it in relation to the vessel radius at equilibrium. For arteries $h_0 = 10\%\ r_0$, while for veins $h_0 = 5\%\ r_0$.

The momentum equation in (2.1) contains the friction term $f(x,t)$, which depends on the local velocity profile (assumed a priori). Here we take

$$f = \frac{8\mu\pi}{\rho}\frac{q}{A}\,, \tag{2.8}$$

with μ being the blood dynamic viscosity.

Variable material properties and augmented equations

As already pointed out, the material and geometric parameters $K(x)$, $A_0(x)$ and $p_{ext}(x,t)$ are in general functions of x along the vessel. Computationally, in order to deal with this situation we adopt the variable-parameter formulation of Toro and Siviglia [289], admitting now, viscoelastic tube laws for arteries and veins [199]. System (2.1), along with the tube law (2.2), is then written as the following extended 5×5 system

$$\begin{cases} \partial_t A + \partial_x q = 0\,, \\ \partial_t q + \partial_x\left(\alpha\frac{q^2}{A}\right) = -\frac{A}{\rho}\partial_x p_{ext} - \frac{A}{\rho}\Phi\partial_x K - \frac{A}{\rho}\left(K\partial_A\Phi - \partial_A\varphi\partial_x q\right)\partial_x A \\ \qquad\qquad -\frac{A}{\rho}\left(K\partial_{A_0}\Phi - \partial_{A_0}\varphi\partial_x q\right)\partial_x A_0 + \frac{A}{\rho}\varphi\partial_x^{(2)} q - f\,, \\ \partial_t K = 0\,, \\ \partial_t A_0 = 0\,, \\ \partial_t p_{ext} = 0\,. \end{cases} \tag{2.9}$$

In succinct form system (2.9) reads

$$\partial_t\mathbf{Q} + \mathbf{A}(\mathbf{Q})\partial_x\mathbf{Q} = \partial_x\mathbf{G}(\mathbf{Q};\partial_x\mathbf{Q}) + \mathbf{S}(\mathbf{Q})\,, \tag{2.10}$$

where $\mathbf{Q}$ is the vector of unknowns

$$\mathbf{Q} = \begin{bmatrix} A & q & K & A_0 & p_{ext}\end{bmatrix}^T\,, \tag{2.11}$$

$\mathbf{A}(\mathbf{Q})$ is the coefficient matrix

$$\mathbf{A}(\mathbf{Q}) = \begin{bmatrix} 0 & 1 & 0 & 0 & 0 \\ c^2 - u^2 + \frac{\varphi\partial_x q}{2\rho} & 2u & \frac{A}{\rho}\Phi & \frac{A}{A_0}\left(\frac{\varphi\partial_x q}{\rho} - c^2\right) & \frac{A}{\rho} \\ 0 & 0 & 0 & 0 & 0 \\ 0 & 0 & 0 & 0 & 0 \\ 0 & 0 & 0 & 0 & 0 \end{bmatrix}\,, \tag{2.12}$$

$\mathbf{S}(\mathbf{Q})$ is the source term vector

$$\mathbf{S}(\mathbf{Q}) = \begin{bmatrix} 0 & -f & 0 & 0 & 0 \end{bmatrix}^T \tag{2.13}$$

and

$$\partial_x \mathbf{G}\left(\mathbf{Q}; \partial_x \mathbf{Q}\right) = \begin{bmatrix} 0 & \frac{\varphi A}{\rho} \partial_x^{(2)} q & 0 & 0 & 0 \end{bmatrix}^T \tag{2.14}$$

is a higher-order differential term emerging from the viscoelastic part of the tube law. This last differential term in the advection-diffusion-reaction system defines a parabolic problem, no longer hyperbolic, as in the case of a purely elastic tube law [289].

Hyperbolic approximation of a parabolic system

Toro and Montecinos [295, 197] proposed a method to approximate time-dependent parabolic problems by hyperbolic systems with stiff source terms, by extending the Cattaneo relaxation approach [49]. Montecinos and collaborators [199] applied the procedure to a network of arterial blood vessels and then Müller et al. [204] proposed a coupling strategy for one-dimensional segments that compose a network of viscoelastic vessels, thereby setting the bases for its extension to the global, closed-loop circulation model of this work, including arteries and veins.

To start with, a new variable ζ and a relaxation parameter $\epsilon > 0$ are introduced. This new variable ζ is constrained to satisfy an additional evolutionary PDE, namely the constitutive Cattaneo's law, which reads

$$\partial_t \zeta = \frac{1}{\epsilon}(\partial_x q - \zeta)\,. \tag{2.15}$$

From (2.15), it holds that

$$\zeta \to \partial_x q \quad \text{as} \quad \epsilon \to 0\,. \tag{2.16}$$

We now have an augmented 6×6 system. Keeping the same notation for the vector of unknowns, the coefficient matrix and the source term, we may write

$$\partial_t \mathbf{Q} + \mathbf{A}(\mathbf{Q})\partial_x \mathbf{Q} = \mathbf{S}(\mathbf{Q})\,, \tag{2.17}$$

with

$$\mathbf{Q} = \begin{bmatrix} A & q & K & A_0 & p_{ext} & \zeta \end{bmatrix}^T, \tag{2.18}$$

$$\mathbf{A}(\mathbf{Q}) = \begin{bmatrix} 0 & 1 & 0 & 0 & 0 & 0 \\ c^2 - u^2 + \frac{a_\Gamma}{2} & 2u & \frac{A}{\rho}\Phi & \frac{A}{A_0}\left(a_\Gamma - c^2\right) & \frac{A}{\rho} & -\frac{A}{\rho}\varphi \\ 0 & 0 & 0 & 0 & 0 & 0 \\ 0 & 0 & 0 & 0 & 0 & 0 \\ 0 & -\frac{1}{\epsilon} & 0 & 0 & 0 & 0 \end{bmatrix}, \tag{2.19}$$

$$\mathbf{S} = \begin{bmatrix} 0 & -f & 0 & 0 & 0 & -\frac{1}{\epsilon}\zeta \end{bmatrix}^T, \tag{2.20}$$

$$c^2 = \frac{A}{\rho} K \partial_A \Phi, \qquad u = \frac{q}{A}, \qquad a_\Gamma = \frac{\varphi \zeta}{\rho}\,. \tag{2.21}$$

Here c is the wave velocity (analogous to the sound speed) associated to the elastic tube law. The 6×6 system (2.17) with the state vector (2.18) and coefficient matrix (2.19) is hyperbolic [199, 295] provided the relaxation parameter is chosen so as to satisfy

$$\epsilon^{-1} \geq -\frac{\zeta}{2A} - \frac{\rho c^2}{\varphi A}\,. \tag{2.22}$$

Under (2.22), all eigenvalues of the coefficient matrix (2.19) are real and given as

$$\lambda_1 = u - \tilde{c}\,, \quad \lambda_2 = \lambda_3 = \lambda_4 = \lambda_5 = 0\,, \quad \lambda_6 = u + \tilde{c}\,, \tag{2.23}$$

where now $\tilde{c}$ denotes the wave speed associated to the complete tube law.

$$\tilde{c} = \sqrt{c^2 + \omega}, \qquad \omega = \frac{\varphi A}{\rho \epsilon} + \frac{a_\Gamma}{2}\,. \tag{2.24}$$

The corresponding right eigenvectors are

$$\left.\begin{aligned}
R_1 &= \begin{bmatrix} 1 & u-\tilde{c} & 0 & 0 & 0 & -\frac{1}{\epsilon} \end{bmatrix}^T, \\
R_2 &= \begin{bmatrix} 1 & 0 & 0 & 0 & 0 & \frac{c^2 + a_\Gamma/2 - u^2}{\varphi A}\rho \end{bmatrix}^T, \\
R_3 &= \begin{bmatrix} 0 & 0 & 1 & 0 & 0 & \frac{\Phi}{\varphi} \end{bmatrix}^T, \\
R_4 &= \begin{bmatrix} 0 & 0 & 0 & 1 & 0 & \frac{(a_\Gamma - c^2)}{\varphi A_0}\rho \end{bmatrix}^T, \\
R_5 &= \begin{bmatrix} 0 & 0 & 0 & 0 & 1 & \frac{1}{\varphi} \end{bmatrix}^T, \\
R_6 &= \begin{bmatrix} 1 & u+\tilde{c} & 0 & 0 & 0 & -\frac{1}{\epsilon} \end{bmatrix}^T.
\end{aligned}\right\} \tag{2.25}$$

These eigenvectors associated to the real eigenvalues (2.23) can be shown to be linearly independent, and hence system (2.17) is hyperbolic.

We now consider two fundamental properties of system (2.17), namely the nature of the characteristic fields and the generalised Riemann invariants. It was observed that characteristic fields associated to eigenvectors R_1 and R_6 are genuinely non-linear for parameters and state variables in physiological ranges. Moreover, it is obvious that the remaining characteristic fields are linearly-degenerate. The generalised Riemann invariants associated to R_1 are

$$\Gamma_1^1 = u + \int \frac{\tilde{c}}{A} dA = \text{constant}\,, \tag{2.26}$$

$$\Gamma_1^2 = K = \text{constant}\,, \tag{2.27}$$

$$\Gamma_1^3 = A_0 = \text{constant}\,, \tag{2.28}$$

$$\Gamma_1^4 = p_{ext} = \text{constant}\,, \tag{2.29}$$

$$\Gamma_1^5 = \zeta + \frac{A}{\epsilon} = \text{constant}\,; \tag{2.30}$$

similarly, Riemann invariants associated to R_6 are

$$\Gamma_6^1 = u - \int \frac{\tilde{c}}{A} dA = \text{constant}\,, \tag{2.31}$$

$$\Gamma_6^2 = K = \text{constant}\,, \tag{2.32}$$

$$\Gamma_6^3 = A_0 = \text{constant}\,, \tag{2.33}$$

$$\Gamma_6^4 = p_{ext} = \text{constant}\,, \tag{2.34}$$

$$\Gamma_6^5 = \zeta + \frac{A}{\epsilon} = \text{constant}\,. \tag{2.35}$$

We also note that for constant p_{ext}, A_0 and K, the generalised Riemann invariants for the linearly degenerate fields associated with R_2, R_3, R_4 and R_5 are

$$\Gamma_1^{LD} = \tilde{p} + \frac{1}{2}\rho u^2 = \text{constant} \tag{2.36}$$

and

$$\Gamma_2^{LD} = q = \text{constant}\,, \tag{2.37}$$

where

$$\tilde{p} = p_{ext} + \psi - \varphi\zeta\,. \tag{2.38}$$

More details about the hyperbolic reformulation of the problem and its eigenstructure are found in [197], [199]. Next we present the 0-dimensional mathematical models, which consist of systems of Ordinary Differential Equations (ODEs).

2.2.2 Equations for lumped-parameter models

In the previous section we described mathematical models for major arterial and venous blood vessels, consisting of systems of partial differential equations. For other districts of the circulation, we present compartmental, or 0-dimensional (0D) models which consist of systems of Ordinary Differential Equations (ODEs). These include the microvasculature (arterioles, capillaries and venules/veins), the heart, the pulmonary circulation, venous valves and Starling resistors. We also present a mathematical model for cerebral autoregulation, which acts on the terminal portion of the cerebral arteries and on the cerebral vascular beds.

The microvasculature

Physiologically, the arterial system is connected to the venous system through arterioles, capillaries and venules. To describe this connection, the microvasculature is represented by lumped-parameter, or 0-dimensional, models. This connection can be simple, such as between one artery and one vein, or entail numerous compartments. The generic vascular bed model for all microvasculature beds, depicted in Figure 2.1, is inspired in the three-element Windkessel model. The model is characterized by

- Characteristic impedances. These couple any number of connecting 1D arteries/veins to lumped-parameter models for the microvasculature (R_{da} or R_{vn}) and regulate the pressure drop between 1D domains and vascular beds;
- Peripheral resistances and compliances divided into arterioles (R_{al}, C_{al}) and capillaries (R_{cp}, C_{cp});
- Venous compartments with related compliance C_{vn}.

As illustrated in Figure 2.1, each connecting artery can be linked to one or both venous capacitors, while each venous capacitor can be connected to any number of terminal veins. Note that the second artery splits into both venous capacitors, while the other arteries supply only one of them. Moreover, any number of veins can be connected to each venous capacitor. For each vascular bed, the variables to be computed are volume, pressure and flow, denoted as follows: for arterioles V_{al}, P_{al}, Q_{al}; for capillaries V_{cp}, P_{cp}, Q_{cp} and for venules V_{vn}, P_{vn} and Q_{vn}. Thus, for each element of the vascular bed one has

$$\begin{cases} \frac{dV}{dt} = Q_{in} - Q\,, \\ P = \frac{V}{C} + P_{ext}\,, \\ Q = \frac{P - P_{out}}{R}\,, \end{cases} \tag{2.39}$$

where C is compliance and P_{ext} is the external pressure, generally taken as zero (relative to atmospheric pressure) or equal to the intracranial pressure in the case of intracranial peripheral beds. Q_{in} and P_{out} are flow and pressure in neighbouring compartments or obtained from the 1D models through boundary conditions. Well-matched coupling to the connecting 1D arterial and venous segments is achieved via the characteristic impedances, as suggested in [6].

FIGURE 2.1: Schematic representation of the generic vascular bed model. The red boxes include the terminal 1D arteries and the corresponding arterioles and capillaries compartments; the green boxes represent the venous capacitors while the light blue boxes refer to terminal venules/1D veins.

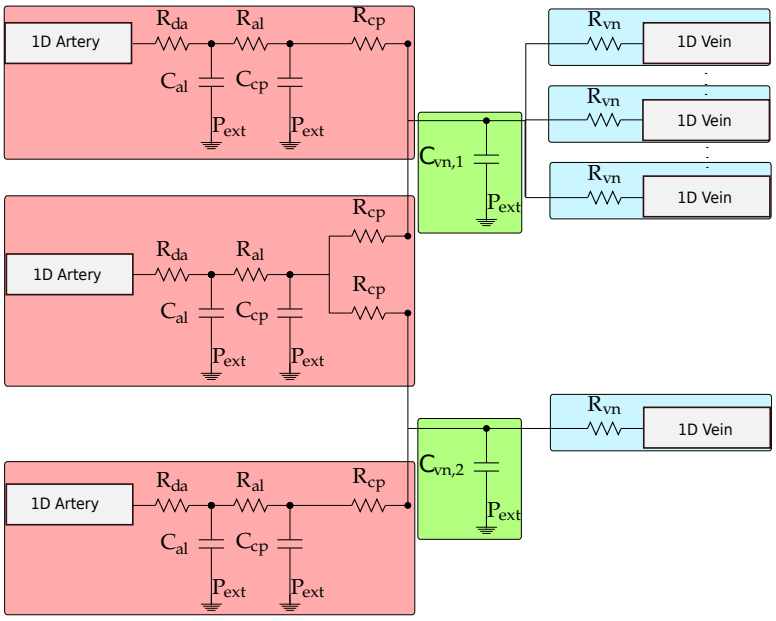

Valves, Starling resistors and stenoses

Here we describe a valve model based on [216] that predicts valve motion on the basis of the instantaneous difference between upstream and downstream pressures. In the present thesis the model is applied to describe cardiac valves, venous valves, Starling resistors in the cerebral circulation and stenoses. Here we illustrate the general model, while for each specific application, more details are given in the following subsections and in 3.4.

The valve dynamics are described by means of the function $A_e(t)$ defining the effective cross-sectional area, expressed as

$$A_e(t) = A_a[M_s\xi(t) + M_r(1-\xi(t))]\,, \tag{2.40}$$

where A_a is the annulus area and the time-dependent function $\xi(t)$ is the valve state, a dimensionless number in the range $[0,1]$ and representing the rate of opening and closing of the valve. $\xi(t)$ is given by the solution of the following variable-coefficient ordinary differential equations

$$\begin{cases} \frac{d\xi}{dt} = K_o\left(\Delta p(t) - \Delta p_o\right)\left(1-\xi(t)\right) & \text{if } \Delta p \geq \Delta p_o \text{ opening state}\,, \\ \frac{d\xi}{dt} = K_c\left(\Delta p(t) - \Delta p_c\right)\xi(t) & \text{if } \Delta p < \Delta p_c \text{ closing state.} \end{cases} \tag{2.41}$$

Here K_o and K_c are rate coefficients for opening and closing respectively; Δp_o and Δp_c are opening and closure threshold pressures. In (2.40), M_r and M_s are parameters representing regurgitating and stenotic valves respectively. Specifically, a healthy valve corresponds to $M_r = 0$ and $M_s = 1$, an incompetent valve is described by $M_r > 0$, while a stenotic valve is represented by $M_s < 1$. Flow variation in time across the valve is given by a first-order, variable coefficients, ordinary differential equation

$$\frac{dq(t)}{dt} = \frac{1}{L(t)}\left(\Delta p(t) - B(t)q(t)|q(t)|\right)\,. \tag{2.42}$$

$\Delta p(t)$ is the pressure difference across the valve length, defined as

$$\Delta p(t) = p_{up}(t) - p_{down}(t)\,, \tag{2.43}$$

where $p_{up}(t)$ and $p_{down}(t)$ are the upstream and downstream pressures at time t, with respect to valve direction. $p_{up}(t)$ and $p_{down}(t)$ are evaluated from other compartments of the global model, specified later. $L(t)$ and $B(t)$ are time-dependent coefficients; $L(t)$ is blood inertance, which accounts for the component of the pressure difference related to blood acceleration; $B(t)$ is the Bernoulli's resistance, which governs pressure differences related to convective acceleration and dynamic pressure losses due to diverging flow. They are expressed as

$$L(t) = \frac{\rho l_e}{A_e(t)}\,, \tag{2.44}$$

and

$$B(t) = \frac{\rho}{2A_e^2(t)}\,. \tag{2.45}$$

Here ρ is the constant blood density and l_e is the effective length. More details on the valve model are found in [216, 201, 202] and in the appendix of [293].

Heart and pulmonary circulation

In the present thesis we consider a heart model for the dynamics of the four chambers and the cardiac valves. The chambers are denoted as $ch = \{RA, RV, LA, LV\}$, where RA and RV are the right atrium and ventricle, while LA and LV represent the left atrium and ventricle. For the chambers we follow the time-varying elastance model in [160, 276], while cardiac valves are modelled as presented in Subsection 'Valves, Starling resistors and stenoses' of 2.2.2 following [216]. Briefly, blood pressure in each cardiac chamber is calculated as

$$P_{ch} = P_{peri} + E(t)(V_{ch} - V_{ch,0}) + \gamma P_{ch}\frac{dV_{ch}}{dt}\,, \tag{2.46}$$

where V_{ch} is the current cardiac volume; $V_{ch,0}$ is the dead volume (assumed to be 0); $\gamma P_{ch}(t)$ is the viscoelasticity coefficient of the cardiac wall and $P_{peri}(t)$ is the external pericardial pressure defined by

$$P_{peri} = \exp\left(\frac{V_H - V_{PC}}{\Phi_{PC}}\right)\,, \tag{2.47}$$

where $V_H(t)$ is the sum of the volume of each heart chamber and V_{PC}, Φ_{PC} are constant parameters. $E(t)$ in (2.46) is the time-varying elastance, defined as

$$E(t) = E_A e(t) + E_B\,, \tag{2.48}$$

where the constants E_A and E_B are the active and passive elastances, respectively, while $e(t)$ is the normalized time-varying elastance, taken as in [276] as

$$e(t) \equiv e_a(t) = \begin{cases} \frac{1}{2}\{1+\cos\left[\pi(t+T-t_{ar})/T_{arp}\right]\}\,, & 0 \le t \le t_{ar}+T_{arp}-T\,,\\ 0\,, & t_{ar}+T_{arp}-T < t \le t_{ac}\,,\\ \frac{1}{2}\{1-\cos\left[\pi(t-t_{ac})/T_{acp}\right]\}\,, & t_{ac} < t \le t_{ac}+T_{acp}\,,\\ \frac{1}{2}\{1+\cos\left[\pi(t-t_{ar})/T_{arp}\right]\}\,, & t_{ac}+T_{acp} < t \le T\,, \end{cases} \tag{2.49}$$

for atria and as

$$e(t) \equiv e_v(t) = \begin{cases} \frac{1}{2}\left[1-\cos(\pi t/T_{vcp})\right]\,, & 0 \le t \le T_{vcp}\,,\\ \frac{1}{2}\{1+\cos\left[\pi(t-T_{vcp})/T_{vrp}\right]\}\,, & T_{vcp} < t \le T_{vcp}+T_{vrp}\,,\\ 0\,, & T_{vcp}+T_{vrp} < t \le T\,, \end{cases} \tag{2.50}$$

for ventricles. T is the duration of a cardiac cycle; T_{acp}, T_{vcp}, T_{arp} and T_{vrp} represent the duration of atrial/ventricular contraction/relaxation while t_{ac} and t_{ar} are the times within the cardiac cycle at which atrial contraction and relaxation begin.

The modelling of cardiac valves is described in what follows. As each chamber of the heart contracts, blood is pushed through a valve either into another chamber or out of the heart into an artery (aorta or pulmonary). The four cardiac valves (tricuspid, pulmonary, mitral and aortic) ensure one-way blood flow by (a) opening to let blood through and (b) closing to prevent backflow. The mechanism that leads to opening or closure of a valve is driven by blood pressure changes as the heart contracts and relaxes. Such mechanism is modelled here following what described in Subsection 'Valves, Starling resistors and stenoses'. The pressure drop across each cardiac-valve length, defined as the pressure difference between the upstream and downstream pressures with respect to the valve direction, depends on the pressure in the neighbouring cardiac chambers and on the pressure in other compartments such as the aortic root and the pulmonary arterial compartment. In particular, the tricuspid and mitral valves are atrioventricular valves that prevent backflow of blood from the ventricles into the atria; in these cases, the upstream pressure is the pressure of the atrium while the downstream pressure is that of the ventricle. The pulmonary valve is located at the opening between the right ventricle and the pulmonary trunk, therefore its upstream and downstream pressures are the right ventricle and the arterial pulmonary pressure, respectively. Finally, the pressure drop across the aortic valve is determined by the difference between the left ventricle and the aortic root pressure. In Eq. (2.41), Δp_o and Δp_c are set to 0 for all the cardiac valves. Other parameters are defined later in Section 2.4.

Venous valves and Starling resistors

The Müller-Toro global model [201, 202] is equipped with submodels for venous valves and Starling resistors (SR) consisting of ideal diodes. In the present thesis, these elements are replaced with the model described in Subsection 'Valves, Starling resistors and stenoses' in Section 2.2.2.

Venous valves. Venous valves are placed at different locations of the venous network; each venous valve is located between two venous vessels and governs flow across this interface. Location of valves are reported in Table 2.5 and are related to the venous network depicted in Figures 2.2 and 2.3. We refer the reader to Section 2.3.7 for more details about the numerical coupling between 1D vessels and 0D valve models. In this case, the pressure drop which governs the flow rate across the valve is determined by the pressure difference between the upstream and downstream vessels with respect to the valve direction. Moreover, the annulus area A_a is assumed to be equal to the mean area between the reference areas of the connecting vessels on the right and left side. In the same way, the effective length l_e is taken as the mean diameter at equilibrium between the upstream and downstream vessels. Finally, Δp_o and Δp_c are set to 0.

Starling Resistors. Venous cerebral blood flow is ensured by a Starling resistor (SR) mechanism, a fluid dynamic construct which governs the flow in collapsible tubes exposed to variable external pressure. The Starling resistors act at the confluence of cortical veins in the dural sinuses; these are located in the dura mater and are more rigid than cerebral veins. During the large physiological fluctuations of the intracranial pressure, the Starling resistor mechanism prevents the vein collapse maintaining the blood pressure upstream the collapsed segment higher than the intracranial pressure.

In previous work, Starling resistors were described simply via ideal diodes [202]. Here we adopt a model that allows for a richer description of opening/closing dynamics, as well as accounting for a better description of underlying physical processes. In our venous network, Starling resistor behaviour is represented through the model proposed in Subsection 'Valves, Starling resistors and stenoses' in Section 2.2.2. The pairs of vessels between which each SR element is placed are reported in Table 2.5, where the left vessel index represents the number of the cortical vein while the right vessel index indicates the corresponding

venous sinus. As for the valves, we refer the reader to Section 2.3.7 for details on how the 1D vessels are numerically coupled to 0D SR models. The annulus area A_a and the effective length l_e are assumed to be the mean area and diameter, respectively, between the reference area and diameter at equilibrium of the pair of vessels connected to the Starling resistor element. The flow across Starling resistors is limited to that given by the pressure difference between the cerebral vein (upstream vessel) and the larger of intracranial pressure and the downstream pressure. When the intracranial pressure is much higher than the downstream pressure, the flow rate through the vessel becomes independent of the downstream pressure and the driving pressure difference is given by the upstream and the external pressures. As for other intracranial compartments, the external pressure is the intracranial pressure. Therefore, the valve state in Equation (2.41) is determined by $\Delta p - \Delta p_o = \Delta p - \Delta p_c = p_{down}(t) - p_{ext}(t)$, where p_{ext} is the intracranial pressure. If $p_{down}(t) < p_{ext}(t)$, in Equation (2.42), the driving pressure difference Δp is given by $\Delta p = p_{up} - p_{ext}$; on the other hand, if the downstream pressure is higher than the external pressure, the flow across the Starling resistor element is determined by the pressure difference between the upstream and downstream pressures $\Delta p = p_{up} - p_{down}$. Other parameters used in the valve and Starling resistor models are reported in Section 2.4.

Control system: cerebral autoregulation

We consider a model of the cerebrovascular regulation mechanisms, which acts by modifying resistances and compliances of the arterial microcirculation; changes in these parameters are not independent but are related through biomechanical and geometrical laws. The model is based on [305] and [234], with appropriate modifications. Only one control mechanism is considered in this work, the myogenic response, which is linked to changes in arterial pressure and cerebral blood flow. The original autoregulation model proposed in [305] reproduces also the metabolic response of cerebral autoregulation, which is linked to carbon dioxide reactivity and the amount of oxygen reaching the brain tissue. This mechanism is not included in the present thesis, as the current version of our model does not yet include a submodel for the transport of CO_2 and oxygen in the brain.

Cerebral myogenic autoregulation is activated by changes in cerebral blood flow; its action on the arterial microvasculature (arterioles and capillaries) includes a static gain G and first-order low-pass dynamics with a time constant τ. An increase in cerebral blood flow (CBF) causes vasoconstriction and, consequently, a decrease in compliance and an increase in resistance. The regulatory response is modelled by a sigmoidal static relationship with upper and lower levels to account for the limits of vasodilatation and vasoconstriction capacities.

The following differential equations describe the actions of autoregulation by means of first-order low-pass dynamics, time constants and gains

$$\tau \frac{dx_i}{dt} = -x_i + G_i \left(\frac{\overline{Q}_i - \overline{Q}_i^T}{\overline{Q}_i^T} \right) ; \tag{2.51}$$

x_i is the state variable of cerebral autoregulation of the i$-th$ cerebral terminal artery that responds to alteration of cerebral blood flow. G_i is the static gain for the i$-th$ cerebral terminal artery; it is evaluated from the total static gain of autoregulation G (which value will be defined in Section 2.4) according to the flow distribution inside the brain. $\overline{Q}_i$ is the time averaged flow and $\overline{Q}_i^T$ is the reference flow at the i-th terminal artery over the period $[t - T, t]$, where t is the current time and T is the cardiac cycle duration.

Once the control actions x_i of each i$-th$ terminal artery are found solving the ordinary differential equation (2.51), arterial compliances are defined through a sigmoidal relationship

$$C_i = \frac{\overline{C}_i \{(1 - \Delta C_i/2) + (1 + \Delta C_i/2) \exp[(-x_i)/k_i]\}}{1 + \exp[(-x_i)/k_i]} , \tag{2.52}$$

with upper and lower saturation levels. In this section, C_i, R_i and V_i stand for compliance (C_{al}, C_{cp}), resistance (R_{al}, R_{cp}) or volume of arteriolar and capillaries compartments (V_{al}, V_{cp}) that are in the vascular beds linked to the i$-th$ terminal artery, k_i is a constant parameter, inversely proportional to the central slope of the sigmoidal curve, $\overline{C}_i$ and ΔC_i are the central value and the amplitude of the sigmoidal curve. ΔC_i depends on whether vasodilation or vasoconstriction is considered and it is chosen for each terminal artery as follows

$$\begin{cases} \Delta C_i = 2sat_1\,,\ k_i = \overline{C}_i sat_1 & \text{if } x_i > 0\,, \\ \Delta C_i = 2sat_2\,,\ k_i = \overline{C}_i sat_2 & \text{if } x_i < 0\,, \end{cases} \tag{2.53}$$

where sat_1 and sat_2 are constant parameters that define the upper and lower saturation levels of the sigmoidal curve. According to the literature [147], the sigmoidal curve is not symmetrical; the increase in blood volume induced by vasodilation is higher than the blood volume decrease induced by vasoconstriction; therefore, two different values must be chosen for the parameter ΔC_i. From (2.52) and (2.53), it follows that the upper and lower saturation levels of the sigmoidal curve are $\overline{C}_i + \frac{sat_2}{2}$ and $\overline{C}_i - \frac{sat_1}{2}$, respectively.

The cerebrovascular control mechanisms affects not only the compliances, but also the arterial resistances. The variation of compliance in time changes the arterial volume. Since blood volume in a vessel, as a first approximation, is proportional to the radius squared ($V \propto r^2$), for a given vessel length, and vessel resistance is proportional to the inverse of radius to the power four ($R \propto 1/r^4$), volume varies according to the inverse square root of the resistance ($V \propto 1/\sqrt{R}$). Therefore, the following relationship is used to update the resistances of regulating arteries

$$\frac{\overline{V}_i}{\overline{V}_i^T} = \sqrt{\frac{\overline{R}_i^T}{R_i}}\,, \tag{2.54}$$

where $\overline{V}_i$ is the mean volume of the i-th arterial compartment (arterioles and capillaries) in the interval $[t - T, t]$, while $\overline{V}_i^T$ is the mean baseline condition volume, R_i is the current resistance of the arteriolar-capillaries compartment and $\overline{R}_i^T$ is the resistance under baseline conditions.

2.3 Numerical Methods

The 1D hyperbolic PDE system of blood flow equations (2.17) is solved using a high-order numerical scheme based on the ADER (Arbitrary high-order DERivatives Riemann solver) framework [294]. For an up to date review of ADER see [288] and references therein. The ADER scheme is based on three building blocks: nonlinear piecewise polynomial spatial reconstruction, solution of the generalized Riemann problem (GRP) at each cell interface to compute numerical fluctuations and space-time integration of the source term to compute the numerical source. In this work we apply the WENO spatial reconstruction technique as presented in [77]. It is worth mentioning that during this thesis work a novel spatial reconstruction scheme, called averaged-ENO (AENO) was developed. It results from a special averaging of the ENO polynomial and its closest neighbour, while retaining the stencil direction decided by the ENO choice. AENO turns out to be comparable to other well-known reconstruction technique, such as ENO and WENO. The thesis' author contributed to the development of AENO and its variant, called modified AENO (m-AENO). These works were published in [291, 198] and are not included in this thesis. As the GRP solver we use the Dumbser-Enaux-Toro (DET) solver proposed in [76] and extended to nonconservative systems in [80, 81]. Moreover, for the computation of the first-order numerical fluctuations we adopt the Riemann problem solver proposed in [205], which is a modification of the original Dumbser-Osher-Toro (DOT) [79] for constructing well-balanced fluctuations for a first order non-oscillatory scheme in the framework of path-conservative schemes. Full details of the schemes for the present appliaction are found in [205] .

The ADER scheme is an explicit numerical scheme; therefore, the so-called Courant-Friedrichs-Lewy (CFL) condition of stability must be satisfied defining the time step by ensuring that the CFL number is smaller than a given threshold. In previous works [201, 199], the same fixed CFL number is used for each 1D domain but a local choice of the time step could improve the accuracy of the method. The first example of local time stepping solver applied to blood flow can be found in [178] where each vessel is characterized by its specific time step and the coupling between neighbouring vessels occurs at a given synchronization step through an implicit Richardson-like iterative method. In [207], a local time stepping solver (LTS) for solving blood flow equations combined with a high-order coupling strategy between neighbouring vessels has been introduced. Here we follow [207], allowing an explicit local time-stepping temporal discretization of the underlying finite-volume type ADER scheme.

2.3.1 Path-conservative scheme

We present here the numerical scheme for a single 1D domain, the j-th vessel. For sake of clarity, we omit to evidence the dependence of the vessel index j, but we underline that all quantities defined in this section are related to the j-vessel. Moreover, we stress the fact that this is true also for the time iteration index n, since we apply a local time step strategy.

Each one-dimensional domain is divided into N computational cells $T_i = \left[x_{i-\frac{1}{2}}, x_{i+\frac{1}{2}}\right]$ for $i = 1, \dots, N$. The finite-volume type formulation of the problem obtained integrating the system of governing equations (2.9) in space and time in the control volume $\left[x_{i-\frac{1}{2}}, x_{i+\frac{1}{2}}\right] \times [t^n, t^{n+1}]$ is

$$\mathbf{Q}_i^{n+1} = \mathbf{Q}_i^n - \frac{\Delta t}{\Delta x}\left(\mathbf{D}^-_{i+\frac{1}{2}} + \mathbf{D}^+_{i-\frac{1}{2}}\right) + \Delta t \mathbf{S}_i - \Delta t \mathbf{G}_i^n \,, \tag{2.55}$$

where

$$\mathbf{Q}_i^n = \frac{1}{\Delta x}\int_{x_{i-\frac{1}{2}}}^{x_{i+\frac{1}{2}}} \mathbf{Q}(x, t^n)\, dx \,, \tag{2.56}$$

$$\mathbf{G}_i^n = \frac{1}{\Delta t \Delta x}\int_{t_n}^{t_{n+1}} \int_{x_{i-\frac{1}{2}}}^{x_{i+\frac{1}{2}}} \mathbf{A}(\mathbf{Q})\partial_x \mathbf{Q}\, dx\, dt \,, \tag{2.57}$$

$$\mathbf{S}_i = \frac{1}{\Delta t \Delta x}\int_{t_n}^{t_{n+1}} \int_{x_{i-\frac{1}{2}}}^{x_{i+\frac{1}{2}}} \mathbf{S}(\mathbf{Q}(x,t))\, dx\, dt \,, \tag{2.58}$$

$$\mathbf{D}^\pm_{i+\frac{1}{2}} = \frac{1}{\Delta t}\int_{t_n}^{t_{n+1}} \boldsymbol{D}^\pm_{i+\frac{1}{2}}\left(\mathbf{Q}^-_{i+\frac{1}{2}}(t), \mathbf{Q}^+_{i+\frac{1}{2}}(t), \Psi(s)\right) dt \,, \tag{2.59}$$

with $\Delta x = x_{i+\frac{1}{2}} - x_{i-\frac{1}{2}}$, $\Delta t = t^{n+1} - t^n$. Moreover, $\mathbf{Q}^\pm_{i+\frac{1}{2}}$ are limiting data states from left and right at the cell interface $x_{i+\frac{1}{2}}$. Given $\mathbf{Q}^-_{i+\frac{1}{2}}$ and $\mathbf{Q}^+_{i+\frac{1}{2}}$, $\boldsymbol{D}^\pm_{i+\frac{1}{2}}\left(\mathbf{Q}^-_{i+\frac{1}{2}}(t), \mathbf{Q}^+_{i+\frac{1}{2}}(t), \Psi(s)\right)$ are fluctuations that depend on the integration path $\Psi(\mathbf{Q}^-_{i+\frac{1}{2}}(t), \mathbf{Q}^+_{i+\frac{1}{2}}(t), s)$.

2.3.2 The numerical fluctuation

Fluctuations $\boldsymbol{D}^\pm_{i+\frac{1}{2}}$ in (2.59) arise from the solution of a Riemann problem at computational cell interfaces. Here, we adopt the DOT Riemann solver [79] for constructing well-balanced fluctuations for a first order non-oscillatory scheme in the framework of path-conservative schemes [205]. Fluctuations in the DOT solver are computed as

$$\boldsymbol{D}^\pm_{i+\frac{1}{2}} = \frac{1}{2}\int_0^1 \left(\mathbf{A}\left(\Psi(\mathbf{Q}^-_{i+\frac{1}{2}}, \mathbf{Q}^+_{i+\frac{1}{2}}, s)\right) \pm |\mathbf{A}\left(\Psi(\mathbf{Q}^-_{i+\frac{1}{2}}, \mathbf{Q}^+_{i+\frac{1}{2}}, s)\right)|\right) \frac{\partial \Psi}{\partial s}\, ds \,, \tag{2.60}$$

with absolute value operator of a matrix defined as

$$|\mathbf{A}(\mathbf{Q})| = \mathbf{R}(\mathbf{Q})|\Lambda(\mathbf{Q})|\mathbf{R}(\mathbf{Q})^{-1}\,, \tag{2.61}$$

where

$$|\Lambda(\mathbf{Q})| = diag(|\lambda_1|, |\lambda_2|, \ldots, |\lambda_6|)\,, \tag{2.62}$$

is the diagonal matrix formed by the eigenvalues of the underlying hyperbolic system of PDEs (2.17) while $\mathbf{R}$ and $\mathbf{R}^{-1}$ is the matrix of right eigenvectors and its inverse, respectively.

$\Psi = \Psi(\mathbf{Q}^-, \mathbf{Q}^+, s)$, with $0 \leq s \leq 1$, is the integration path, a Lipschitz continuous function that connects the left state $\mathbf{Q}^-$ to the right state $\mathbf{Q}^+$ in phase-space, satisfying

$$\Psi(\mathbf{Q}^-, \mathbf{Q}^+, 0) = \mathbf{Q}^-,\ \Psi(\mathbf{Q}^-, \mathbf{Q}^+, 1) = \mathbf{Q}^+\,. \tag{2.63}$$

In order to obtain a well-balanced scheme that correctly reproduces steady and unsteady states, we adopt the path proposed in [205], wherein a segment path is used for all variables except for the cross-sectional area; the used path reads

$$\Psi(s) = \begin{bmatrix} \overline{A}(s) \\ \overline{q}(s) \\ \overline{K}(s) \\ \overline{A_0}(s) \\ \overline{p_{ext}}(s) \\ \overline{\zeta}(s) \end{bmatrix} = \begin{bmatrix} \overline{A}(s) \\ q^-_{i+\frac{1}{2}} + s(q^+_{i+\frac{1}{2}} - q^-_{i+\frac{1}{2}}) \\ K^-_{i+\frac{1}{2}} + s(K^+_{i+\frac{1}{2}} - K^-_{i+\frac{1}{2}}) \\ A^-_{0,i+\frac{1}{2}} + s(A^+_{0,i+\frac{1}{2}} - A^-_{0,i+\frac{1}{2}}) \\ p^-_{ext,i+\frac{1}{2}} + s(p^+_{ext,i+\frac{1}{2}} - p^-_{ext,i+\frac{1}{2}}) \\ \zeta^-_{i+\frac{1}{2}} + s(\zeta^+_{i+\frac{1}{2}} - \zeta^-_{i+\frac{1}{2}}) \end{bmatrix}. \tag{2.64}$$

$\overline{A}(s)$ is obtained from the arch joining two states $A^-_{i+\frac{1}{2}}$ and $A^+_{i+\frac{1}{2}}$, through the curve defined by Riemann invariant Γ^{LD}_1 of the linearly degenerated field in Eq. (2.36). $\overline{A}(s)$ can be obtained as an implicit function of Φ from (2.4), which in turn is computed as

$$\overline{\Phi}(s) = \frac{\overline{\Gamma}^{LD}_1(s) - \overline{p_{ext}}(s)}{\overline{K}(s)}\,, \tag{2.65}$$

with

$$\overline{\Gamma}^{LD}_1(s) = \Gamma^{LD,-}_{1,i+\frac{1}{2}} + s\left(\Gamma^{LD,+}_{1,i+\frac{1}{2}} - \Gamma^{LD,-}_{1,i+\frac{1}{2}}\right). \tag{2.66}$$

The integral for the DOT solver using the proposed path is performed numerically and reads

$$\boldsymbol{D}^{\pm}_{i+\frac{1}{2}} = \frac{1}{2}\left(\sum_{j=1}^{G} \omega_j \left\{ \left(\mathbf{A}\left(\Psi(s_j)\right) \pm |\mathbf{A}\left(\Psi(s_j)\right)|\right) \frac{\partial \Psi}{\partial s}\bigg|_{s_j} \right\}\right), \tag{2.67}$$

where ω_j and s_j are the j-th weight and coordinate of a Gaussian quadrature rule with G points. Note that, because of this choice of the path, vector $\frac{\partial \Psi}{\partial s}$ cannot be taken out of the integral (2.60); derivatives for most variables are easily computed, besides that for $\overline{A}(s)$, which is an implicit function of Φ so that its derivative at each quadrature point $s = s_j$ is computed as

$$\frac{\partial \overline{A}}{\partial s}(s_j) = \left(\frac{\partial \overline{\Phi}}{\partial s}(s_j) - \frac{\partial \overline{\Phi}}{\partial \overline{A_0}}\bigg|_{s=s_j} \frac{\partial \overline{A_0}}{\partial s}(s_j)\right)\left(\frac{\partial \overline{\Phi}}{\partial \overline{A}}\bigg|_{s=s_j}\right)^{-1}. \tag{2.68}$$

2.3.3 The ADER-DET scheme

We proceed with a brief explanation of the steps followed for the implementation of the ADER scheme with the DET solver. For the spatial reconstruction, we use the WENO methodology proposed in [77]. We introduce reference coordinates $0 \leq \chi \leq 1$ given by $x = x_{i-\frac{1}{2}} + \chi \Delta x_i$. For a scheme of order k, at time level t^n, a reconstruction operator is computed

$$\mathbf{w}_h = \mathbf{w}_h(\chi, t^n) = \sum_{l=1}^{M+1} \phi_l(\chi) \hat{\mathbf{w}}_l(t^n) \,. \tag{2.69}$$

$M = k-1$ is the polynomial degree, $\phi_l(\chi)$, $l = 1, \ldots, M+1$ are the corresponding basis functions and $\hat{\mathbf{w}}_l(t^n)$, $l = 1, \ldots, M+1$, are the expansion coefficients at time $t = t^n$.
The spatial reconstruction is performed on a set of stencils defined as

$$S_i^s = \bigcup_{e=i-L}^{i+R} T_e \,, \tag{2.70}$$

where L and R are the stencil extents to the left and to the right. In particular, for odd order schemes, we use three stencils, central ($s = 1$, $L = R = M/2$), fully left-sided ($s = 2$, $L = M$, $R = 0$) and a fully-right sided stencil ($s = 3$, $L = 0$, $R = M$); on the other hand, for even order schemes, we use four stencils, two central stencils ($s = 0$, $L = floor(M/2)+1$, $R = floor(M/2)$, $s = 1$, $L = floor(M/2)$, $R = floor(M/2)+1$) and the other ones fully left and right sided ($s = 2$, $L = M$, $R = 0$, $s = 3$, $L = 0$, $R = M$). For each element T_e inside the stencil S_i^s, the reconstructed polynomial is computed requiring integral conservation

$$\int_{T_j} \mathbf{w}_h^s(\chi, t^n)\, d\chi = \hat{\mathbf{w}}_l^s(t^n) \int_{T_j} \phi_l(\chi)\, d\chi = \mathbf{Q}_j^n \quad \forall T_j \in S_i^s \,. \tag{2.71}$$

This equation leads to a linear system for unknown coefficients $\hat{\mathbf{w}}_l^s(t^n)$; we compute $\hat{\mathbf{w}}_l(t^n)$ as

$$\hat{\mathbf{w}}_l(t^n) = \sum_{s=1}^{N_s} \omega_s \hat{\mathbf{w}}_l^s(t^n) \,, \tag{2.72}$$

where N_s is the total number of stencils used and ω_s are nonlinear weights given by relations

$$\omega_s = \frac{\tilde{\omega}_s}{\tilde{\omega}_0 + \tilde{\omega}_{-k} + \tilde{\omega}_k} \,, \tag{2.73}$$

$$\tilde{\omega}_s = \frac{\lambda_s}{(\sigma_s + \epsilon)^r} \,, \tag{2.74}$$

$$\sigma_s = \sum_{l=1}^{M} \int_0^1 \left(\frac{\partial^l}{\partial \chi^l} \mathbf{w}_h^s(\chi, t^n) \right)^2 d\chi \,. \tag{2.75}$$

ϵ and r are constants, generally taken as $\epsilon = 10^{-14}$ and $r = 8$; for linear weights one usually takes $\lambda_0 = 10^5$, $\lambda_{-k} = 1$ and $\lambda_k = 1$. When we apply the reconstruction procedure for any order of accuracy greater than one, we need computational cells to both sides of the cell of the reconstruction stencil but in the case of cells near the boundaries, the stencil will fall outside the 1D domain. Therefore, ghost cells are necessary. This aspect was addressed in [203] and will be briefly illustrated in Section 2.3.6. Moreover, application of WENO reconstruction operator is not straightforward if well-balancing is to be preserved. Full details for how to address this issue are given in [207].

Once that the spatial reconstruction is available, we can define a generalized Riemann problem (GRP) at the cell interface $x = x_{i+\frac{1}{2}}$ (locally at $x = 0$) with initial data given by the piecewise polynomials at both sides of the cell interface

$$\begin{cases} \partial_t \mathbf{Q} + \mathbf{A}(\mathbf{Q}) \partial_x \mathbf{Q} = \mathbf{S}(\mathbf{Q}) & x \in R \,,\ t > t^n \,, \\ \mathbf{Q}(x,0) = \begin{cases} \mathbf{w}_i(x, t^n) & \text{if } x < 0 \,, \\ \mathbf{w}_{i+1}(x, t^n) & \text{if } x > 0 \,. \end{cases} \end{cases} \tag{2.76}$$

The DET solver is characterized by a local data evolution at both sides of the cell interface in order to obtain space-time predictions and the solution of the classical Riemann problems at points along $x/t = 0$. A distinct feature of the DET solver is the time evolution of the initial data left and right of the interface by a space-time local discontinuous-Galerkin scheme, which provides local space-time polynomial $\mathbf{Q}_h = \mathbf{Q}_h(x,t)$ to be later used to approximate integrals in (2.11) and (2.13).

We start by transforming system (2.17) to a reference space-time element $T_E = [0;1] \times [0;1]$ with normal coordinates χ and τ related to the physical domain by $x = x_{i+\frac{1}{2}} + \Delta x_i \chi$ and $t = t^n + \Delta t^n \tau$. The resulting system reads

$$\partial_t \mathbf{Q}_h + \mathbf{A}^* \partial_\chi \mathbf{Q}_h = \mathbf{S}^*, \tag{2.77}$$

with modified coefficient matrix and source term vector

$$\mathbf{A}^* = \frac{\Delta t^n}{\Delta x} \mathbf{A}(\mathbf{Q}_h), \qquad \mathbf{S}^* = \Delta t^n \mathbf{S}(\mathbf{Q}_h)\,. \tag{2.78}$$

In order to simplify the notation, we introduce

$$[a,b]^\tau = \int_0^1 a(\chi,\tau) b(\chi,\tau)\, d\chi\,, \tag{2.79}$$

$$< a,b >_{T_E} = \int_0^1 \int_0^1 a(\chi,\tau) b(\chi,\tau)\, d\chi\, d\tau\,. \tag{2.80}$$

Multiplying by a space-time basis function $\theta(\chi,\tau)$ and integrating over the reference element, we obtain

$$[\theta, \mathbf{Q}_h]^1 - < \partial_\tau \theta, \mathbf{Q}_h >_{T_E} + < \theta, \mathbf{A}^* \partial_\chi \mathbf{Q}_h >_{T_E} = [\theta, \mathbf{w}_h]^0 + < \theta, \mathbf{S}^* >_{T_E}\,. \tag{2.81}$$

The same space-time basis functions θ are used for $\mathbf{Q}_h$, $\mathbf{A}^* \partial_\chi \mathbf{Q}_h$ and $\mathbf{S}^*$, so that

$$\mathbf{Q}_h(\chi,\tau) = \sum_{l=1}^{(M+1)^2} \theta_l \hat{\mathbf{Q}}_l\,,$$

$$\mathbf{A}^* \partial_\chi \mathbf{Q}_h(\chi,\tau) \sum_{l=1}^{(M+1)^2} \theta_l \widehat{\mathbf{A}^* \partial_\chi \mathbf{Q}}_l\,,$$

$$\mathbf{S}^*(\chi,\tau) = \sum_{l=1}^{(M+1)^2} \theta_l \hat{\mathbf{S}}^*_l\,,$$

where $\hat{\mathbf{S}}^*_l = \Delta t^n \mathbf{S}(\hat{\mathbf{Q}}_l)$. At each iteration step m we solve the following system of non-linear algebraic equations by the fixed point iteration procedure

$$\left([\theta_k,\theta_l]^1 - < \partial_\tau \theta_k, \theta_l >_{T_E}\right) \hat{\mathbf{Q}}_l^{m+1} - < \theta_k, \theta_l >_{T_E} \hat{\mathbf{S}}^*{}_l^{m+1} = [\theta_k, \phi_l]^0 \widehat{\mathbf{w}}_l - < \theta_k, \theta_l >_{T_E} \widehat{\mathbf{A}^* \partial_\chi \mathbf{Q}}_l^m\,, \tag{2.82}$$

for $k = 1, \ldots, (M+1)^2$.

Once that $\hat{\mathbf{Q}}_l$ are available for all computational cells, the solution to the GRP at time $t \in [t^n, t^n + \Delta t^n]$ is found by solving classical Riemann problems (as many as necessary according to the quadrature rule used to approximate the integral in time) using the space-time reconstructed states at both sides of the cell interface. The source term space-time average and the non-conservative product space-time average are now computed by numerical integration using a quadrature rule of appropriate accuracy; as basis functions θ we adopt a nodal basis function given by Gauss-Lobatto quadrature points and the corresponding Lagrange polynomials.

In order to ensure that the local truncation error of the numerical solution of (2.17) with space-time order of accuracy k is smaller than the formulation error with respect to the original advection-diffusion-reaction problem, the following sufficiency criterion, proposed in [199], must be satisfied

$$\Delta := \frac{\epsilon}{(\Delta x)^k} \frac{1 - 2^{\frac{-1}{2}}}{2^{k-\frac{1}{2}} - 1} = O(1)\,, \tag{2.83}$$

where Δx is the characteristic size of the computational cells and ϵ is the relaxation parameter.

2.3.4 Local time stepping

Within the context of the ADER finite-volume type schemes, we adopt the high-order Local Time Stepping (LTS) scheme presented in [207]. As observed before, the numerical scheme used in this work is explicit in time. Therefore, the Courant-Friedrichs-Lewy (CFL) condition must be satisfied in each computational cell to guarantee numerical stability. In the context of the LTS technique adopted here, each vessel is allowed to evolve in time according to its local stability criteria.

Let us assume to work with a network of N_v vessels in which each one evolves with its local time step. At the beginning of the simulation, we set the initial local time step for each j-th vessel

$$\Delta t_j^0 = \frac{\Delta t_{max}}{2^{k_j^0}}, \tag{2.84}$$

where

$$k_j^0 = \left\lceil \frac{\log(\Delta t_{max}/\widetilde{\Delta t}_j^0)}{\log(2)} \right\rceil, \tag{2.85}$$

$\widetilde{\Delta t}_j^0$ is the vessel time step at t_j^0, given by the CFL condition of the numerical scheme (in this work, CFL = 0.9), while Δt_{max} is a user-defined value (fixed or changed adaptively during the simulation). We refer the reader to [207] for a detailed description of the local time stepping procedure; here we briefly summarize the main steps for updating the local time step of the j-th vessel at the general n_j-th time iteration. At time level $t_j^{n_j}$, we evaluate

$$\widetilde{\Delta t}_j^{n_j} = CFL \frac{\tilde{\lambda}_j^{n_j}}{\Delta x_j}, \tag{2.86}$$

where

$$\tilde{\lambda}_j^{n_j} = \max_{i=1,\dots,N_j} \left(|u_{j,i}^{n_j}| + \tilde{c}\left(A_{j,i}^{n_j}, \zeta_{j,i}^{n_j}\right) \right), \tag{2.87}$$

with N_j the total number of computational cells of the j-th vessel. Then, we calculate

$$\Delta t_j^{n_j} = \frac{\Delta t_{max}}{2^{k_j^{n_j}}}, \tag{2.88}$$

where

$$k_j^{n_j} = \left\lceil \frac{\log(\Delta t_{max}/\widetilde{\Delta t}_j^{n_j})}{\log(2)} \right\rceil. \tag{2.89}$$

Once these quantities are computed, we have to verify if the resulting time step fullfils the global CFL condition. To that end, we set the local variables in this way

$$CFL_{loc} = \tilde{\lambda}_j^{n_j} \frac{\Delta t_j^{n_j}}{\Delta x_j}, \tag{2.90}$$

$$\Delta t_{loc} = \Delta t_j^{n_j}, \tag{2.91}$$

$$k_{loc} = k_j^{n_j}. \tag{2.92}$$

If CFL_{loc} number exceeds the CFL condition of the numerical scheme, the time step must be reduced. Therefore, we change it until CFL_{loc} results equal or less than CFL, namely we iterate as follows until $CFL_{loc} \leq CFL$:

$$k_{loc} = k_{loc} + 1, \tag{2.93}$$

$$\Delta t_{loc} = \min\left(\Delta t_{max}, \frac{\Delta t_{max}}{2^{k_{loc}}}\right), \tag{2.94}$$

$$CFL_{loc} = \tilde{\lambda}_j^{n_j} \frac{\Delta t_{loc}}{\Delta x_j}. \tag{2.95}$$

On the contrary, if $CFL_{loc} < CFL$, the local time step might be increased. Particular attention is needed in this case for the synchronization of the solution at junctions. As long as $CFL_{loc} < CFL$, we iterate as follows:

$$k_{loc} = k_{loc} - 1\,, \tag{2.96}$$

$$\Delta t_{loc} = \min\left(\Delta t_{max}, \frac{\Delta t_{max}}{2^{k_{loc}}}\right), \tag{2.97}$$

$$CFL_{loc} = \tilde{\lambda}_j^{n_j} \frac{\Delta t_{loc}}{\Delta x_j}. \tag{2.98}$$

After that, we set

$$k_{loc} = k_{loc} + 1\,, \tag{2.99}$$

$$\Delta t_{loc} = \min\left(\Delta t_{max}, \frac{\Delta t_{max}}{2^{k_{loc}}}\right). \tag{2.100}$$

The procedure used to update the local time takes into account the synchronization criteria of the solution at junctions; for this reason the time step can be updated only if the new time level $t_j^{n_j} + \Delta t_{loc}$ is a multiple of Δt_{max}. If the condition is not satisfied, the time step is set to be equal to (2.84). In practice, for the j-th vessel to evolve from $t_j^{n_j}$ to $t_j^{n_j+1}$, the following criteria must be fulfilled

$$t_j^{n_j} + \Delta t_j^{n_j} \leq \min_{m=1,\dots,N_{j,neigh}} (t_m^{n_m} + \Delta t_m^{n_m})\,, \tag{2.101}$$

where $N_{j,neigh}$ is the set of vessels that share a junction with the j-th vessel. This relation is necessary to guarantee that the information to evaluate the fluctuations at the boundary of a vessel is available for the entire time step, as explained in the following section.

2.3.5 The coupling of vessels

The coupling of several 1D vessels is treated using the methodology proposed in [203] and [207]; here we formulate it for the case of N_P vessels converging at node P. In the case of boundary cell interfaces at junctions, the predicted states are only available at one side of the interface; in these cases, fluctuations for the j-th vessel at time step n_j are computed as

$$\mathbf{D}^+_{j,1-\frac{1}{2}} = \frac{1}{\Delta t_j^{n_j}} \int_{t_j^{n_j}}^{t_j^{n_j+1}} \boldsymbol{D}^+_{j,1-\frac{1}{2}} \left(\mathbf{Q}^*_{j,1-\frac{1}{2}}(t), \mathbf{Q}^h_{j,1}(0, (t - t_j^{n_j})/\Delta t_j^{n_j}), \Psi\right) dt\,, \tag{2.102}$$

for a cell located at $x_j = 0$ and

$$\mathbf{D}^-_{j,N_j+\frac{1}{2}} = \frac{1}{\Delta t_j^{n_j}} \int_{t_j^{n_j}}^{t_j^{n_j+1}} \boldsymbol{D}^-_{j,N_j+\frac{1}{2}} \left(\mathbf{Q}^h_{j,N_j}(1, (t - t_j^{n_j})/\Delta t_j^{n_j}), \mathbf{Q}^*_{j,N_j+\frac{1}{2}}(t), \Psi\right) dt\,, \tag{2.103}$$

for a cell interface located at $x_j = L_j$. $\mathbf{Q}^h_{j,i}$ are the predicted space-time polynomials for j-th vessel and i-th cell obtained by the DET solver and evaluated at $\chi = 0$ and $\chi = 1$ for fluctuations computed at $x_j = 0$ and $x_j = L_j$, respectively. L_j and N_j are the length and number of computational cells of the j-th vessel, respectively. $\mathbf{Q}^*_{1-\frac{1}{2}}(t)$ and $\mathbf{Q}^*_{N+\frac{1}{2}}(t)$ are still to be defined.

Since each vessel is advancing in time with its own time step, integrals (2.102) and (2.103) have to be computed as the sum of partial integrals. Each of these partial integrals at a given junction will be performed using a Gauss-Lobatto integration rule. For each quadrature point at a junction shared by N_P vessels, we can define a Riemann problem at time t_c as

$$\begin{cases} \partial_t \mathbf{Q}_k + \mathbf{A}_k(\mathbf{Q}_k)\partial_x \mathbf{Q}_k = \mathbf{S}_k(\mathbf{Q}_k),\ x_k \in \mathrm{R},\ t > t_c\,, \\ \mathbf{Q}_k(t_c) = \mathbf{Q}^h_{k,\hat{i}_k}(\chi_{\hat{i}_k}, (t_c - t_k^{n_k})/\Delta t_k^{n_k})\,, \end{cases} \tag{2.104}$$

for $k = 1, ..., N_P$, with $\hat{i}_k = 1$ if the k-th vessel shares its first computational cell with the junction node ($x_k = 0$) or $\hat{i}_k = N_k$ if the shared cell is the last one ($x_k = L_k$). Consequently, $\chi_1 = 0$ and $\chi_{N_k} = 1$. This system cannot be recast in conservative form, so we use a two-rarefaction type Riemann solver. Note that in the case of system that admits a conservative form, appropriate wave relations for shocks (derived from Rankine-Hugoniot conditions) can be enforced. The unknown state vectors $\mathbf{Q}^*_{k,\hat{i}_k}$ are computed solving a system of $3N_P$ non-linear equations that reads

$$\begin{cases} \sum_{k=1}^{N_P} g_k A^*_{k,\hat{i}_k} u^*_{k,\hat{i}_k} = 0\,, \\ \tilde{p}(A^*_{1,\hat{i}_1}) + \frac{1}{2}\rho(u^*_{1,\hat{i}_1})^2 - \tilde{p}(A^*_{k,\hat{i}_k}) - \frac{1}{2}\rho(u^*_{k,\hat{i}_k})^2 = 0\,,\ k = 2, \dots, N_P\,, \\ u^*_{k,\hat{i}_k} - u^h_{k,\hat{i}_k}(\chi_{\hat{i}_k}, (t_c - t_k^{n_k})/\Delta t_k^{n_k}) + g_k \beta_k\,,\ k = 1, \dots, N_P\,, \\ \zeta^*_{k,\hat{i}_k} + \frac{A^*_{k,\hat{i}_k}}{\epsilon_k} - \zeta^h_{k,\hat{i}_k}(\chi_{\hat{i}_k}, (t_c - t_k^{n_k})/\Delta t_k^{n_k}) - \frac{A^h_{k,\hat{i}_k}(\chi_{\hat{i}_k}, (t_c - t_k^{n_k})/\Delta t_k^{n_k})}{\epsilon_k} = 0,\ k = 1, \dots, N_P\,, \end{cases} \tag{2.105}$$

where

$$\beta_k = \int_{A^h_{k,\hat{i}_k}(\chi_{\hat{i}_k}, (t_c - t_k^{n_k})/\Delta t_k^{n_k})}^{A^*_{k,\hat{i}_k}} \frac{c(\tau)}{\tau} d\tau \tag{2.106}$$

and

$$g_k = \begin{cases} 1, & \text{if } x_k = L_k\,, \\ -1 & \text{if } x_k = 0\,. \end{cases} \tag{2.107}$$

If space-time predictions for all N_P vessels sharing a node are available at time t_c, then a Riemann problem at a junction can be defined and solved, so we can find the needed states for the computation of first-order fluctuations at specified quadrature points for a partial integral of (2.102) and (2.103).

Remark. In order to ensure mass conservation at a discrete level, we replace the first component of integrands in (2.102) and (2.103) by

$$\begin{cases} \boldsymbol{D}^+_{j,1-\frac{1}{2}}\left(\mathbf{Q}^*_{j,1-\frac{1}{2}}(t), \mathbf{Q}^h_{j,1}(0, (t - t_j^{n_j})/\Delta t_j^{n_j}), \Psi\right)[1] = q^h_{k,\hat{i}_k}(\chi_{\hat{i}_k}, (t_c - t_k^{n_k})/\Delta t_k^{n_k}) - q^*_{k,\hat{i}_k}\,, \\ \boldsymbol{D}^-_{j,N_j+\frac{1}{2}}\left(\mathbf{Q}^h_{j,N_j}(1, (t - t_j^{n_j})/\Delta t_j^{n_j}), \mathbf{Q}^*_{j,N_j+\frac{1}{2}}(t), \Psi\right)[1] = q^*_{k,\hat{i}_k} - q^h_{k,\hat{i}_k}(\chi_{\hat{i}_k}, (t_c - t_k^{n_k})/\Delta t_k^{n_k})\,. \end{cases} \tag{2.108}$$

Such approach enforces that mass exchange between vessels is based on flows $q^*_{k,\hat{i}_k}$, which in turn satisfy mass conservation according to first condition in (2.105). See [79] for further details.

2.3.6 Ghost cell for spatial reconstruction

The WENO reconstruction procedure requires, at each time step, the state variable value at M ghost cells at each side for one dimensional domain. In order to obtain an accurate approximation of the solution outside the domain used to evaluate the cell averages of ghost cells, we use a Taylor series expansion around the vertex P shared by the j-th vessel [207]. So, given δ, a local spatial coordinate with origin in P, the extrapolated state vector is

$$\mathbf{Q}^g_j(\delta, t_j^{n_j}) = \mathbf{Q}^*_{j,\hat{i}_j}(t_j^{n_j - 1} + \Delta t_j^{n_j - 1}) + \sum_{r=1}^{M} \frac{1}{r!} \partial_x^{(r)} \mathbf{Q}^*_{j,\hat{i}_j}(t_j^{n_j - 1} + \Delta t_j^{n_j - 1}) \delta^r\,, \tag{2.109}$$

where $\mathbf{Q}^*_{j,\hat{i}_j}(t_j^{n_j-1}+\Delta t_j^{n_j-1})$ is the solution of the Riemann problem at a junction described in the previous section. Spatial derivatives $\partial_x^{(r)}\mathbf{Q}^*_{j,\hat{i}_j}(t_j^{n_j-1}+\Delta t_j^{n_j-1})$ are computed from a linearized version of the original PDE system by a procedure inspired in the Titarev–Toro generalized Riemann problem solver [296]. The following Riemann problem is solved

$$\begin{cases} \partial_t\left(\partial_x^{(r)}\mathbf{Q}_k(t_j^{n_j-1}+\Delta t_j^{n_j-1})\right)+\bar{\mathbf{A}}_k\partial_x\left(\partial_x^{(r)}\mathbf{Q}_k(t_j^{n_j-1}+\Delta t_j^{n_j-1})\right)=0 \quad x\in R\,,\ t>t_j^{n_j-1}+\Delta t_j^{n_j-1}\,, \\ \partial_x^{(r)}\mathbf{Q}_k(t_j^{n_j-1}+\Delta t_j^{n_j-1})=\partial_x^{(r)}\mathbf{Q}^h_{k,\hat{i}_k}(\chi_{\hat{i}_k},(t_j^{n_j-1}-t_k^{n_k})/\Delta t_k^{n_k})\,, \end{cases} \tag{2.110}$$

for $k=1,\dots,N_P$. $\bar{\mathbf{A}}_k$ is the linearized coefficient matrix

$$\bar{\mathbf{A}}_k=\mathbf{A}\left(\mathbf{Q}^*_{k,\hat{i}_k}\left(t_j^{n_j-1}+\Delta t_j^{n_j-1}\right)\right). \tag{2.111}$$

Note that we use index k to put in evidence the fact that in order to compute spatial gradients for the j-th vessel we solve a linear Riemann problem involving the spatial gradients of the predicted space-time polynomials of all vessels shared by junction P and evaluated at the time $t_j^{n_j-1}+\Delta t_j^{n_j-1}$. Initial conditions for this problem are directly taken from implicit discontinuous Galerkin prediction of the previous time step by recursively considering

$$<\theta_k,\theta_l>\widehat{\partial_\chi^{(r)}\mathbf{Q}_l}=<\theta_k,\partial_\chi\theta_l>\widehat{\partial_\chi^{(r-1)}\mathbf{Q}_l}\,, \tag{2.112}$$

with $r=1,\dots,M$ and $l=1,\dots,(M+1)^2$. For a second order scheme, the computational cost of solving the Riemann problem for linearized system is only one linear system of $3N_P$ unknowns.

2.3.7 1D-0D coupling

First we address the case of a 1D vessel coupled to a 0D model of the microvasculature. Let's suppose that the j-th vessel shares the interface of its last computational cell N_j with a zero-dimensional sub-model of the microvasculature, with a proximal resistance R_p connected to one dimensional domain, followed by a compliant compartment with pressure $P_{lumped}(t)$. In order to compute fluctuations at the boundary, $\mathbf{Q}^*_{j,N_j+\frac{1}{2}}(t)$ must be known at each quadrature point t_c for time integral (2.103), while $\mathbf{Q}^h_{j,N_j}(1,(t-t_j^{n_j})/\Delta t_j^{n_j})$ is delivered by the DET prediction step. $\mathbf{Q}^*_{j,N_j+\frac{1}{2}}(t)$ is obtained by solving the following system of equations

$$\begin{cases} A^*_{j,N_j+\frac{1}{2}}u^*_{j,N_j+\frac{1}{2}}-\dfrac{p(A^*_{j,N_j+\frac{1}{2}})-P_{lumped}(t)}{R_p}=0, \\ \dfrac{q^*_{j,N_j+\frac{1}{2}}}{A^*_{j,N_j+\frac{1}{2}}}-\dfrac{q^h_{j,N_j}(1,(t_c-t_j^{n_j})/\Delta t_j^{n_j})}{A^h_{j,N_j}(1,(t_c-t_j^{n_j})/\Delta t_j^{n_j})}+\beta_j=0, \\ \zeta^*_{j,N_j+\frac{1}{2}}+\dfrac{A^*_{j,N_j+\frac{1}{2}}}{\epsilon_j}-\zeta^h_{j,N_j}(1,(t_c-t_j^{n_j})/\Delta t_j^{n_j})-\dfrac{A^h_{j,N_j}(1,(t_c-t_j^{n_j})/\Delta t_j^{n_j})}{\epsilon_j}=0, \end{cases} \tag{2.113}$$

with β_j defined as in Equation (2.106). As for the case of coupling vessels at a junction, the first component of the integrand in (2.103) is replaced by the flux difference form using obtained flow rate $q^*_{j,N_j+\frac{1}{2}}=A^*_{j,N_j+\frac{1}{2}}u^*_{j,N_j+\frac{1}{2}}$, in order to ensure mass conservation at a discrete level. The case of a vessel sharing its first computational cell with the microvasculature is analogous to this one, changing only the Riemann invariants to be enforced.

Now we consider the case of a 1D vessel coupled to a valve or Starling resistor 0D model. This case is analogous to the one presented in the previously. However, in this case the valve or Starling resistor model is directly providing one of the state variables to be enforced at the interface, namely the flow rate.

Therefore, in this case we only need to find the unknown area $A^*_{j,N_j+\frac{1}{2}}$ and auxiliary variable $\zeta^*_{j,N_j+\frac{1}{2}}$. For example, for a vessel sharing its last computational cell with a valve or Starling resistor model we have

$$\begin{cases} \frac{q_{0D}}{A^*_{j,N_j+\frac{1}{2}}} - \frac{q^h_{j,N_j}(1,(t_c-t_j^{n_j})/\Delta t_j^{n_j})}{A^h_{j,N_j}(1,(t_c-t_j^{n_j})/\Delta t_j^{n_j})} + \beta_j = 0, \\ \zeta^*_{j,N_j+\frac{1}{2}} + \frac{A^*_{j,N_j+\frac{1}{2}}}{\epsilon_j} - \zeta^h_{j,N_j}(1,(t_c-t_j^{n_j})/\Delta t_j^{n_j}) - \frac{A^h_{j,N_j}(1,(t_c-t_j^{n_j})/\Delta t_j^{n_j})}{\epsilon_j} = 0, \end{cases} \tag{2.114}$$

where q_{0D} is the flow rate provided by the 0D valve or Starling resistor model. Also in this case we replace the first component of the integrand in (2.103) by the flux difference form in order to ensure mass conservation at a discrete level.

2.4 Parametrization of the model

In this section we present all the parameters needed for the implementation of the global closed-loop model. The parameters assignment correspond to a healthy young male subject. We underline that the parameters are, unless otherwise specified, the ones proposed in [201, 202].

Arteries and veins. The 1D vascular network contains 323 one-dimensional segments, of which 98 are arteries and 209 are veins, all linked by 143 junctions. Figure 2.2 shows a schematic representation of such networks, while Figures 2.3 (A) and 2.3 (B) provide a detailed description of head and neck arteries and veins. Compared to the network used in [201, 202], in the present thesis we propose a detailed description of the highly vascularized regions of the posterior part of the brain. Blood supply to the brainstem is crucial for the function of sensory and motor pathways, as the nerve connections of these systems from the main part of the brain to the rest of the body pass through it. More importantly, the brainstem plays a key role in maintaining cardiac and respiratory functions, such as heart rate and breathing. Three main arteries supply blood to the cerebellum: the superior cerebellar artery (SCA), the anterior inferior cerebellar artery (AICA) and the posterior inferior cerebellar artery (PICA). AICA (No. 304, 305, 306, 307) was previously included in our model for the ear circulation network [297]; the other arteries are added here using data from the ADAN network [29] and from the literature [213]. PICA (No. 285, 286, 310, 311) arises from the vertebral artery at about 15 mm from the vertebrobasilar junction. SCA (No. 287, 288) arises from the basilar artery near the bifurcation of the basilar into the posterior cerebral artery. The brainstem is supplied by the medullary branch of the posterior inferior cerebellar artery (No. 308, 309), the anterior spinal artery (No. 312, 313), which arises from the terminal part of the vertebral artery and the pontine arteries (No. 316, 317, 318, 319), lateral branches from the basilar artery that supply the pons. All these arteries end in the vascular beds of the cerebellum and brainstem.

According to experimental observations [314, 73, 131], the mean value of blood flow to the cerebellum and the brainstem is about 10% of the total cerebral blood flow. Following [314], we estimate that flow to the cerebellum and to the brainstem are 1.01 ml/s and 0.13 ml/s, respectively. The posterior part of the brain is drained by the group of cerebellar veins, such as the superior cerebellar veins and the inferior cerebellar veins. In this work, the intricate venous vasculature is represented by three main veins: the superior vermian vein (No. 289, 290), the superior petrosal vein (No. 298 299, 300, 301) in the superior part and the inferior vermian vein (No. 291, 292, 295, 296) in inferior area. The superior vermian vein drains into the vein of Galen (No. 106), the superior petrosal vein drains into the petrous sinus (No. 111, 112) while the inferior vermian vein drains into the transverse sinus (No. 101, 102). The addition of the posterior brain vasculature is essential to explore some medical conditions that affect the brainstem and the cerebellum, such as the effect of vertebral artery hypoplasia in the ipsilateral posterior inferior cerebellar artery

FIGURE 2.2: Arterial and venous network composed of 114 arteries and 209 veins; numbers refer to those used in Tables A.1 and A.2.

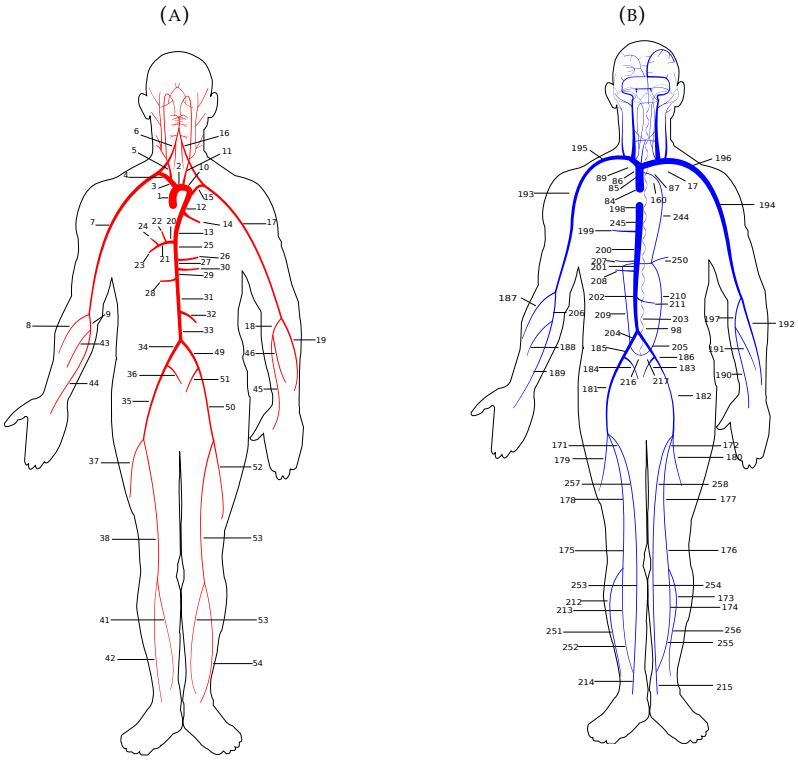

[286]. Moreover, in order to analyze better the implications of venous strictures in the pathophysiology of Ménière's disease, we redefine the ear vasculature previously included in [297]. The ear is mainly supplied by the labyrinthine artery [188, 316, 269], which arises from the anterior inferior cerebellar artery, passes through the internal acustic meatus and then perfuses the inner ear. More details about the complete vessel network can be found in the appendix.

The coefficient K present in tube law (2.5) is obtained from the reference wave speed c_0 assumed for each vessel; in this work we estimate its value, distinguishing arteries, veins and dural sinuses. For arteries, this wave speed is computed as proposed by Olufsen et al. [225], namely,

$$c_0^2 = \frac{2}{3\rho}(k_1 \exp(k_2 r_0) + k_3) \,, \tag{2.115}$$

where r_0 is the artery's radius at the reference configuration, k_1, k_2 and k_3 are empirical constants and are taken to achieve normal wave speeds in the large vessels for a young adult human and a reasonable increase in smaller vessels. We set $k_1 = 3 \times 10^6$ g/s^2/cm, $k_2 = -7$ cm^{-1} and $k_3 = 40 \times 10^4$ g/s^2/cm. Following [201], the venous reference wave speed is estimated as follows

$$c_0 = c_{0,max} - (c_{0,max} - c_{0,min}) \left(\frac{r - r_{min}}{r_{max} - r_{min}} \right)^{\frac{1}{2}} \,, \tag{2.116}$$

where $c_{0,max} = 400$ cm/s, $c_{0,min} = 150$ cm/s and $r_{max} = 0.8$ cm, $r_{min} = 0.08$ cm are the maximum and minimum vein radii in the network. Due to the physiological rigid nature of the dural sinuses, for them we set a constant reference wave speed equal to 1500 cm/s.

Vascular beds As a consequence of the addition of vessels to the original network presented in [201, 202], the present work includes four new terminal models representing the microvasculature of inner ear

FIGURE 2.3: Detail of head and neck arteries (left) and veins (right); numbers refer to those used in Tables A.1 and A.2.

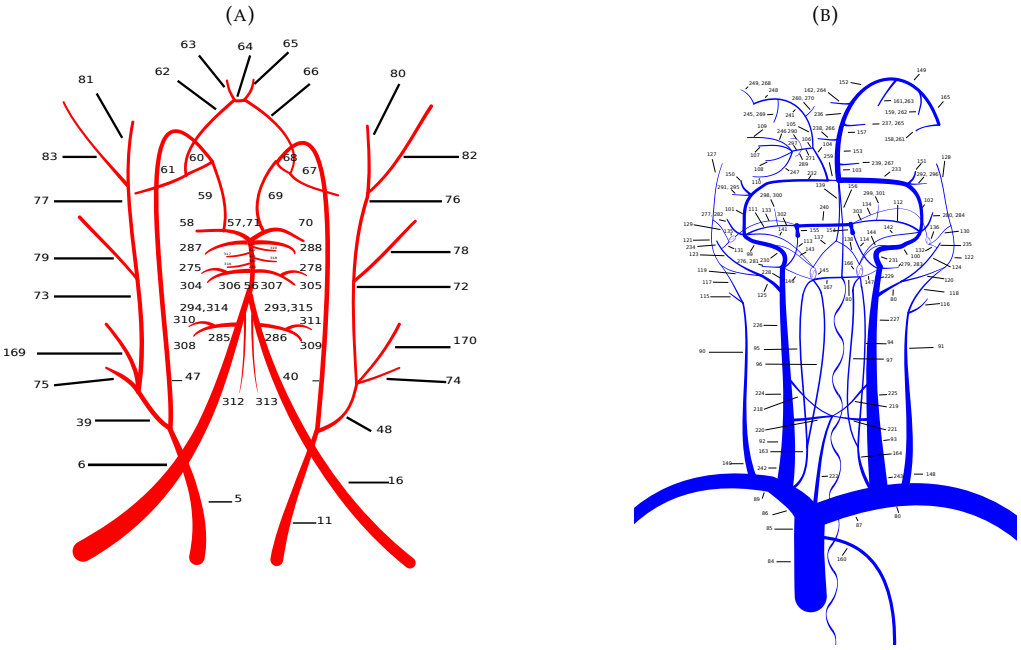

and brainstem-cerebellum. Table 2.1 summarizes the simple connections between one artery and one vein while Figure 2.4 shows the complex vascular beds.

Parameters corresponding to the microcirculation are not always retrievable from the literature; therefore, we use the strategy proposed by [160] and [215]. Total arterial resistance, arterial compliance and venous compliance are fixed up to a constant, according to literature data. Total arterial resistance is fixed to 0.85 mmHg/(ml s^{-1}) while arterial and venous compliances are 1.7 ml/mmHg and 146 ml/mmHg, respectively. For each terminal artery, we set a total arterial resistance R^T (taken as the equivalent resistance of the circuit formed by distal arteries, arterioles and capillaries, using data from [201, 202], and then modified to match the fixed arterial resistance). Then, each resistance is distributed between vascular districts according to the general pressure distributions among vascular segments. Arterial characteristic impedance R_{da} is set to be 15% of R^T while the remaining part is partitioned between arterioles and capillaries as 70% for R_{al} and 30% for R_{cp}; if an artery splits into two venous capacitors (as for the second artery in the Figure 2.1), we divide the resistance of the capillaries part according to the flow distribution into venous capacitors. In order to approximate the flow distribution of each venous capacitor, we use the Murray's law, i.e. we assume that the flow rate of a vessel is proportional to the cube of its radius; therefore, the flow rate of each venous capacitor is proportional to the sum of the cube of the radii of 1D terminal veins draining from this capacitor. As for the total arterial resistance, the total arterial compliance is fixed to a value taken from [215] and then it is distributed among the respective vascular bed compartments (C_{art}) according to [160]. Finally, C_{al} is set equal to C_{art} and C_{cp} is set to be $0.15C_{art}$. In Table A.1 we report the total arterial resistance R^T and compliance C_{art} for each terminal artery.

Concerning the venous compliances, we redistribute the venous compliance of each territory following Liang et al. [160]. If a vascular bed is composed of two venous capacitors, we divide the venous compliance of the entire vascular beds according to flow divisions among them. The venous impedance R_{vn} is taken as in [201, 202]. In the appendix, Table A.2 shows the venous resistance R_{vn} of each terminal vein and the value of the venous compliance C_{vn} of the venous capacitor associated to the vein.

FIGURE 2.4: Complex vascular beds. Red rectangles refer to connecting arteries, green squares to venous capacitors while blue rectangles to terminal veins, as depicted in Figure 2.1. Arrows show if an artery is linked to one or both capacitors and the veins connected to each capacitor. Vessel numbers refer to those used in Tables A.1 A.2.

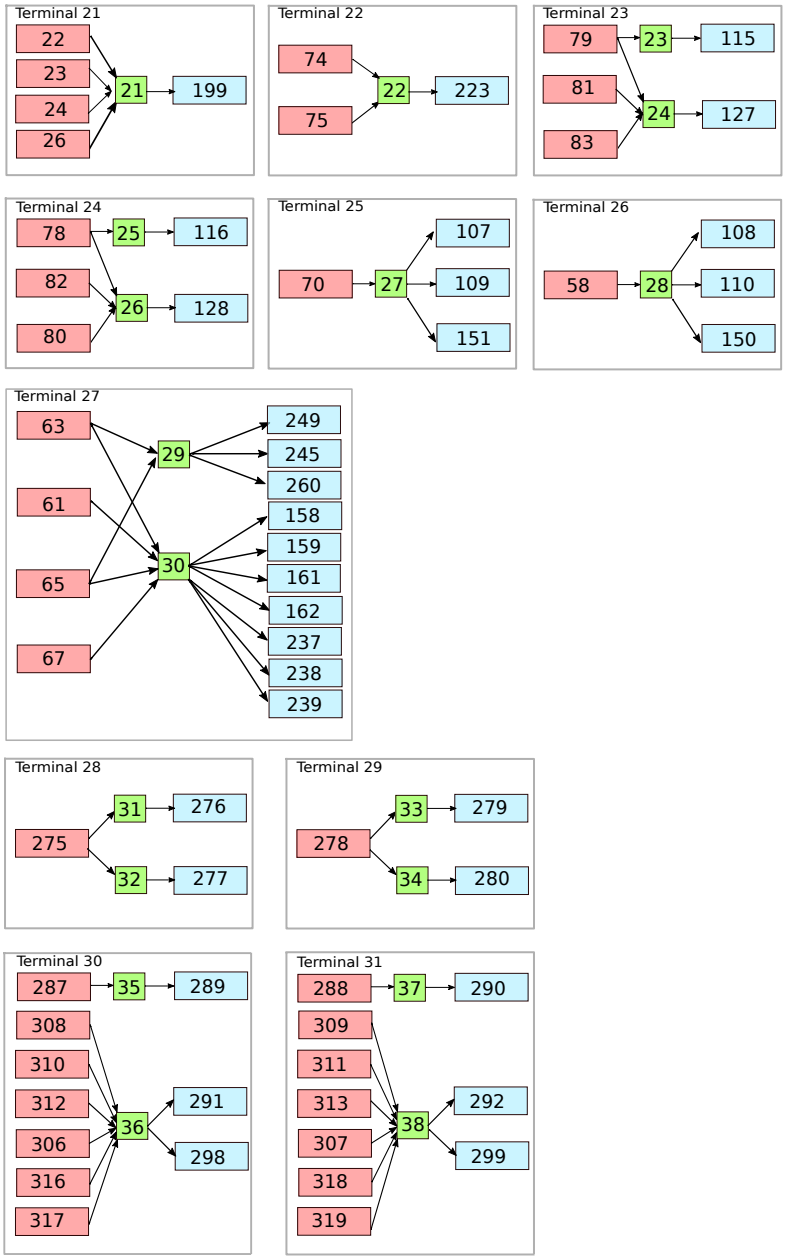

TABLE 2.1: Vascular beds - simple connections between one artery and one vein. C_{vn} index: number of the venous capacitor.

Terminal index	Artery index	C_{vn} index	Vein index
1	8	1	187
2	43	2	188
3	44	3	189
4	45	4	190
5	46	5	191
6	19	6	192
7	41	7	251
8	42	8	214
9	37	9	179
10	55	10	215
11	54	11	256
12	52	12	180
13	36	13	184
14	51	14	183
15	32	15	211
16	28	16	208
17	30	17	207
18	169	18	234
19	170	19	235
20	14	20	250

TABLE 2.2: Heart chambers parameters. RA: right atrium, RV: right ventricle, LA: left atrium, LV: left ventricle.

	RA	RV	LA	LV
$E_A\ (mmHg/ml)$	0.07	0.55	0.07	2.75
$E_B\ (mmHg/ml)$	0.04	0.05	0.09	0.12
$T_{cp}\ (s)$	0.25	0.4	0.17	0.4
$T_{rp}\ (s)$	0.17	0.15	0.17	0.15
$t_c\ (s)$	0.7	0.3	0.8	0
$t_r\ (s)$	0.97	0.0005	0.97	0.3
α	0.0005	0.0005	0.0005	0.001
$P_{ini}\ (mmHg)$	5.09	5.06	6.56	8.6

Heart and pulmonary circulation Parameters for heart chambers and cardiac valves are taken from literature [201] and [215] and then adjusted accordingly to our vessel network. The duration of a cardiac cycle is set to 0.8 s. Other parameters are reported in Tables 2.2 and 2.3. Parameters for the pulmonary circulation are the same as in the Müller-Toro model, previously taken from [276], and reported in Table 2.4. Finally, concerning the pericardium parameters, we set V_{PC} equal to 400 ml and Φ_{PC} equal to 100 ml.

Venous valves and Starling resistors According to the vessel network extension, this work presents additional valves and Starling resistors, for a total of 17 valves and 21 resistors. Table 2.5 shows the location of these elements in the vessel network. Parameter values for venous valves are set to describe a normal functioning valve and are given by $M_s = 1$, $M_r = 0.001$, $K_o = 133.32\ \frac{1}{mmHg\ s}$, $K_c = 40\ \frac{1}{mmHg\ s}$. Parameters for Starling resistors are set to $M_s = 0.5$, $M_r = 0.05$, $K_o = K_c = 133.32\ \frac{1}{mmHg\ s}$.

Autoregulation The cerebral autoregulation model works on twelve terminal cerebral arteries; the baseline haemodynamic parameters of these arteries are set from the periodic solution obtained for a baseline simulation and reported in Table 2.6.

TABLE 2.3: Cardiac valves parameters. TriVal: tricuspid valve, PulVal: pulmonary valve, MitVal: mitral valve, AorVal: aortic valve.

	TriVal	**PulVal**	**MitVal**	**AorVal**
M_s	1	1	1	1
M_r	0.00001	0.00001	0.00001	0.00001
K_o (cm^2/dynes/s)	0.03	0.02	0.02	0.02
K_c (cm^2/dynes/s)	0.04	0.02	0.04	0.02
l_e (cm)	2	1.5	2	1
A_a (cm^2)	6	5.7	5.1	4.9

TABLE 2.4: Parameters for pulmonary circulation. E_0: baseline elastance (mmHg/ml); Φ: volume constant (ml); R: resistance (mmHg/s/ml); L: inductance (mmHg/s^2/ml); S: viscoelasticity (mmHg/s/ml).

	$\mathbf{E_0}$	$\mathbf{\Phi}$	**R**	**L**	**S**
Artery	0.02	20.0	0.040	0.0005	0.01
Capillary	0.02	60.0	0.040	0.0005	0.01
Vein	0.02	200.0	0.005	0.0005	0.01

Other parameters of the model are taken from Ursino & Giannessi work [305] and adjusted to match our cerebral vessel network values (Table 2.7). For each terminal artery, the gain of autoregulation $G_{aut,i}$ is computed from the total G, according to the flow distribution inside the brain.

2.5 Concluding remarks

We have described a global closed-loop multiscale mathematical model of the entire circulation that departs from the original Müller-Toro model [201, 202]. We have in addition presented the numerical methods for the solution of one-dimensional system of equations for blood flow in viscoelastic vessels. Finally, all the parameters for the implementation of such a model are furnished. A complete validation of the global model will be performed in Chapter 3.

This global model of the entire circulation constitutes the basis on which this thesis is constructed. In the next two chapters, it will be coupled to the cerebrospinal fluid system while in Chapters 4, 5, it will be adopted for arterial hypertension modelling. Unless specified otherwise in the next chapters, the mathematical model of the human circulation and its parametrization, as well as the numerical methods to solve it, are the same as the one reported in this chapter and in [292].

TABLE 2.5: Location of venous valves (on the left) and Starling Resistors (on the right). Vessels numbers refer to those used in Table A.2

No.	Left vessel index	Right vessel index
1	193	195
2	194	196
3	244	160
4	257	171
5	258	172
6	253	257
7	254	258
8	175	178
9	176	177
10	251	212
11	256	173
12	252	213
13	255	174
14	92	242
15	93	243
16	90	140
17	91	148

No.	Left vessel index	Right vessel index
1	158	261
2	159	262
3	161	263
4	162	264
5	237	265
6	238	266
7	239	267
8	249	268
9	245	269
10	260	270
11	271	106
12	150	272
13	151	273
14	276	281
15	277	282
16	279	283
17	280	284
18	291	295
19	292	296
20	298	300
21	299	301

TABLE 2.6: Baseline values of cerebral haemodynamic variables obtained from a periodic baseline simulation.

No.	Vessel Name	$\overline{\mathbf{Q}}^{\mathbf{T}}$ [ml/s]	$\overline{\mathbf{R}}^{\mathbf{T}}$ [mmHg/ml/s]	$\overline{\mathbf{C}}$ [ml/mmHg]	$\overline{\mathbf{V}}^{\mathbf{T}}$ [ml]
58	Right posterior cerebral artery II	1.42	39.15	3.324E-06	0.26
61	Right middle cerebral artery	3.01	19.06	6.649E-06	0.55
63	Right anterior cerebral artery II	1.54	38.08	3.324E-06	0.28
65	Left anterior cerebral artery II	1.54	38.08	3.324E-06	0.28
67	Left middle cerebral artery	3.01	19.06	6.649E-06	0.55
70	Left posterior cerebral artery II	1.42	39.15	3.324E-06	0.26
287	Right SCA	0.30	132.55	6.649E-07	0.06
288	Left SCA	0.30	132.55	6.649E-07	0.06
306	Right AICA II	0.08	714.26	6.589E-07	0.058
307	Left AICA II	0.08	714.26	6.589E-07	0.058
308	Right PICA MB	0.005	11885.65	6.589E-07	0.058
309	Left PICA MB	0.005	11,887.52	6.589E-07	0.058
310	Right PICA II	0.13	449.13	6.589E-07	0.058
311	Left PICA II	0.13	449.13	6.589E-07	0.058
312	Right anterior spinal a.	0.06	1,048.93	6.589E-07	0.058
313	Left anterior spinal a.	0.06	1,048.93	6.589E-07	0.058
316	Right pontine a. I	0.001	63,752.68	6.589E-07	0.058
317	Right pontine a. II	0.001	63,669.28	6.589E-07	0.058
318	Left pontine a. I	0.001	63,726.28	6.589E-07	0.058
319	Left pontine a. II	0.001	63,668.30	6.589E-07	0.058

TABLE 2.7: Parameters for the autoregulation model, taken from [305].

Parameter	**Value**
τ (s)	20
G	0.9
sat_1	0.55
sat_2	2.0

Chapter 3

Cerebrospinal fluid dynamics coupled to the global circulation in holistic setting

3.1 Introduction

The present work results from the amalgamation of two substantial and independently developed pieces of work and attempts to incorporate the major extracellular fluid compartments of the human body. The first piece consists of a substantially improved version of the original Müller-Toro mathematical model [201] for the global systemic and pulmonary circulations in the entire human body, described in detailed in the previous chapter. Then, the second piece of work, a major novelty of this chapter, is the coupling of the circulation as described, to a refined mathematical description of the cerebrospinal fluid dynamics in the craniospinal cavity, building upon the model proposed by Linninger [162]. This includes all major CSF pathways and the brain parenchyma, accounting for deformations and interaction between the cerebral vasculature, brain parenchyma and cerebrospinal fluid compartments during the cardiac cycle. The present mathematical model is depicted in Fig. 3.1. Major fluid components are the arterial system (right) and the venous system (left) for the entire body, comprising 323 major blood vessels. The craniospinal cavity, in addition to the vasculature and the two-phase brain parenchyma, contains cerebrospinal fluid represented by 0-D compartments for the cranial subarachnoid space, the four cerebral ventricles, the aqueduct of Sylvius and the spinal subarachnoid space. Additional components include the four heart chambers, cardiac valves, three compartments for the pulmonary circulation, 31 compartmental models describing the connections between terminal arteries and veins through the microcirculation, 17 venous valves, 21 Starling resistors. The potential medical applications of the resulting model are numerous. Here we have chosen to illustrate the applicability of our model to two classes of fluid-dynamics related pathologies that involve the close dynamical interaction of all major fluid compartments in the craniospinal space. The first class of pathologies concerns transverse sinus stenoses and its relation to Idiopathic Intracranial Hypertension (IIH) [20, 194, 4]. The second class of fluid-related pathologies concerns the altered haemodynamics of the inner ear circulation resulting from extra-cranial venous outflow strictures, and its implications for Ménière's disease [96, 13, 40, 297].

Even if the resulting model is suitable for the study of several physiological and pathophysiological phenomena, it must be noted that its application for patient-specific simulations would be complex. Indeed, it is characterized by many parameters that are difficult to be measured in the clinic, in particular for the cerebrospinal fluid part. Thus, while the main goal of this model is to explore fundamental aspects of physiological and pathological states, an attempt towards a patient-specific application was done with a previous version of the Müller-Toro model [201]. In that work, major head and neck veins were modified according to patient-specific MRI-derived geometrical information.

FIGURE 3.1: Schematic representation of the global model for the full human circulatory system coupled to the craniospinal fluids and brain parenchyma. The arterial 1D network is represented in the right dotted box with red vessels while the venous 1D network is displayed in the left dotted box with blue vessels. The terminal arteries of the arterial network are connected to draining veins of the venous circulation through 0D models representing arterioles, capillaries, small arteries (red boxes) and venules, small veins (blue boxes). The dotted arrows indicate the connection between 1D network and terminal vessels, depicted for simplicity as dots in the yellow bar. Left and right cardiac chambers are displayed by red and blue boxes, respectively, connected to green atrioventricular valves; the left ventricle is connected to aortic root and venae cavae are linked to right atrium through black arrows. Cardiac chambers are connected to the pulmonary circulation, comprising arteries, capillaries and veins, represented by the pink box, through the aortic and pulmonary valves (green arrows). The CSF compartments are represented by cyan boxes. The arrows between cardiovascular system and CSF circulation represent the fluid exchange between these systems through production and absorption while the green dashed boxes indicate the mechanical interaction between between all components in the cranial cavity through the Monro-Kellie hypothesis.

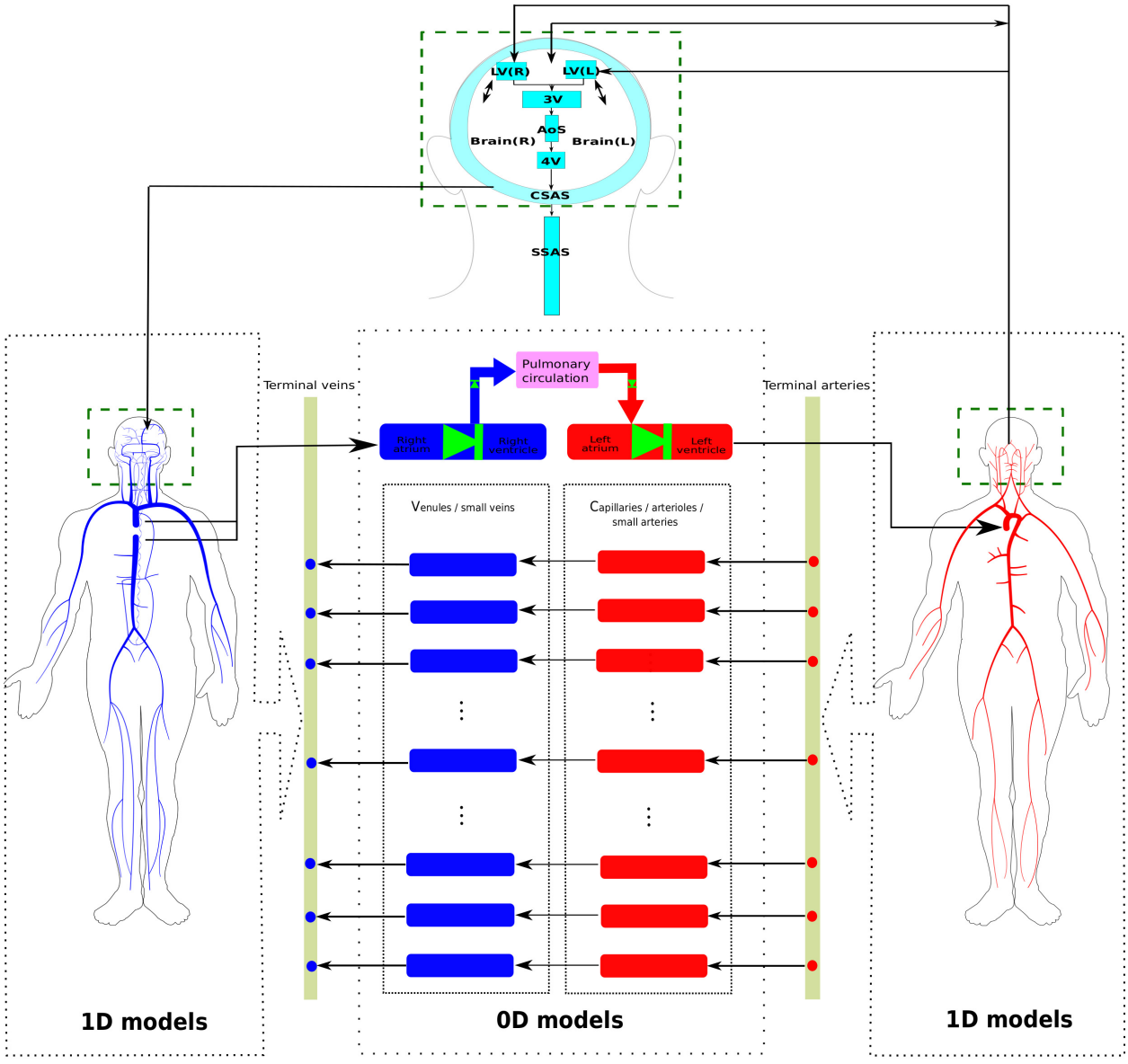

The rest of the chapter is structured as follows. Section 3.2 presents the equations for cerebrospinal fluid and brain dynamics (3.2.1), its numerical coupling to the blood circulation (3.2.2) and the parametrization of the cerebrospinal fluid model (3.2.3). Section 3.3 shows sample computations and validation of results against published data and MRI measurements for the systemic haemodynamics (3.3.1), the cerebral haemodynamics (3.3.2) and the CSF and brain dynamics (3.3.3). In Section 3.4, we illustrate the potential applicability of the full model to fluid-dynamics related pathologies. Discussion and conclusions are found in Section 3.5.

3.2 Mathematical model for cerebrospinal fluid and brain dynamics and its coupling to the blood circulation

3.2.1 Equations for cerebrospinal fluid and brain dynamics

A major aspect of the present work is the coupling of the circulatory system to a more refined description of the cerebrospinal fluid dynamics than in the first version of our model [201, 202]. We depart from the model proposed by Linninger and collaborators [162]. The Linninger model [162] was chosen because it integrated results of extensive MR imaging studies [167, 164, 236] with detailed two and three-dimensional mathematical models into a comprehensive mathematical description of the major intracranial dynamics with fluid structure interactions of blood, cerebrospinal fluid in the ventricular system, as well as cranial and the spinal subarachnoid spaces and the deformable brain parenchyma. The version of the Linninger model we present here differs somehow from the original version and includes nine CSF compartments: the lateral (LV and RV), the third (3V) and the fourth (4V) ventricles; the cerebral aqueduct (aqueduct of Sylvius, AoS), the cranial subarachnoid space (CSAS), the spinal subarachnoid space (SSAS) and the bi-phasic brain parenchyma, comprising the left and right hemispheres. Each compartment is spatially idealised as a cylinder of length l and variable cross-sectional area $A(t)$. Each brain parenchyma hemisphere is treated as an incompressible, deformable medium composed of two phases, the solid cell matrix, representing neurons, glial cells and axon fibers (70% of its total volume), and the extracellular fluid (remaining 30 %); the model assumes that the volume of the solid matrix does not change and therefore brain parenchyma size changes depend only on the extracellular fluid content variations, i.e. changes in porosity. All CSF compartments are interconnected and contain CSF assumed to be a Newtonian and incompressible liquid, with a constant viscosity of 0.001 kg/(ms) and a constant density of 998.2 kg/m^3 [162].

In our model we assume that CSF is secreted by the choroid plexuses, a highly vascularized region from the microcirculation of the anterior and posterior cerebral arteries, into the lateral ventricles. Also included is a constant CSF production from arterioles to the ventricles and the diffuse capillary production throughout the brain parenchyma to the ventricles. Then, CSF flows from the lateral ventricles to the third ventricle and, through the cerebral aqueduct, to the fourth ventricle. Then CSF is assumed to enter the subarachnoid space. Here CSF is absorbed into the venous system through arachnoid villi into the superior sagittal sinus. Moreover, from the cranial subarachnoid space, CSF is displaced into another CSF compartment, namely the SSAS.

Figure 3.2 shows the craniospinal compartments involved in the CSF system and their connectivity. The arrows indicate fluid exchange between compartments driven by pressure differences, while dashed arrows denote constant production of CSF, from the cerebral arterioles into the lateral ventricles $q_{Al\rightarrow LVs,const}$ and from the brain capillaries into the extracellular space of the parenchyma. The type of arrows identifies whether the exchange of CSF between different compartments is unidirectional or bidirectional.

Flow of CSF in CSF compartments is governed by mass conservation and momentum balance. Such equations are accompanied by a tube law, relating deformation state and pressure, as for 1D vessels. Other

FIGURE 3.2: Schematic representation of the cerebrospinal fluid (CSF) compartments. **RV**: right lateral ventricle; **LV**: left lateral ventricle; **3V**: third ventricle; **4V**: fourth ventricle; **AoS**: aqueduct of Sylvius; **CSAS**: cranial subarachnoid space; **SSAS**: spinal subarachnoid space; **SSS**: superior saggital sinus **Brain**: fluid part of brain parenchyma; **Al**: cerebral arterioles; **Cp**: cerebral capillaries. Solid double arrows denote fluid exchange between different compartments driven by pressure differences, while dashed arrows describe constant CSF production. The combination of a single dashed arrow and a solid double arrow between the brain parenchyma and the capillaries indicates that there are both fluid exchange driven by pressure differences (q^{in}_{br} driven by $p_{Cp} - p_{br}$) and constant CSF production ($q_{Cp\to br,const}$). Single solid arrow denotes CSF reabsorption into the venous system (**SSS**).

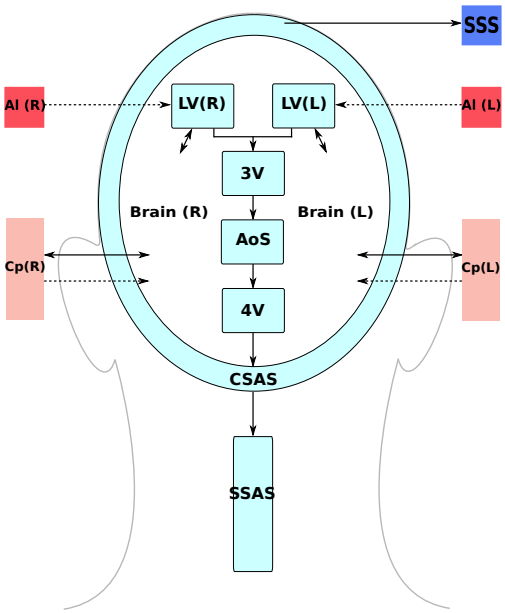

equations are included in the model to account for fluid exchange between different compartments of the CSF system or with the vasculature. The full CSF model is composed of 36 equations and 36 unknowns. The continuity equations read

$$l_{RV}\frac{dA_{RV}}{dt} = q^{in}_{RV} - q^{out}_{RV}\,, \tag{3.1}$$

$$l_{LV}\frac{dA_{LV}}{dt} = q^{in}_{LV} - q^{out}_{LV}\,, \tag{3.2}$$

$$l_{3V}\frac{dA_{3V}}{dt} = q^{in}_{3V} - q^{out}_{3V}\,, \tag{3.3}$$

$$l_{AoS}\frac{dA_{AoS}}{dt} = q^{in}_{AoS} - q^{out}_{AoS}\,, \tag{3.4}$$

$$l_{4V}\frac{dA_{4V}}{dt} = q^{in}_{4V} - q^{out}_{4V}\,, \tag{3.5}$$

$$l_{CSAS}\frac{dA_{CSAS}}{dt} = q^{in}_{CSAS} - q^{out}_{CSAS}\,, \tag{3.6}$$

$$l_{SSAS}\frac{dA_{SSAS}}{dt} = q^{in}_{SSAS} - q^{out}_{SSAS}\,, \tag{3.7}$$

$$l_{br,R}\frac{dA_{br,R}}{dt} = q^{in}_{br,R} + q_{Cp\to br,const} - q^{out}_{br,R} - q_{br\to RV,const}\,, \tag{3.8}$$

$$l_{br,L}\frac{dA_{br,L}}{dt} = q^{in}_{br,L} + q_{Cp\to br,const} - q^{out}_{br,L} - q_{br\to LV,const}\,. \tag{3.9}$$

Equations (3.1) to (3.9) are continuity equations that ensure that cerebrospinal fluid is neither gained nor lost. Equations (3.1) to (3.7) refer to continuity equations for ventricles, Aqueduct of Sylvius, cranial and spinal subarachnoid space. Each equation guarantees that the volume change is given by the difference between the volumetric flow rates in and out of that compartment. Equations (3.8) and (3.9) are the continuity equations for the right and left fluid part of the brain parenchyma, respectively. In this case, the right-hand-side of the equations considers both the volumetric flow rate in and out of the compartment that is driven by pressure differences and the constant mass transfer. Flow into the the brain parenchyma is the sum of a constant CSF production from the brain capillaries into the extracellular space of the parenchyma, $q_{Cp\to br,const}$ and the pressure driven seepage from the capillaries to the brain parenchyma, q^{in}_{br}. Flow exiting the brain parenchyma is the sum of a constant seepage from the extracellular space of the parenchyma into the ventricles, $q_{br\to LV,const}$, and a pressure driven exchange between brain parenchyma and lateral ventricles $q^{out}_{br,L}$.

The momentum equations are effectively Darcy's law of flow and relate the pressure difference between two compartments to the volumetric flow q exchanged between them and a resistance to flow R. For the brain parenchyma compartments, there are two momentum equations, one refers to cerebrospinal fluid exchange between the lateral ventricles and the extracellular fluid matrix of the brain, while the other one relates to the secretion of CSF from cerebral capillaries. As seen in Figure 3.2, these exchange pathways are bi-directional, depending on the hydrostatic pressure differences. When intracranial pressure exceeds the capillary pressure, reverse flow occurs, that is, in the present model capillaries are a pathway for CSF drainage. The equations for CSF flow are

$$q^{out}_{RV} = \frac{p_{RV} - p_{3V}}{R_{3V}}\,, \tag{3.10}$$

$$q^{out}_{LV} = \frac{p_{LV} - p_{3V}}{R_{3V}}\,, \tag{3.11}$$

$$q^{in}_{AoS} = \frac{p_{3V} - p_{AoS}}{R_{AoS}}\,, \tag{3.12}$$

$$q^{in}_{4V} = \frac{p_{AoS} - p_{4V}}{R_{4V}}\,, \tag{3.13}$$

$$q^{in}_{CSAS} = \frac{p_{4V} - p_{CSAS}}{R_{CSAS}}\,, \tag{3.14}$$

$$q^{in}_{SSAS} = \frac{p_{CSAS} - p_{SSAS}}{R_{SSAS}}\,, \tag{3.15}$$

$$q^{in}_{br,R} = \frac{p_{Cp,R} - p_{br,R}}{R_{br}}\,, \tag{3.16}$$

$$q^{in}_{br,L} = \frac{p_{Cp,L} - p_{br,L}}{R_{br}}\,, \tag{3.17}$$

$$q^{out}_{br,R} = \frac{p_{br,R} - p_{RV}}{R_{br,2}}\,, \tag{3.18}$$

$$q^{out}_{br,L} = \frac{p_{br,L} - p_{LV}}{R_{br,2}}\,. \tag{3.19}$$

The notation for pressures is obvious for most compartments; for example p_{CSAS} denotes pressure in the cerebral subarachnoid compartment. Just for clarity, in the last four equations $p_{Cp,R}$ is pressure in the capillary compartments of the right side of the brain, while $p_{Cp,L}$ is pressure in the capillary compartments of the left part of the brain; $p_{br,R}$ is pressure in the extracellular fluid part of the right brain parenchyma and $p_{br,L}$ is pressure in extracellular fluid part of the left brain parenchyma. We note that Equation (3.16) attempts

to account for the interacting dynamics of two major CSF compartments. We are currently investigating these aspects as it has clearly some limitations, particularly regarding the omission of inertial terms that are known to influence the timing of flow exchange between CSAS and SSAS [279].

As already pointed out, the distensibility equations play the role of the tube law; they relate the internal pressure with the cross-sectional area of the compartment in a linear manner. They describe the dilation and compression of a compartment; if the pressure of the compartment exceeds the external pressure, the compartment is dilated with respect to the reference state "0"; in the opposite case, the compartment is compressed. For each compartment inside the cranial cavity, the external pressure is that of the brain parenchyma; for the spinal subarachnoid space, the external pressure is taken equal to zero. For a generic compartment z, the distensibility equation expresses pressure p_z as a function of cross-sectional area A_z in the compartment and three additional parameters, namely an external pressure $p_{ext,z}$, baseline cross-sectional area A_z^0 and a coefficient E_z denoting elastance, that is

$$p_z = p_{ext,z} + E_z \left(\frac{A_z}{A_z^0} - 1 \right) , \tag{3.20}$$

Therefore, for each specific compartment the equations are

$$p_{RV} = p_{br,R} + E_{RV} \left(\frac{A_{RV}}{A_{RV}^0} - 1 \right) , \tag{3.21}$$

$$p_{LV} = p_{br,L} + E_{LV} \left(\frac{A_{LV}}{A_{LV}^0} - 1 \right) , \tag{3.22}$$

$$p_{3V} = \frac{1}{2}(p_{br,R} + p_{br,L}) + E_{3V} \left(\frac{A_{3V}}{A_{3V}^0} - 1 \right) , \tag{3.23}$$

$$p_{AoS} = p_{br} + E_{AoS} \left(\frac{A_{AoS}}{A_{AoS}^0} - 1 \right) , \tag{3.24}$$

$$p_{4V} = \frac{1}{2}(p_{br,R} + p_{br,L}) + E_{4V} \left(\frac{A_{4V}}{A_{4V}^0} - 1 \right) , \tag{3.25}$$

$$p_{CSAS} = \frac{1}{2}(p_{br,R} + p_{br,L}) + E_{CSAS} \left(\frac{A_{CSAS}}{A_{CSAS}^0} - 1 \right) , \tag{3.26}$$

$$p_{SSAS} = E_{SSAS} \left(\frac{A_{SSAS}}{A_{SSAS}^0} - 1 \right) . \tag{3.27}$$

Additional equations connecting different compartments are required to complete the description of cerebrospinal fluid flow. Specifically, for the right lateral ventricle RV, the amount of CSF that enters the right lateral ventricle RV is equal to the amount of CSF exiting the fluid part of the brain parenchyma plus the constant production rate from arterioles $q_{Al\to RV,const}$ plus the constant production rate from capillaries $q_{Cp\to br,const}$, namely

$$q_{RV}^{in} = q_{br,R}^{out} + q_{br\to RV,const} + q_{Al\to RV,const} . \tag{3.28}$$

Similarly for the left lateral ventricle LV,

$$q_{LV}^{in} = q_{br,L}^{out} + q_{br\to LV,const} + q_{Al\to LV,const} . \tag{3.29}$$

Then, CSF flows from lateral ventricles to the third ventricle

$$q_{RV}^{out} + q_{LV}^{out} = q_{3V}^{in} , \tag{3.30}$$

from the third ventricle to the aqueduct of Sylvius

$$q_{3V}^{out} = q_{AoS}^{in} \,, \tag{3.31}$$

from the AoS to the fourth ventricle

$$q_{AoS}^{out} = q_{4V}^{in} \,, \tag{3.32}$$

and from the fourth ventricle to the cranial subarachnoid space

$$q_{4V}^{out} = q_{CSAS}^{in} \,. \tag{3.33}$$

From the cerebral subarachnoid space CSAS, CSF is temporarily displaced into the spinal cavity and reabsorbed into the superior saggital sinus (SSS) through the arachnoid granulations [260, 162]. Reabsorption is represented by a mass transfer flux, which is a function of the pressure difference between the CSAS and CSAS and a reabsorption constant coefficient k

$$q_{CSAS}^{out} = q_{SSAS}^{in} + \max\left(0, k(p_{CSAS} - p_{sinus})\right) . \tag{3.34}$$

We take the maximum value between zero and the mass transfer flux to enforce the unidirectional flow from the cranial SAS to the venous sinus. Previous MRI measurements [172] have shown that in a normal subject CSF reabsorption in the spinal cavity is negligible, since almost the total flow into the spinal SAS goes back into the cerebral SAS; for this reason, we set the CSF outflow from the SSAS equal to zero,

$$q_{SSAS}^{out} = 0 \,. \tag{3.35}$$

Finally, the Monro-Kellie hypothesis is enforced: all compartments, except the spinal subarachnoid space, are enclosed inside the cranium and the volume of each cerebral hemisphere remains constant over time

$$V_{Blood,R} + V_{RV} + \frac{1}{2}V_{3V} + \frac{1}{2}V_{AoS} + \frac{1}{2}V_{4V} + \frac{1}{2}V_{CSAS} + V_{br,R} + V_{Solid\,Parenchyma} = \text{constant} \,, \tag{3.36}$$

$$V_{Blood,L} + V_{LV} + \frac{1}{2}V_{3V} + \frac{1}{2}V_{AoS} + \frac{1}{2}V_{4V} + \frac{1}{2}V_{CSAS} + V_{br,L} + V_{Solid\,Parenchyma} = \text{constant} \,. \tag{3.37}$$

The volume of each compartment is evaluated as product of its length and its cross-sectional area.

3.2.2 Numerical treatment of CSF equations and its coupling to the circulation

The description of CSF and brain dynamics leads to a system of 36 equations with 36 unknowns. The unknowns for each CSF compartment are pressure, cross-sectional area (which defines a volume since each compartment has an assigned length), inflow and efflux. The coupling between blood flow and CSF dynamics is explicit. The two systems are solved in a sequential manner. As we are using a local time stepping technique in a vessel-wise fashion, each 1D vessel is allowed to evolve in time according to a local time step given by its local stability criterion. All vessels have a common synchronization time defined by the prescribed maximum time step Δt_{max} allowed by the LTS procedure. Therefore, the coupling between blood flow and the craniospinal systems is performed every synchronization time $t^n = t_0 + n\,\Delta t_{max}$, with t_0 the initial time. Figure 3.3 describes the coupling procedure from time t^n to time t^{n+1}. At the beginning of each time step, the vectors $\mathbf{S}^n$ and $\mathbf{B}^n$ are known. The vector $\mathbf{S}^n$ represents the unknowns for the blood circulation system that includes area, flow and pressure in 1D vessels, as well as other 0D blood compartments. The vector $\mathbf{B}^n$ represents the unknowns for the CSF and brain dynamics models. In the first step, the equations for the blood circulation models are solved. First, the system of ordinary differential equations for the cerebral autoregulation model are solved by the explicit Euler scheme, in order to find the new cerebral resistances and compliances, as described in Section 2.2.2. Then we solve the system of partial differential

FIGURE 3.3: Schematic representation of the coupling between blood circulation and CSF and brain dynamics models. $\mathbf{S}^n$ and $\mathbf{B}^n$ are the vectors of unknowns in the blood circulation models (1D vessels and other 0D blood compartments) and in the CSF and brain dynamics model at time t^n. From $\mathbf{B}^n$, the pressures of the left and right fluid part of the brain parenchyma $p^n_{br,R}$ and $p^n_{br,L}$ at time t^n are used to find the solution $\mathbf{S}^{n+1}$ for the hemodynamics equations and the cerebral regulation. From $\mathbf{S}^{n+1}$, the superior sagittal sinus pressure p^{n+1}_{sinus}, the pressure of capillaries $p^{n+1}_{br,R}$, $p^{n+1}_{br,L}$ and the total cerebral blood volume $V^{n+1}_{blood,R}$, $V^{n+1}_{blood,L}$ are used to find the solution $\mathbf{B}^{n+1}$ for the CSF and brain equations.

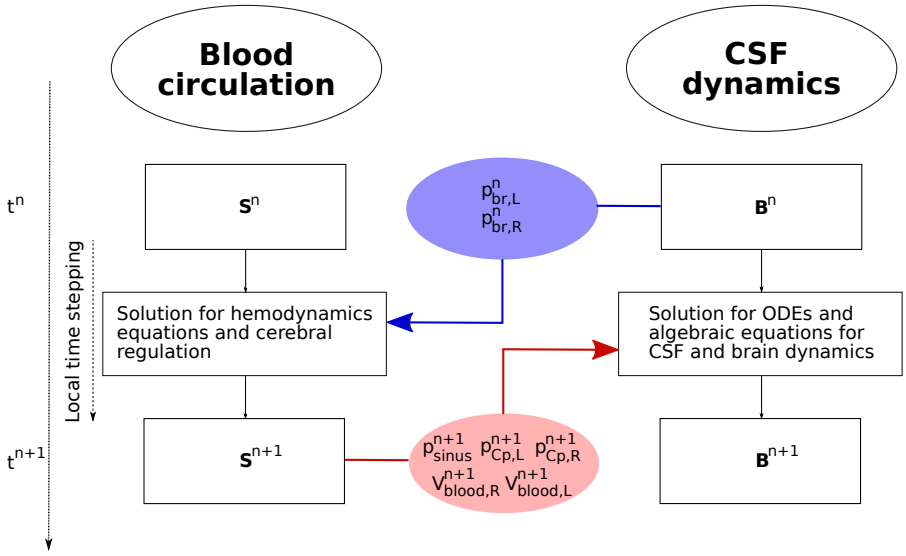

equations for blood flow in 1D vessels and the 0D blood compartments for the heart and pulmonary circulation, microvasculature, Starling resistors and venous valves. Each j-*th* vessel is evolved using the ADER scheme according to its local time step until it reaches the next time step $t^{n+1} = t^n + \Delta t_{max}$. The 0D blood compartments are solved by an explicit Euler scheme and coupled to the 1D vessels. The external pressure for the intracranial 1D vessels and vascular beds, as well as for the Starling resistor models, is given by the mean pressure between the left and right sides of the brain parenchyma ($p_{br,R}$ and $p_{br,L}$) at time t^n. Once the blood circulation equations have been solved, the cerebral capillary pressures ($p_{Cp,R}$ and $p_{Cp,L}$), the superior sagittal sinus pressure (p_{sinus}) and the intracranial blood volume ($V_{blood,R}$, $V_{blood,L}$) are provided to the CSF models. This determines the CSF production, reabsorption rates and the blood volume inside the skull for the Monro-Kellie hypothesis. At this point, the system of differential and algebraic equations for the CSF and brain dynamics are solved by an implicit Euler scheme.

At the beginning of the simulation, given the initial conditions for the blood circulation models, the ODEs and systems of equations for the CSF and brain dynamics models are solved. In this way the initial intracranial pressures are found and used as external pressure in the first time step update of the blood circulation.

3.2.3 CSF model parametrization

Parameters for the CSF model are based on Linninger et al. [162]. Table 3.1 shows length and area at rest of the cylindrical volume representing each cerebral compartment, and different values of elastance taken from the literature. Table 3.2 reports flow resistance values; they account for the pressure drop in the fluid along the length of a compartment due to viscous forces and they are obtained from the dynamic fluid viscosity μ, the length of the compartment l and the square of the compartments' cross-sectional area.

As already written in Section 3.2.1, the CSF model adopted here accounts for constant production of cerebrospinal fluid, from capillaries $q_{Cp\rightarrow br,const}$ and from arterioles to lateral ventricles $q_{Al\rightarrow LV,const}$.

Almost two-thirds of the total CSF production takes place in the choroid plexus of the lateral ventricles; it was found clinically that this process is almost invariant to pressure changes suggesting an active transport process [134]. As in [162], we fix a constant mass transfer independent from pressure equal to $q_{Al\rightarrow LVs,const} = 0.00583$ ml/s. Moreover, there is CSF mass transfer from capillary beds into the brain parenchyma; the constant diffuse CSF production is set equal to $q_{Cp\rightarrow br,const} = 0.0005$ ml/s. The active exchange between capillaries and brain parenchyma is governed by Equations (3.16) and (3.17), where CSF seepage is governed by pressure differences.

CSF reabsorption is described in (3.34) by a mass transfer flux that is a function of the pressure difference between the subarachnoid space and the superior sagittal sinus and a reabsorption constant k. In this work we use $k = 0.0027$ mmHg/ml/s. We underline that variation of reabsorption constant could simulate pathological situations; for example, an increase of the reabsorption resistance may be due to inflammation of meninges while acute communicating hydrocephalus could be simulated by reducing k [162, 164].

TABLE 3.1: Hydraulic length, area at rest and elastance of each CSF compartment.

Compartment	**Length** $[cm]$	**Area at rest** $[cm^2]$	**Elastance** $[mmHg]$
LVs	0.75	12	7.55
3V	1	2.5	7.55
AoS	1.8	0.00785	7.55
4V	1	3.5	7.55
CSAS	1.69	17.76	80
SSAS	43	2	160
Brain parenchyma (Fluid)	14	30	
Brain parenchyma (Solid)	14	70	

TABLE 3.2: Flow resistances of CSF compartments.

Compartment	**Resistance** $[mmHg/ml]$
3V - R_{3V}	0.2
AoS - R_{AoS}	5.5
4V - R_{4V}	0.2
CSAS - R_{SSAS}	0.2
SSAS - R_{CSAS}	0.1
Brain - R_{br}	81520
Brain - $R_{br,2}$	500

3.3 Sample numerical results and validation

In this section we present computational results obtained with the presented model in order to perform a comprehensive validation of the model's outputs. 1D domains are divided into computational cells with a reference length of $\Delta x = 1\ cm$, imposing a minimum of one computational cell in each vessel. Once that the mesh spacing of a vessel is fixed, the respective relaxation time ϵ for each vessel is computed in order to ensure that the accuracy criterion for the hyperbolic reformulation proposed in [199] is satisfied. The CFL coefficient is set to $CFL = 0.9$ according to the linear stability limit of ADER finite volume schemes for one-dimensional problems. A maximum time step of $\Delta t_{max} = 1 \times 10^{-3}\ s$ is allowed. All computations are run using a second-order accurate version of the numerical scheme described in Chapter 2. Other parameters linked to the blood characteristics are the blood viscosity taken as $\mu = 0.045\ P$ and the blood density $\rho = 1.06\ g/cm^3$. The reference pressures taken as initial conditions are reported in Table 3.3. Given

TABLE 3.3: Initial pressure conditions for vascular compartments.

Compartment	$\mathbf{P_{ini}}$ $[mmHg]$
Arteries	70.0
Veins	5.0
Arterioles	45.0
Capillaries	25.0
Venules	10.0

the closed-loop nature of our model, such pressures are important since they determine the periodic solution that the system will reach by defining the stretched blood volume. All the computational results shown in this section are obtained with simulations of 2000 cardiac cycles. A periodic state is reached after approximately 1600 cycles; compared to [201], the time used to reach the periodicity of the simulation is higher due to coupling between two systems (blood and CSF) that have different time scales. Therefore, the verification of convergence of the solution is mainly based on the equality of the CSF production and CSF reabsorption, since CSF production involves the arterial pressure, and the CSF reabsorption rate is related to intracranial venous pressure. While future work will regard a more efficient treatment of coupling for the two systems under investigation, it is interesting to note that this difference in time scales poses severe constrains as to the mass conservation properties of the numerical schemes used to solve this problem. In fact, a discretization that is not able to enforce mass conservation at a discrete level would result in inability to reach a periodic solution due to mass conservation error accumulation.

3.3.1 Validation of systemic haemodynamics

Arteries and veins. Figures 3.4 to 3.6 show computed pressure and flow rate at the midpoint of selected vessels in the arterial and venous networks. In particular, Figure 3.4 shows the computed waveforms along the aorta and major arteries of the lower limb. We can notice that, as the wave travels away from the heart towards the periphery, the systolic peak pressure increases according to physiological patterns, with a pulse pressure from 25 mmHg in ascending aorta to 45 mmHg in femoral artery. Moreover, the pressure range covers normal values of a young subject. Along the aorta pathway, the peak flow decreases progressively. Flow distribution along systemic arteries is assessed by comparing computational results with literature data and results obtained with the previous version of the model [201]; the corresponding bar plots are reported in Figure 3.5 (left). We note that when using the terminology *literature data* we always make reference to experimental data gathered in vivo and published by other research groups. Main cardiovascular indexes, such as systolic, diastolic and mean blood pressure and pulse pressure are computed and compared to literature data in Table 3.4. We conclude that waveform patterns in the arterial system are in accordance with general physiological data and that blood flow distribution along the aorta is reasonable. Concerning the venous circulation, Figure 3.6 shows the pressure and flow rate along the main systemic veins while Figure 3.5 (right) depicts a comparison of the predicted flow at different locations of the systemic venous circulation with literature data and results obtained in [201].

It is well known that blood flow in large to medium vessels is a convection-dominated process; therefore neglecting viscoelasticity of vessel walls in one-dimensional models is often chosen as compromise. However, the viscoelastic behavior of arterial and venous walls is well-known. It has an impact on fundamental hemodynamic characteristics of the cardiovascular system and plays a determinant role in setting the functional level of the cardiovascular system under physiological and under pathological conditions. Previous works [7, 241, 215] have shown the benefits of considering viscoelastic properties of vessel walls

in arterial circulation comparing model predictions and in vivo measurements of pressure and flow at different location. The effects of viscoelasticity become more significant in the periphery, especially on the flow wave. The same happens in the venous circulation. Zòcalo et al. [327] showed the importance of the dynamic process of veins walls to understand venous functioning under normal and pathological conditions; pressures and diameters of anterior cava, jugular and femoral veins from sheep were registered during cyclical volume-pressure pulses. The vein viscosity was higher in the peripheral segments and this could be important in the response to acute overloads and in haemodynamic control. In this work, we introduce a viscoelastic tube law not only for the arterial tree but also in the venous circulation. Both arteries and veins are represented as a Voigt-type viscoelastic material (Eq. (2.7)). Figures 3.7 and 3.8 compare computed pressure and flow rate when vessels are represented with elastic and viscoelastic behaviour of their walls. Figure 3.7 refers to thoracic aorta, femoral and carotid artery while Figure 3.8 depicts superior vena cava, femoral and jugular vein; the effect of the viscoelastic tube law is more evident in peripheral vessels (femoral artery and vein, carotid artery and jugular vein) with respect to central vessels. In particular, it can be seen that the solution obtained for viscoelastic vessels presents significantly less high-frequency components with respect to the solution obtained for elastic vessels. This fact is consistent with the dissipative capacity of real vessels, which, at least for physiological states, do not display pressure and flow waveforms with very high-frequency components.

Vascular beds. Figure 3.9 shows the computed pressures during a cardiac cycle for three different compartments. The pressure values display a physiologically behaviour in all compartments; from arterioles to venules, the pressure slowly decreases. It ranges between 40-80 mmHg for arterioles, between 20-25 mmHg for capillaries and between 5-15 mmHg for venules. In particular, 3.9a refers to a simple connection in the kidney, 3.9b is a vascular bed in the abdominal region with four supplying arteries and one draining vein while 3.9c represents the microcirculation pressures in the left part of the posterior brain.

Heart. Figure 3.10 shows the computed pressures and volumes for the four cardiac chambers while Figure 3.11 displays the pressure-volume relationship for the left and right ventricles. The heart model well represents the physiological variations of pressure over the cardiac cycle for both atria and ventricles. Moreover, Table 3.4 compares the predicted values for selected cardiovascular indexes to literature data, showing overall satisfactory agreement.

3.3.2 Validation of cerebral haemodynamics

Figure 3.12 illustrates predicted pressure and flow waveforms in the head and neck arterial circulation. Moreover, flow distribution among cerebral arteries is assessed via comparison to literature data and results reported in [201] in Figure 3.13 (left). The functioning of cerebral autoregulation is verified by changing arterial resistances of all but the cerebral arteries in order to cause a mean arterial pressure change, which would cause an increment in cerebral flow if peripheral cerebral resistance would not adapt. Figure 3.14 shows the computed autoregulation curve compared with literature data from [305]. The autoregulation curve relates mean arterial pressure (pressure of vessel No. 1) and the percentage change in cerebral blood flow with respect to the baseline situation (evaluated as sum of mean flow over a cardiac cycle of internal carotid arteries and vertebral arteries).

Particular attention is given to the head and neck veins; in this case, PC-MRI flow measurements were available from [201]; these data were collected by the MR Research Facility at Wayne State University, Detroit (USA) and were used in [201] to construct the head and neck venous network of the present model. For details on the image acquisition procedure and a discussion on expected agreement between MRI-derived

FIGURE 3.4: Computed blood pressure p (continuous black line) and blood flow q (dashed red line) in the aortic tree at different locations a) to g). Cardiac-cycle averaged values are denoted by $\bar{p}$ and $\bar{q}$.

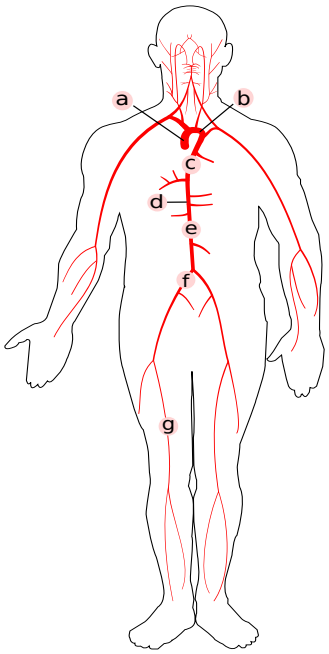

(A) Ascending Aorta (No.1)

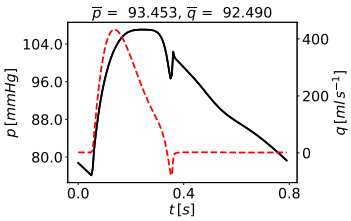

(B) Aortic Arch II (No. 10)

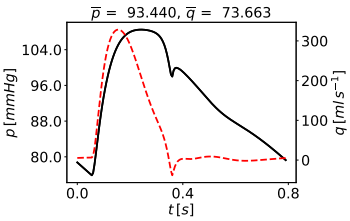

(C) Thoracic Aorta II (No. 13)

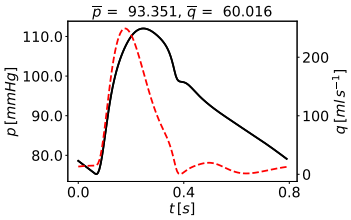

(D) Abd. Aorta II (No. 27)

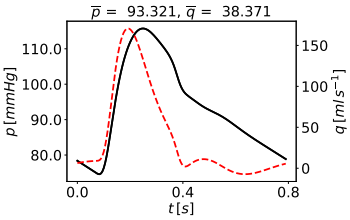

(E) Abd. Aorta IV (No. 31)

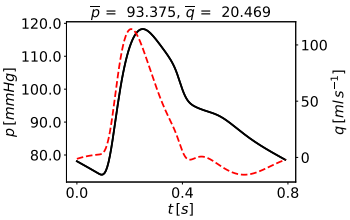

(F) R. C. Ili. Artery (No. 34)

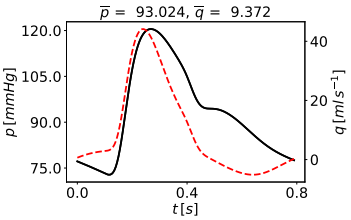

(G) R. Fem. Artery (No. 38)

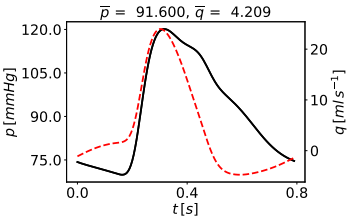

FIGURE 3.5: Blood flow distribution in selected systemic arteries (left frame) and veins (right frame): computational results of the present model, computational results from [201] and literature data (average and standard deviation).

Asc. Ao.: Ascending Aorta; Kidneys: sum of both Renal Arteries; Tho. Ao.: Thoracic Aorta; Abd. Ao.: Abdominal Aorta; Ext. Il. A.: External Iliac Artery; Fem. A.: Femoral Artery; SVC: Superior Vena Cava; IVC: Inferior Vena Cava; AzG V.: Azygos Vein; SCV: Subclavian Vein. Literature: [a]Murgo *et al.* [211]; [b]Wolf *et al.* [322]; [c]Zitnik *et al.* [325]; [d]Cheng *et al.* [54]; [e]Itzchak *et al.* [128]; [f]Lewis *et al.* [155]; [g] Be'eri *et al.* [22]; [h] Cheng *et al.* [54]; [i] Nabeshima *et al.* [217]; [j] Fortune & Feustel [95].

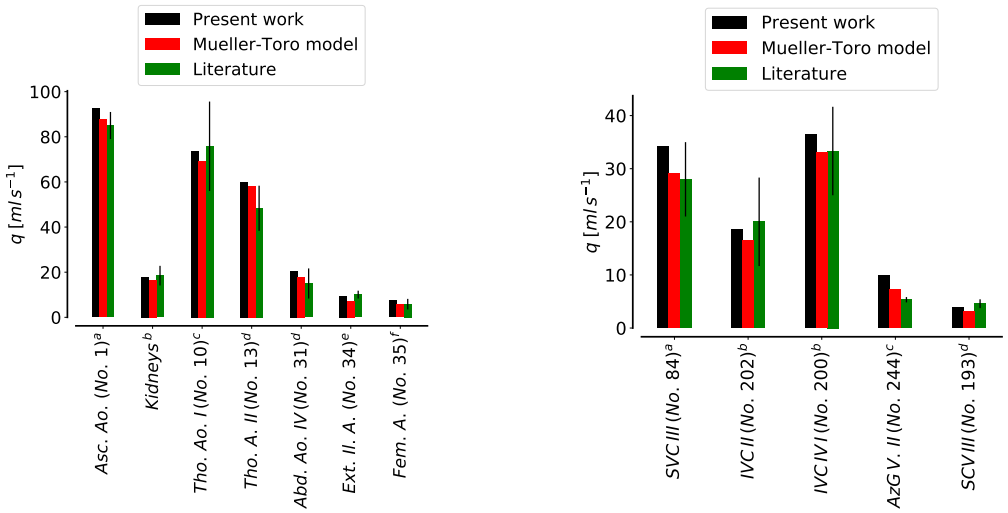

FIGURE 3.6: Computed blood pressure p (continuous black line) and blood flow q (dashed red line) in selected systemic veins in different locations a) to d). Cardiac-cycle averaged values are denoted by $\bar{p}$ and $\bar{q}$.

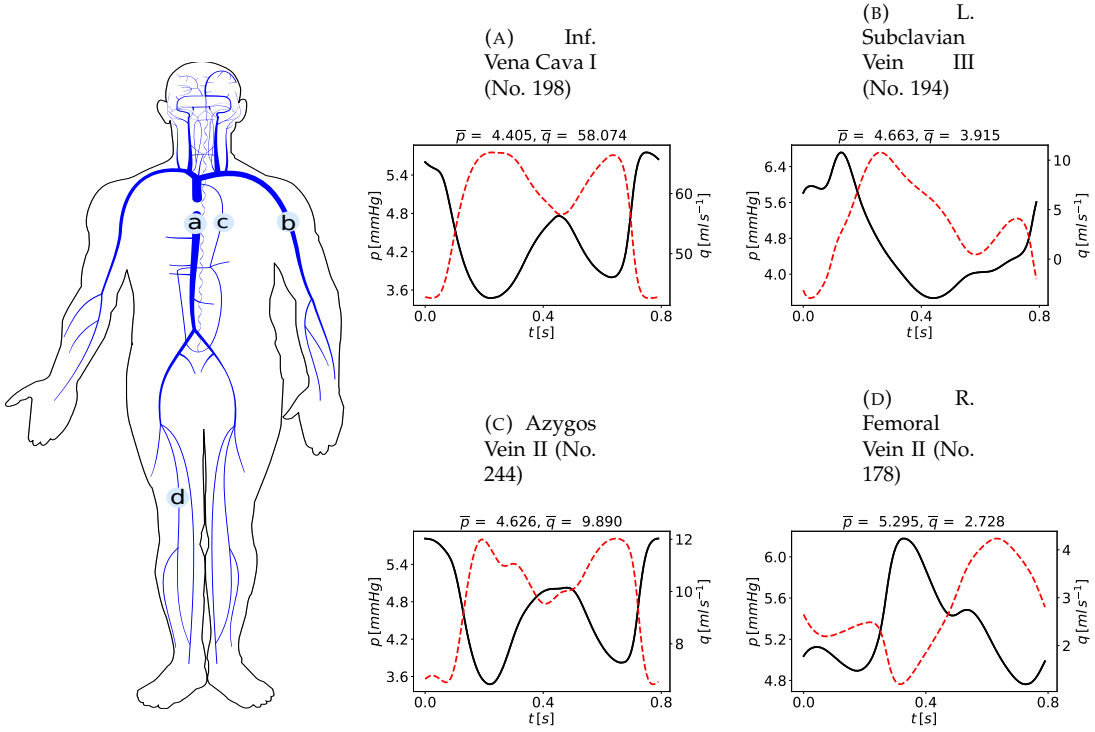

FIGURE 3.7: Computed blood pressure p and blood flow q in selected arteries obtained with viscoelastic (continuous black line, Visco) and elastic (dashed red line, Elas) model for vessels wall. Cardiac-cycle averaged values are denoted by $\overline{p}_{Visco}$ and $\overline{q}_{Visco}$ for viscoelastic vessels and by $\overline{p}_{Elas}$ and $\overline{q}_{Elas}$ for elastic vessels.

(A) Thoracic Aorta II (No. 13)

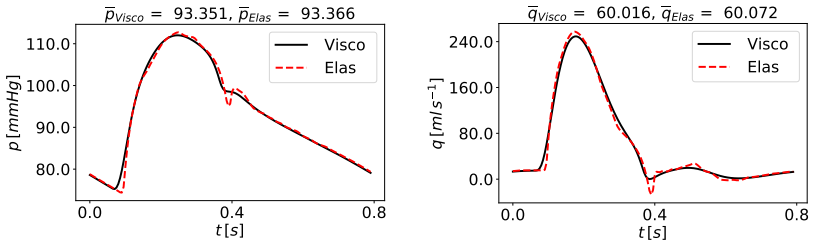

(B) R. Femoral Artery (No. 38)

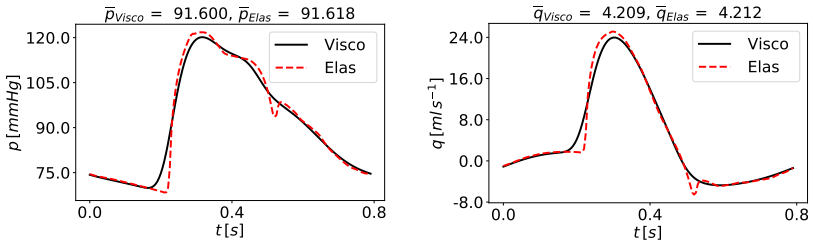

(C) R. Com. Car. Artery (No. 47)

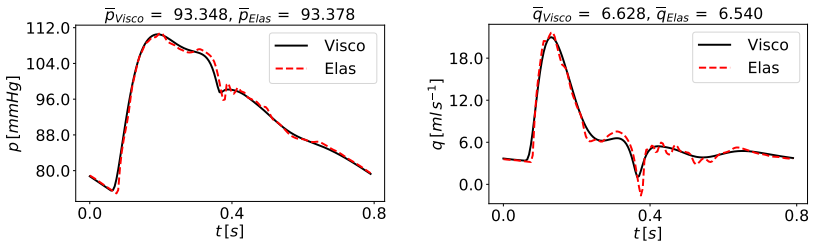

FIGURE 3.8: Computed blood pressure p and blood flow q in selected veins obtained with viscoelastic (continuous black line, Visco) and elastic (dashed red line, Elas) model for vessels wall. Cardiac-cycle averaged values are denoted by $\overline{p}_{Visco}$ and $\overline{q}_{Visco}$ for viscoelastic vessels and by $\overline{p}_{Elas}$ and $\overline{q}_{Elas}$ for elastic vessels.

(A) Sup. Vena Cava I (No. 84)

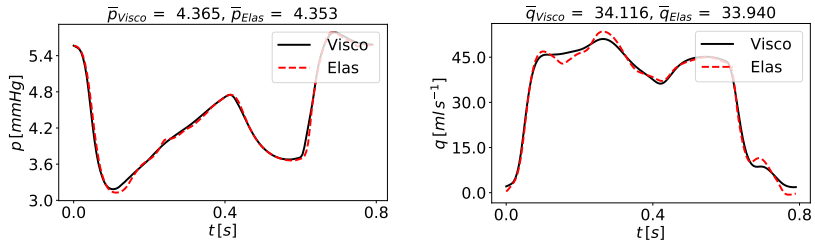

(B) R. Femoral Vein II (No. 178)

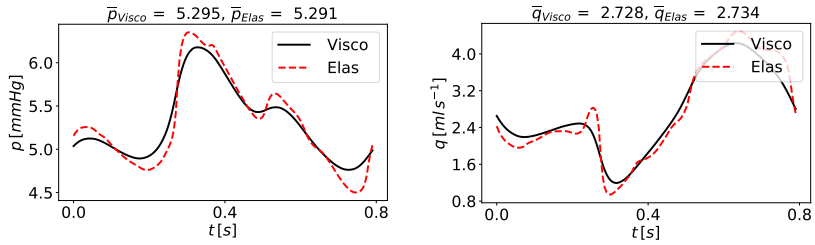

(C) R. IJ Vein III (No. 224)

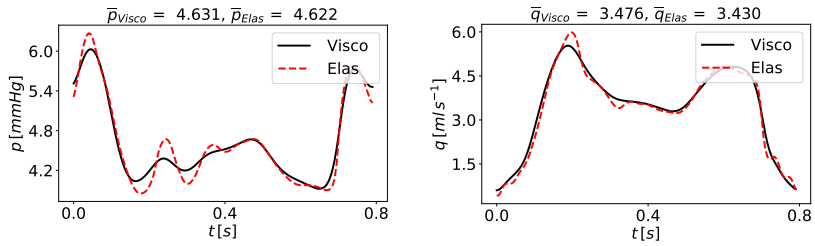

FIGURE 3.9: Computed pressure values for three vascular beds. p: pressure of supplying artery; pAl: pressure in arterioles; pCp: pressure in capillaries; pVen: pressure in venules at venous capacitor; pV: pressure of draining vein. Numbers for supplying arteries and draining veins refer to numeration in Tables 2.1 and 2.4.

(A) Simple connection (No. 16)

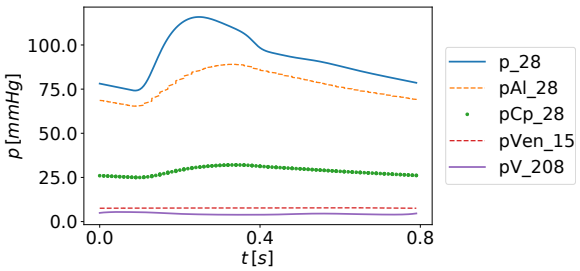

(B) Vascular beds (No. 21)

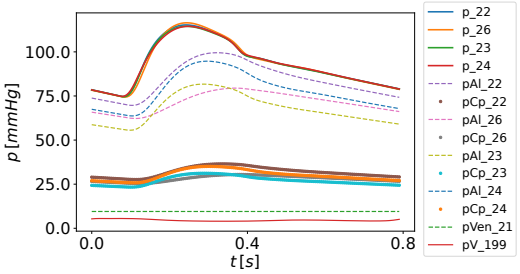

(C) Vascular beds (No. 25)

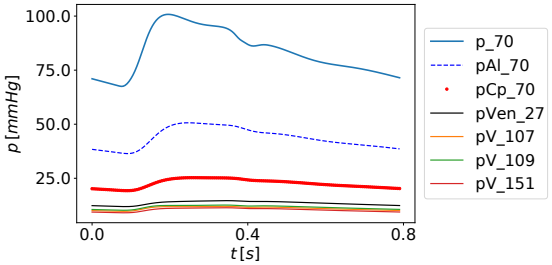

FIGURE 3.10: Computed pressures p and volumes V in the heart. Continuous black line denotes pressure, dashed red line refers to volume.

(A) Right atrium

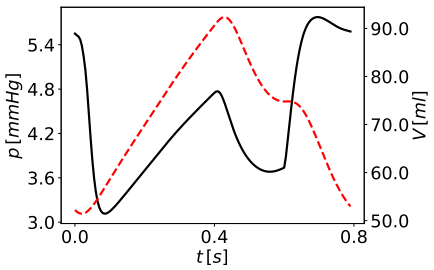

(B) Left atrium

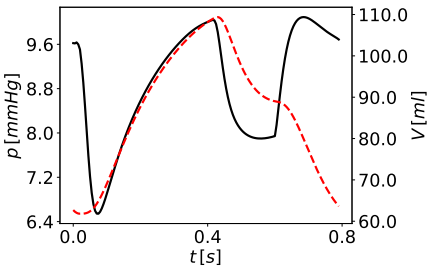

(C) Right ventricle

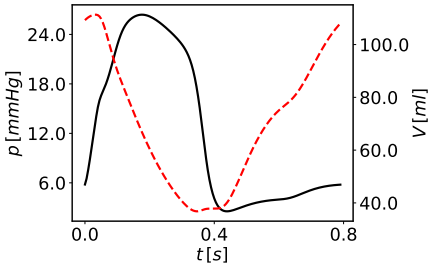

(D) Left ventricle

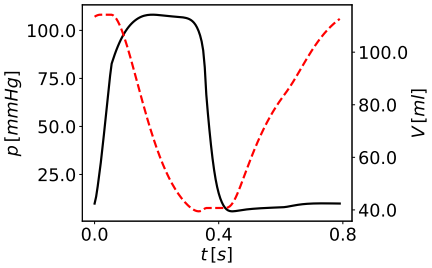

FIGURE 3.11: Computed Pressure-Volume loop for the right and left ventricles.

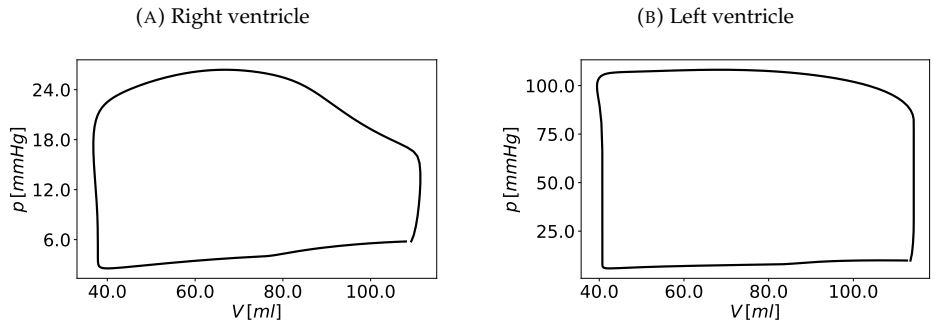

TABLE 3.4: Cardiovascular indexes. Num. Value: computed numerical value; Ref. Value: literature reference value with mean and standard deviation. (S/D)BP: systolic/diastolic aortic blood pressure; MBP: mean blood pressure; PP: pulse pressure in aortic root and in brachial artery; $PP_{Amplification}$: ratio between pulse pressure in brachial artery and aortic root; CO: cardiac output; C_a: arterial compliance evaluated as the ratio between stroke volume and brachial pulse pressure [9]; E_a: arterial elastance; E_{es}: left ventricle elastance; E_a/E_{es}: arterial-ventricular coupling index; LV_{max}: maximum left ventricle volume; LV_{EF}: averaged left ventricle volume; max. $\frac{dP_{LV}}{dt}$: maximum pressure rate of left ventricle; min. $\frac{dP_{LV}}{dt}$: minimum pressure rate of left ventricle.

Index	Current Value	Ref. Value	Ref.
SBP [mmHg]	107.065	105 ± 8	[191]
DBP [mmHg]	76.126	71 ± 7	[191]
MBP [mmHg]	93.272	89 ± 8	[191]
PP_{Aorta} [mmHg]	30.939	30 ± 6	[191]
$PP_{Brachial}$ [mmHg]	37.382	49 ± 9	[191]
$PP_{Amplification}$ [mmHg]	1.208	1.7 ± 0.14	[191]
CO [ml/s]	91.363		
C_a [ml/mmHg]	2.001	1.7	[9]
E_{es} [mmHg/ml]	5.205	4.5	[218]
E_a [mmHg/ml]	2.746	2.3	[218]
E_a/E_{es}	0.528	0.58	[218]
LV_{max}	114.263	150 ± 67	[215]
LV_{EF}	0.655	0.68 ± 0.12	[215]
max. $\frac{dP_{LV}}{dt}$	1546.419	1915 ± 410	[215]
min. $\frac{dP_{LV}}{dt}$	-2861.828	-2296 ± 530	[215]

flow and model predictions refer to [201]; flow waveforms are compared with the underlying patient-specific MRI flow quantification data. Furthermore, the average flow rate is compared with phase-contrast MRI data in Figure 3.13 (right). Predicted flow waveforms display characteristic features of cerebral venous flow with a bi-phasic character. Moreover, agreement of PC-MRI-derived average flows and predicted ones is reasonable.

Figure 3.16 depicts computed intracranial pressure and pressures of a dural sinus and a cerebral vein; the effect of the Starling resistor is evident: pressure in cerebral veins is always higher than intracranial pressure while dural sinus pressure is governed by downstream conditions. Figure 3.17 shows the changes

FIGURE 3.12: Computed blood pressure p (continuous black line) and blood flow q (dashed red line) in the main cerebral and neck arteries. Cardiac-cycle averaged values are denoted by $\bar{p}$ and $\bar{q}$.

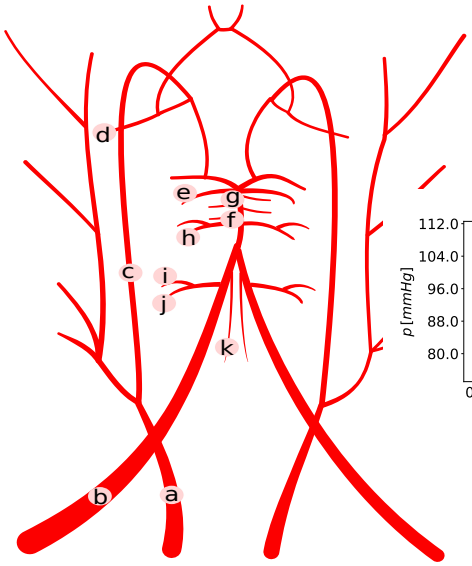

(A) R. Com. Car. Artery (No. 47)

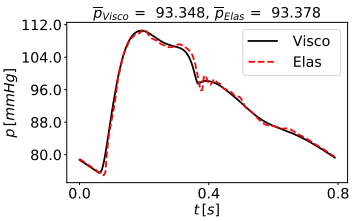

(B) R. Vertebral Artery (No. 6)

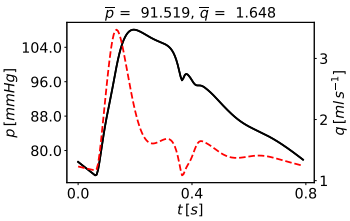

(C) R. Int. Car. Artery (No. 5)

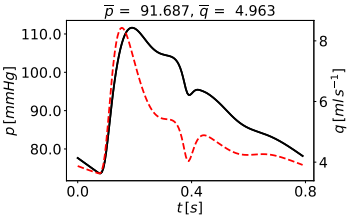

(D) R. M. Cerebral Artery (No. 61)

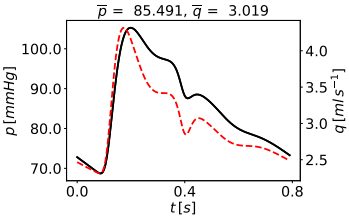

(E) R. Sup. Cer. Artery (No. 287)

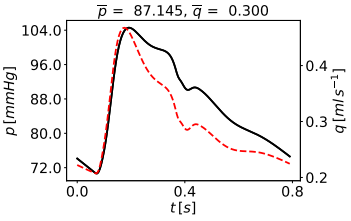

(F) R. Pon. Artery I (No. 316)

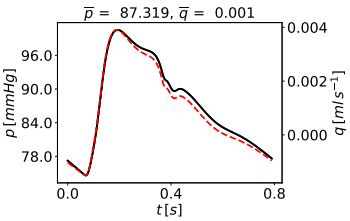

(G) R. Pon. Artery II (No. 317)

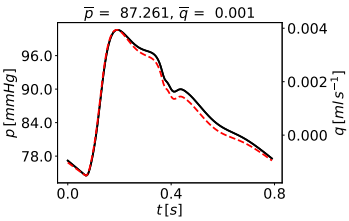

(H) R. Ant. Inf. Cer. Artery (No. 306)

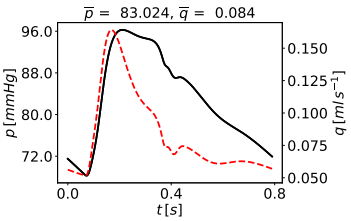

(I) R. Post. Inf. Cer. Artery (No. 310)

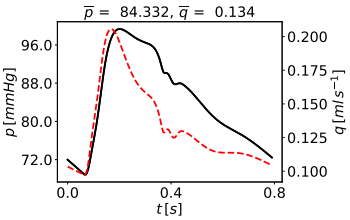

(J) R. PICA Med. Artery (No. 308)

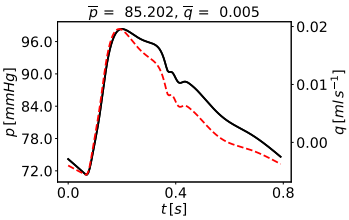

(K) R. Ant. Spi. Artery (No. 312)

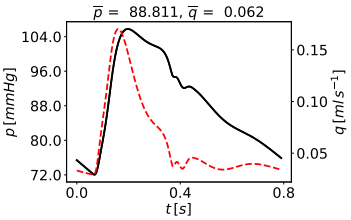

FIGURE 3.13: Comparison between present computed results, other computed results [201] and literature data (average and standard deviation) or MRI flow quantification data [201] for blood flow in head and neck arteries and veins.

Brain: sum of average flow rate in both internal carotid and vertebral arteries; ICA: Internal Carotid Artery; MCA: Middle Cerebral Artery; BA: Basilar Artery; VA: Vertebral Artery; SSS: Superior sagittal Sinus; StS: Straight Sinus; TS: Transverse Sinus; IJV: Internal Jugular Vein. Literature: [a]Stoquart-ElSankari *et al.* [274]; [b]Stock *et al.* [272]; [c]Boorder *et al.* [35].

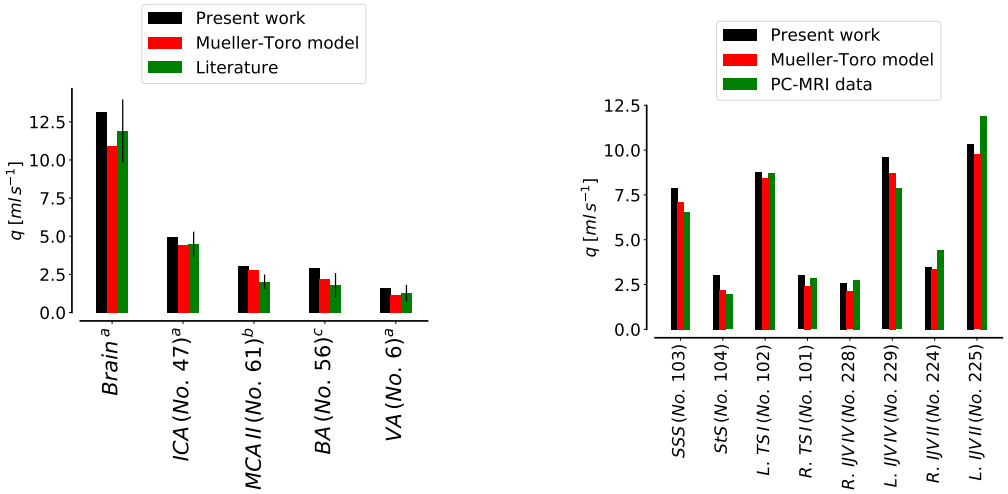

FIGURE 3.14: Computed autoregulation curve (blue continuous line) compared to Ursino's data [305] (red dots). Mean arterial pressure, MAP, against the percentage change in cerebral blood flow, % CBF, with respect to the baseline situation.

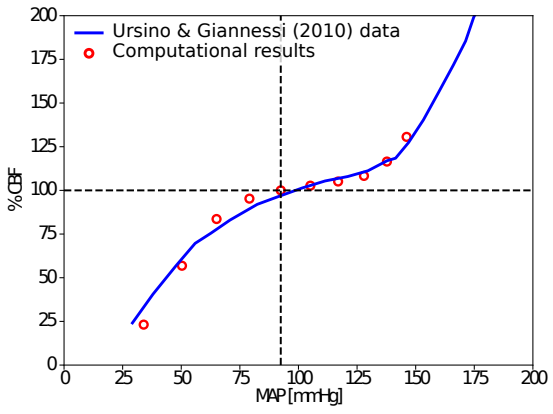

FIGURE 3.15: Comparison between computed blood flow q and PC-MRI flow quantification [201] in dural sinuses and internal jugular veins. Full line denotes present model results, PC-MRI flow quantification data is shown with symbols and full line. Cardiac-cycle averaged values are denoted by $\bar{q}$ and $\bar{q}_{MRI}$.

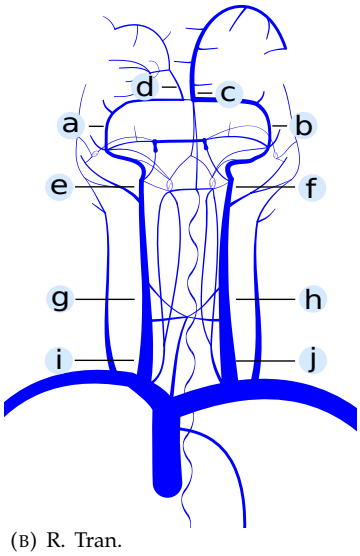

(A) L. Tran. Sinus (No. 101)

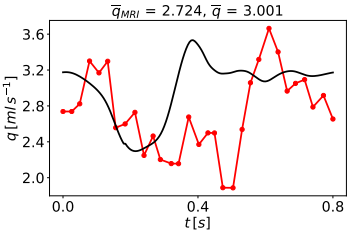

(B) R. Tran. Sinus (No. 102)

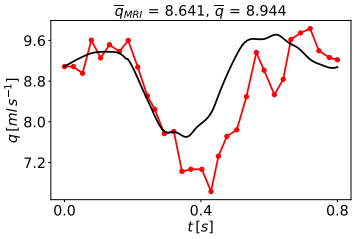

(C) Sup. Sag. Sinus (No. 103)

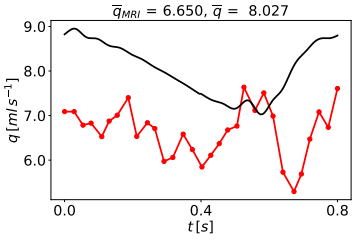

(D) Str. Sinus (No. 104)

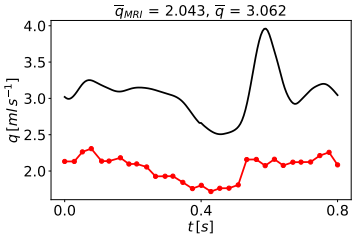

(E) IJ Vein I (No. 229)

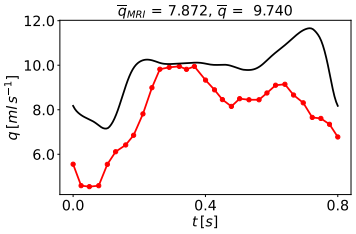

(F) IJ Vein I (No. 228)

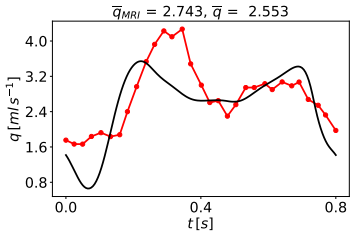

(G) IJ Vein III (No. 225)

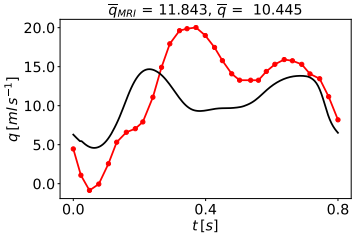

(H) IJ Vein III (No. 224)

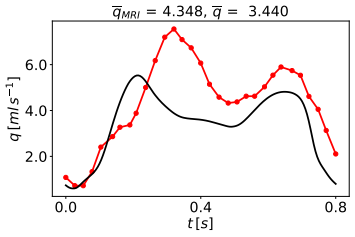

(I) IJ Vein VI (No. 243)

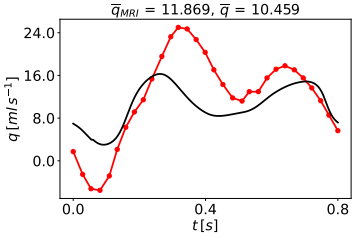

(J) IJ Vein VI (No. 242)

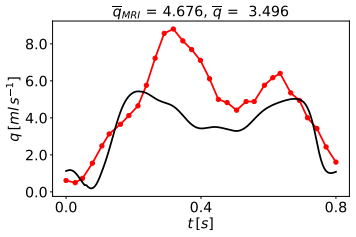

FIGURE 3.16: Computed cerebral venous pressure p and CSF dynamics. CV: cerebral vein (No. 158); SSS: superior sagittal sinus (No. 165); ICP: intracranial pressure (pressure of the fluid parts of the brain parenchyma compartments).

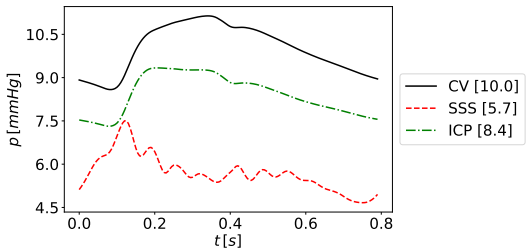

FIGURE 3.17: Variation in time of $V - V_{av}$ where V is the volume of a compartment and V_{av} is the averaged volume over a cardiac cycle. A: arteries; Al: arterioles; Cp: capillaries; Vn: venules; V: veins.

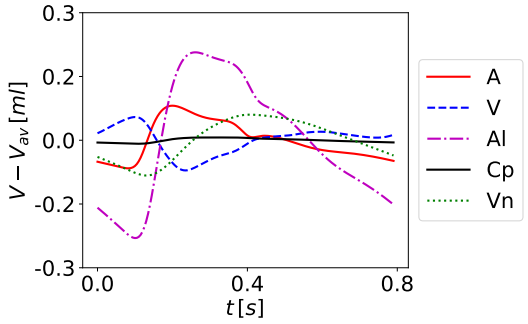

in volume of the main blood cerebral compartments: arteries, arterioles, capillaries, venules and veins.

3.3.3 Validation for CSF and brain dynamics

Here we analyse pressure, flow and volume of different CSF compartments and their interaction with arterial and venous blood within the brain; see Figures 3.18 to 3.21. Physiological intracranial pressure (ICP) values have been investigated extensively, ranging from 7 mmHg to 15 mmHg for an adult in supine position [101]. Generally, ICP refers to the CSF pressure, regardless of where it is measured. In our simulation, slight differences are found between the mean pressure of the extracellular fluid part of the brain parenchyma and other cranial and spinal CSF compartments. In this context, we call ICP the pressure of CSF located in the brain parenchyma compartments; specifically, ICP is defined as $\frac{1}{2}(p_{br,R} + p_{br,L})$, that is the average between the CSF pressure of the right and left extracellular fluid part of the brain parenchyma compartments. Figure 3.18 reports the pressures of the CSF compartments. The ventricular pressure ranges from 7.7 to 9.7 mmHg with a pulse pressure of about 2 mmHg. The cranial and spinal subarachnoid spaces pressures values lie between 8.1/8.2 and 9.3/9.2 mmHg and the pulse pressure is around 1.0 mmHg. Comparing the left and right hemisphere, there are no distinct differences concerning pressures. The brain parenchymal pressure varies from 7.8 to 9.8 mmHg, with a mean value of 8.42 mmHg on the right and left sides.

Figure 3.19 shows an analysis of the intracranial pressure waveform according [45, 140, 48, 67]. We can notice three physiological peaks: the first one, P1 or percussion wave, is the highest, followed by P2 or tidal wave and finally there is P3 or dicrotic wave, which appears after the dicrotic notch. The peaks come from the arterial pulse wave from the heartbeat on the brain which essentially floats in cerebrospinal fluid; the ICP waveform can usually be seen in time-synchronized fashion relation to the arterial waveform. The three typical peaks of the intracranial pressure can be observed in all CSF compartments but in the spinal

FIGURE 3.18: Pressure in CSF compartments over a cardiac cycle. Mean pressure over the cardiac cycle is reported in brackets. Brain: pressure in fluid part of brain parenchyma; LVs: pressure in lateral ventricles; 3V: third ventricle; AoS: aqueduct of Sylvius; 4V: fourth ventricle; CSAS: cranial subarachnoid space; SSAS: spinal subarachnoid space.

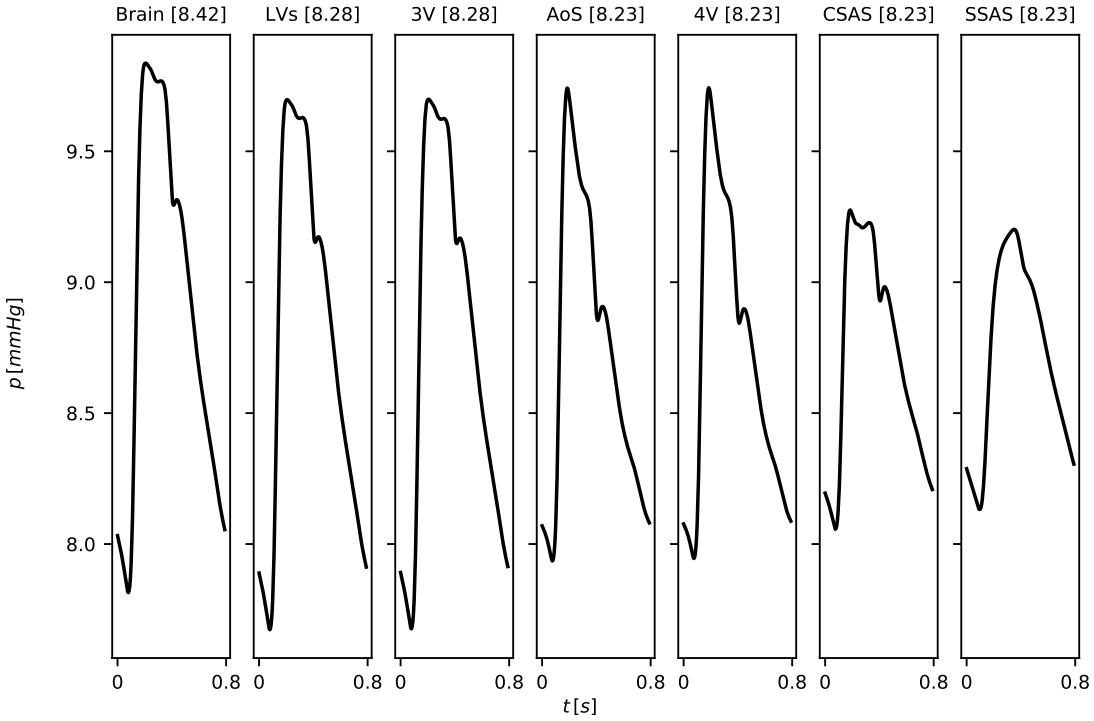

FIGURE 3.19: Cerebrospinal fluid pressure. Left frame shows computed pressure of lateral ventricles (LVs), cranial subarachnoid space (CSAS) and spinal canal (SSAS). Right frame shows computed intracranial pressure with present blood circulation model and the Linninger's CSF model [162] with analysis of the peaks following [65] and computed intracranial pressure with current blood circulation model and Ursino's CSF model [307].

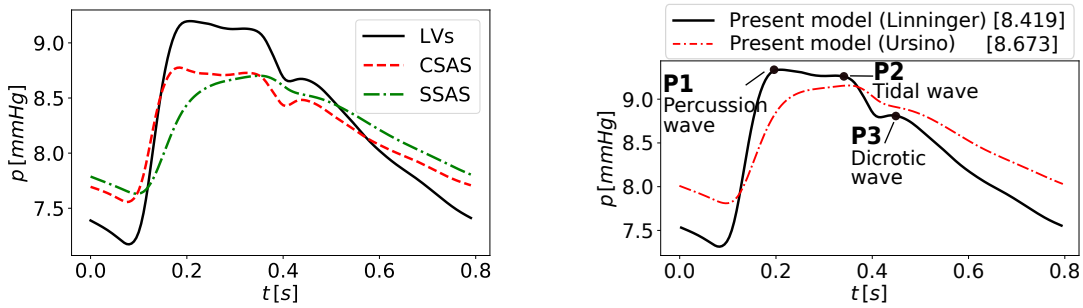

FIGURE 3.20: Cerebrospinal fluid volumes. Variation in time of $V - V_{av}$, where V is the volume of the compartment and V_{av} is the averaged volume over the cardiac cycle (value reported in brackets). LVs: lateral ventricles; 3V: third ventricle; AoS: aqueduct of Sylvius; 4V: fourth ventricle; CSAS: cranial subarachnoid space; SSAS: spinal subarachnoid space.

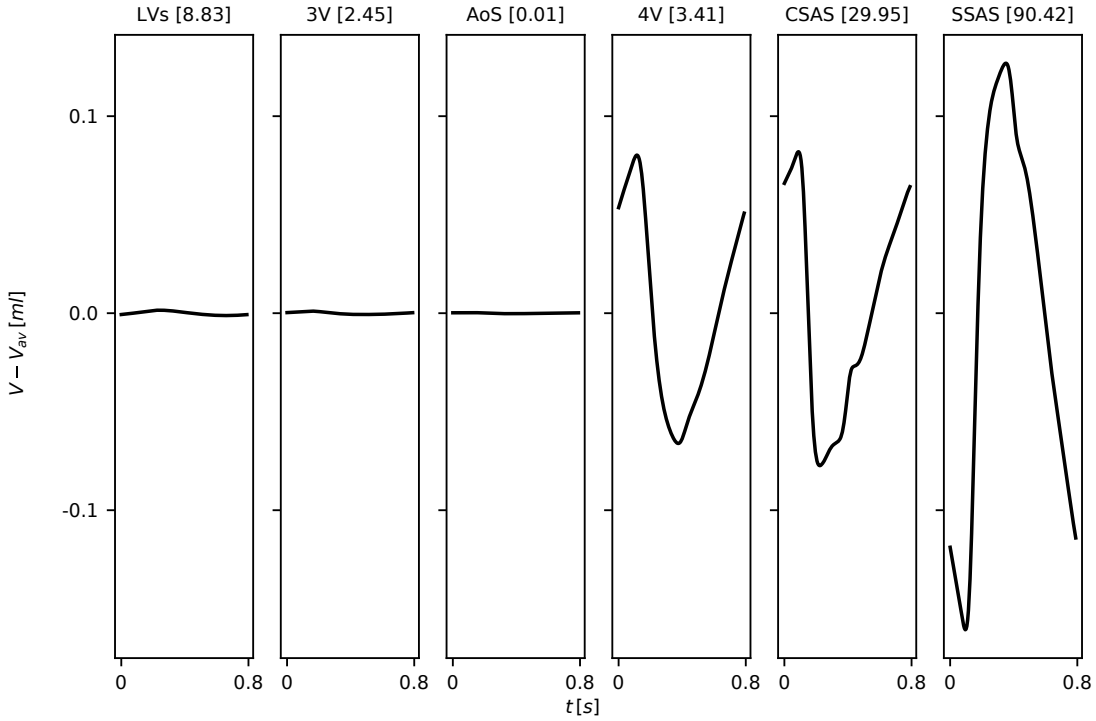

canal they are less pronounced. P1 is caused by the arrival of the arterial flow pulse. P2 is caused by the second arterial flow peak, which happens before the dicrotic notch, while the third peak, P3, is related to the increased flow occurring right after the dicrotic notch.

Figure 3.19 compares the intracranial pressure waveform of the current CSF model based on [162] and that evaluated considering the simple CSF model proposed by [307] and adopted in [202]. While mean ICP depends on initial conditions for both models, in this second case, the waveform peaks are less well defined. Figure 3.20 reports changes in volume of the CSF model compartments. The major part of CSF is contained in the cranial and spinal subarachnoid spaces, about 30 and 90 ml respectively, where the changes over the cardiac cycle take place.

Figure 3.21 shows the time variation of the volumes occupied by different compartments of the craniospinal system, stressing the effect of the Monro-Kellie hypothesis. During systole, intracranial arterial blood increases and arterial pulsations are transmitted directly into the incompressible CSF filled SAS. This evokes a chain of events in the following temporal order: CSF shifts out of the skull into the spinal canal; venous blood from the sinuses flows out of the brain mainly through the internal jugular veins and part of the CSF from the ventricles is displaced out through the aqueduct of Sylvius. Figure 3.22 underlines the relation between blood and CSF compartments' flow. In Figure 3.22 (left), arterial inflow, venous outflow through internal jugular veins, flow in aqueduct of Sylvius and inflow in spinal subarachnoid space are depicted during a cardiac cycle. In Figure 3.22 (right), the CSF and blood normalized flow of the same compartments is shown over a cardiac cycle. The lag in time between the systolic peaks is reported in Table 3.5. The arterio-spinal CSF delay is underestimated by the mathematical model compared to the

FIGURE 3.21: Time variation of $V - V_{av}$ of fluid volumes within the cardiac cycle, where V is the volume of the compartment and V_{av} is the averaged volume over the cardiac cycle. A: cerebral 1D arteries, arterioles and capillaries; V: cerebral 1D veins and venules; C-CSF: cranial CSF (CSF in all compartments inside the skull); SSAS: spinal CSF.

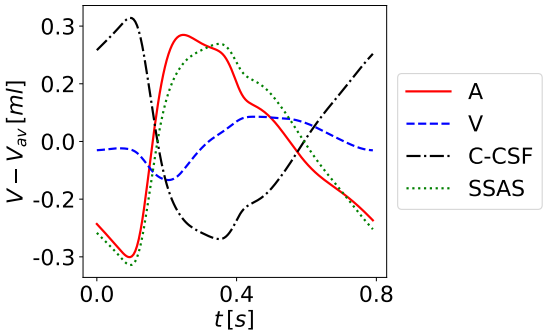

FIGURE 3.22: Time variation of blood and CSF flow within a cardiac cycle. Left frame shows blood and CSF flow within a cardiac cycle, where axis on the right refers to AoS flow. Right frame shows CSF and blood normalized flow analysis over a cardiac cycle. To highlight the temporal dynamic sequence in the four fluid compartments, each flow profile was normalized between 0 and 1 such that all four systolic peaks correspond to 1. A: arterial flow of internal carotid arteries and vertebral arteries at C2/C3 level; V: internal jugular veins flow at C2/C3 level; SSAS: flow of the spinal subarachnoid space; AOS: flow in the aqueduct of Sylvius.

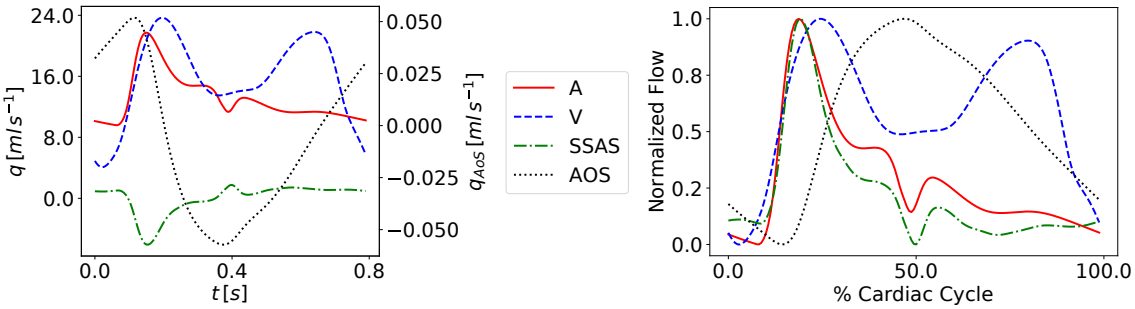

literature range, although the lag in time between arterial systolic peak and CSF peak in the Aqueduct of Sylvius follows the literature data. This mismatch in the time lag of the flow of CSF into the spinal canal can be attributed to the lack of inertia of the model describing flow in the spinal canal [42]. A one-dimensional model for computing the flow of cerebrospinal fluid within the spinal subarachnoid space under the simplifying assumption that it consists of two coaxial tubes representing the spinal cord and the dura [290] could better capture the physiology and the interaction with other compartments. Despite this, the comparison of arterial cerebral inflow and inflow of the spinal subarachnoid space with MRI data from [12], depicted in Figure 3.23, shows a good match between numerical results and physiological behaviour. Finally, Figure 3.24 shows flow and CSF velocity through the aqueduct of Sylvius, featuring an oscillatory behaviour with shape and amplitudes similar to those obtained from PC-MRI flow quantification studies [24].

3.4 Applications: impact of head and neck venous strictures on blood and CSF dynamics

In order to show the applicability of the presented model to situations of clinical relevance, we carry out a preliminary analysis of the effects of transverse sinus stenoses and of strictures in the main extra-cranial venous outflow routes on the cerebral circulation, CSF and brain dynamics.

TABLE 3.5: CSF and blood flow over a cardiac cycle. Literature range taken from [4]. Arterial flow: flow in internal carotid arteries and vertebral arteries; Venous Flow: flow in internal jugular veins at C2/C3 level; CSF flow: inflow of spinal subarachnoid space; tIJV/tA: ratio between total internal jugular veins flow and arterial flow at C2/C3 level; AV, Arterio-CSF$_{SSAS}$, Arterio-CSF$_{AoS}$ Delay: lag in time between arterial and venous, spinal CSF and AoS CSF systolic peaks represented as a percentage of cardiac cycle.

Index	Current Value	Ref. Value
Mean Arterial Flow [ml/s]	13.13	13.55±3.07
Mean Venous Flow [ml/s]	12.15	9.42±2.37
Mean CSF Flow [ml/s]	0.01	0.08±1.33
Mean AoS Flow [ml/s]	0.01	0.03±0.013
tIJV/tA [%]	92.52	71.1±22
AV Delay [%CC]	5.62	12.5±8.06
Arterio-CSF$_{SSAS}$ Delay [%CC]	0.625	5.35±2.36
Arterio-CSF$_{AoS}$ Delay [%CC]	28.12	22.1±74.66

FIGURE 3.23: Computed results compared to measured data. Left frame: normalized cerebral arterial inflow (internal carotid arteries and vertebral arteries) over a cardiac cycle compared with MRI data from [12]. Right frame: normalized inflow of spinal subarachnoid space at C2/C3 level over a cardiac cycle compared with MRI data from [12].

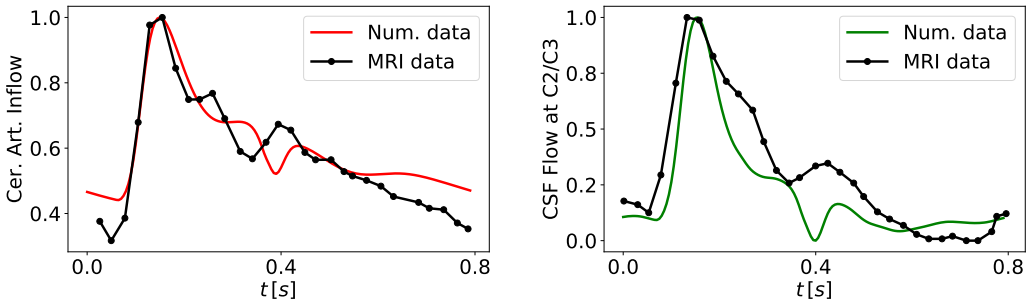

FIGURE 3.24: Computed flow and velocity in the aqueduct of Sylvius. Left frame: computed CSF flow through the aqueduct of Sylvius over a cardiac cycle compared with MRI data (mean and standard deviation) from [24]. Right frame: computed CSF velocity in the aqueduct of Sylvius over a cardiac cycle compared with MRI data (mean and standard deviation) from [24].

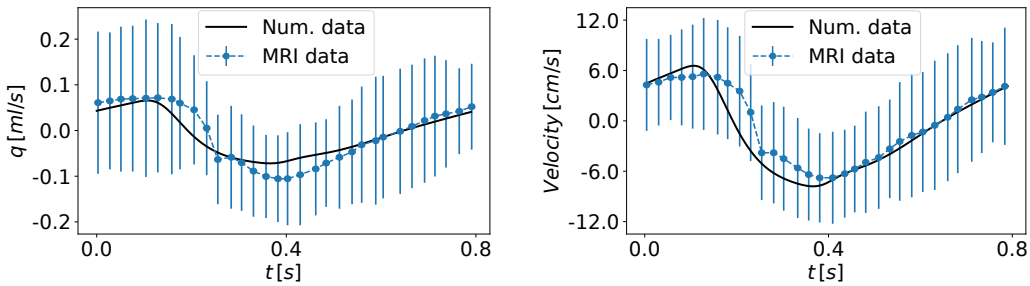

3.4.1 Idiopathic intracranial hypertension patient with transverse sinus stenoses

The role of vascular abnormalities in the onset and course of neurological diseases has long been recognized. In the last decade, the influence of intra- and extra-cranial venous pathology as a trigger/cause of certain neurological disorders has gained attention. Idiopathic intracranial hypertension (IIH) is a neurological condition of unknown aetiology, which requires prompt diagnosis and if left untreated can result in a rapidly progressive visual loss. As said before, how increased CSF pressure in the subarachnoid space influences intracranial arterial and venous fluid dynamics within the framework of the Monroe-Kellie hypothesis remains unclear. Bateman showed that in IIH, the total cerebral arterial inflow is increased by 21% [20]. On the venous front, there is evidence that almost 93% of patients with IIH harbor some degree of dural sinus stenosis [200].

Problem setup

We investigate the impact of bilateral transverse sinus stenosis on cerebral venous flow and CSF dynamics, paying special attention to the role played by collateral flow pathways between deep cerebral vessels and extra-cranial regions. We introduce stenoses to the reference venous network presented in Table A.2 dividing the vessels affected by the stricture (the right and left transverse sinuses, No. 101 and 102, Figure 3.25) in two segments and putting between them a stenosis model. This model is based on [323, 275] and it evaluates the flow variation in time across the stenosis by means of a first-order ordinary differential equation

$$\frac{dq(t)}{dt} = \frac{1}{L}\left(\Delta p(t) - Rq(t) - Bq(t)|q(t)|\right) . \tag{3.38}$$

where Δp is the difference between the upstream and downstream pressures and L, R and B are defined by

$$L = \frac{k_u \rho l_s}{A_0},\ R = \frac{k_v \mu}{2 r_0 A_0},\ B = \frac{k_t \rho}{2 A_0^2}\left(\frac{A_0}{A_s} - 1\right)^2 . \tag{3.39}$$

A_0 and r_0 are the mean reference area and radius of the vessels wherein the stenosis model is placed while l_s and A_s are the length and the minimum area of the stricture, taken equal to 1 cm and 10 % A_0. Finally, $k_u = 1.2$, $k_t = 1.52$ and $k_v = 16 A_0^2/(r_0 A_s^2)(0.83 l_s + 3.28 r_s)$ are empirical coefficients [323, 275].

Comparison between healthy and IIH patient

Figure 3.25 shows computed flow in the transverse sinuses for the healthy control (HC) and for the stenotic case (ST), along with MRI data for a healthy subject; there is a reduction of average flow rate of about 70%. Moreover, due to the stenosis, there is a re-distribution of flow in dural sinuses and an increase in dural pressure (Figure 3.26). As a consequence, there is an increase in pressure in intracranial veins while the arterial flow and pressure are not modified. The venous hypertension due to transverse sinuses stenosis leads to decreased CSF reabsorption via arachnoid granulation which depends linearly on the pressure difference between intracranial pressure and superior sagittal sinus pressure. As a consequence, in order to maintain the balance between CSF generation and absorption, the intracranial pressure rises; moreover, following the Monro-Kellie hypothesis, a major amount of CSF is displaced into the spinal canal. For equal narrowing of the transverse sinuses, the severity of intracranial hypertension depends on the ability of the venous vascular network in developing collateral pathways to brain drainage. Occipital vein and sinus are the main collateral routes for flow limited by stenosis; the flow through these vessels increases significantly, in particular in the occipital vein (from 0.722 ml/s to 6.567 ml/s). We must consider that the venous network for head and neck used here represents a best-case scenario, with all possible collaterals present. If the collateral circulation is impaired, the consequences of a stenosis in the dural sinuses should be aggravated.

In order to explore this hypothesis, we performed a simulation where blood is forced to flow exclusively through the dural sinuses. Results are shown in Figure 3.27. There we show the computed intracranial pressure for the healthy control and for the patient with stenotic transverse sinuses, when the collateral routes are activated and also when they are compromised. In the first case, there is an increased intracranial pressure from 8.42 to 9.83 mmHg in brain parenchyma and a comparable increase in other intracranial compartments; on the other hand, when the collateral routes are excluded, the averaged intracranial pressure over the cardiac cycle rises from 8.42 to 31.16 mmHg in the brain. Concerning the intracranial pressure waveform, in Figure 3.28 (left) we observe that the pulse amplitude between the healthy subject and the one with transverse sinus stenosis does not change, both in case of complete collateral circulation and without collaterals. According to [45], if the ICP values were low, the pulse wave presents a descending saw-tooth appearance, with a clearly distinct P1 component; as the mean ICP rises, there is a progressive elevation in the magnitude of P2 and to a lesser extent of P3. Increase in the P2 component of the intracranial pressure wave is thought to represent decreased intracranial compliance [65, 114]. Moreover, the increase in the P2 and P3 components of the ICP waveform may result from retrograde transmission of venous pressures to the CSF when there are changes in the cerebral venous system [140]. From the numerical experiments shown here, we barely observe such changes in the ICP waveform. We attribute this fact to the linear character of intracranial compliant compartments. We consider it a limitation of our model in its current form, that will be addressed in future work.

Table 3.6 reports the cardiac cycle-averaged cerebral arterial volume (1D arteries and arterioles), venous flow (capillaries, venules and 1D veins), cranial CSF and spinal CSF. Arterial volume is 28.98 % of total blood volume; this data is in line with [124] where the percentage of arterial blood volume with respect to total cerebral blood volume was estimated to be approximately 20-30 %. When the collateral routes are blocked, the spinal CSF volume increases from 90.42 ml to 100.90 ml without significant changes in cerebral venous blood and cranial CSF. This rather insensitive behaviour of venous blood volume is thought to be related to the modelling approach adopted for representing Starling resistors, which resistance to flow is not influenced by transmural pressure, see Section 3.5 for more details. Figure 3.28 (right) shows flow through the aqueduct of Sylvius. As for the case of ICP, we observe small changes in flow pulsatility for all cases considered. This observation is not in line with experimental observations of flow across the aqueduct of Sylvius in patients with venous obstructions to cerebral blood drainage, where visible increase in flow pulsatility is observed [24, 119, 177]. As already remarked for ICP, we believe that this behaviour is due to the lack of non-linear compliance in intracranial compartments.

Cerebral arterial inflow is similar between healthy and stenotic subjects with collaterals, 13.13 ml/s and 12.92 ml/s, showing that the cerebral autoregulation is maintaining the cerebral perfusion. The cerebral arterial pressure evaluated in the middle cerebral artery is 85.49 mmHg in healthy subject and 85.64 mmHg in the stenotic case. However, the ratio between total jugular veins flow and arterial inflow is decreased from 93% in healthy control to 87% in subject with transverse sinuses stenosis; the outflow is deviated to external jugular veins and vertebral veins. When the collateral circulation is blocked in the stenotic case, the arterial inflow is decreased to 10.11 ml/s and the ratio between total jugular veins flow and arterial inflow is 94 %. The pressure in main cerebral arteries is increased by 3 mmHg. In this case, the cerebral blood flow is significantly lower than that of healthy control, since the cerebral autoregulation is not able to fully compensate the drop in perfusion pressure (cerebral arterial pressure minus intracranial pressure) by reducing peripheral arterial resistances. According to [20], standard MRI, MR venography and MR flow quantification studies revealed that the mean arterial inflow in stenotic patient with IIH is 21 % above normal, but the SSS outflow was within the normal range; this means that the mean outflow as a percentage of the total inflow was reduced: this is evidence of collateral flow. In our mathematical model, we don't observe an increase in arterial inflow, both with and without collaterals circulation. However, when the

FIGURE 3.25: Location of transverse sinus stenosis and computed flow in healthy control (HC) and stenotic case (ST) compared with MRI data [201].

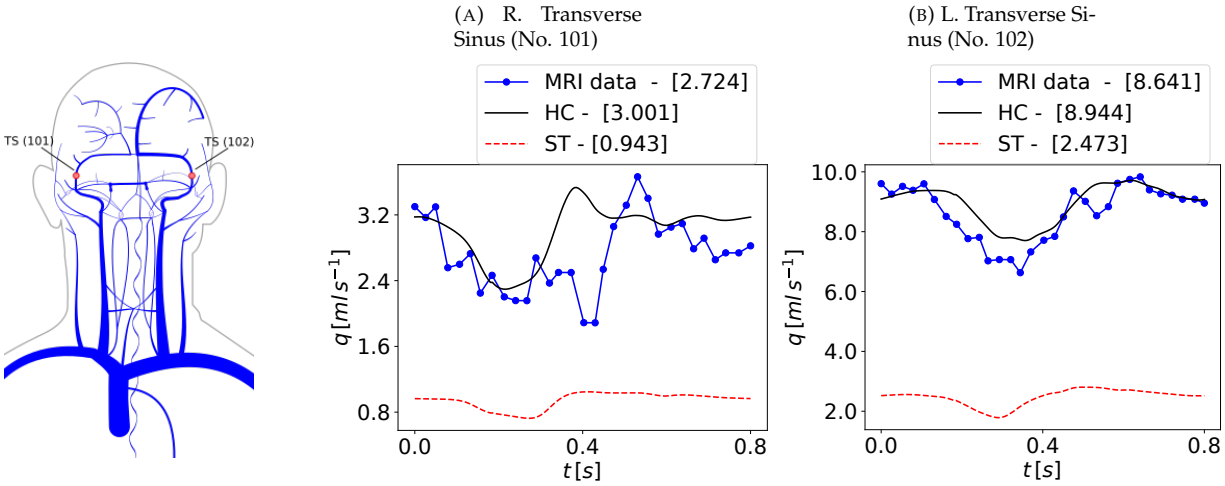

FIGURE 3.26: Averaged pressure over a cardiac cycle of different dural sinuses: comparison between healthy control (HC) and stenotic case (ST). HC: healthy control subject; ST - with Cols.: subject with transverse sinus stenosis and complete collateral circulation; ST - no Cols.: subject with transverse sinus stenosis without collateral circulation. TS: transverse sinus; SS: straight sinus; SPS: superior petrosal sinus; IPS: inferior petrosal sinus; SSS: superior sagittal sinus; ISS: inferior sagittal sinus.

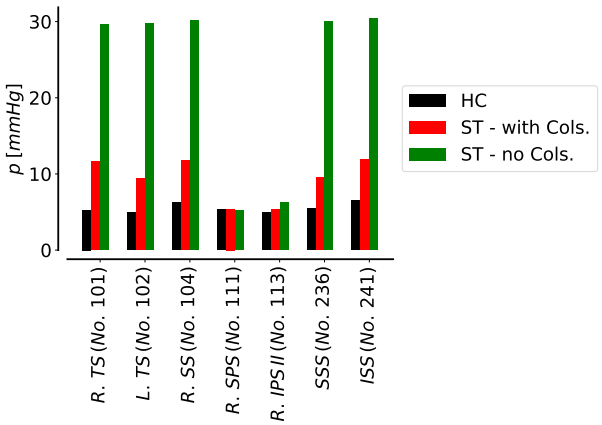

collaterals are present, the percentage of venous outflow to arterial inflow is decreased, as in [20]. When the collateral circulation is reduced, the arterial inflow predicted by our model decreases. While this is the expected behaviour if one analyses how our model is constructed, it contradicts observations in [20]. This disagreement could be due to the fact that we consider a sudden change from a baseline situation to a pathological one. There certainly are short- and/or long-term mechanisms not considered in our model that produce the above mentioned experimental observation of increase cerebral flow in IIH patients. This aspect will be investigated in future work. Table 3.7 shows the flow coming in and out of the left and right brain parenchyma (considering the pressure driven and the constant flow) and the brain porosity, evaluated as the ratio between the volume of the fluid part of the brain parenchyma and its total volume. The flow through the brain parenchyma decreases when there are stenotic transverse sinuses with respect to the healthy control; when the collateral circulation is blocked, this decrease reaches 5 %, that is almost 16 % if we consider the pressure driven seepage of extracellular fluid flow from capillaries into the brain. The brain porosity remains almost constant in all cases.

TABLE 3.6: Computed averaged volume of blood and CSF over a cardiac cycle in main cerebral compartments. Arterial Blood: 1D arteries and arterioles; Venous Blood: capillaries, venules, 1D veins; Cranial CSF: lateral, third and fourth ventricles, aqueduct of Sylvius, cranial subarachnoid space and fluid part of the brain parenchyma; Spinal CSF: spinal subarachnoid space. Comparison between healthy control and stenotic cases. HC: healthy control; ST - with Cols.: stenotic case with collaterals; ST - no Cols.: stenotic case without collaterals.

	HC	**ST - with Cols.**	**ST - no Cols.**
Arterial Blood [ml]	48.01	48.00	48.05
Venous Blood [ml]	117.84	118.12	119.83
Cranial CSF [ml]	469.55	469.86	471.53
Spinal CSF [ml]	90.42	91.18	100.90

FIGURE 3.27: Pressure in CSF compartments over a cardiac cycle: comparison between healthy control (HC) and subject with transverse sinuses stenosis (ST). When the collateral routes are blocked, the intracranial pressure rises by 30 mmHg. HC: healthy control subject; ST - with Cols.: subject with transverse sinus stenosis and complete collateral circulation; ST - no Cols.: subject with transverse sinus stenosis without collateral circulation. Brain: fluid part of brain parenchyma; LVs: lateral ventricles; 3V: third ventricle; AoS: aqueduct of Sylvius; 4V: fourth ventricle; CSAS: cranial subarachnoid space; SSAS: spinal subarachnoid space.

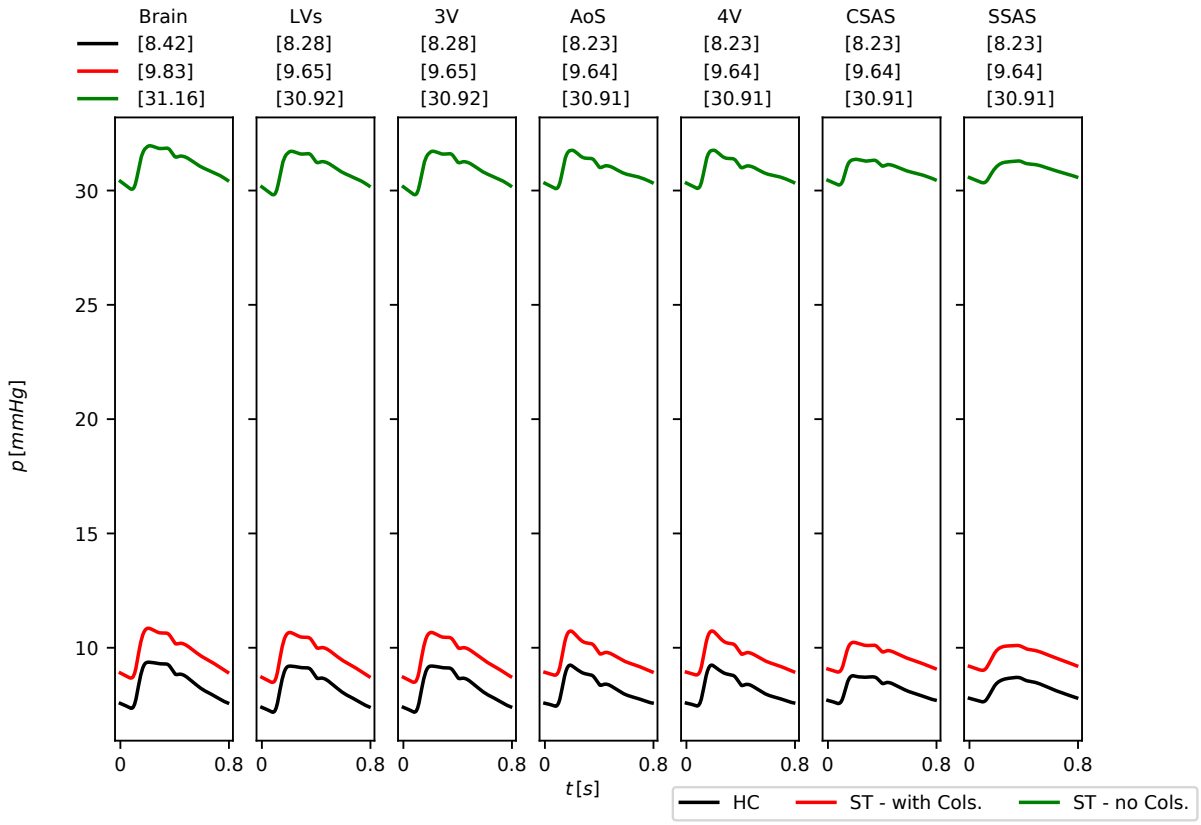

FIGURE 3.28: **Left frame** Intracranial pressure waveform: comparison between healthy control (HC) and subject with transverse sinuses stenosis (ST) with and without collateral circulation. We consider as intracranial pressure the pressure in the fluid part of the brain parenchyma. p: computed intracranial pressure, $\overline{p}$: averaged pressure over a cardiac cycle (value written in brackets).
Right frame Variation in time of flow through the aqueduct of Sylvius for the healthy control (HC), a patient with transverse sinus stenosis with collaterals (ST - with Cols.) and a patient with transverse sinus stenosis without collaterals (ST - no Cols.).
HC: healthy control subject; ST - with Cols.: subject with transverse sinus stenosis and complete collateral circulation; ST - no Cols.: subject with transverse sinus stenosis without collateral circulation.

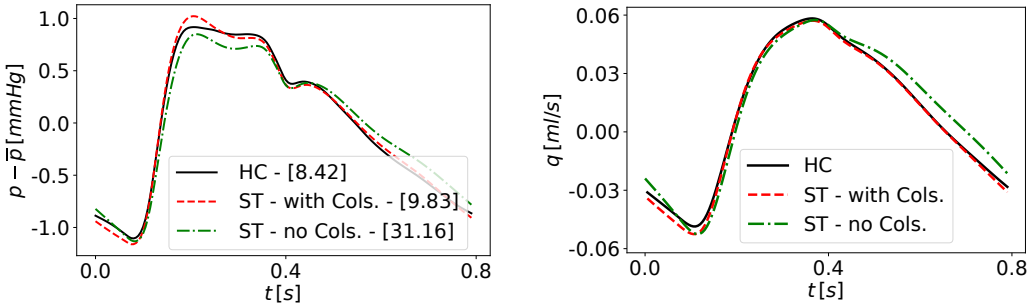

TABLE 3.7: Cerebrospinal fluid exchange $q^{in}_{br,L-R}$ and q^{out}_{br,L_R} and brain porosity Φ_{br} (ratio between fluid part and total volume of brain parenchyma, considering a solid part of 980 ml): Comparison between healthy control and subject with transverse sinuses stenosis with and without collaterals. Percentage variation with respect to healthy case in brackets. HC: healthy control; ST - with Cols.: stenotic case with collaterals; ST - no Cols.: stenotic case without collaterals.

	HC	**ST - with Cols.**	**ST - no Cols.**
$q^{in}_{br,L} \times 10^{-4}$ [ml/s]	7.4	7.3 (-1.37)	7.0 (-5.4)
$q^{in}_{br,R} \times 10^{-4}$ [ml/s]	7.4	7.3 (-1.37)	7.0 (-5.4)
$q^{out}_{br,L} \times 10^{-4}$ [ml/s]	7.4	7.3 (-1.37)	7.0 (-5.4)
$q^{out}_{br,R} \times 10^{-4}$ [ml/s]	7.4	7.3 (-1.37)	7.0 (-5.4)
Φ_{br}	0.298	0.298	0.298

3.4.2 Extracranial venous outflow strictures and their implication for Ménière's disease

Chronic cerebrospinal venous insufficiency (CCSVI) has been described as a chronic syndrome, characterized by extracranial venous malformations involving internal jugular veins, vertebral veins and the azygos vein [324]. The narrowing of these veins hampers the normal outflow from the brain, causing an impact on intracranial haemodynamics, as well as on CSF and brain dynamics. Some works on modelling this condition are available in the literature. In [202] and [208], stenoses of the internal jugular veins were studied, while [293] concerns stenotic venous valves. In [297], the neck venous strictures are associated to Ménière's disease, a pathology of the inner ear. These works reveal that CCSVI leads to a significant increase in intracranial pressure; however, since in previous versions of our work, a single CSF compartmental model was used, no refined information about the CSF dynamics could be obtained. Here, we investigate the impact on the CSF and brain dynamics resulting from the CCSVI condition, using a more sophisticated multi-compartment model for CSF.

Problem setup

We consider two different malformations of the extracranial venous vessels. The first one (case A) includes left and right stenotic internal jugular veins, symmetrically above the insertion of the middle thyroid vein, and also a stenosis in the azygos vein. In order to account for these strictures in the model, we introduce stenoses as represented in Section 3.4.1 for vessels No. 224, 225, 244. The minimum area of the strictures is taken equal to 10 % of the reference cross-sectional area of the vessels where the stenosis model is placed (Table A.2). As for transverse sinuses stenosis, this area, as well as the reference cross-sectional area of the vessels, defines the parameters of the stenosis model in Equation (3.39). The second configuration (case B) takes into account stenotic valves, symmetric in both left and right internal jugular veins. The parameter M_s of Equation (2.40) is taken equal to 0.25, causing an obstruction of 75% of the reference cross-sectional area.

Comparison between healthy and pathological patients

As expected, the CCSVI condition is related to a significant pressure drop across strictures. Pressure drops between the pre- and post-stenotic locations are negligible in the case of the healthy control while in case A it is almost 1.37 mmHg and in case B it is 2.25 mmHg. The pressure rise observed in the extracranial venous strictures is transmitted to the intracranial circulation. Figure 3.29 (left) depicts the computed cardiac-cycle averaged pressures in the main dural sinuses of the venous network. Moreover, Figure 3.29 (right) shows averaged pressures for veins of the right inner ear. As reported in [297], the venous pressure in the ear veins is increased due to the extra-cranial venous stenoses; because of the functioning of the Starling resistors located in the ear circulation, this rise is not caused by the backward transmitted pressure waves from the obstructed sites, as occurs in dural sinuses, but it is due to the increased intracranial pressure. As shown in Figure 3.30, in all intracranial compartments the pressure is raised by 1 mmHg in case A and 2 mmHg in case B. By early animal experiments in [46], it was proved that the subarachnoid space is linked to the endolymphatic space and the CSF pressure increase could be transmitted via the endolymphatic duct and sac to the inner ear, leading to the formation of the endolymphatic hydrops, one of the main anomalous conditions in Ménière's disease patients.

As in the previous pathological setting, the ability of developing collateral routes for brain drainage are important in determining the severity of intracranial hypertension. When there are stenoses in the internal jugular veins, the flow is redirected to the extracranial jugular and vertebral veins. The arterial inflow and the ratio between internal jugular vein flow and arterial inflow are 13.11 ml/s and 76.31 % for case A, while

FIGURE 3.29: Computed cardiac-cycle averaged pressures p for the healthy control (HC) and the CCSVI subjects with case 1 and case 2 with collateral circulation. **Left frame** Pressures p in main dural sinuses. SPS: superior petrosal sinus, IPS: inferior petrosal sinus; TS: transverse sinus; SSS: superior sagittal sinus; ISS: inferior sagittal sinus. **Right frame** Brain parenchyma pressure and results in main veins of the right inner ear. VCAQ: vein of the cochlear aqueduct; LABV: labyrinthine vein.

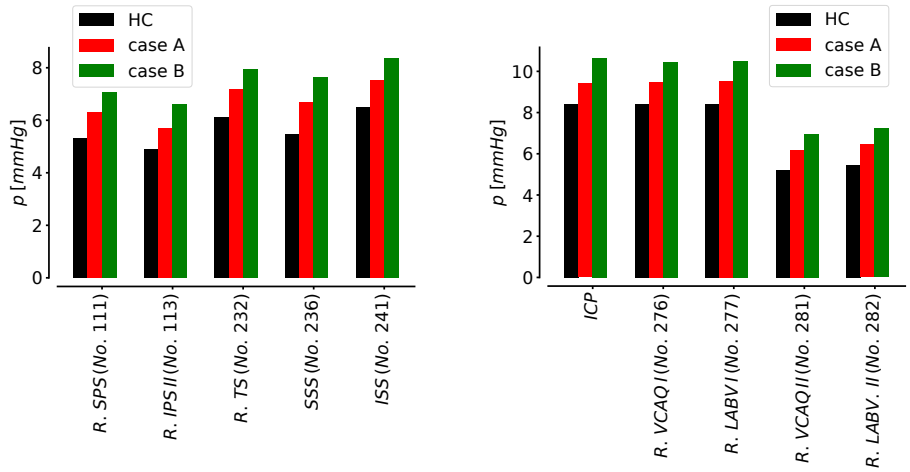

for case B they are 13.10 ml/s and 62.64 %. When the collateral routes are blocked, the internal jugular veins are the main drainage alternatives. We simulated such a situation where collateral pathways are blocked; in this case the arterial inflow is 12.52 ml/s and the ratio between internal jugular veins outflow and arterial inflow is 99.4 %. The intracranial pressure increases by 5.5 mmHg (see Figure 3.30). This raise in pressure is of the same order of magnitude of the pressure drop through the stenosis (10.13 mmHg above the stenosis and 4.48 mmHg below in the right internal jugular vein); in fact, the increase in venous pressure is transmitted up the vessels into the superior sagittal sinus (from an averaged pressure of 5.31 mmHg in the healthy control to 10.97 mmHg), causing a proportional reduction in CSF absorption and then an increase in intracranial pressure until equilibrium between CSF generation and absorption is reestablished [23]. Table 3.8 reports data about the CSF flow in the brain parenchyma; due to the presence of stenoses, the pressure driven CSF seepage from the capillaries to the brain parenchyma is decreased. Figure 3.31 shows flow through the aqueduct of Sylvius. Deviations in terms of pulsatility are very small, even for the configuration featuring no collaterals. However, in [24] changes in pulsatility were observed for patients with CCSVI. The fact that our model correctly captures the trend, i.e. increased pulsatility, but fails to capture the magnitude of such increment, is certainly due to how well our model characterizes intracranial space compliance in the pathological case. Clearly some modelling aspects have to be improved, specifically the model of the Starling resistor (see discussion in next section), as well as mechanical properties of brain dynamics model compartments for patients with CCSVI.

FIGURE 3.30: Computed pressure p in CSF compartments over a cardiac cycle: comparison between the healthy control (HC) and CCSVI patient (ST). Brain: fluid part of brain parenchyma; LVs: lateral ventricles; 3V: third ventricle; AoS: aqueduct of Sylvius; 4V: fourth ventricle; CSAS: cranial subarachnoid space; SSAS: spinal subarachnoid space.

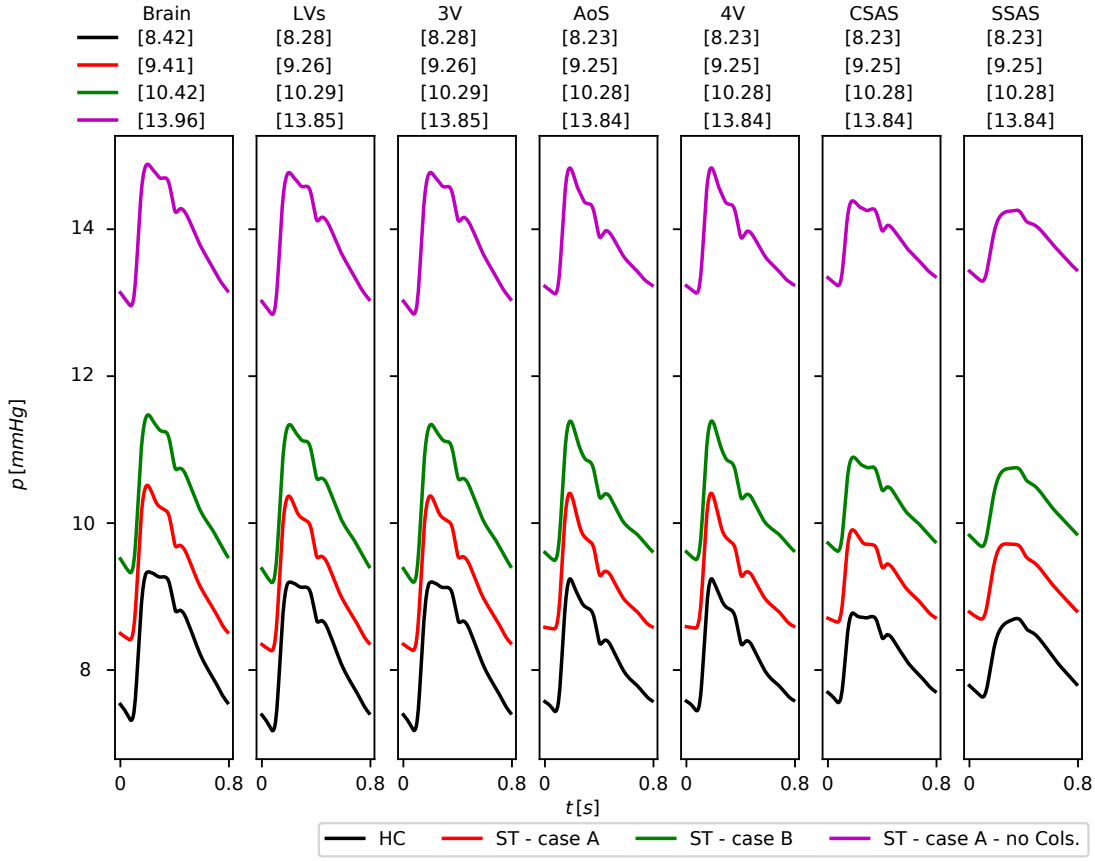

FIGURE 3.31: Variation in time of flow through the aqueduct of Sylvius for the healthy control (HC), the CCSVI patient with collaterals (ST - with Cols.) and the CCSVI patient without collaterals (ST - no Cols.).

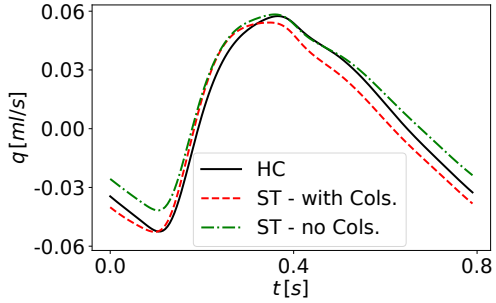

TABLE 3.8: Cerebrospinal fluid exchange $q^{in}_{br,L}$, $q^{in}_{br,R}$, $q^{out}_{br,L}$, $q^{out}_{br,R}$ and brain porosity Φ_{br} (ratio between fluid part and total volume of brain parenchyma, considering a solid part of 980 ml): Comparison of results for a healthy control and subject with IJV stenoses (Case A) with and without collaterals, and subject with IJV stenotic valves (Case B). Percentage variation with respect to healthy case in brackets. HC: healthy control; ST - with Cols.: stenotic case with collaterals; ST - no Cols.: stenotic case without collaterals.

	HC	**ST - case A - with Cols.**	**ST - case A - no Cols.**	**ST - case B - with Cols.**
$q^{in}_{br,L}$ [ml/s]	0.00074	0.00074 (-0.84)	0.00073 (-2.05)	0.00073 (-1.75)
$q^{in}_{br,R}$ [ml/s]	0.00074	0.00074 (-0.84)	0.00073 (-2.05)	0.00073 (-1.75)
$q^{out}_{br,L}$ [ml/s]	0.00074	0.00074 (-0.84)	0.00073 (-2.05)	0.00073 (-1.75)
$q^{out}_{br,R}$ [ml/s]	0.00074	0.00074 (-0.84)	0.00073 (-2.05)	0.00073 (-1.75)
Φ_{br}	0.298	0.298	0.298	0.298

3.5 Concluding remarks

In the first chapters of this thesis (Chapters 2 and 3), we have presented a global, closed-loop, multiscale model of the human circulation coupled with a multi-compartmental model for the cerebrospinal-fluid dynamics. The model comprises one-dimensional descriptions for medium to large blood vessels, arteries and veins, accounting for the viscoelastic property of the blood vessel wall. Lumped-parameter descriptions are used for other components of the full model that include the heart, the pulmonary circulation, the microvasculature, venous valves, Starling resistors and the dynamics of cerebrospinal fluid in the craniospinal cavity, along with cerebral autoregulation. The present work departs from the Müller-Toro mathematical model [201, 202] for the global systemic and pulmonary circulations in the entire human body. The main improvements with respect to the original Müller-Toro model and other works fall into three categories: (a) mathematical models for a better description of the physiology of the circulatory system, (b) the computational methods used to solve the governing equations and (c) the enlarged range of potential applications of the resulting model.

On the physiological aspects of the present work, the improvements include the adoption of a viscoelastic tube law, not just for the arterial tree as in [7, 241, 215], but also for the entire venous circulation. We find that computed pressures and flow waveforms for the arterial and venous circulations are more realistic for the viscoelastic tube laws, than for the purely elastic case. The heart model in the present work is also an improvement over that in the original global model [201, 202]; the cardiac valves are represented through a model based on [216]. A novelty of the present thesis is the coupling of the blood circulation to a refined mathematical description of the cerebrospinal fluid dynamics in the craniospinal cavity [162]. The CSF model comprises the cerebral ventricles, the aqueduct of Sylvius, the cranial and spinal subarachnoid spaces and the brain parenchyma. Other additions include the parametrization of the vascular beds, which together with the cerebral autoregulation model, is relevant when studying anatomical malformations of the cerebral circulation. The computational results for the arterial and venous circulation are compared with literature data, while MRI measurements are used for assessing our results for the cerebral venous circulation. Our results are in good agreement with literature and MRI data.

The physiology modelling improvements have resulted in new mathematical problems to be solved, notably, the viscoelastic nature of all major blood vessels. The associated parabolic system of equations has been approximated by a hyperbolic system with stiff source terms following a relaxation approach [295, 197, 199]. The resulting stiff system is solved numerically with the same high-order ADER-type numerical scheme [294, 76], as in the original model [201, 202]. An additional numerical improvement is the adoption

of the local time stepping technique [78], first introduced for blood flow in [204] for solving a simplified one-dimensional vessel network. This technique results in significant computational savings, which are more evident when coupling the blood circulation to the CSF and brain dynamics, as these two systems have different temporal scales and the computational time needed to reach periodicity of the solution is considerably larger than the time scale of a cardiac cycle.

The model as presented is applicable to many pathophysiological conditions associated to the circulatory system, involving both the arterial and the venous systems. In the present thesis we have placed considerable emphasis on the central nervous system (CNS) fluids in the craniospinal cavity, in which blood (arteries, microvasculature and veins) interact with the CNS fluids. To illustrate the applicability of the present model that couples the blood circulation and the CSF dynamics in a holistic setting, we have presented two specific medical applications, namely idiopathic intracranial hypertension as associated to transverse sinus stenoses, and Ménière's disease as associated to extracranial venous outflow strictures. Our results reveal that obstructions in the cerebral venous network lead to intracranial hypertension and disruption of the fluid dynamics in the entire craniospinal cavity. The severity of the consequences of intracranial or extracranial venous outflow obstructions depends on the balance between CSF generation and absorption, the displacement of CSF into the spinal cord and the ability of the venous network in developing collateral routes to respond to the venous outflow obstructions. These findings are relevant to the study of a very important function of central nervous system fluids, namely the clearance of brain metabolic waste and neurotoxins from the CNS. Impairment of the cerebral venous drainage will directly disrupt this clearance function. Indirectly, CSF absorption into the venous system will be hampered, due to venous hypertension, leading to decreased CSF turnover, which will also affect the clearance function.

In spite of the progress reported in this work, there are several limitations to be addressed in future developments. One limitation is the description of Starling resistors, which are major determinants of cerebral venous dynamics; blood flow through these compliant vessels is controlled by sphincter-like structures, which regulate discharge into the main dural sinuses. Another limitation is the absence of a model for solute transport. This limitation prevent us at present from properly describing, via Starling forces [152], the transport of fluid and selected solutes across the blood-brain barrier (BBB), for example. Overcoming this limitation will be crucial for tackling the brain waste clearance function of the CNS, alluded to earlier. Mathematical modelling steps in this direction are outlined in [41, 166]. Another limitation involves the linear distenibility equations of the CSF model. Following [162], these equations link the internal pressure with the cross-sectional area of the compartment in a linear manner. A simple linear pressure-volume relationship is acceptable in the physiological pressure range, but could give under- and/or over-estimation of pressure changes in case of large volume changes, especially when addressing pathological conditions. Future work will address the non-linear behaviour of the pressure-volume relationship in the CSF compartments. Another potential improvement concerns the representation of CSF in the spinal canal, which at present consists of a single 0D model; a possible improvement could be the adoption of a 1D model, as proposed in [290], which is based on two coaxial compliant tubes representing the spinal cord and the CSF between the cord and the dura. Potentially, such representation admitting spatial variations could provide the bases for adding new potential routes for CSF reabsorption.

Addressing the modelling of the microcirculation is a challenging task. Here, the microcirculation was simplified as a lumped resistor capacitor system. While this simplification gave acceptable system-wide predictions, it is not able to account for biphasic blood flow phenomena [102] and network effects [118] that occur in the microcirculation. Significant progress has been made to develop realistic microvascular networks models [163, 103, 117] which could be integrated with the proposed system models in future work.

On balance, the mathematical model presented here is a significant improvement of the original model

[201, 202] published seven years ago, represents the current state of the art and could provide the bases for realistic applications that require the representation of all extracellular body fluids in a holistic setting, along with regulatory processes.

Chapter 4

A multiscale model for the dynamic of the cerebrospinal fluid coupled to the systemic circulation

4.1 Introduction

Cerebrospinal fluid (CSF) plays an essential role in homeostasis and metabolism of the central nervous system. It is a clear, colorless fluid, that is composed mostly of water (99 %) and other substances, such as proteins, glucose, lipids and hormones [154]. According to the classical theory [71, 37], CSF is produced by choroid plexus in the ventricles and travels through the intraventricular foramina from the lateral ventricles to the third ventricle and then to the fourth ventricle through the cerebral aqueduct; finally, it flows into the subarachnoid space via the median aperture of the fourth ventricle. In the cranial subarachnoid space, CSF circulates rostrally to the sites of absorption into the blood, the arachnoid villi, or caudally to the spinal subarachnoid space [113, 298]. CSF circulation is a dynamic phenomenon; such movement is responsible for the transport of the choroid plexus secretion products to their site of action, the balance of the electrolytes and the elimination of catabolites. CSF provides homeostatic regulation of the brain's parenchymal interstitial fluid.

The dynamics of cerebrospinal fluid flow are directly linked to those of the cardiovascular system. Expansion and contraction of cerebral blood vessels are at the origin of CSF pulsation. Moreover, cerebrospinal fluid pressure is the result of a dynamic equilibrium between CSF secretion, absorption and resistance to flow. It varies with the systolic pulse wave, respiratory cycle, abdominal pressure, jugular venous pressure and posture.

CSF dynamics can be altered by diseases and conditions such as hydrocephalus, syringomyelia, spinal cord injury, Chiari malformations, spinal tumors, to name but a few. In these pathological cases, it is necessary quantifying critical parameters of normal intracranial dynamics as well as establishing the gravity of deviations in diseases. Intracranial pressure (ICP) is generally measured invasively in the clinical practice, since invasive methods are currently the most accurate ways of ICP monitoring. Its analysis can reveal fundamental information about the status of cerebral haemodynamics, cerebral perfusion, and autoregulation reserve [114].

In this context, mathematical models describing intracranial fluid dynamics and its interaction with the blood circulation have become important tools for this purpose. An early contribution includes the pioneering work by Marmarou and co-workers [181, 182]. In their work, an electrical model approximated the hydrodynamics of the CSF system; the main aspects of the kinetics of ICP were included, such as nonlinear cerebrospinal fluid production and absorption, as well as non linear intracranial elasticity. Ursino et al.

[301, 302] proposed a simple lumped-parameter model of ICP which accounted for cerebral venous pressure instability, cerebral blood volume and autoregulation; the aim of this kind of model is to improve the comprehension of the physiological ICP time pattern and the interaction between CSF and cerebral blood flow. The main simplification of this work is that all the CSF spaces, i.e. the entire craniospinal cavity, are represented by only one compartment. Sorek et al. [270] introduced a lumped-parameter seven compartmental model of the intracranial cerebrovascular fluid system with CSF, blood, and a deformable brain parenchyma. They calculated the amplitude and timing of volumetric expansion, intracranial pressures, and volumetric fluid exchange as functions of arterial blood pressure pulsations. However, that model did not include the spinal subarachnoid space, hence it did not consider the spinal compliance. In 2009, Linninger at el. [162] incorporated the entire central nervous system with full interaction of the expanding vasculature, the brain parenchyma, the ventricular system, and a compliant spine in a lumped-parameter model which predicts intracranial pressure differences, blood and CSF flow, and deviations from normal to pathological conditions (hydrocephalus).

Unlike the lumped-parameter approach, computational fluid dynamics models can provide spatially resolved information on flow, pressure and mass transport, which opens the door to subject-specific calculations of intracranial dynamics based on medical imaging data. The description of the underlying mechanisms stems from the basic principles of fluid dynamics and it is translated into systems of partial differential equations, supplied with suitable initial and boundary conditions of particular importance. Specifically, CSF is often considered as an incompressible Newtonian fluid, therefore the Navier–Stokes equations are employed. In addition, the fluid dynamics description can be enriched to take into account the combined effects of flow and different structures from a multiphysics perspective including poroelasticity and fluid-structure interaction. However, these models are demanding both as regards geometric and boundary conditions setup than computational cost and complexity; therefore, the existing models focus on individual compartments or small groups of these instead of representing CSF space in its entirety. An example includes the work by Kurtcuoglu et al. [145], who investigated the flow in the cerebral aqueduct and in the third ventricle of normal and hydrocephalic patients using patient-specific geometries reconstructed from magnetic resonance imaging scans.

There are several computational fluid dynamic works about the CSF flow in the spine. A first example was proposed by Loth et al. [172], wherein CSF flow in the spine is assessed by means of a two-dimensional model in small cross-sections of the spinal CSF space derived from imaging data. Bertram et al. [27] used a two-dimensional axi-symmetric numerical model of the spinal cord, consisting of elastic cord tissue surrounded by aqueous cerebrospinal fluid, in turn surrounded by elastic dura, to look quantitatively at wave travel along the cord, also in the presence of a syrinx in the spinal cord [28]. Another option to study the wave propagation in the spine is represented by one-dimensional models. In this case, the spine is generally idealised by a coaxial geometry composed of an inner cylinder for the spinal cord and an outer tube for the dura, with CSF flowing in between. Examples along those lines are the works by Berkouk [26], Carpenter [47], Cirovic [59], Toro [290]. Concerning the coupling between cerebral heamodynamic and one-dimensional models of the spine, Kim and Cirovic [139] proposed a computational model of the cerebrospinal fluid system incorporating lumped-parameter cranial compartments for arteries and veins, and one-dimensional distributed spinal CSF compartment. Martin et al. [183] coupled the cardiovascular and cerebrospinal fluid systems. Their representation of the cardiovascular system was composed by a one-dimensional network of viscoelastic arteries, linked to a varying elastance model of the left ventricle and terminated by three-element Windkessel models. The cerebrospinal fluid system was modelled by one tube-like structure which represents the spinal subarachnoid space; this kind of model is able to study the axial distribution of flow and pressure along the spinal canal. However, the rest of the cranial space is described by a transfer function that delivers spinal CSF flow from arterial flow curves.

The present work departs from a global closed-loop model of the entire human circulation coupled to a refined lumped-parameter description of the cerebrospinal fluid dynamics in the craniospinal cavity [292]. The main addition consists of replacing the lumped-parameter model for the spinal compartment with a one-dimensional coaxial model [59, 290, 259] which comprises an inner tube representing the spinal cord and the spinal subarachnoid space encased in the dura mater. Moreover, cranial and spinal non-linear behaviour of the pressure-volume relationship are introduced to better represent the deviation from the normal craniospinal CSF dynamic in pathological conditions. The model will be validated in healthy condition through comparison with published MRI data and computational results will be compared to the previous version of the model [292]. We will focus on the ICP waveform through a sensitivity analysis of the main parameters of the craniospinal CSF model. To stress the importance of the nonlinear pressure-volume relation, cranial infusion of CSF will be tested and the pressure-volume index (PVI) will be evaluated, as well as the outflow resistance to CSF reabsorption. Finally, as an example of the applicability of the model in studying the interaction between blood and CSF dynamics, we will assess the effects of transverse sinus stenoses on ICP.

4.2 Methods

4.2.1 A brief overview of the global mathematical model of the circulation

The entire human circulation is represented by means of a closed-loop model is fully described in [292]. See also [201, 202] for previous version of the model. It is a geometric multiscale type model which includes one-dimensional models for blood flow in major vessels and zero-dimensional lumped-parameters models describing blood flow in the remaining compartments. Figure 4.1 illustrates schematically the structure of the model: it includes 323 vessels, comprising arteries and veins; four heart chambers and cardiac valves; 3 compartments for the pulmonary circulation; 31 compartmental models describing connections between terminal arteries and veins through the microcirculation; 17 venous valves; 21 Starling resistors.

Blood flow in major vessels was modelled using a 1D system of partial differential equations. The resulting system of equations is given by

$$\begin{cases} \partial_t A + \partial_x q = 0 \,, \\ \partial_t q + \partial_x \left(\hat{\alpha} \frac{q^2}{A} \right) + \frac{A}{\rho} \partial_x p = -f \,. \end{cases} \tag{4.1}$$

The three unknowns of the problem are the cross-sectional area of the vessel's lumen, $A(x,t)$; the blood flow rate through a section of the vessel, $q(x,t)$; and the cross-sectionally averaged internal pressure, $p(x,t)$. $\hat{\alpha}$ is the Coriolis coefficient linked to the velocity profile, here taken equal to 1, ρ is the blood density, and $f = 8\pi\mu/\rho q/A$ is the friction force per unit length of the tube. To close the system, we adopted a pressure-area relation which describes the viscoelastic nature of vessels wall

$$p(x,t) = p_{ext}(x,t) + \underbrace{K(x)\left(\left(\frac{A(x,t)}{A_0(x)}\right)^m - \left(\frac{A(x,t)}{A_0(x)}\right)^n\right) + P_0}_{\textit{Elastic term}} + \underbrace{\frac{\Gamma}{A_0\sqrt{A}}\partial_t A}_{\textit{Viscoelastic term}} \,. \tag{4.2}$$

In this tube law, the internal pressure $p(x,t)$ is expressed as a function of the cross-sectional area $A(x,t)$ and other parameters, $A_0(x)$, $p_{ext}(x,t)$, m, n, $K(x)$, P_0, Γ, that account for mechanical and geometrical properties of the vessel. For a discussion on the choice of these parameters, we refer to [292].

Other districts of the blood circulation are modelled by lumped-parameter models. The connection between arteries and veins through arterioles, capillaries, and venules is represented by generic vascular bed models based on the three-element Windkessel model. The heart model considers time-varying elastance model [160, 276] to describe the dynamics of relaxation/contraction of the four cardiac chambers, while

FIGURE 4.1: Schematic representation of the global model used in this work [292]. 1D models refer to networks of major arteries and veins and to the spine, which are modelled using evolutionary partial differential equations, providing space- and time-resolved pressure and flow. Rectangles represent lumped-parameter models, which are used to describe the heart chambers, the pulmonary circulation, the microcirculation, as well as brain and cranial CSF dynamics. Such compartments are modelled using ordinary differential equations, which provide time-resolved haemodynamic variables.

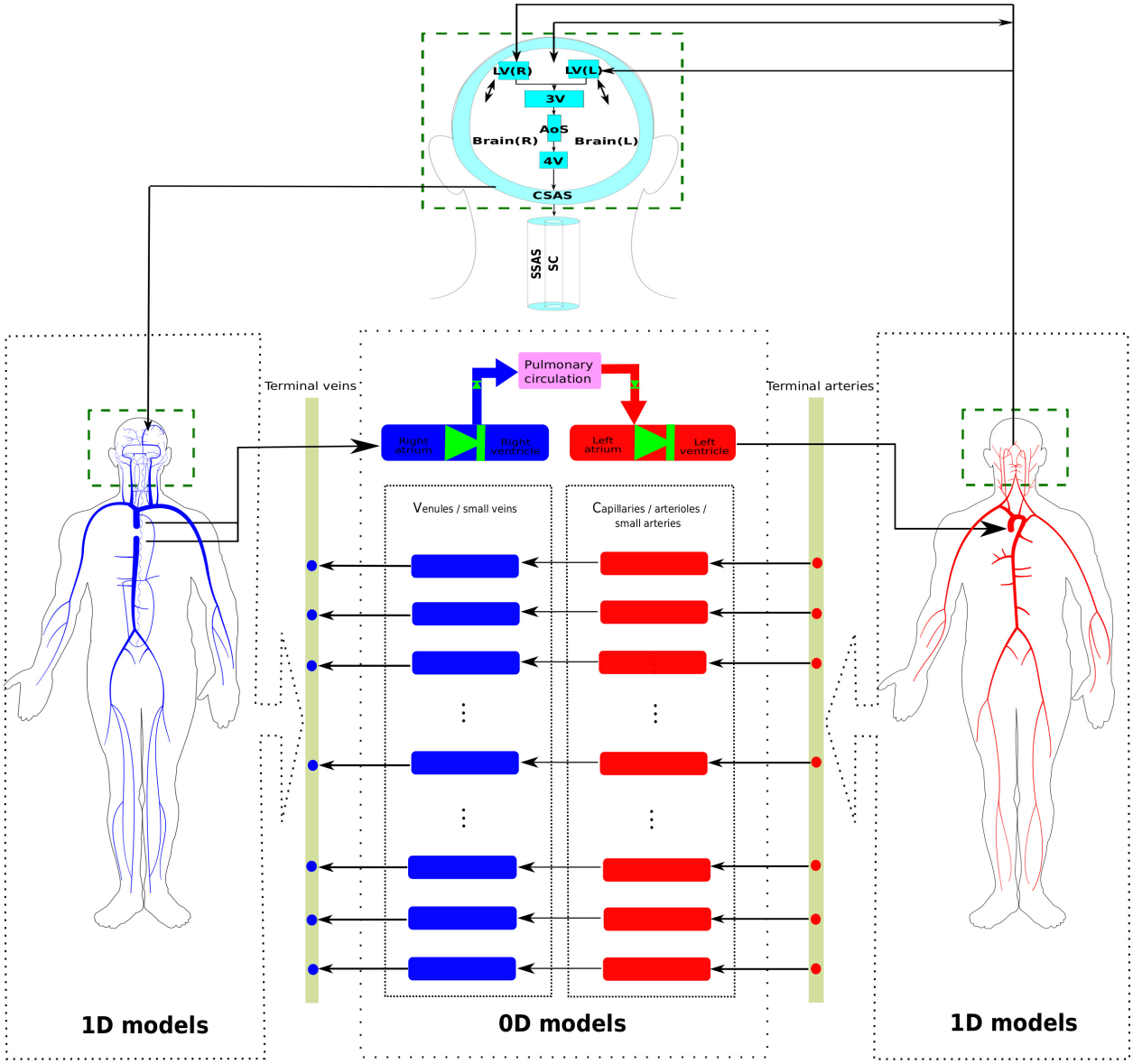

cardiac valves were modelled as in [216]. The pulmonary circulation is divided into arteries, capillaries, and veins, and is modelled as in [276]. Venous circulation was equipped by venous valves which governs the flow across the interface between two vessels and Starling resistors were placed at the confluence of cortical veins in the dural sinuses; both venous valves and Starling resistors were represented by the model presented in [216]. Finally, a mathematical model for cerebral autoregulation, which works on the terminal

portion of the cerebral arteries and on the cerebral vascular beds, was included; this model is based on [305] and [234].

We refer the reader to the works in [201, 202, 292] for more details about the model description, the numerical methods, parameter selection and validation.

4.2.2 Governing equations for the craniospinal CSF model

In [292], the blood circulation was coupled to a fully zero-dimensional (0D) model of the CSF and brain dynamics (based on [162]) which includes nine compartments. In this work, we consider lumped-parameters compartments for the cranial CSF and brain dynamics as in [292, 162], while a distributed one-dimensional model [59, 290] (1D) is used to describe motion of the spinal cord and CSF flow in the spinal subarachnoid space. Appropriate matching conditions are adopted to couple the zero-dimensional models of the cranial CSF and the spinal 1D model.

FIGURE 4.2: Schematic representation of the cerebrospinal fluid (CSF) cranial compartments and spinal model. With respect to previous work [292], here the spinal column is represented by means of a coaxial tube which includes the spinal cord and the spinal subarachnoid space. RV: right lateral ventricle; LV: left lateral ventricle; 3V: third ventricle; 4V: fourth ventricle; AoS: aqueduct of Sylvius; CSAS: cranial subarachnoid space; SSAS: spinal subarachnoid space; SC:spinal cord; SSS: superior sagittal sinus Brain: fluid part of brain parenchyma; Al: cerebral arterioles; Cp: cerebral capillaries. Solid double arrows denote fluid exchange between different compartments driven by pressure differences, while dashed arrows describe constant CSF production. The combination of a single dashed arrow and a solid double arrow between the brain parenchyma and the capillaries indicates that there are both fluid exchange driven by pressure differences and constant CSF production. Single solid arrow denotes CSF reabsorption into the venous system (SSS).

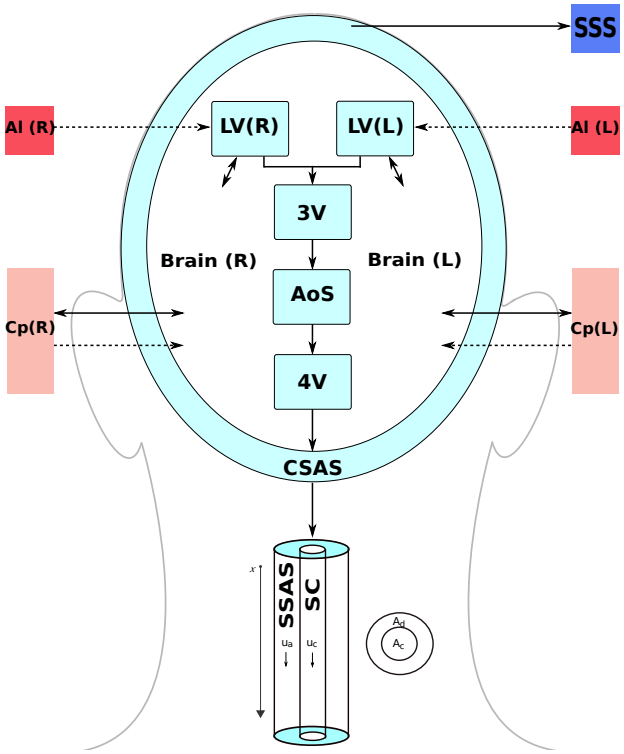

Governing equation for the cranial CSF and brain dynamics

CSF and brain dynamics are represented by means of lumped-parameter models. The resulting system of ordinary differential equations and algebraic equations is composed by 33 equations which comprise continuity equations, momentum equations and distensibility equations for the lateral (LV, RV), third (3V) and fourth (4V) ventricles, aqueduct of Sylvius (AoS), cranial subarachnoid space (CSAS). Left and right brain parenchyma (br,R and br,L) hemispheres are described as a simplified bi-phasic material, with a constant solid cell matrix and an extracellular fluid part which are represented by continuity equations and momentum equations. Moreover, a nonlinear distensibility equation for each brain hemisphere is added to describe the link between the intracranial pressure, that in this work is considered as the pressure in the extracellular fluid part of the brain parenchyma, and the volume inside the skull. This is different with respect to the original model proposed in [162] wherein the linear distensibility equation was represented by the Monro-Kellie doctrine which states that the volume inside the skull is constant. Such nonlinear equation was previously used in [166] and in [64] to represent the dynamic of the intracranial pressure as function of the intracranial volume. Other equations of the system are algebraic equations that connect different CSF cranial compartments. Finally, there is an additional momentum equation which relates the pressure drop between the cranial and spinal subarachnoid space to the volumetric flow rate at the cranial junction of the spinal subarachnoid space. Some equations are summarized here, but we refer the reader to [292] for a complete description of the model equations.

The continuity equation for cranial CSF compartments reads

$$l_j \frac{dA_j}{dt} = q_j^{in} - q_j^{out} \ , \qquad j \in \{\text{LV, RV, 3V, AoS, 4V, CSAS}\} \ , \tag{4.3}$$

where l_j, A_j, q_j^{in}, q_j^{out} are the length, the cross-sectional area, the inflow and outflow of a compartment. The continuity equations for the right and left fluid part of the brain parenchyma consider both the volumetric flow rate in and out of the compartment that occurs in two ways: pressure-driven (q_{br}^{in}, q_{br}^{out}) and constant-rate transfer ($q_{Cp\to br,const}$, from the brain capillaries into the extracellular space of the parenchyma, and $q_{br\to LV,const}$, from the parenchyma into the ventricles):

$$l_{br,R} \frac{dA_{br,R}}{dt} = q_{br,R}^{in} + q_{Cp\to br,const} - q_{br,R}^{out} - q_{br\to RV,const} \ , \tag{4.4}$$

$$l_{br,L} \frac{dA_{br,L}}{dt} = q_{br,L}^{in} + q_{Cp\to br,const} - q_{br,L}^{out} - q_{br\to LV,const} \ . \tag{4.5}$$

The momentum equations are effectively Darcy's law of flow and relate the pressure difference between two compartments to the volumetric flow q exchanged between them and a resistance to flow R:

$$q_j^{in} = \frac{p_{up} - p_{down}}{R_j} \ , \qquad j \in \{\text{LV, RV, 3V, AoS, 4V, CSAS, br,R , br,L}\} \ . \tag{4.6}$$

For the brain parenchyma compartments, there are two momentum equations, one refers to cerebrospinal fluid exchange between the lateral ventricles and the extracellular fluid matrix of the brain, while the other one relates to the secretion of CSF from cerebral capillaries. Another momentum equation which regulates the CSF exchange (q_{SSAS}^{in}) between the cranial and the spinal (SSAS) subarachnoid spaces according to a resistance (R_{SSAS}) is added to link the 0D cranial models to the 1D spinal model:

$$q_{SSAS}^{in} = \frac{p_{CSAS} - p_{SSAS,1D}}{R_{SSAS}} \ . \tag{4.7}$$

The distensibility equations play the role of the tube law relating the internal pressure with the cross-sectional area of the compartment:

$$p_j = p_{ext} + E_j \left(\frac{A_j}{A_j^0} - 1 \right) \ , \qquad j = \text{LV, RV, 3V, AoS, 4V, CSAS} \ . \tag{4.8}$$

For each compartment inside the cranial cavity, the external pressure is that of the brain parenchyma, E_j and A_j^0 are the elastance and the reference area of the compartment, respectively. Two additional pressure-volume relationships are introduced to describe the relation between ICP, that is the pressure of the brain parenchyma, and the intracranial volume:

$$p_{br,R} = p_{br,0} e^{\frac{V_R - V_{R,0}}{\Phi}} , \tag{4.9}$$

$$p_{br,L} = p_{br,0} e^{\frac{V_L - V_{L,0}}{\Phi}} , \tag{4.10}$$

where $p_{br,0}$ is the pressure at the reference volume $V = V_0$ and ϕ is a parameter related to the intracranial compliance. V_R and V_L are the intracranial volumes in the right and left hemisphere, respectively. Specifically,

$$V_R = V_{Blood,R} + V_{RV} + \frac{1}{2}V_{3V} + \frac{1}{2}V_{AoS} + \frac{1}{2}V_{4V} + \frac{1}{2}V_{CSAS} + V_{br,R} + V_{Solid\ Parenchyma} , \tag{4.11}$$

$$V_L = V_{Blood,L} + V_{LV} + \frac{1}{2}V_{3V} + \frac{1}{2}V_{AoS} + \frac{1}{2}V_{4V} + \frac{1}{2}V_{CSAS} + V_{br,L} + V_{Solid\ Parenchyma} . \tag{4.12}$$

Equations (4.9) and (4.10) represent a relaxed version of the Monro-Kellie doctrine. In fact, here we assume that the sum of all intracranial fluid compartments is almost constant and it is linked nonlinearly to the ICP. The parameter Φ is chosen such that the intracranial volume variation during a cardiac cycle is less than 0.1 % of the intracranial volume.

Additional algebraic equations are added to describe the cerebrospinal fluid flow in cranial cavity. The CSF that enters the lateral ventricle is equal to the CSF flowing from the brain parenchyma plus the constant production rate from arterioles. Then, CSF flows from lateral ventricles to the third ventricle, from the third ventricle through the aqueduct of Sylvius to the fourth ventricle, and finally from the fourth ventricle to the cranial subarachnoid space. From the cerebral subarachnoid space CSAS, CSF is displaced into the spinal subarachnoid space (Eq. (4.7)) and reabsorbed into the superior sagittal sinus (SSS) through the arachnoid granulations. Reabsorption is represented by a mass transfer flux, which is a function of the pressure difference between the CSAS and SSS and a reabsorption constant coefficient k

$$q_{CSAS}^{out} = q_{SSAS}^{in} + \max\left(0, k(p_{CSAS} - p_{sinus})\right) . \tag{4.13}$$

Governing equation for the one-dimensional model of the spine

The spinal column is represented by the one-dimensional coaxial flexible pipe mathematical model, firstly presented by Cirovic and collaborators [59] and then used in [290, 259]. The coaxial tube includes a solid elastic inner tube, which represents the spinal cord encased by a relatively stiff pia mater, and an outer tube, which plays the role of the dura mater. The spinal subarachnoid space between the pia mater and the arachnoid is filled with CSF. The system of governing equations of the one-dimensional coaxial model reads as follows

$$\begin{cases} \partial_t A_c + \partial_x(A_c u_c) = 0 \\ \partial_t(A_c u_c) + (c_c^2 + u_c^2)\partial_x A_c + 2u_c A_c \partial_x u_c + \frac{A_c}{A_d} c_d^2 \partial_x A_d = -f_1 \\ \partial_t(A_d - A_c) + \partial_x((A_d - A_c)u_a) = 0 \\ \partial_t((A_d - A_c)u_a) + \frac{A_d - A_c}{A_d} c_d^2 \partial_x A_d + u_a^2 \partial_x(A_d - A_c) + 2u_a(A_d - A_c)\partial_x u_a = -f_2 , \end{cases} \tag{4.14}$$

where

$$f_1 = 8\pi\mu_c \frac{u_c}{\rho} , \tag{4.15}$$

$$f_2 = 8\pi\mu_d \frac{u_a}{\rho} \frac{A_d - A_c}{A_d + A_c - \frac{A_d - A_c}{\log\left(\sqrt{\frac{A_d}{A_c}}\right)}} . \tag{4.16}$$

The unknowns of the system are A_d and A_c, cross-sectional areas of the dura mater and of the spinal cord, u_a and u_c, axial velocities of the cerebrospinal fluid flowing in the spinal subarachnoid space and of the spinal cord, and p_d and p_c, the pressure in the spinal subarachnoid space and the normal compressive stress in the cord. The first and third equations of the partial differential equations system represent conservation of mass for the spinal cord and for the spinal subarachnoid space, while the other equations describe the balance of momentum, wherein the right hand sides are dissipation terms, modelled by a Poiseuille laminar flow. In particular, the dissipation term for the last equation is modelled as the pressure drop per unit length for laminar flow in a concentric annulus [130, 318]. To close the system, the following tube laws, that relate the cross-sectional area to the pressures, are applied

$$p_c = E_{lc}\left(\frac{A_c}{A_{0c}} - 1\right) + p_d , \tag{4.17}$$

$$p_{d,\mathrm{L}} = \hat{E}_{ld}\left(\frac{A_d}{\hat{A}_{0d}} - 1\right) \tag{4.18}$$

$$p_{d,\mathrm{NL}} = p_{0d} \mathrm{e}^{E_{ld}(A_d - A_{0d})} . \tag{4.19}$$

Equation (4.17) describes the linear pressure-area relationship of the spinal cord; E_{lc} and A_{0c} are the elastance and the reference cross-sectional area, respectively, while the pressure of the CSF in the SSAS p_d is taken as external pressure. Equations (4.18) and (4.19) represent a linear ($p_{d,\mathrm{L}}$) and a nonlinear ($p_{d,\mathrm{NL}}$) pressure-area relationship for the CSF in the SSAS. As for the spinal cord, the linear tube law relates the pressure p_d to the cross-sectional area of the dura A_d and $\hat{E}_{ld}$, $\hat{A}_{0d}$, the elastance and the reference cross-sectional area, respectively. Equation (4.19) describes a exponential-like behaviour that characterizes the CSF pressure with respect to the CSF volume [17, 181]. (A_{0d}, p_{0d}) represents the reference set point of the curve, obtained from a baseline simulation with linear tube law. E_{ld} is the elastance coefficient and it is defined such that the elastance at the reference point of the pressure-area curve is equal to the elastance of the linear relationship: $\frac{\partial p_{d,\mathrm{L}}}{\partial A_d}\Big|_{A_{0d}} = \frac{\partial p_{d,\mathrm{NL}}}{\partial A_d}\Big|_{A_{0d}}$, hence $E_{ld} = \frac{\hat{E}_{ld}}{\hat{A}_{0d} p_{0d}}$. Wave speeds of spinal cord and cerebrospinal fluid in the spinal subarachnoid space are defined as c_c and c_d; they link pressure p, area A and density ρ as follows

$$c = \sqrt{\frac{A}{\rho}\frac{\partial p}{\partial A}} . \tag{4.20}$$

The system (4.14) can be written in vector form as

$$\partial_t \mathbf{Q} + \mathbf{A}(\mathbf{Q})\partial_x \mathbf{Q} = \mathbf{S}(\mathbf{Q}) , \tag{4.21}$$

$$\mathbf{Q} = \begin{bmatrix} A_c \\ A_d - A_c \\ A_c u_c \\ (A_d - A_c) u_a \end{bmatrix} , \tag{4.22}$$

$$\mathbf{A}(\mathbf{Q}) = \begin{bmatrix} 0 & 1 & 0 & 0 \\ c_c^2 + A_c c_d^2/A_d - u_c^2 & 2u_c & A_c c_d^2/A_d & 0 \\ 0 & 0 & 0 & 1 \\ (A_d - A_c)c_d^2/A_d & 0 & (A_d - A_c)c_d^2/A_d - u_a^2 & 2u_a \end{bmatrix} , \tag{4.23}$$

$$\mathbf{S}(\mathbf{Q}) = \begin{bmatrix} 0 \\ -8\pi\mu_c \frac{u_c}{\rho} \\ 0 \\ -8\pi\mu_{csf} \frac{u_a}{\rho} \frac{A_d - A_c}{A_d + A_c - \frac{A_d - A_c}{\log\left(\sqrt{\frac{A_d}{A_c}}\right)}} \end{bmatrix} . \tag{4.24}$$

Vector $\mathbf{Q}$ includes the unknowns of the problem, $\mathbf{A}(\mathbf{Q})$ is the coefficient matrix and $\mathbf{S}(\mathbf{Q})$ is the vector of source terms. As pointed out in [259], it can be proved that system (4.14) can be either strictly hyperbolic or mixed elliptic-hyperbolic system. The sign of the discriminant of the characteristic polynomial of system (4.14) depends on the two cross-sectional areas A_c and A_d, the velocity difference $|u_c - u_a|$ and the physical parameters A_{0c}, A_{0d}, ρ, E_c, E_d. As we move in the parameters' space, the character of the system changes; however, for parameter values within the physiological range, system (4.14) is always hyperbolic [290]. Great care is required in choosing the numerical method, which should deal with the non-conservative character of the advective part and with source term. The numerical strategy followed here is a finite volume method based on the ADER approach [193] in combination with FORCE [287] for non-conservative systems. The resulting scheme is nonlinear and second-order accurate in space and time. The one-dimensional domain is divided into N computational cells $T_i = \left[x_{i-\frac{1}{2}}, x_{i+\frac{1}{2}}\right]$ for $i = 1, \dots, N$. The finite-volume type formulation of the problem obtained integrating the system of governing equations (4.14) in space and time in the control volume $\left[x_{i-\frac{1}{2}}, x_{i+\frac{1}{2}}\right] \times \left[t^n, t^{n+1}\right]$ is

$$\mathbf{Q}_i^{n+1} = \mathbf{Q}_i^n - \frac{\Delta t}{\Delta x}\left(\mathbf{D}^-_{i+\frac{1}{2}} + \mathbf{D}^+_{i-\frac{1}{2}}\right) + \Delta t \mathbf{S}_i - \Delta t \mathbf{G}_i^n , \tag{4.25}$$

where

$$\mathbf{Q}_i^n = \frac{1}{\Delta x} \int_{x_{i-\frac{1}{2}}}^{x_{i+\frac{1}{2}}} \mathbf{Q}(x, t^n)\, dx , \tag{4.26}$$

$$\mathbf{G}_i^n = \frac{1}{\Delta t \Delta x} \int_{t_n}^{t_{n+1}} \int_{x_{i-\frac{1}{2}}}^{x_{i+\frac{1}{2}}} \mathbf{A}(\mathbf{Q}) \partial_x \mathbf{Q}\, dx\, dt , \tag{4.27}$$

$$\mathbf{S}_i = \frac{1}{\Delta t \Delta x} \int_{t_n}^{t_{n+1}} \int_{x_{i-\frac{1}{2}}}^{x_{i+\frac{1}{2}}} \mathbf{S}(\mathbf{Q}(x,t))\, dx\, dt , \tag{4.28}$$

$$\mathbf{D}^{\pm}_{i+\frac{1}{2}} = \frac{1}{\Delta t} \int_{t_n}^{t_{n+1}} \boldsymbol{D}^{\pm}_{i+\frac{1}{2}}\left(\mathbf{Q}^L_{i+\frac{1}{2}}(t), \mathbf{Q}^R_{i+\frac{1}{2}}(t), \Psi(s)\right) dt , \tag{4.29}$$

with $\Delta x = x_{i+\frac{1}{2}} - x_{i-\frac{1}{2}}$, $\Delta t = t^{n+1} - t^n$. Moreover, $\mathbf{Q}^{L/R}_{i+\frac{1}{2}}$ are limiting data states from left and right at the cell interface $x_{i+\frac{1}{2}}$. Given $\mathbf{Q}^L_{i+\frac{1}{2}}$ and $\mathbf{Q}^R_{i+\frac{1}{2}}$, $D^{\pm}_{i+\frac{1}{2}}\left(\mathbf{Q}^-_{i+\frac{1}{2}}(t), \mathbf{Q}^+_{i+\frac{1}{2}}(t), \Psi(s)\right)$ are fluctuations that depend on the integration path $\Psi(\mathbf{Q}^L_{i+\frac{1}{2}}(t), \mathbf{Q}^R_{i+\frac{1}{2}}(t), s)$.

The first step of the ADER approach [193] consists in a nonlinear spatial reconstruction. For a second order scheme, a first order reconstruction polynomial for each computing cell i reads as follows

$$\mathbf{P}_i(x, t^n) = \mathbf{Q}_i^n + (x - x_i)\Delta_i , \tag{4.30}$$

where Δ_i is a slope vector chosen with ENO criteria [116].

Then, at each cell interface, the following local generalized Riemann problem is defined

$$\begin{cases} \partial_t \mathbf{Q} + \mathbf{A}(\mathbf{Q})\partial_x \mathbf{Q} = \mathbf{S}(\mathbf{Q}) , \\ \mathbf{Q}(x,0) = \begin{cases} \mathbf{P}_i(x) & \text{if } x < 0 , \\ \mathbf{P}_i(x) & \text{otherwise} . \end{cases} \end{cases} \tag{4.31}$$

The Harten, Engquist, Osher and Chakravarthy (HEOC) method [115] is followed to find the solution of the generalized Riemann problem. From the reconstruction polynomial, two boundary extrapolated values arise

$$\begin{cases} \mathbf{Q}^{-}_{i+\frac{1}{2}} = \mathbf{Q}^{n}_{i} + \frac{1}{2}\Delta x \Delta_i \,, \\ \mathbf{Q}^{+}_{i+\frac{1}{2}} = \mathbf{Q}^{n}_{i+1} - \frac{1}{2}\Delta x \Delta_{i+1} \,; \end{cases} \tag{4.32}$$

these boundary values are then evolved in time ($\frac{1}{2}\Delta t$) via a truncated Taylor expansion and by means of the Cauchy-Kowaleskaya procedure, the time derivative is re-written in term of spatial derivative.The final form of the evolved boundary extrapolated values up to time $\frac{1}{2}\Delta t$ is

$$\begin{cases} \mathbf{Q}^{L}_{i+\frac{1}{2}} = \mathbf{Q}^{-}_{i+\frac{1}{2}} + \frac{\Delta t}{2}\left[-\mathbf{A}\left(\mathbf{Q}^{-}_{i+\frac{1}{2}}\right)\Delta_i + \mathbf{S}\left(\mathbf{Q}^{-}_{i+\frac{1}{2}}\right)\right] \,, \\ \mathbf{Q}^{R}_{i+\frac{1}{2}} = \mathbf{Q}^{+}_{i+\frac{1}{2}} + \frac{\Delta t}{2}\left[-\mathbf{A}\left(\mathbf{Q}^{+}_{i+\frac{1}{2}}\right)\Delta_{i+1} + \mathbf{S}\left(\mathbf{Q}^{+}_{i+\frac{1}{2}}\right)\right] \,. \end{cases} \tag{4.33}$$

Fluctuations $\mathbf{D}^{\pm}_{i+\frac{1}{2}}$ in (4.29) arise from the solution of the following classical Riemann problem at computational cell interfaces $x_{i+\frac{1}{2}}$

$$\begin{cases} \partial_t \mathbf{Q} + \mathbf{A}(\mathbf{Q})\partial_x \mathbf{Q} = \mathbf{0} \,, \\ \mathbf{Q}(x,0) = \begin{cases} \mathbf{Q}^{L}_{i+\frac{1}{2}} & \text{if } x < 0 \,, \\ \mathbf{Q}^{R}_{i+\frac{1}{2}} & \text{otherwise} \,. \end{cases} \end{cases} \tag{4.34}$$

Here, we adopted the FORCE scheme [287] for non-conservative systems; therefore, the fluctuations read

$$\mathbf{D}^{\pm}_{i+\frac{1}{2}} = \mathbf{A}^{\pm}_{i+\frac{1}{2}}\left(\mathbf{Q}^{R}_{i+\frac{1}{2}} - \mathbf{Q}^{L}_{i+\frac{1}{2}}\right) \,, \tag{4.35}$$

where the matrices are

$$\mathbf{A}^{\pm}_{i+\frac{1}{2}} = \frac{1}{2}\hat{\mathbf{A}}_{i+\frac{1}{2}} \pm \frac{1}{4}\frac{\Delta t}{\Delta x}\left[\hat{\mathbf{A}}^{2}_{i+\frac{1}{2}} + \left(\frac{\Delta x}{\Delta t}\right)^{2}\mathbf{I}\right] \,. \tag{4.36}$$

Here, $\mathbf{I}$ is the identity matrix and $\hat{\mathbf{A}}_{i+\frac{1}{2}}$ is a path integral of the coefficient matrix $\mathbf{A}$, which is approximated numerically as

$$\hat{\mathbf{A}}_{i+\frac{1}{2}} = \int_0^1 \mathbf{A}\left(\Psi(s; \mathbf{Q}^{L}_{i+\frac{1}{2}}, \mathbf{Q}^{R}_{i+\frac{1}{2}})\right) \, ds \approx \sum_{j=1}^{M} \omega_j \mathbf{A}\left(\Psi(s_j; \mathbf{Q}^{L}_{i+\frac{1}{2}}, \mathbf{Q}^{R}_{i+\frac{1}{2}})\right) \,, \tag{4.37}$$

where ω_j and s_j are weights and integration points of a Gauss quadrature rule. In particular, we use a Gauss-Legendre quadrature rule with three integration points.

The high order term $\mathbf{G}^{n}_{i}$ is evaluated by means of a second-order approximation of integral in (4.27) (mid-point integration rule in space and time); it reads

$$\mathbf{G}^{n}_{i} \approx \mathbf{A}\left(\mathbf{Q}^{M}_{i}\right)\frac{\mathbf{Q}^{L}_{i+\frac{1}{2}} - \mathbf{Q}^{R}_{i-\frac{1}{2}}}{\Delta x} \,, \tag{4.38}$$

where $\mathbf{Q}^{M}_{i}$ is defined as

$$\mathbf{Q}^{M}_{i} = \mathbf{Q}^{n}_{i} + \frac{\Delta t}{2}\left[-\mathbf{A}\left(\mathbf{Q}^{n}_{i}\right)\Delta_i + \mathbf{S}\left(\mathbf{Q}^{n}_{i}\right)\right] \,. \tag{4.39}$$

Concerning the source term, the mid-point integration rule in space and time is applied; it becomes

$$\mathbf{S}_i = \mathbf{S}(\mathbf{Q}^{M}_{i}) \,. \tag{4.40}$$

Appropriate boundary conditions are necessary for the determination of the numerical solution in the spinal coaxial tube. At the sacral end, we impose a reflexive boundary condition, that is zero velocity of the cord and CSF. At the cranial junction, the 1D spinal model is connected to the cranial subarachnoid space of the 0D model imposing continuity of CSF flow. In the next subsection, the strategy for the coupling is described in detail.

4.2.3 Coupling between blood circulation, cranial CSF model, spinal CSF model

Figure 4.3 shows schematically the coupling between the blood circulation model, the cranial CSF 0D model and spinal 1D CSF model. The three systems are solved in a sequential manner and the coupling is explicit. Since we are using a local time stepping (LTS) technique in a vessel-wise fashion [207], each 1D vessel is allowed to evolve in time according to a local time step given by its local stability criterion. All vessels have a common synchronization time defined by the prescribed maximum time step allowed by the LTS procedure. Such global synchronization time is referred as t^n and it is defined as $t^n = t^0 + n\Delta t_{max}$, with t^0 the initial time, Δt_{max} the maximum time in the LTS procedure and n is a counter for the global synchronization times. Therefore, the coupling between blood flow and the craniospinal systems is performed at every synchronization time. At the beginning of each time step, the vectors $\mathbf{S}^n$, $\mathbf{B}^n$ and $\mathbf{U}^n$ are known. The vector $\mathbf{S}^n$ represents the unknowns for the blood circulation system that includes area, flow and pressure in 1D vessels, as well as other 0D blood compartments. The vector $\mathbf{B}^n$ represents the unknowns for the cranial CSF and brain dynamics models. The vector $\mathbf{U}^n$ consists of the vector of unknowns for the spinal system of partial differential equations. In the first step, the equations for the blood circulation models are solved. First, the system of ordinary differential equations for the cerebral autoregulation model are solved by the explicit Euler scheme, then we solve the system of partial differential equations for blood flow in 1D vessels and the 0D blood compartments for the heart and pulmonary circulation, microvasculature, Starling resistors and venous valves. The 0D blood compartments are solved by an explicit Euler scheme and coupled to the 1D vessels. The external pressure for the intracranial 1D vessels and vascular beds, as well as for the Starling resistor models, is given by the mean pressure between the left and right sides of the brain parenchyma at time t^n. Once the blood circulation equations have been solved, the cerebral capillary pressures ($p_{Cp,R}$ and $p_{Cp,L}$), the superior sagittal sinus pressure (p_{sinus}) and the intracranial blood volume ($V_{blood,R}$, $V_{blood,L}$) are provided to the cranial CSF model. This determines the CSF production, reabsorption rates and the blood volume inside the skull for the intracranial pressure-volume relation. Then, the spinal 1D system of partial differential equations is solved using the numerical method described in Section 4.2.2.

FIGURE 4.3: Schematic representation of the coupling between blood circulation, cranial CSF and brain dynamics models and spinal CSF dynamic. $\mathbf{S}^n$, $\mathbf{B}^n$, $\mathbf{U}^n$ are the vectors of unknowns in the blood circulation models (1D vessels and other 0D blood compartments), in the CSF and brain dynamics model and in the spinal 1D model ($\mathbf{U}^n = [A_c^n, A_c^n u_c^n, A_d^n - A_c^n, (A_d^n - A_c^n)u_a^n]$) at time t^n, where n is a counter for the global synchronization time of the local time stepping procedure.

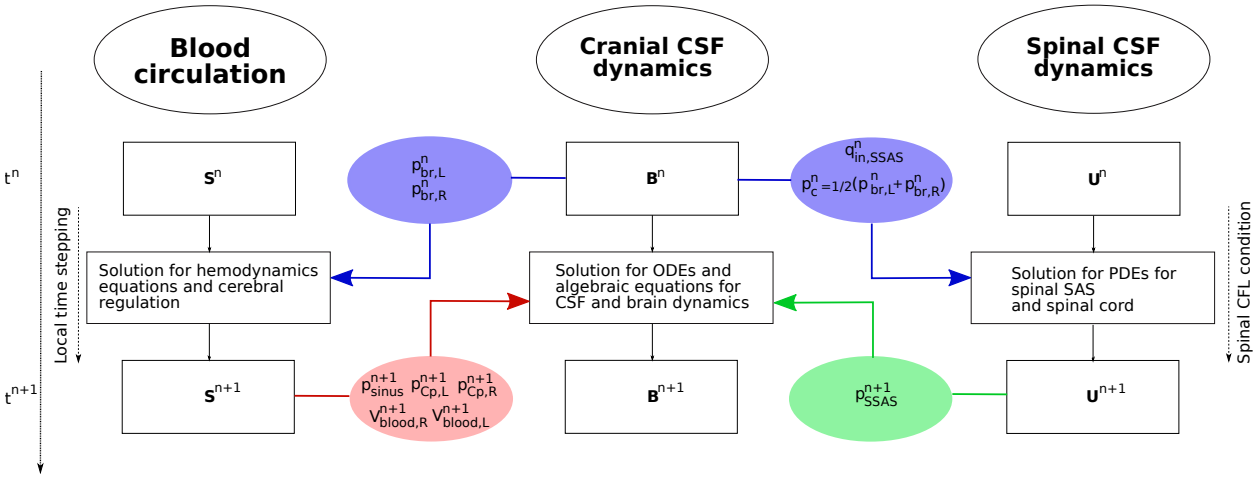

As previously stated, at the inlet of the coaxial tube, boundary conditions are implemented. We prescribe flow at the inlet of the spinal subarachnoid space, obtained from Eq. (4.7) and the mean pressure

between the left and right sides of the brain parenchyma ($p_{br,R}$ and $p_{br,L}$) as the pressure in the cord at time t^n. Two additional conditions are required to resolve all of the unknowns. These are obtained using the method of characteristics, as described in [59, 139, 290]. The original governing system of equations can be linearised by assuming that each of the variables consists of a stationary state component (zero in case of velocities) and a small disturbance; we define $A_c = a_c + A_{0c}$, $A_d = a_d + A_{0d}$, $u_c = v_c + 0$, $u_a = v_a + 0$, where a_c, a_d, v_c, v_a are small perturbations. The four distinct real eigenvalues of the linearised hyperbolic system are

$$\lambda_{1,4}^2 = c_2^2 = \frac{1}{2}(C_d^2 + C_c^2) + \sqrt{\frac{1}{4}(C_d^2 + C_c^2)^2 - \frac{A_{0d} - A_{0c}}{A_{0d}} C_d^2 C_c^2}\,, \tag{4.41}$$

$$\lambda_{2,3}^2 = c_1^2 = \frac{1}{2}(C_d^2 + C_c^2) - \sqrt{\frac{1}{4}(C_d^2 + C_c^2)^2 - \frac{A_{0d} - A_{0c}}{A_{0d}} C_d^2 C_c^2}\,, \tag{4.42}$$

with $\lambda_1 < \lambda_2 < \lambda_3 < \lambda_4$ and $C_{c,d} = c(A_{d,c} = A_{0,d,c})$. Moreover, four characteristic variables (each one associated to one eigenvalue) can be written

$$W_{1,4} = \mp \frac{c_2(c_1^2 - C_c^2)}{A_{0c}(c_1^2 - c_2^2)} a_c + \frac{c_2^2(c_1^2 - C_c^2)}{C_c^2(c_1^2 - c_2^2)} v_c \pm \frac{c_2 C_d^2}{A_{0d}(c_1^2 - c_2^2)} a_d - \frac{c_1^2 c_2^2}{C_c^2(c_1^2 - c_2^2)} v_a\,, \tag{4.43}$$

$$W_{2,3} = \pm \frac{c_1(c_2^2 - C_c^2)}{A_{0c}(c_1^2 - c_2^2)} a_c - \frac{c_1^2(c_2^2 - C_c^2)}{C_c^2(c_1^2 - c_2^2)} v_c \mp \frac{c_1 C_d^2}{A_{0d}(c_1^2 - c_2^2)} a_d - \frac{c_1^2 c_2^2}{C_c^2(c_1^2 - c_2^2)} v_a\,. \tag{4.44}$$

For the linearized system, we have that characteristic variables W_i, $i = 1, \dots, 4$, remain constant on the paths defined by $dx/dt = \lambda_i$, and hence it holds $W_i(x,t) = W_i^{(0)}(x - \lambda_i t)$, where $^{(0)}$ indicates the state of the system of decoupled equations for the characteristic variables at each time step t^n. We use this information to prescribe the missing conditions at the cranial junction of the model. Hence, the boundary conditions at $x = 0$ can be summarized as follows

$$\begin{cases} p_c(0,t) = \frac{1}{2}(p_{br,L} + p_{br,R}) \\ (A_d(0,t) - A_c(0,t))u_a(0,t) = q_{SSAS}^{in} \\ W_1(0,t) = W_1^{(0)}(-\lambda_1 \Delta t) \\ W_2(0,t) = W_2^{(0)}(-\lambda_2 \Delta t)\,. \end{cases} \tag{4.45}$$

The first two equations of this system provide the boundary values of the variables p_c and $(A_d - A_c)u_a$. The pressure in the brain parenchyma refers to the extracellular fluid part of the brain parenchyma. In the other two equations, the missing information is obtained from the projection of the differential equations of the linearized system along the outgoing characteristics (extrapolation of the characteristic variable). At the boundary of the first computational cell $x = 0$ and time t, the characteristic is equal to the characteristic evaluated in $x - \lambda_i \Delta t$, $i = 1, 2$ at the previous time step t^n. The conserved properties required at positions $x - \lambda_i \Delta t$ are determined by second-order interpolation from the first two cells in the computational domain, using the local values of λ_1 and λ_2. Solving system (4.45) provides the values of the vector of unknowns $[A_c, u_c, A_d, u_a]$ at the interface $x = 0$ of the coaxial tube; A_d is then used in Eq. (4.19) for the evaluation of the pressure of the CSF in the spinal subarachnoid space at the interface between the 0D-1D models. This value is then used in the momentum equation (4.7). At this point, the system of differential and algebraic equations for the CSF and brain dynamics is solved by an implicit Euler scheme.

4.2.4 Assessment of normal and pathological conditions

Healthy subject: model setting

In order to test the validity of the present global closed-loop model coupled to the CSF and brain dynamics, we perform a baseline simulation that regards the physiology of a healthy young male subject. All

the parameters for the blood circulation models, 1D models for arteries and veins and lumped-parameters for the remaining districts, are the ones proposed in [292]. The same holds for the cranial CSF and brain dynamics. Parameters for the spinal 1D model are reported in Table 4.1. Numerically, the spinal 1D model is discretized with 100 computational cells to ensure mesh independence of the numerical solution. The simulation was run until a periodic solution was reached.

TABLE 4.1: Parameters for the spinal one-dimensional model.

Parameter	Value	Reference
E_{lc} [Pa]	125000	[290]
A_{0c} [m^2]	7.853×10^{-5}	[290]
μ_c [Pa s]	1.5	[290]
$\hat{E}_{ld}$ [Pa]	21331.2	[292]
$\hat{A}_{0d}$ [m^2]	2.27×10^{-4}	[290]
μ_d [Pa s]	0.0045	[290]
l_{SSAS} [m]	0.43	[292]

Sensitivity analysis of the CSF system

Due to the paucity of data in the literature, most baseline parameters for the CSF and brain dynamics were derived and estimated on the basis of normal physiological pressures and flows. In order to explore the sensitivity of ICP to changes in parameters of the CSF models, we perform a local sensitivity analysis. We compute sensitivities for some of the variables linked to the ICP with respect to a set of parameters of both the cranial and the spinal CSF models. For a selected parameter $\mathcal{P}$, we consider a deviation of 20% above ($\mathcal{P}^+$) and below ($\mathcal{P}^-$) the reference value $\hat{\mathcal{P}}$. Hence, the local sensitivity $S_{\mathcal{P}}^{\mathcal{V}}$ of a variable $\mathcal{V}$ to changes in parameter $\mathcal{P}$ can be approximated as

$$S_{\mathcal{P}}^{\mathcal{V}} \approx \frac{\hat{\mathcal{P}}}{\hat{\mathcal{V}}} \frac{\mathcal{V}(\mathcal{P}^+) - \mathcal{V}(\mathcal{P}^-)}{\mathcal{P}^+ - \mathcal{P}^-}, \tag{4.46}$$

wherein $\hat{\mathcal{V}}$ is the reference value for the variable (obtained in the baseline simulation).

Analysis of pressure-volume relationship and outflow resistance of the CSF system

The introduction of nonlinear pressure-volume relationship for the spinal CSF and the cranial CSF allows for a better quantification of the deviations in ICP due to volume variations. Clinically, the pressure-volume index (PVI) is used as a measure of craniospinal compliance or CSF volume buffering capacity. It was defined by Marmarou and collaborators [181] as the amount of volume that has to be added in the craniospinal cavity to raise the ICP by a factor of 10. Experimentally, PVI was determined in animals and humans by means of rapid bolus injection of CSF [181, 182, 262, 17, 283, 284, 185, 285, 313, 151, 277, 254, 141, 21, 309]. We computationally determine the PVI modelling a rapid CSF infusion at 1 ml/s of 2 to 7 ml in the cranial subarachnoid space. Mathematically, the PVI is then defined as

$$\mathrm{PVI} = \frac{\Delta V}{\log_{10}\left(\frac{ICP^p}{ICP}\right)}, \tag{4.47}$$

where ΔV is the amount of CSF injected in the craniospinal CSF system, ICP is the mean intracranial pressure over a cardiac cycle in the baseline condition before the bolus injection and ICP^p is the maximal mean pressure reached at the end of the infusion.

While the initial rise in pressure following bolus injection is used to calculate PVI, the rate of intracranial pressure return toward baseline following injection provides data for calculating outflow resistance to CSF absorption. Following Marmamou et al. [181, 182, 262], we evaluate the outflow resistance to CSF absorption as

$$R = \frac{t\, ICP}{\text{PVI}\, \log_{10}\left(\frac{ICP^t\,(ICP^p - ICP)}{ICP^p\,(ICP^t - ICP)}\right)}, \tag{4.48}$$

where t is the time (in minutes) after injection and ICP^t the corresponding mean intracranial pressure. Following [181, 182], we consider $t = 1,\ 2$ minutes.

Pathological condition: effects of transverse sinus stenoses on the blood and CSF systems

We show computations about the impact of transverse sinuses stenoses on cerebral venous flow and CSF dynamics and its relation to Idiopathic Intracranial Hypertension. Our stenotic case study is reproduced by introducing stenosis models based on [323, 275] into the right and left transverse sinuses. The flow variation in time across the stenosis is modelled by means of a first-order ordinary differential equation. We suppose that the strictures cause a reduction of 70 % the vessel equilibrium cross-sectional area. Special attention is paid to the role played by collateral flow pathways between deep cerebral vessels and extra-cranial regions; to this end, the simulations are run in two scenarios: the first one considers a best-case venous network for head and neck veins wherein all the collateral routes for flow limited by the stenosis are present, while in the second case the occipital vein and sinus are absent, hence the collateral circulation is eliminated.

4.3 Results

4.3.1 Baseline condition

In this section we present computational results obtained with the current closed-loop model of the circulation coupled to a multiscale model of the CSF and brain dynamics. For a complete assessment of the validity of the model, we compare three versions of the current model:

- Entire blood circulation coupled to 0D cranial CSF models and 1D spinal CSF model; the conventional version of the Monro-Kellie hypothesis is adopted (contant volume inside the skull) [292] and a linear tube law for the SSAS (4.18); we refer to this case as '1dS'.
- Entire blood circulation coupled to 0D cranial CSF models and 1D spinal CSF model; the conventional version of the Monro-Kellie hypothesis is adopted and a nonlinear tube law for the SSAS (4.19) is used; we refer to this case as '1dS + nlSSAS'.
- Entire blood circulation coupled to 0D cranial CSF models and 1D spinal CSF model; the relaxed version of the Monro-Kellie hypothesis (Eq. (4.10), (4.9)) is adopted and a nonlinear tube law for the SSAS (4.19) is used; we refer to this case as '1dS + nlSSAS + rMK'.

Moreover, current computational results are compared with computational results obtained with the previous version of the model [292], wherein the global circulation is coupled to a fully 0D model of the craniospinal CSF system. From now on we refer to computational results obtained with the current most complete version of the model with 'Current model' or '1dS + nlSSAS + rMK', while computational results obtained with the previous version [292] is referred with 'Previous model' or 'PM'.

A comparison between computational results and MRI and experimental data is performed. Figure 4.4 shows the intracranial pressure in different districts of the CSF circulation. Both versions of the model result

in comparable average pressure values. The main difference between the two models becomes evident in the ICP waveform. Thanks to the distributed model of the spinal column, the computed ICP better captures the three physiological peaks that characterize the ICP. Figure 4.5 displays the computed ICP for the different versions of the model considered here. Black dots show the physiological landmark peaks of the ICP waveform [65].

FIGURE 4.4: Pressure in CSF compartments over a cardiac cycle. Mean pressure over a cardiac cycle is reported in brackets. Brain: pressure in fluid part of brain parenchyma; LVs: pressure in lateral ventricles; 3V: third ventricle; AoS: aqueduct of Sylvius; 4V: fourth ventricle; CSAS: cranial subarachnoid space; SSAS: spinal subarachnoid space (C2/C3 level).

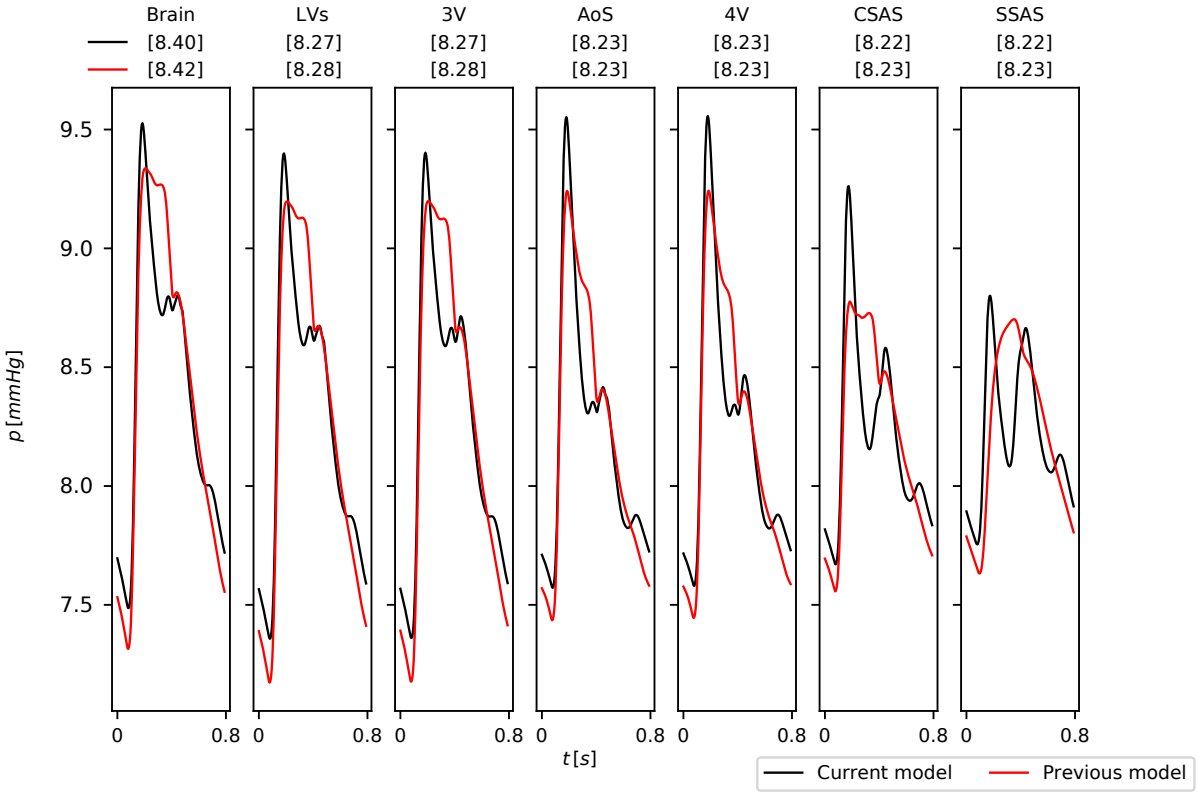

FIGURE 4.5: Cerebrospinal fluid pressure. Computed ICP with different version of the current model (1dS, 1dS + nlSSAS, 1dS + nlSSAS + rMK) and computed ICP with previous model (PM) [292]. Analysis of the peaks following [65] is underlined by black dots. P1: percussion wave; P2: tidal wave; P3: dicrotic wave.

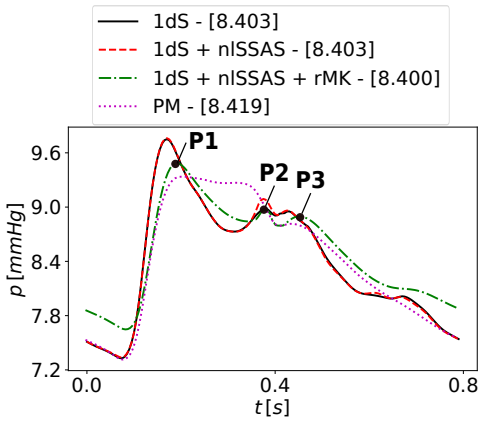

Figures 4.6 and 4.7 compare computational results of blood and CSF flow with respect to MRI data [12, 24]. In particular, Figure 4.6 (left) refers to normalized cerebral arterial inflow, evaluated as the sum of internal carotid arteries and vertebral arteries normalized with respect to the maximum value. Figure 4.6 (right) shows the CSF flow at the C2/C3 level in the spinal subarachnoid space. Figures 4.7 (left) and 4.7 (right) refer to the aqueduct of Sylvius, in particular the CSF flow through the cerebral aqueduct and the CSF velocity.

FIGURE 4.6: Computed results compared to measured data. Left frame: normalized cerebral arterial inflow (internal carotid arteries and vertebral arteries) over a cardiac cycle compared with MRI data from [12]. Right frame: normalized CSF inflow of spinal subarachnoid space at C2/C3 level over a cardiac cycle compared with MRI data from [12].

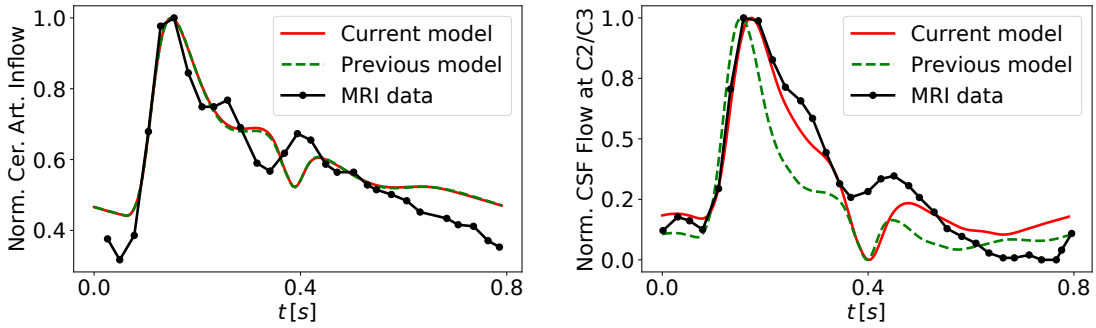

FIGURE 4.7: Computed flow and velocity in the aqueduct of Sylvius. Left frame: computed CSF flow through the aqueduct of Sylvius over a cardiac cycle compared with MRI data (mean and standard deviation) from [24]. Right frame: computed CSF velocity in the aqueduct of Sylvius over a cardiac cycle compared with MRI data (mean and standard deviation) from [24].

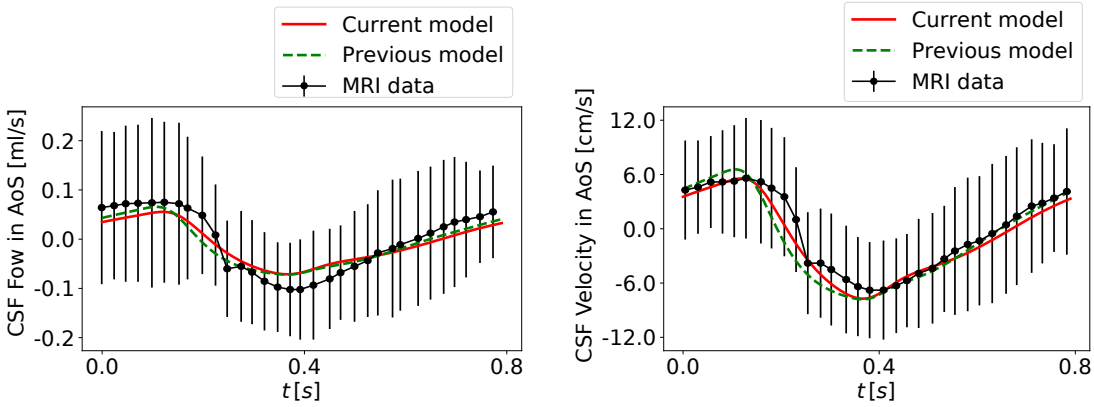

Figure 4.8 stresses the interaction between the cerebral blood and the cerebrospinal fluid and brain dynamics. Figure 4.8 (left) shows the time variation of the volume of different compartments of the craniospinal system; an increase in intracranial arterial blood volume causes a displacement of CSF from the cranial to the spinal district. This behaviour is underlined in Figure 4.8 (right) which illustrates the normalized (with respect to maximum and minimum) arterial inflow, venous outflow through internal jugular veins, flow in AoS and inflow in SSAS over a cardiac cycle. The lag in time between the systolic peaks is reported in Table 4.2 and compared to the results obtained with the previous version of the model.

Adopting a coaxial model of the spinal column allows to assess the cranio-caudal spinal cord motion.

FIGURE 4.8: Left frame: Time variation of $V - V_{av}$ of fluid volumes within the cardiac cycle, where V is the volume of the compartment and V_{av} is the averaged volume over the cardiac cycle. A: cerebral 1D arteries, arterioles and capillaries; V: cerebral 1D veins and venules; C-CSF: cranial CSF (CSF in all compartments inside the skull); SSAS: spinal CSF. Right frame: Time variation of blood and CSF flow within a cardiac cycle. Each flow profile was normalized between 0 and 1 such that all four systolic peaks correspond to 1. A: arterial flow of internal carotid arteries and vertebral arteries at C2/C3 level; V: internal jugular veins flow at C2/C3 level; SSAS: flow of the spinal subarachnoid space; AOS: flow in the aqueduct of Sylvius.

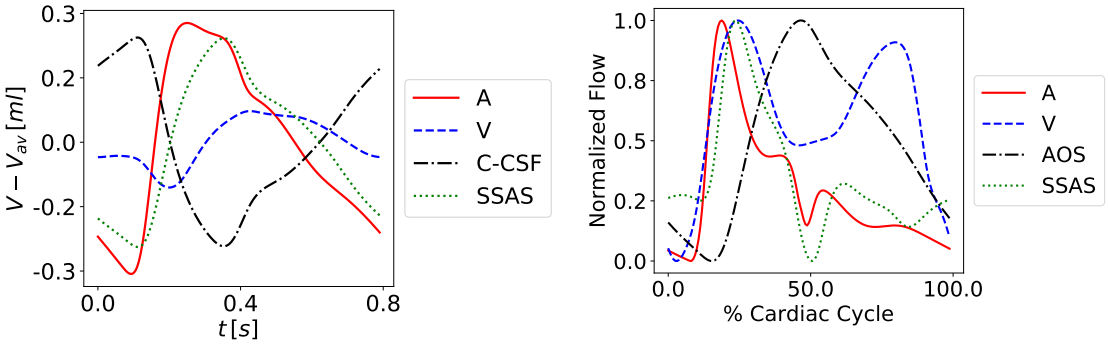

TABLE 4.2: CSF and blood flow over a cardiac cycle. Literature range taken from [4]. Arterial flow: flow in internal carotid arteries and vertebral arteries; Venous Flow: flow in internal jugular veins at C2/C3 level; CSF flow: inflow of spinal subarachnoid space; tIJV/tA: ratio between total internal jugular veins flow and arterial flow at C2/C3 level; AV, Arterio-CSF$_{SSAS}$, Arterio-CSF$_{AoS}$ Delay: lag in time between arterial and venous, spinal CSF and AoS CSF systolic peaks represented as a percentage of cardiac cycle.

Index	Current Value	Previous Value	Ref. Value
Mean Arterial Flow [ml/s]	13.16	13.13	13.55±3.07
Mean Venous Flow [ml/s]	12.16	12.15	9.42±2.37
Mean CSF Flow [ml/s]	0.003	0.01	0.08±1.33
Mean AoS Flow [ml/s]	0.008	0.01	0.03±0.013
AV Delay [%CC]	5.62	5.62	12.5±8.06
Arterio-CSF$_{SSAS}$ Delay [%CC]	5.00	0.625	5.35±2.36
Arterio-CSF$_{AoS}$ Delay [%CC]	28.12	28.12	22.1±74.66

Figure 4.9 shows the spinal cord motion in each cervical segment during one cardiac cycle; over all segments, a cranio-caudal followed by a caudo-cranial movement of the spinal cord can be observed. Maximum cranial and caudal velocity, as well as velocity amplitude, are compared to literature data [126].

The 1D model of the spinal compartment predicts the wave propagation along the spine. Figure 4.10 reports contour plots for the main variables of the spinal model and the CSF flowing in the spinal SSAS, p_c, p_d, A_c, A_d, u_c, u_a. The waves that travel from the cranial junction to the caudal end become evident.

4.3.2 Sensitivity analysis

Table 4.3 reports local sensitivities evaluated as in Equation (4.46); the first fifteen significant parameters are ranked according to sensitivity absolute value. For a complete analysis of ICP, variables under consideration are ICP, mean ICP over a cardiac cycle, PP_{ICP}, pulse amplitude of ICP waveform, and min ICP, max ICP, the minimum and maximum value of ICP over a cardiac cycle. The analysed parameters of the 1D spinal model are spinal length, l_{SSAS}, SSAS elastance, E_{ld}, viscosity of the CSF in the SSAS, μ_d, spinal cord elastance, E_{lc}, spinal cord viscosity, μ_c. For the cranial zero-dimensional model, the following parameters are analysed: intracranial compliance, Φ, elastance of different CSF intracranial compartments,

FIGURE 4.9: Spinal cord motion at the cervical level. Spinal cord velocity is displayed from C2 to C7 level; amplitude, maximum cranial and caudal velocities are compared to literature data from [126], whose values are reported as mean ± standard deviation under the computed values.

	C2	C3	C4	C5	C6	C7
Amplitude [cm/s]	0.543 0.296 ± 0.088	0.43 0.335 ± 0.108	0.347 0.387 ± 0.139	0.296 0.445±0.163	0.267 0.358±0.095	0.243 0.339± 0.083
Max cranial [cm/s]	0.143 0.115 ± 0.041	0.119 0.132 ± 0.042	0.102 0.161 ± 0.052	0.097 0.186 ± 0.078	0.091 0.161 ± 0.050	0.083 0.168 ± 0.053
Max caudal [cm/s]	-0.399 -0.182 ± 0.060	-0.311 -0.204 ± 0.072	-0.244 -0.226 ± 0.096	-0.199 -0.259 ± 0.094	-0.176 -0.197 ± 0.061	-0.159 -0.169 ± 0.055

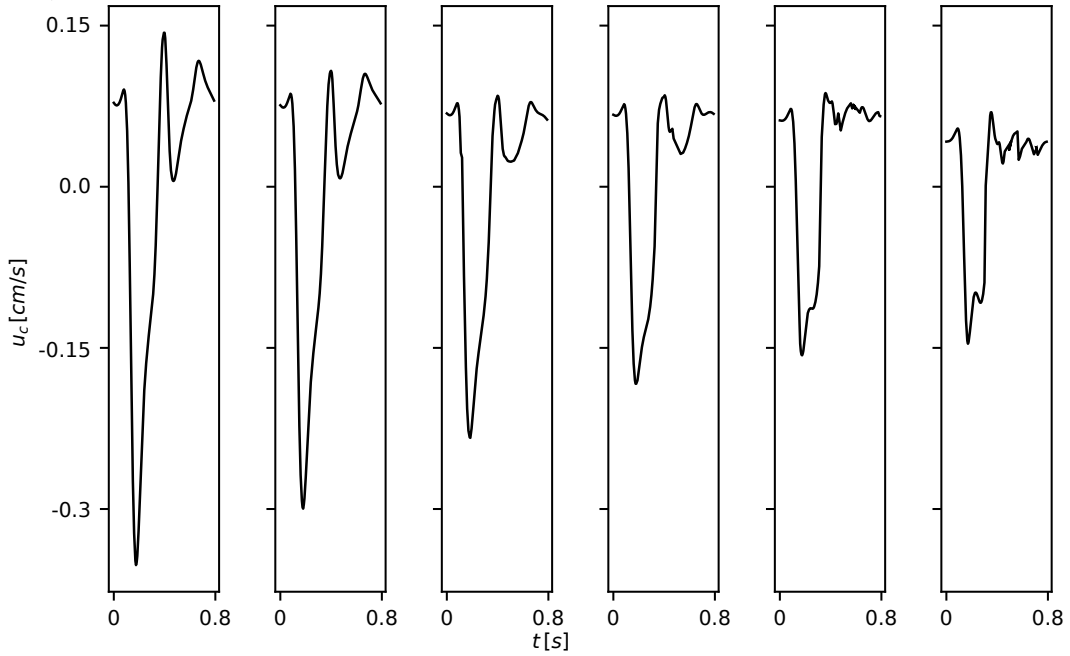

E_{LV}, E_{RV}, E_{3V}, E_{AoS}, E_{4V}, E_{CSAS}, resistances which regulates fluid exchange between compartments, R_{3V}, R_{AoS}, R_{4V}, R_{CSAS},, resistance which regulates the exchange between the cranial and the spinal compartments, R_{SSAS}, resistance for the exchange between capillaries and brain parenchyma, $R_{br,1}$, resistance to flow between brain parenchyma and lateral ventricles, $R_{br,2}$, absorption coefficient to arachnoid villi of superior sagittal sinus, k. Figure 4.11 shows the intracranial pressure waveform over a cardiac cycle obtained by increasing the selected parameters by 20 %, $\mathcal{P}^+$, with respect to the baseline $\hat{\mathcal{P}}$. Seven parameters are considered: spinal length, l_{SSAS}, viscosity of the CSF in the SSAS, μ_d, SSAS elastance, E_{ld}, spinal cord viscosity, μ_c, spinal cord elastance, E_{lc}, absorption coefficient to arachnoid villi of superior sagittal sinus, k, intracranial compliance, Φ. Figure 4.11 helps in identifying the parameters that mostly influence the waveform and the three main peaks of the ICP waveform.

4.3.3 PVI and outflow resistance estimation

PVI is estimated with injection of CSF at the rate of 1 ml/s in the cranial subarachnoid space, while recording the induce ICP rise. Figure 4.12 (left) shows the exponential-like behaviour of the mean ICP as the volume increases. In turn, as ICP increases, its waveform amplitude increases, as shown in Figure 4.12 (right); the correlation between these quantities shows an almost linear relationship, underlined by the red linear regression line. With a bolus infusion of 3 ml of CSF, the PVI calculated according to Eq. (4.47) gives a

FIGURE 4.10: Contour plots in space and time of pressure, area and velocity in the cord and in spinal CSF over a cardiac cycle.

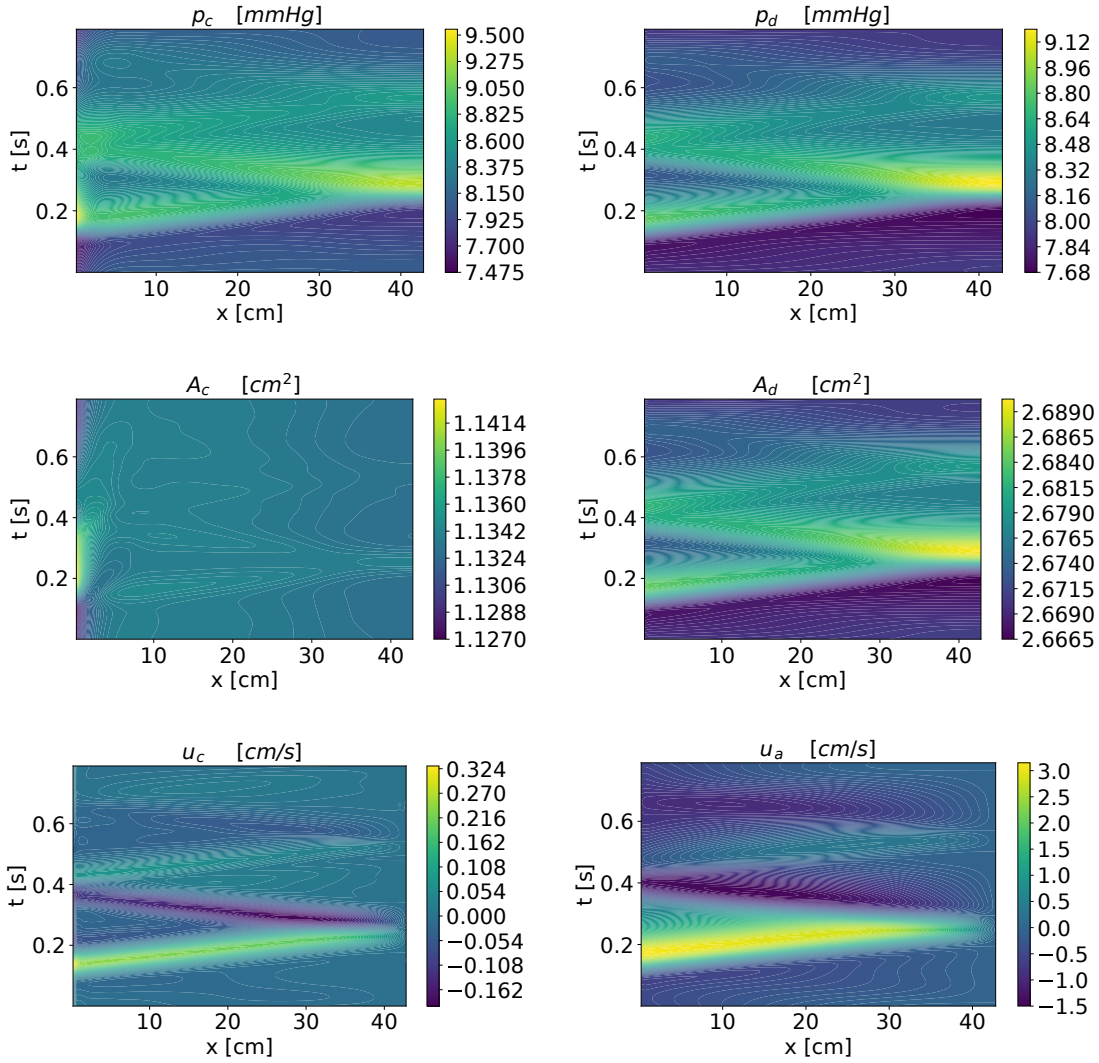

FIGURE 4.11: Sensitivity analysis of the intracranial pressure waveform. Computed intracranial pressure when selected parameters are increased by 20 % is compared with reference solution (Ref).

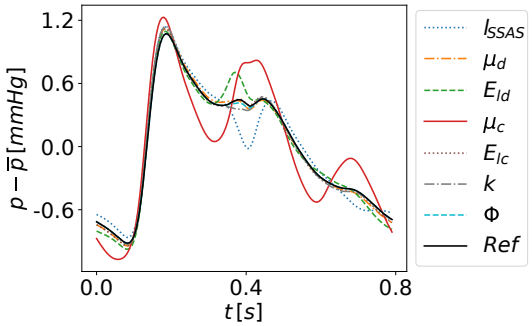

value of 20.21 ml if linear pressure-volume relationships are used for both cranial and spinal compartments and 15.95 ml if a nonlinear pressure-area relationship is adopted only in the spinal SAS (Eq. (4.19)). When both the cranial and spinal tube law are nonlinear (Eq. (4.9), (4.10), (4.19)), a PVI of 17.83 ml is measured.

TABLE 4.3: Sensitivity analysis results. Local sensitivities $S_{\mathcal{P}}^{\mathcal{Y}}$ of variables ICP, mean intracranial pressure over a cardiac cycle, PP_{ICP}, pulse amplitude of intracranial pressure waveform, min ICP, max ICP, minimum and maximum values of intracranial pressure over a cardiac cycle. The first fifteen parameters are ranked according to sensitivity absolute value.

Rank	ICP	PP_{ICP}	min ICP	max ICP
1	k (-0.3222)	Φ (-0.1827)	k (-0.3474)	k (-0.2767)
2	$R_{br,1}$ (-0.0334)	R_{SSAS} (0.1683)	l_{SSAS} (0.039)	l_{SSAS} (0.0314)
3	$R_{br,2}$ (0.0306)	E_{ld} (0.1241)	$R_{br,1}$ (-0.0363)	R_{SSAS} (0.0297)
4	R_{AoS} (0.0047)	E_{CSAS} (0.1052)	E_{ld} (-0.0345)	$R_{br,1}$ (-0.0283)
5	E_{ld} (-0.0026)	R_{CSAS} (0.0341)	$R_{br,2}$ (0.0337)	$R_{br,2}$ (0.0261)
6	E_{LV} (-0.0024)	E_{4V} (-0.0081)	Φ (0.0188)	Φ (-0.0231)
7	E_{RV} (-0.0024)	k (-0.0077)	E_{CSAS} (-0.0169)	E_{4V} (-0.0114)
8	l_{SSAS} (0.0016)	E_{lc} (-0.0077)	E_{4V} (-0.0123)	E_{CSAS} (0.0085)
9	E_{4V} (-0.0009)	μ_c (0.0058)	R_{SSAS} (-0.0067)	R_{AoS} (0.0037)
10	Φ (0.0007)	μ_d (-0.0051)	R_{AoS} (0.0053)	R_{CSAS} (0.0031)
11	E_{3V} (-0.0007)	$R_{br,2}$ (-0.0027)	R_{CSAS} (-0.005)	E_{LV} (-0.0019)
12	E_{CSAS} (-0.0007)	l_{SSAS} (0.0026)	E_{LV} (-0.0026)	E_{RV} (-0.0019)
13	E_{lc} (0.0003)	R_{AoS} (-0.0024)	E_{RV} (-0.0026)	E_{ld} (-0.0015)
14	R_{CSAS} (0.0002)	$R_{br,1}$ (0.0022)	μ_d (0.0025)	μ_d (0.0009)
15	R_{4V} (0.0002)	E_{RV} (0.0002)	E_{lc} (0.0016)	μ_c (0.0006)

The bolus injection test is also used for the estimation of the absorption resistance, following Eq. (4.48). After reaching the peak pressure, the ICP starts to decrease, displaying an hysteresis loop (Figure 4.13) in the pressure-volume plot. The absorption resistance evaluated at 1 minute after the end of the bolus infusion is 6.42 mmHg/ml/min.

FIGURE 4.12: Computational results from CSF bolus injection test. Left frame shows the exponential-like behaviour of mean ICP as an amount ΔV of CSF volume is injected in the cranial subarachnoid space. Right frame displays the relationship between mean ICP (ICP on x axis) and intracranial pulse amplitude (PP_{ICP} on y axis); red dashed-dotted line is the linear regression obtained from computational data.

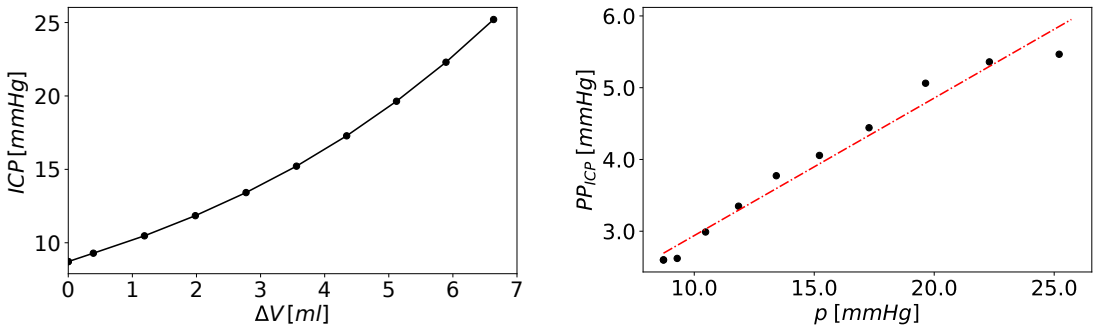

4.3.4 Transverse sinus stenoses

Stenoses in transverse sinuses causes a reduction of average flow rate of about 50 %; this is followed by an increase in dural pressure and in pressure of intracranial veins. As a consequence, the CSF reabsorption via arachnoid granulation is disrupted. Following the Monro-Kellie hypothesis, a major amount of CSF is displaced into the spinal subarachnoid space, which causes an increase in ICP. In particular, ICP rises

FIGURE 4.13: PVI and outflow resistance estimation: computational results from an infusion of 3 ml of CSF at 1 ml/s in the CSAS. After reaching a peak ICP at the end of the infusion, ICP starts to decrease and to return to its basal value according to the reabsorption resistance. Left frame shows the CSF pressure-volume curve; it displays an hysteresis loop. Right frame shows how the mean ICP decreases after the end of the infusion. Infusion begins at time 0 and within 3 seconds, 3 ml of CSF are added; then, simulation is run for 500 s for the evaluation of the absorption resistance. Both plots compare computational results obtained with the current CSF model with linear pressure-volume equation for the spinal SAS (continuous black line, 1dS), with nonlinear pressure volume relation in the spinal SAS (dashed red line, 1dS + nlSSAS) and in case of nonlinear cranial and spinal pressure-volume relation (dashed-dotted green line, 1dS + nlSSAS + rMK).

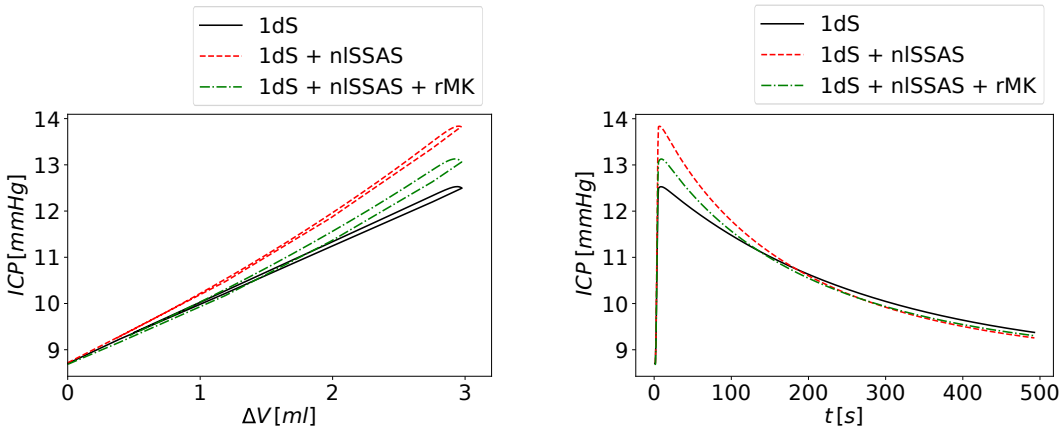

from 8.40 mmHg to 10.75 mmHg with an optimal collateral venous vascular network; when the collateral pathways to brain drainage are compromised, the ICP becomes 16.42 mmHg. Figure 4.14 shows the CSF pressure in different compartments. The presence of transverse sinuses stenoses affects also the ICP waveform, as it can be observed in Figure 4.15. The pulse amplitude between the healthy subject and the one with transverse sinus stenosis increases, especially in the case without collaterals routes. Moreover, there is a progressive elevation in the magnitude of the second peak P2 that becomes higher than the first peak when the venous collateral pathways are compromised.

4.4 Discussion

4.4.1 Comparison between computational results and literature data in healthy subjects

In this chapter we have presented a global, closed-loop, multiscale model of the human circulation coupled to a multiscale model for the cerebrospinal fluid and brain dynamics. The model comprises one-dimensional descriptions for medium to large blood vessels, arteries and veins, accounting for the viscoelastic property of the blood vessel wall. Lumped-parameter descriptions are used for other components of the full model that include the heart, the pulmonary circulation, the microvasculature, venous valves, Starling resistors, along with cerebral autoregulation. The dynamics of cerebrospinal fluid in the craniospinal cavity includes one-dimensional description of the spine, which comprises the spinal cord and the CSF flowing in the spinal subarachnoid space, and lumped-parameter models for the cranial CSF and brain dynamics, which include eight compartments (lateral, third and fourth ventricles, aqueduct of Sylvius, cranial subarachnoid space and left/right brain parenchyma). This work departs from a previous version of the model [292] wherein the blood circulation was coupled to a fully zero-dimensional model of the CSF and brain dynamics based on [162]. The main improvement of this work with respect to the previous one

FIGURE 4.14: Pressure in CSF compartments over a cardiac cycle: comparison between healthy control (HC) and subject with transverse sinuses stenosis (ST). Mean pressure over a cardiac cycle is reported in brackets. When the collateral routes are blocked, the ICP rises by 8 mmHg. HC: healthy control subject; ST - with Cols.: subject with transverse sinus stenosis and complete collateral circulation; ST - no Cols.: subject with transverse sinus stenosis without collateral circulation. Brain: fluid part of brain parenchyma; LVs: lateral ventricles; 3V: third ventricle; AoS: aqueduct of Sylvius; 4V: fourth ventricle; CSAS: cranial subarachnoid space; SSAS: spinal subarachnoid space.

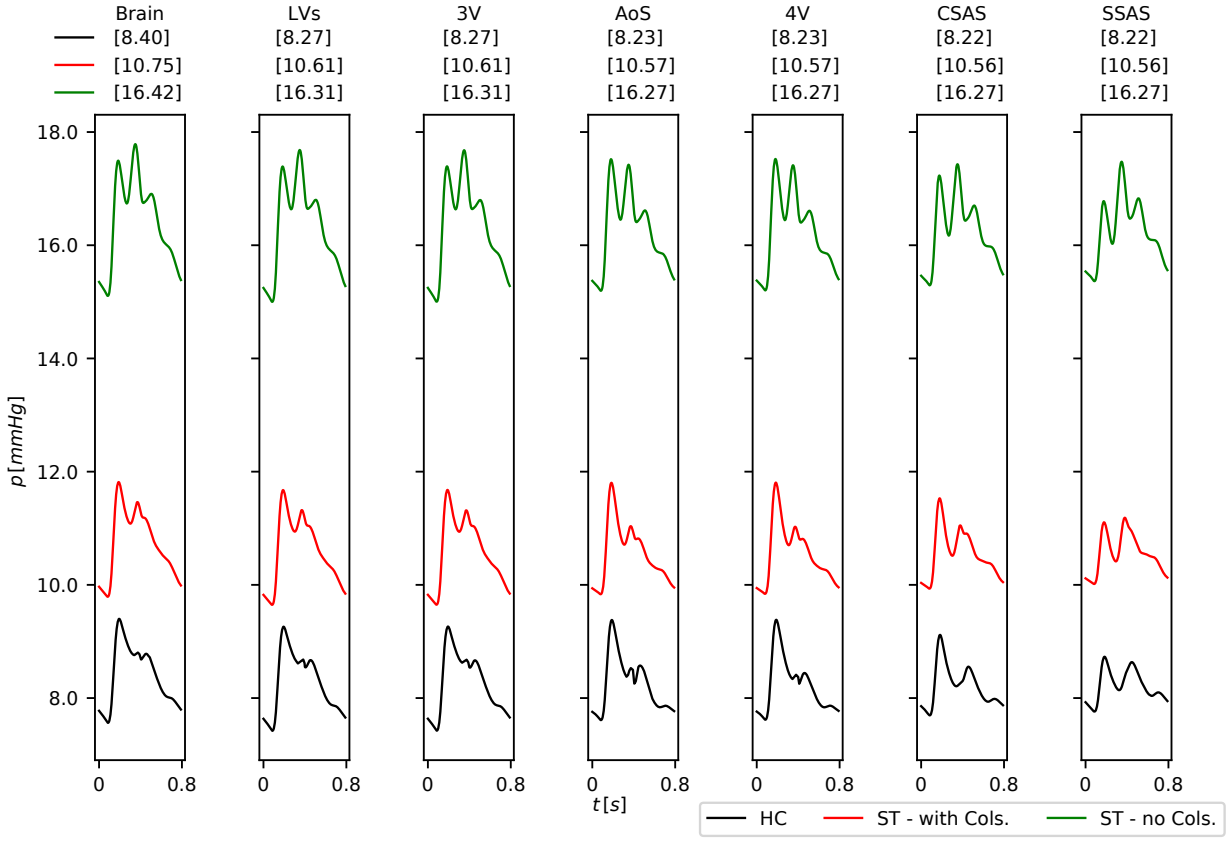

involves the introduction of a distributed model of the CSF dynamic in the spinal subarachnoid space. Such a model departs from [290, 139, 59] and it includes two coaxial tubes representing the spinal cord and the spinal subarachnoid space encased by the dura mater. Comparing the computational results obtained with the current version of the model and the previous one, it becomes evident the importance of including a one-dimensional model for the spinal column, which is able to capture the wave propagation and reflection along the spine. The ICP wave configuration is the sum of various components which have been named percussion wave (P1), tidal wave (P2) and dicrotic wave (P3) [45]. The percussion wave has a sharp peak and is almost constant in amplitude; the tidal wave is much more variable in shape and amplitude, and ends on the dicrotic notch, which is followed by the dicrotic wave. After the dicrotic wave, the pressure wave usually tapers down to its diastolic position, with some single or multiple minor waves during the descending phase of the wave [45]. Analysis of the cerebrospinal fluid pressure can reveal information about the compliance of the craniospinal system and also highlight pathological situations. With our previous version of the model [292], computed ICP exhibited three typical peaks, that can be observed in all CSF compartments but in the spinal canal they are less pronounced. Moreover, the difference in amplitude between the first and the second peaks is small. The introduction of a distributed model for the spinal SAS improves the CSF pressure waveform: three peaks can be observed in all CSF compartments, both in cranial and spinal districts. The first peak is more pronounced with respect to the others, especially in the

FIGURE 4.15: Cerebrospinal fluid pressure waveform. Computed ICP normalized with repect to its average value over a cardiac cycle. Comparison between healthy control subject (HC), subject with transverse sinus stenosis and complete collateral circulation (ST - with Cols.) and subject with transverse sinus stenosis without collateral circulation (ST - no Cols.). Mean pressure over a cardiac cycle is reported in brackets. The tidal wave (P2), according to the analysis in [65], is underlined by a green dot in the stenotic case without collateral circulation in order to stress that it is the highest compared to other peaks.

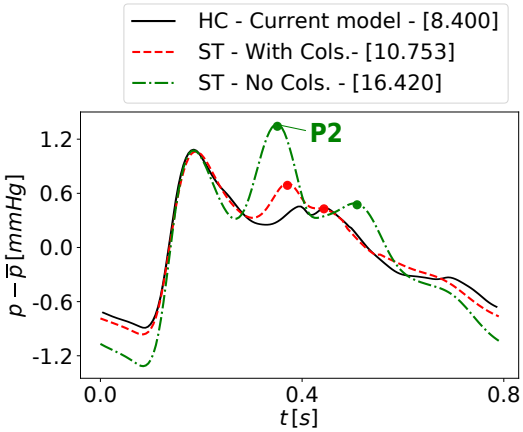

cranial compartments. P2 and P3 have similar amplitude in the pressure of the extracellular part of the brain parenchyma and in the lateral ventricles; in the spinal SAS, the amplitude of the second peak is closer to the first one. Concerning the total CSF pulse amplitude, it is comparable between the current and the previous version of the model; it ranges between 2 mmHg in the brain parenchyma to about 1 mmHg in the spinal SAS. Both versions of the model give similar mean CSF pressure value in all compartments, with a mean value of 8.40 mmHg in the brain parenchyma. Observing the contour plot for the pressure in the spinal subarachnoid space (Figure 4.10), the lightest regions highlight the waves and how they propagate along the spine. At the craniospinal junction (x=0), three light regions can be noticed: the first one, before 0.2 s, which corresponds to P1, the second one at 0.4 s, which is related to P2 and the third one at 0.5 s. P1 is caused by the arrival of the arterial flow pulse in the cerebral circulation, P2 is caused by the second arterial flow peak, which happens before the dicrotic notch, while the third peak, P3, is related to the increased flow occurring right after the dicrotic notch. The interaction between blood and CSF compartments can be seen in Figure 4.8: during systole, intracranial arterial blood increases and arterial pulsations are transmitted directly into the incompressible CSF filled SAS. Then, CSF shifts out of the skull into the spinal SAS, venous blood from the sinuses flows out of the brain mainly through the internal jugular veins and CSF from the ventricles is displaced out through the cerebral aqueduct. Even if we are adopting a relaxed version of the Monro-Kellie hypothesis which aims at reproducing the nonlinear intracranial pressure-volume relation, the interaction between blood and CSF systems is maintained as in the previous version of the following model. Indeed, we can notice an improvement in the lag in time between the systolic peaks, that are reported in Table 4.2: the arterio-spinal CSF delay is now in line with the literature range. This is due to the one-dimensional spinal model, but mainly to the relaxed version of the Monro-Kellie doctrine. The distributed spinal model permits to evaluate CSF flow at different locations of the spine. Here we consider the C2/C3 level; as CSF travels along the spinal column, the CSF peak is delayed with respect to the peak at the craniospinal junction. Moreover, the relaxed version of the Monro-Kellie introduces a small delay between the propagation of the arterial pulse to the CSF, that is not simultaneously shifted to the spinal SAS (see Figures 4.6 and 4.8), as in the previous version of the model. The effect of the relaxed Monro-Kellie hypothesis can be observed also in Figure 4.5: comparing the ICP waveform obtained with current CSF model and linear pressure-volume relations (1D spinal) to the one obtained with the relaxed Monro-Kellie, it can

be seen a small delay between P1, which is due to the transmission of arterial pulsation to the CSF. In order to assess the validity of the coupled model, we compared computational results with respect to MRI data from literature. Figures 4.6 and 4.7 show normalized cerebral arterial inflow, CSF flow at C2/C3 level and CSF flow and velocity in the cerebral aqueduct, while Table 4.2 compares CSF and blood flow over a cardiac cycle to the literature range. There is a good match between numerical results and MRI measurements; this holds for both versions of the global model, proving that the introduction of the one-dimensional model for the spinal column does not affect the physiological behaviour of the computational results.

Pulsatile movement of the spinal cord with the cardiac cycle has been studied by means of various techniques [44, 88, 192, 126], and is generally believed to be mainly due to the transmission of the arterial pulse. Multiple imaging modalities, such as sonography, ultrasound, and magnetic resonance imaging (MRI), have been employed to measure spinal cord motion. Novel MRI techniques can measure the displacement and velocity of spinal cord very accurately. Spinal cord movement can be in the anterior/posterior, right/left and cranio-caudal directions. Cord motion is largest in the anterior/posterior direction [88]. However, the largest part of reported studies have focused on the cranio-caudal movement of the cervical cord. It was proved that the cervical spinal cord moves with an oscillatory pattern in the cranio-caudal direction, and the maximum velocity gradually decreases caudally along the cord. No definite cranio-caudal motion was observed in the middle thoracic spinal cord or conus medullaris [192]. The coaxial one-dimensional model for the spine adopted in this work allows to study the spinal cord motion only in the cranio-caudal direction, while the other movements cannot be addressed. A three-dimensional model of the spinal cord would permit a complete study of the cord motion, in all the three possible directions. Figure 4.9 displays the spinal cord velocity at different locations of the cervical level. It can be observed that the amplitude of the velocity decreases as we move from the cranial junction to the caudal direction; this behaviour characterizes also the maximal cranial and caudal velocities. However, the computed velocity amplitude at the C2 level is higher that the measured one; moreover, data from [126] reveals that the amplitude increases up to C5 level and then starts decreasing, while computational data show a maximum amplitude at the craniospinal junction and then it decreases along the spine. A possible explanation can be found in the boundary conditions. At the cranial junction, there are limited coupling options because we coupled a zero-dimensional and a one-dimensional model. Moreover, at the end of the spine, we imposed reflexive boundary conditions with zero velocity of the spinal cord; this could be an excessively strong imposition since it does not allow any caudal displacement at the lumbar level; Mikulis et al. [192] observed very little longitudinal motion at the conus medullaris, but this could depend on the accuracy of the MR images method adopted in that study. More appropriate boundary conditions at the sacral end of the cord could be introduced, but more available data are needed to this end. Cervical level velocity measurements showed that the spinal cord moved first caudally and then this oscillation was followed by a cranial movement of lower velocity [192, 126]. The mathematical model proposed in this work is able to reproduce this motion. Another aspect which requires attention is the influence of cardiac cycle and respiration on spinal cord movement [320]. The present version of the model does not incorporate the effects of the respiration; variations of intrathoracic pressure affect the venous haemodynamics as well as the ICP, which is modulated by the respiratory cycle. This represents a limitation of the current model that will be addressed in future works.

4.4.2 Sensitivity analysis of the intracranial pressure

The multiscale model of the cerebrospinal fluid and brain dynamics adopted in this work is characterized by several parameters that describe the physical properties of each compartment and regulate the fluid exchange. Each one of them contributes to the determination of model output variables. The sensitivity analysis performed here aims to establish the main determinants of the ICP, its value and waveform. Data

reported in Table 4.3 shows that the major significant parameter for the mean ICP is the reabsorption coefficient into the arachnoid villi of the superior sagittal sinus. For the same pressure difference between cranial subarachnoid space and superior sagittal sinus, an increase in k leads to an increase in the cerebrospinal fluid reabsorbed into the venous system, hence a reduction in the amount of CSF in the craniospinal system, with a consequent decrease in the mean ICP. On the contrary, a decrease in k limits the reabsorption of CSF into the venous circulation causing an increase in ICP. Physiologically, this is the case of communicating hydrocephalus; infection, meningitis, and subarachnoid hemorrhage are pathological situations that can result in an inflammatory response that affects arachnoid granulations with a resultant dysregulation of CSF absorption [138]. The second relevant parameter for the mean ICP value is the resistance which regulates the exchange between capillaries and brain parenchyma. Departing from the original CSF model developed by Linninger et al. [162], there is CSF mass transfer from the capillary bed to the parenchyma, which comprises the diffuse CSF production rate $q_{Cp\rightarrow br,const}$ and the CSF seepage $q_{Cp\rightarrow br}$, which in turn depend on $R_{br,1}$ and the pressure difference between capillary bed and brain parenchyma. This pressure driven exchange could be bidirectional; CSF could flow from brain parenchyma to capillaries if its pressure is higher than capillaries' pressure. An increase in $R_{br,1}$ reduces the pressure driven exchange between capillaries and brain parenchyma with a consequent reduction in circulating CSF and ICP. However, we can notice that the sensitivity to $R_{br,1}$ is small; in fact, only a small amount of CSF flows into the CSF system following the momentum equation Eq. (4.6) (about 6 % of total CSF production from the cerebral circulation). According to our sensitivity analysis, we can conclude that mean ICP is mainly affected by alterations in CSF reabsorption, secretion and then circulation, in particular between brain parenchyma and lateral ventricle ($R_{br,2}$) and between third ventricle and aqueduct of Sylvius R_{AoS}. These processes are involved in the pathogenesis of different pathologies of the central nervous system [268]. Elastances, resistances to flow between other CSF compartments and parameters of the spinal 1D model do not significantly change the mean ICP value.

Concerning the pulse pressure, a slightly different ranking of sensitivities can be observed. Reabsorption constant k and $R_{br,1}$, resistance to flow between capillaries and brain parenchyma, are not significant for the intracranial pulse pressure. Intracranial compliance parameter Φ wins over other cranial parameters while elastance of spinal subarachnoid space overcomes other spinal 1D model parameters. Other relevant parameters for the pulse pressure are the resistances to flow between cranial and spinal subarachnoid spaces R_{SSAS}, elastance of cranial SAS, E_{CSAS}, and resistance to flow between fourth ventricle and cranial subarachnoid space, R_{CSAS}. Our computational results suggest that brain parenchyma and cranial/spinal SAS are the most relevant CSF compartments for the intracranial pulse pressure; intracranial compliance, as well as compliances of cranial and spinal SAS compartments and how CSF flows between them are the main determinants for the pulsatility of ICP. Intracranial compliance parameter Φ is introduced in this work for the description of the nonlinear exponential pressure-volume relationship of the brain parenchyma pressure and intracranial volume inside the skull leading to a relaxed version of the Monro-Kellie doctrine, which admits an intracranial volume variation of < 0.1 % over a cardiac cycle. This mathematical assumption is in line with the observations in [11] about the misconception of constant intracranial volume that arises from the Monro-Kellie hypothesis. Sensitivity analysis results support the importance of introducing a compliance which regulates the ICP-volume curve and determines the pulsatility of the ICP.

To conclude our discussion on the sensitivity analysis results, we assessed which parameters are more relevant ones for the ICP waveform. Elastances of intracranial compartment, as well as resistances to flow exchange, do not affect the waveform which on the contrary is mainly determined by the spinal 1D model. Elastances of dura mater and spinal cord and viscosity of CSF in the SSAS and of the porous tissue of the cord play a major role in the determination of the localization of landmark ICP waveform peaks. This stresses the importance of using a one-dimensional model for the CSF dynamics in the spinal column but

also its interaction with the tissue of the spinal cord. Varson et al. [310] analysed the intraspinal pressure and the spinal cord perfusion pressure after spinal cord injury, showing that the spinal pressure behaves in a similar way of the ICP. In our computational results, changes in the viscosity of the spinal cord increases the second and third peaks to a similar degree and exhibits an higher peak at the end of the cardiac cycle; on the other hand, elastance of the dura rises the second peak, while maintaining the third peak to the same level of the reference configuration. Elastance of the spinal cord slightly decreases the second peak, that becomes lower than the third peak. Varson et al. [310] highlighted also the importance of the spinal autoregulatory capacity and the blood supply to the spinal cord in the determination of spinal pressure in case of spinal cord injury. One limitation of this mathematical work is that the vasculature of the spinal cord is not considered; future works will address this aspect, posing attention on the interaction between the spinal circulation, the spinal cord and the CSF in the SSAS, as well as on alternative routes of CSF absorption at the spinal level.

4.4.3 Pressure-volume relationship and outflow resistance of the CSF system

Compliance of a distensible or elastic compartment is defined as the ratio between change in volume to the corresponding change in pressure. For the craniospinal CSF compartments, compliance gives a measure of the CSF volume distensibility and it is particularly important in the context of the Monro-Kellie hypothesis, since it determines the magnitude of CSF pressure variations required to return to the equilibrium point when a change in volume of any intracranial compartments (blood, CSF, brain parenchyma) occurs. If pressure varies linearly with volume, the slope of the volume-pressure curve, that is the compliance, is constant. However, this is not the case for CSF compartments. The first demonstration of a nonlinear volume-pressure relationship was due to Ryder et al. [246] in 1953, who described this relation to be hyperbolic. Marmarou et al. [181, 182] confirmed this observation by means of invasive injection of known quantities of saline into the cisterna magna or ventricles of adult cats while recording the rapid ICP response. Moreover, since the nonlinear behaviour makes the quantification of compliance difficult, they introduced the pressure-volume index (PVI), defined as the slope of the linear volume-log pressure plot or equivalently as the change in volume necessary to raise the CSF pressure to a level 10 times the baseline pressure (Eq. (4.47)). In the same papers, the authors observed that to a fast rise in ICP due to volume addition, it follows a return to equilibrium thanks to fluid absorption. This permits the evaluation of the total resistance to CSF reabsorption, as expressed in Eq. (4.48); the proposed technique for the determination of outflow resistance is a two-step process: firstly, the PVI is evaluated from the rise in pressure, and then the resistance is calculated from the PVI and the values of baseline initial, peak and recovery pressures. Shapiro et al. [262] used the experimental procedure proposed by Marmarou et al. [181, 182] for the evaluation of PVI and outflow resistance in twenty-three children and seven adults (that underwent diagnostic or therapeutic procedures). In order to inject a safe amount of CSF, they estimated the magnitude of bolus injection from a previous estimation of PVI determined by withdrawal of CSF. In their measurements, mean PVI for the 7 adults was 25.9 ± 3.7 ml with smaller values in young children. There was a statistically significant variation (standard deviation/mean) of 13 ± 6 % in adults, which were attributed to intracranial and spinal volumes differences. PVI was also estimated in a group of pathological patients, examples along these lines include [141, 185, 285, 254], to name but a few. More recent studies provide estimation of PVI by means of less invasive techniques. In [313], PVI was derived from lumbar CSF infusion tests and PC-MR imaging flow measurements and compared to classical PVI estimation from bolus injection in the lumbar space with lumbar pressure recording. They found that in 30 healthy elderly subjects the PVI was 10.2 ± 3.7 ml. Sundström et al. [277] compared three different methods for the evaluation of PVI (constant pressure infusion, bolus injection, constant flow infusion methods) in patients with probable or possible idiopathic normal-pressure hydrocephalus; the PVI derived from computerized fitting analysis of the bolus infusion

method was 22.5 $\pm$ 15.9 ml, higher with respect to the values obtained with the other methods. Beck et al. [21] evaluated a PVI in the range 5.46-23.04 by means of lumbar infusion test in patients with suspected spontaneous intracranial hypotension without spinal CSF leakage. Vallet et al. [309] analysed results of lumbar infusion study performed in adult patients suspected of normal pressure hydrocephalus and found a mean PVI of 18.25 $\pm$ 7.23 ml. The range of PVI values in the literature is large, often evaluated in pathological conditions, and could depend on methodological constrains and velocity of infusion. Geregele et al. [100] reported that the pressure-volume compensatory reserve is insufficient when PVI $<$13 ml, while the brain is over-compliant if PVI $>$26 ml, and these values are valid if PVI is calculated by means of slow infusion while higher values are indicated for fast bolus infusion. Computational infusion tests give PVI values between 15 and 20 ml in all considered situations when 3 ml of CSF are injected at 1 ml/s. PVI is higher if both cranial and spinal CSF compartments are characterized by a nonlinear pressure-volume relationship. We stress here that ICP-volume relations in Eq. (4.10), (4.9) are used for the determination of pressure in brain parenchyma, while other cranial compartments are described by distensibility equations of the form Eq. (4.3), that look like linear equations. However, pressure of a cranial CSF compartment is influenced by the extracellular fluid pressure, that is used as external pressure, hence it still exhibits nonlinear exponential behaviour as volume increases in the infusion test. Testing different velocity of infusion (0.5, 1, 2 ml/s) or different amount of CSF injected at 1 ml/s (from 2 to 7 ml), we observed that PVI is not significantly affected, giving values between 17.35 and 17.83 ml. This is valid if nonlinear pressure-volume tube laws are adopted, but not in the case of linear relationships. Indeed, as the amount of CSF injected into the subarachnoid space increases, the PVI increases significantly: it is 20.21 ml when 3 ml are injected while it is 25.40 ml with an infusion of 10 ml. The linear pressure-volume relationship of the SSAS and the classical Monro-Kellie hypothesis well capture the main features of the cerebrospinal system at the baseline setting point; one can observe Figures 4.5, 4.6, 4.7 wherein computational results obtained with the nonlinear tube law for the CSF in the SSAS and the relaxed MK are compared with those obtained with the previous completely linear version of the model. The mean intracranial pressure, as well as its waveform, are not significantly modified by the introduction of nonlinearity in pressure-volume relationships. However, the infusion test stresses the role of modelling the nonlinear behaviour: the use of linear pressure-volume curves is acceptable as long as moderate blood volume changes are simulated. As the amount of volume injected in the cerebrospinal system increases, that is, as large deviations from the baseline model state are introduced, the model equipped with linear tube law models fails to reproduce the relations observed in the literature. Another aspect that is influenced by the nonlinearity is the intracranial pulse pressure. Figure 4.12(right) shows the linear regression curve obtained from the relationship between mean intracranial pressure and its pulse: as the pressure increases, its pulse pressure increases. When a linear tube law is used, the intracranial pressure rise is not accompanied by a proportional increase in pulse pressure.

At the end of the infusion, ICP reaches a peak and then starts decreasing, as can be observed in Fig. 4.13. The descending pressure is slightly higher than those of the ascending phase, displaying a mild hysteresis effect. This behaviour is in line with that observed by Marmarou et al. [182] in cats. Resistance to absorption evaluated at 1 minute is comparable to resistance evaluated at 2 minutes after the end of infusion. The computational experiment gives a value of 6.42 mmHg/ml/min, that is in line with the literature range of $<$ 12 mmHg/ml/min [262, 66, 285, 309] regardless of the adopted method of infusion.

Computed results about estimation of PVI and total resistance to CSF absorption return reasonable values compared to the literature. These indexes are strictly related to the compliance of the cerebrospinal system, as well to production and reabsorption processes. The current mathematical model is limited to well-known fluid exchange routes between the CSF space, brain parenchyma and blood; however, recent insights into the biology of CSF posed the attention on the role of other possible pathways of exchange, such as the meningeal lymphatic vessels associated with the dural sinuses throughout the cranium [16,

173] and the glymphatic system [127, 268]. All these systems could influence the dynamic of CSF during the infusion test; however, there are no quantitative data to allow for alternative models of fluid exchange between different compartments into the current mathematical context.

4.4.4 Impact of transverse sinus stenoses on blood and CSF dynamics

Idiopathic intracranial hypertension (IIH) is a neurological condition of unknown aetiology, which requires prompt diagnosis and if left untreated can result in a rapidly progressive visual loss. There is emerging evidence of the influence of dural sinus stenosis as a trigger/cause of IIH [200, 4]. In order to demonstrate an example of the applicability of the present model, we studied the effects of right and left transverse sinus stenosis on blood and CSF dynamics. As a consequence of the 70 % reduction of reference cross-sectional area in the stenotic vessels, the average flow rate of transverse sinuses decreases by 50 %; this caused an increase in pressure in intracranial veins and the venous drainage from the cranial circulation is disrupted with consequent reduced CSF reabsorption through the arachnoid granulation (which depends linearly on the pressure difference between ICP and superior sagittal sinus pressure). Following the Monro-Kellie hypothesis, a major amount of CSF is shifted into the spinal subarachnoid space leading to ICP rising. Figures 4.14 and 4.15 show the CSF pressure in all CSF compartments in the healthy control, in the stenotic case and when the stenoses affect a venous network without collateral pathways. In the last case, the venous head network is missing the occipital vein and sinus. If the collateral circulation is impaired, the severity of intracranial hypertension increases. CSF pressure rises in all compartments by 2.3 mmHg when the collateral circulation is complete, while it is doubled compared to the healthy case when the collateral routes are compromised. Not only the mean ICP is affected by the transverse sinuses stenoses, but also its waveform. Following the nonlinear pressure-volume relations that characterize both the cranial and the spinal models, as the ICP rises, its amplitude increases and there are changes in the shape of the pulse wave. When the collateral routes are activated, there is a progressive elevation in the magnitude of P2 while P3 remains as in the healthy control. As the ICP rises due to the absence of the major collateral pathways, P2 shows a disproportionate elevation, resulting in a pyramidal shape, with P2 the highest peak. Moreover, P3 is delayed in time with respect to the healthy case. Increase in the P2 component of the ICP wave is thought to represent decreased intracranial compliance. The previous version of the model [292] was not able to capture the changes in pressure waveform as ICP rises due to the stenotic condition; this was due to the linear pressure-volume relationships that characterize all craniospinal compartments. In order to stress the differences with respect to the previous version of the model, we tested how the current model behaves in the case of bilateral transverse sinus stenoses described by stenosis models with a reduction of 90% of vessel's equilibrium cross-sectional area, the same reduction proposed in [292]. Figure 4.16 shows the ICP waveform for the healthy control and in case of bilateral transverse sinus stenoses obtained with the previous and current versions of the model. As previously observed, in the healthy condition the two versions of the model result in comparable mean ICP, even if the current model better captures the landmark peaks of the ICP waveform. This is not true in the pathological condition of intracranial hypertension due to transverse sinus stenosis: in this case, both the mean ICP value and its waveform display significant differences. Due to the stenosis, there is an increase in dural pressure followed by a decreased CSF reabsorption via arachnoid granulation. Therefore, the ICP rises in order to maintain the balance between CSF generation and absorption. How much ICP rises depends on the answer of the craniospinal CSF system to volume variations; this is regulated by the compliance of the cranial and the spinal compartments and their pressure-volume relationships. For the same CSF volume variation, computed ICP results in a lesser increase when the previous model was used. Moreover, if the current version of the model is adopted, the ICP waveform displays a significant increase in the second peak with respect to the healthy control that was not observed when the previous version was used. This underlines that a linear tube law for the spinal

subarachnoid space, as well as the classical Monro-Kellie hypothesis, underestimates the pressure changes due to pathological conditions. The introduction of nonlinearity is an added value for this model, especially when studying deviations from the baseline state.

FIGURE 4.16: Cerebrospinal fluid pressure waveform in subject with transverse sinus stenoses. Computed ICP in healthy control subject (HC) and in subject with transverse sinus stenoses (ST) with collateral circulation (With Cols.). Comparison between results obtained with the current (CM) and the previous version of the model (PM) [292]. Values in brackets refers to mean ICP over a cardiac cycle.

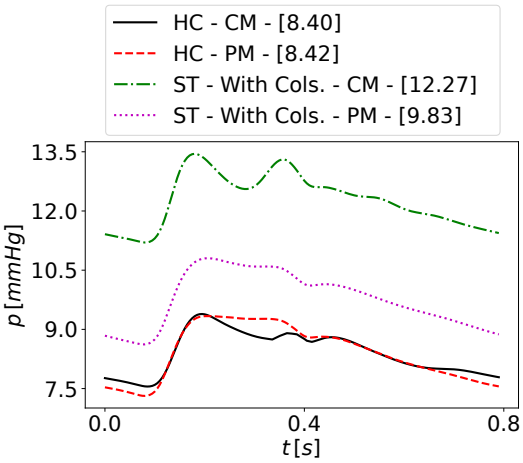

4.5 Conclusions

In this work, we coupled a global closed-loop model of the entire circulation, which comprises one-dimensional models for major arteries and veins and zero-dimensional models for other districts of the circulation, to a multiscale model of the cerebrospinal fluid and brain dynamics. Such a model includes zero-dimensional compartments for the cranial CSF representation and a one-dimensional coaxial model for the spine. Moreover, the intracranial dynamics and the CSF in the spinal subarachnoid space were enriched with a nonlinear pressure-volume relationship. Computational results were assessed through comparison with literature data, sensitivity analysis on the ICP, pressure-volume index estimation and application to the pathological condition of intracranial hypertension caused by transverse sinus stenoses. Our results capture in a satisfactory manner the interplay between blood, CSF and brain parenchyma, both in healthy and pathological condition. The introduction of the one-dimensional model for representing the spinal dynamics improves the ICP waveform and the arterio-CSF$_{SSAS}$ delay, that both depend on the interaction between CSF and cerebral arterial volume and pulsation, as well as from the wave propagation along the spine. The nonlinearity in the pressure-volume relationships of the cranial and spinal compartments permits to resemble the exponential-like behaviour that physiologically characterizes the CSF dynamics and well describes the modifications in pressure waveform in case of pathological condition. The model as presented is applicable to many pathophysiological conditions associated to the circulatory system and to the central nervous system fluids in the craniospinal cavity. Despite the progress reported in this work, there are several limitations to be addressed in future developments. One limitation is represented by the boundary conditions at the end of the spine, which need to be improved to well capture the spinal cord motion. Spinal CSF dynamics are highly sensitive to respiratory performance and instantaneously reflect intrabdominal and intrathoracic volume and associated pressure changes [5]. Evaluation of cardiac and respiration-dependent spinal cord motion within the spinal canal from the cervical to lumbar segments proved that breathing conditions have a considerably greater impact than cardiac activity on spinal cord

motion [320]. Future work will focus on the effects of respiration on the ICP pulsatility and on the adaptation of the CSF dynamics to abrupt changes of abdominal and thoracic pressures, like coughing. Moreover, intracranial and spinal compliance contributes to the determination of ICP under postural changes [220, 279]; the CSF modelling elements introduced in this work open the way for future investigations on the CSF dynamics in the upright position. Furthermore, the introduction of the one-dimensional model for the spinal column provides the basis for including new CSF reabsorption routes; as previously discussed, CSF can be reabsorbed also at the spinal level, hence a first step in this direction might address the blood supply to the spinal cord.

Chapter 5

Determination of the Total Effective Vascular Compliance of a Global Mathematical Model for the Cardiovascular System

This chapter begins the second part of the present thesis, which refers to arterial hypertension modelling. One of the major novelties of this work is addressing to this pathology in the context of a global closed-loop multiscale mathematical model which aims to describe the entire cardiovascular system. This global approach poses the need of controlling the total amount of blood that is in the circulation and its relation to vascular compliance, since it can be proved that arterial pressure is highly sensitive to total blood volume. This chapter reports a study that is preliminary to arterial hypertension modelling; it focuses on total effective vascular compliance and total control of blood volume of a global closed-loop model of the circulation. The following Chapter 6 will address to the adaptation of the global closed-loop model to remodelling that is cause/consequence of arterial hypertension.

5.1 Introduction

The vascular compliance of the circulatory system is defined as the slope of the relationship between intravascular volume and circulatory filling pressure; this property reflects the inherent elasticity of the vascular system. Changes in vascular compliance are of primary importance in the control of cardiovascular function and extracellular fluid volume regulation [249]. In animals, an estimation of total vascular compliance can be obtained by determining Mean Circulatory Filling Pressure (MCFP)-blood volume curves. MCFP refers to the pressure, constant in all vascular districts, that can be obtained by stopping the heart and waiting for blood to redistribute in the vascular system according to the capacity of the different districts [110]. Compliance is thus defined as the change in blood volume divided by the change in MCFP, thus total vascular compliance (TVC) is

$$\mathrm{TVC} = \frac{\mathrm{V} - \mathrm{V_u}}{\mathrm{MCFP}}\,, \tag{5.1}$$

where V is total blood volume and $\mathrm{V_u}$ is unstressed blood volume, i.e., the blood volume contained in the vascular system for zero MCFP. Different methods were used to evaluate the TVC in different animal species [110, 75, 256]; some of them imply stopping the circulation to measure MCFP, while others require the use of anesthesia and extensive surgery, as in the constant cardiac output reservoir technique [265, 264], to determine compliance as the ratio of a change in volume to a change in venous pressure. However, the

values for total vascular compliance are very close whatever the method adopted; in dogs, values from 1.4 to 4.2 ml/kg/mmHg were observed with an average of 2.57 ml/kg/mmHg [265, 75, 120, 122].

Classical estimation of MCFP requires stopping systemic flow, posing ethical limitations to its application to humans. To avoid this methodological limitation, a different index of capacitance was introduced as a measure of total vascular compliance. This method was first presented in [82] and then used in [171, 169, 170, 251, 249, 99, 315, 142]; it involves simultaneous recording of right atrial pressure and volume changes induced by transfusion, bleeding, or rapid iso-oncotic dextran infusion. Based on the experiment first presented in [82], London et al. [171] determined the total effective vascular compliance (TEVC) using an infusion of 500 ml of 6% dextran carried out within four minutes in a large forearm vein in control and hypertensive patients in supine position. Dextran is an osmotically neutral fluid that is used in intravenous solutions as volume expanders to replace lost blood in emergency situations; it is effective in expanding and maintaining the plasma volume. According to the authors of [321], total blood volume after dextran infusion increased only by the amount of solution administered. The slope of the relationship between central venous pressure (CVP) and blood volume was called TEVC in order to differentiate it from the compliance obtained from MCFP measurements [82]. CVP, usually considered as representative of the right atrial pressure, depends on the venous return and the pumping ability of the heart, thus it does not rely exclusively upon vascular volume and the elastic properties of the vascular bed [231]. Moreover, a four-minute long infusion is not rapid enough to prevent the participation of some regulatory mechanisms such as the short-term regulation of blood pressure, which occurs within seconds. Modification in CVP and also arterial pressure due to blood volume variations activates various reflexes that modify specific cardiovascular system properties like vascular compliance, vascular tone, heart rate, etc. [244]. In turn, such modifications influence the final CVP change for a given blood volume variation and thus the estimated TEVC [264, 174]. Even if CVP is influenced by several factors during blood volume changes via transfusion or bleeding, Echt et al. [82] showed that the pressure-volume relationship is practically linear; in normal men, it ranges from 2.1 to 2.7 ml/kg.

Arterial compliance was estimated in animals and men. Shoukas and Sagawa [264] used the constant cardiac output reservoir method to determine arterial compliance in dogs by shifting blood between the arterial system and the reservoir by a second roller pump while cardiac output, venous pressure and intrasinus pressure were maintained at constant levels; the ratio between the volume change measured in the reservoir and the change in arterial blood pressure was considered as arterial compliance. In men, arterial compliance was calculated as ratio between the time constant (derived from the analysis of the diastolic pressure decay) and the total peripheral resistance (evaluated as ratio between mean arterial pressure and cardiac output) [266]. Arterial compliance represents 1-3% of total vascular compliance. Compliance of the cardiopulmonary circulation was estimated by Echt et al. [82] using lower body negative pressure and norepinephrine infusion; they concluded that intrathoracic compliance is between 42 to 55% of total vascular compliance. More direct evaluation of the intrathoracic circulatory compliance was obtained in [170]. In that work, in addition to total vascular compliance, the peripheral vascular compliance was determined as the ratio between changes in peripheral volume (evaluated as difference between total blood volume and cardiopulmonary blood volume) and central venous pressure. Assuming that peripheral and intrathoracic compliance are connected in series in a lumped model, the effective compliance of the intrathoracic vascular bed was obtained from the difference between total and peripheral compliances. This measurement resulted in a value of 0.45 ml/mmHg/kg [170], i.e., about 20% of total vascular compliance. This value is closer to those observed experimentally in animals.

In mathematical models of the human circulation, the vascular compliance, that is, the relationship between stressed volume and the transmural pressure of a vascular segment, is generally represented by either linear or nonlinear relationships that include physical parameters. The values assigned to these

parameters are usually based on experimental evidence of effective compliance and blood volume distribution among different vascular compartments. For example, in the lumped model of the entire circulation proposed by Sun et al. [276], the elastance (the inverse of the compliance) and volume in each vascular territory were estimated from the blood volume distribution in [113]. Ursino et al. [304] proposed a model of the cardiovascular system represented as six lumped compartments arranged in series, which synthesizes the main haemodynamic properties of the systemic arterial, systemic venous, pulmonary arterial, and pulmonary venous, as well as of the left and right cardiac volumes. In that work, a total vascular compliance was assigned based on human and animal TEVC [248], and then this value was distributed among different compartments following literature data on blood flow distribution. Mynard and Smolich [215] adopted a vascular compliance of 170 ml/mmHg for the entire circulation, that was distributed in the following way: 1.7 ml/mmHg in the arterial circulation, following [9], 146 ml/mmHg in the venous circulation, based on [280], and 6.7 and 15.8 ml/mmHg in the arterial and venous pulmonary circulation respectively. The same was done in the previous version of the global mathematical model adopted here [292]. As we can see in these works, mathematical modellers set the total vascular compliance equal to a parameter. However, this parameter value is usually based on the index of TEVC that is the result of an experiment wherein the elastic properties of the vascular system interact with the pumping ability of the heart and the reflex control of blood pressure. This choice is necessary to represent the vascular capacity, that is the amount of blood held by the systemic vascular bed at a specific pressure. However, this assumption could lead to inappropriate results, especially if we move from the baseline status, i.e., the model state for which the model was parametrized and validated.

The aim of this mathematical work was to determine in silico the effective total vascular compliance of a global mathematical model for the cardiovascular system. To this end, we reproduced the experiment of London et al. [171]. Changes in blood volume and changes in central venous pressure were recorded during the infusion. The model used for this kind of test is based on the works in [201, 202, 292]. It is composed of networks of major arteries and veins where blood flow is described by means of a mathematical model consisting of a nonlinear hyperbolic PDE system. This system can be derived assuming axial symmetry of flow [19] or using a more general framework based on mass and momentum balance, as well as a specialized version of Reynolds transport theorem, as proposed in [125]. Other cardiovascular compartments, i.e., heart, pulmonary circulation, microvasculature, venous valves, Starling resistors and cerebrospinal fluid dynamics, are described by lumped parameter models. A high-order well-balanced nonlinear numerical scheme based on the ADER [294] (Arbitrary high-order DERivatives) framework was used for discretization of one-dimensional blood flow equations. Compared to previous versions of the mathematical model, some changes were introduced to better capture the main physiological processes involved in the infusion test as well as to update modelling assumptions that needed to be improved in order to consider a deviation from the baseline state. First of all, we performed a physiologically sound parametrization of the mathematical model in the baseline pre-infusion status: this required the introduction of the unstressed volume in all vascular compartments. Assuming that each vascular compartment has an average pressure, a value of compliance was assigned such that the stressed volume together with the unstressed volume gave the desired total blood volume. As the major part of total blood volume is located in the lumped-parameters model of the venules/distal veins, nonlinear resistances and compliances were introduced in the venous 0D compartments to take into account the distension of the vasculature during volume expansion. Moreover, the global mathematical model of the circulation was coupled to a model for short-term regulation of pressure that considers the activity of high- and low-pressure baroreceptors. Such activity was represented by sigmoid functions, featuring a symmetric response to low/high arterial and/or venous pressure deviations from baseline values, that generate efferent sympathetic and parasympathetic firing rates. Results reported here show that a good parametrization of the vascular compliance and blood volume of the

human body gives a reasonable representation of the vascular capacity in the baseline setting. However, when total blood volume is changed with the infusion test, this parametrization becomes necessary but not sufficient for reproducing the effective behaviour of the human circulation. The main short-term regulatory mechanisms of arterial pressure play an essential role in the capacity of the model to correctly describe experimental results. In fact, TEVC reflects the interaction between the assigned parameters but also the functioning of the regulatory mechanisms.

The rest of the chapter is structured as follows. In Section 5.2, we present the global closed-loop mathematical model of the human circulation and the modifications introduced in this work as well as the baroreflex control mechanism. Section 5.3 presents the main results about the infusion test; the evaluation of the TEVC; and how mean arterial pressure, cardiac output, heart rate, and cardiopulmonary blood volume change during the blood volume expansion; moreover, a discussion on the modelling choices and the main outcomes is provided. Section 5.4 summarizes the main findings and poses some directions for further investigations.

5.2 Methods

In this section, we briefly describe the closed-loop model of the cardiovascular system used in this work, focusing on the main improvements with respect to previous versions of the model. These include the parametrization of the global model with the introduction of total blood volume and the nonlinear relationship in venous resistances and compliances. Moreover, we present the equations that describe the functioning of baroreflex control mechanisms considered in our work and how we performed the infusion test reported in [171].

5.2.1 A global closed-loop model for the human circulation

The mathematical model used in this work is an extension of the closed-loop model for the entire human circulation presented in [201, 202]. It is a geometric multiscale type model which includes one-dimensional models for blood flow in major vessels and zero-dimensional lumped-parameters models describing blood flow in the remaining compartments. Figure 5.1 illustrates schematically the structure of the model: it includes 323 vessels, comprising arteries and veins; four heart chambers and cardiac valves; 3 compartments for the pulmonary circulation; 31 compartmental models describing the connections between terminal arteries and veins through the microcirculation; 17 venous valves; 21 Starling resistors; and one cerebrospinal fluid compartment.

Blood flow in major vessels - arteries and veins - was modelled using a 1D system of partial differential equations. A complete derivation of the governing equations can be found in [94], where such equations were derived from conservation principles. A vessel is represented as a single compliant rectilinear tube with impermeable walls. Moreover, blood is assumed to be an incompressible Newtonian fluid. The resulting system of equations is given by

$$\begin{cases} \partial_t A + \partial_x q = 0 \,, \\ \partial_t q + \partial_x \left(\hat{\alpha} \frac{q^2}{A} \right) + \frac{A}{\rho} \partial_x p = -f \,. \end{cases} \tag{5.2}$$

The first equation representsthe conservation of mass in the flexible tube, while the second one describes momentum balance. The three unknowns of the problem are the cross-sectional area of the vessel's lumen, $A(x,t)$; the blood flow rate across a section of the vessel, $q(x,t)$; and the cross-sectionally averaged internal pressure, $p(x,t)$. $\hat{\alpha}$ is the Coriolis coefficient linked to the velocity profile, here taken equal to 1 to represent a flat velocity profile, ρ is the blood density, and f is the friction force per unit length of the tube. The

FIGURE 5.1: Schematic representation of the global model used in this work [292]. 1D models refer to networks of major arteries and veins, which are modelled using evolutionary partial differential equations, providing space- and time-resolved blood pressure and flow. Rectangles represent lumped-parameter models, which are used to describe the heart chambers, the pulmonary circulation, the microcirculation, as well as intracranial dynamics. Such compartments are modelled using ordinary differential equations, which provide time-resolved haemodynamic variables.

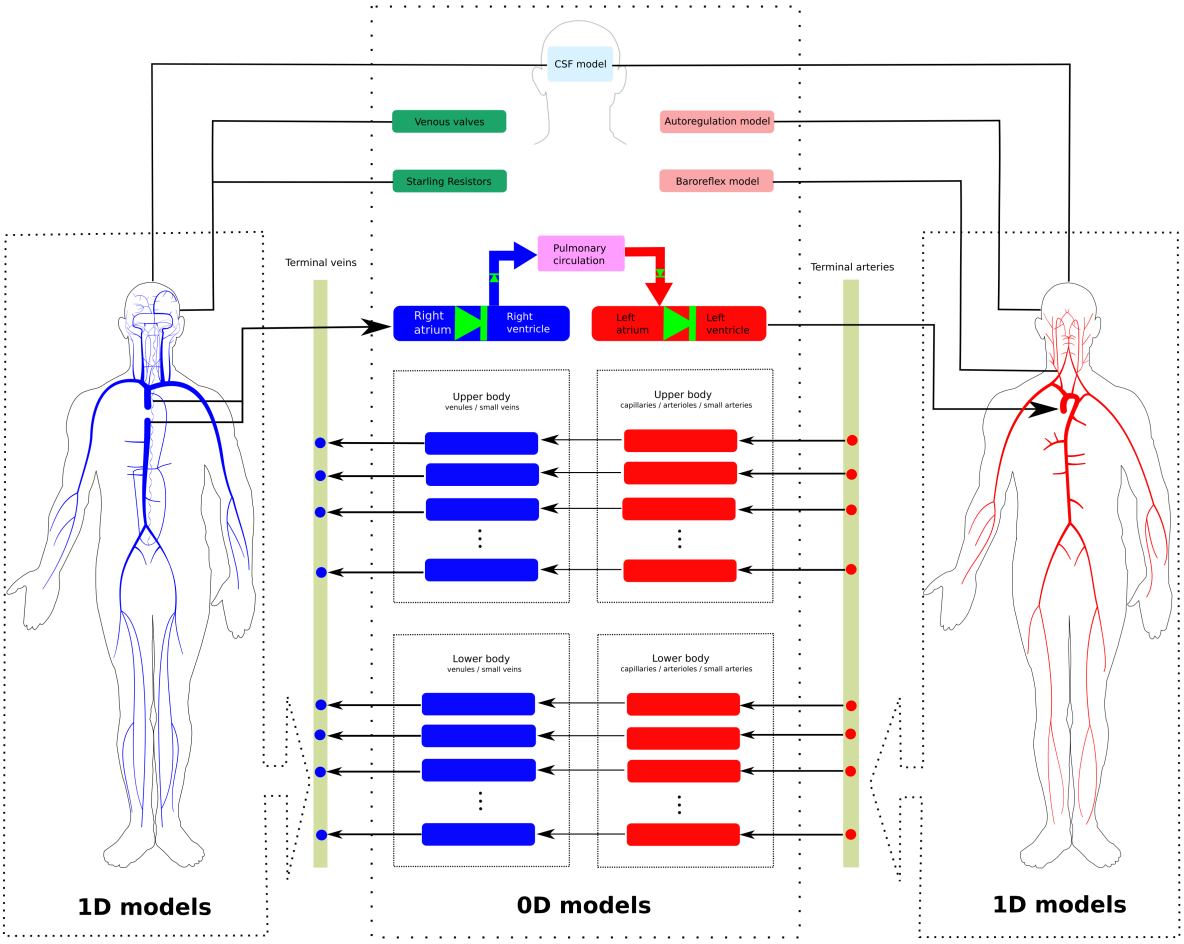

problem has more unknowns than equations, thus an extra closure condition is required. This condition couples the internal blood flow distribution with the mechanical properties of the solid moving vessel wall. We adopted a pressure-area relation which describes the viscoelastic nature of vessels wall

$$p(x,t) = p_{ext}(x,t) + \underbrace{K(x)\left(\left(\frac{A(x,t)}{A_0(x)}\right)^m - \left(\frac{A(x,t)}{A_0(x)}\right)^n\right) + P_0}_{\textit{Elastic term}} + \underbrace{\frac{\Gamma}{A_0\sqrt{A}}\partial_t A}_{\textit{Viscoelastic term}} . \tag{5.3}$$

In this tube law, the internal pressure $p(x,t)$ is expressed as a function of the cross-sectional area $A(x,t)$ and other parameters. The first part of the tube law represents the elastic behaviour of the vessel wall. It depends on $A_0(x)$, the vessel cross-sectional area for which the transmural pressure $(p(x,t) - p_{ext}(x,t))$ is zero. The parameters m and n are two real numbers that can be derived from experimental measurements; throughout this work, we assume $m = 0.5$ and $n = 0$ for arteries, while we assume $m = 10$ and $n = -1.5$ for veins. Moreover, $K(x)$ is a positive function representing the vessel stiffness, which accounts for mechanical and geometrical properties of the vessel; in this work, $K(x)$ was obtained from the reference wave speed c_0 assumed for each vessel, distinguishing arteries, veins, and dural sinuses [292]. P_0 is the reference pressure while p_{ext} is the external pressure, generally prescribed. The second term of the tube law describes the viscoelastic nature of vessel walls; it depends on the time partial derivative of the cross-sectional area of the vessel and on Γ, a constant related to the viscoelastic properties of the vessel wall and expressed, following the work in [7], as

$$\Gamma = \frac{2}{3}\sqrt{\pi}\gamma h_0(x)\,, \tag{5.4}$$

where γ is the wall viscosity and $h_0(x)$ is the wall thickness. The value of these parameters are chosen such that the hysteresis behaviour of pressure-area plots in peripheral arteries and veins reproduces the physiological behaviour. We refer the reader to [292] for more details about the chosen parameters of the viscoelastic term in the tube law.

The friction term $f(x,t)$ on the right hand side, which depends on the local velocity profile, is set as follows

$$f = \frac{8\mu\pi}{\rho}\frac{q}{A}\,, \tag{5.5}$$

with μ being the blood dynamic viscosity. This formulation is obtained by assuming a fully developed laminar flow in an axially symmetric tube.

Note that $A_0(x)$, $K(x)$, and $p_{ext}(x,t)$ are variable material and geometrical parameters that depend on x. To deal with parameters that vary in space, the system in Equation (5.2) is rewritten as in Toro and Siviglia [289, 271], obtaining a 5×5 first-order system whose vector of unknowns is $\mathbf{Q} = [A, q, K, A_0, p_{ext}]^T$. When the tube law in Equation (5.3) is inserted in the momentum balance equation in system (5.2), the problem becomes an advection-diffusion-reaction problem as a second-order spatial derivative of the flow variable arises. Using a relaxation technique [49], one can obtain a nonlinear hyperbolic PDE system that is solved using a high-order well-balanced nonlinear numerical scheme based on ADER [294] (Arbitrary high-order DERivatives) framework for networks of elastic and viscoelastic vessels [197, 199] and an explicit local time-stepping temporal discretization (LTS) approach [207]. We refer the reader to the works in [294, 288] for an up-to-date review of the ADER scheme, to the works in [205, 206] for full details about the high-order well-balanced scheme in the framework of path-conservative schemes, to the works in [295, 197, 199] for clarification about the hyperbolic reformulation of the parabolic system incorporating the viscoelastic nature of the vessel wall mechanics, and finally to the works in [207, 78] for the local time-stepping procedure which is implemented so that the local time step is defined at the level of the vessels (and not computational cells).

Lumped-parameter models for the microcirculation describe the connection between arteries and veins through arterioles, capillaries, and venules; the generic vascular bed model used for all microvasculature beds is based on the three-element Windkessel model. This model is characterized by

- characteristic impedances that couple any number of connecting 1D arteries/veins to lumped-parameter models for the microvasculature (R_{da} or R_{vn}) and regulate the pressure drop between 1D domains and vascular beds,
- peripheral resistances and compliances divided between arterioles (R_{al}, C_{al}) and capillaries (R_{cp}, C_{cp}), and
- venous compartments with related compliances (C_{vn}), which represent venules and distal veins not included in the 1D network.

Figure 5.2 shows an example of a generic terminal vascular beds connecting three 1D arteries and multiple 1D veins.

The heart model considers the 'time-varying elastance' model [160, 276] to describe the dynamics of relaxation/contraction of the four cardiac chambers, while cardiac valves were modelled as in [216]. For each heart chamber, the time-varying elastance $E(t)$ is defined by

$$E(t) = E_A e(t) + E_B \,, \tag{5.6}$$

where E_A and E_B are respectively the maximal elastance at systole and the baseline elastance, while $e(t)$ is the normalized time-varying elastance taken as in [276].

The pulmonary circulation is divided into arteries, capillaries, and veins, and it was modelled as in [276]; each compartment is characterized by a pulmonary resistance and a pulmonary inertance that are used for the evolution of the fluid exchange between compartments and by an exponential pressure–volume relationship describing vascular capacitance. Venous circulation was equipped by venous valves which governs the flow across the interface between two vessels. Starling resistors were placed at the confluence of cortical veins in the dural sinuses; they prevent the vein collapse maintaining the blood pressure upstream the collapsed segment higher than the intracranial pressure. Both venous valves and Starling resistors were represented by the model presented in [216]. Finally, the blood circulation model was coupled to a simple cerebrospinal fluid model. This model, based on the works in [307, 202], is characterized by a simple compartment representing the cranial and spinal cavity with elastic behaviour. An ordinary differential equation which depends on cerebral blood volume (cerebral arteries, arterioles, capillaries, venules, and veins), capillaries, and superior sagittal sinus pressures was used for the evaluation of the intracranial pressure that was then adopted as external pressure in cerebral 1D vessels and lumped-parameters compartments.

The parameters needed for the implementation of the global closed-loop model were defined in order to simulate a young healthy subject. Unless specified otherwise in this work, the parametrization is the same as the one reported in [292]. We refer the reader to the works in [201, 202, 292] for more details about the model description, parameter selection, and validation of the baseline state.

5.2.2 Compliances, unstressed volumes, and total blood volume distribution

As in this work we would like to describe a change in blood volume through an infusion test, we first defined basal parameters describing total blood volume and total vascular compliance. Following the work in [249], the total vascular compliance is ∼2.1 ml/mmHg/kg for humans; ∼70% of this value may characterize the systemic circulation, while the remaining part is ascribed to the pulmonary circulation [244]. Moreover, the systemic vascular compliance may be divided between systemic arterial and venous compliances, assuming that ∼3% of the systemic compliance is in the arterial side [265]. For the pulmonary

TABLE 5.1: Basal value for model parameters of compliance and unstressed volume in the main vascular compartments.

Vascular Territory	Compliance [ml/mmHg]	Unstressed Volume [ml]
Systemic arterial circulation	4	615
Systemic venous circulation	111	2500
Pulmonary arterial circulation	6.56	90
Pulmonary venous circulation	25.37	490
Cardiac circulation		50

circulation, few data are available about the distinction between arterial and venous compliances; we considered here that 20% of total pulmonary compliance is in the arterial side, as in [304]. Table 5.1 reports the compliance value for each vascular territory. As in [292], arterial and venous compliance were distributed in 1D vessels following the work in [160]. Moreover, after determination of 1D vessel vascular compliance, the remaining part of the arterial compliance was distributed among C_{al} in arterioles according to [160] and 15% of the arterioles compliance was assigned to the capillaries C_{cp} (see Figure 5.2). The remaining part of the venous compliance was assigned to venule compartments according to blood flow distribution. For the heart circulation, atria and ventricular baseline elastances were set as in previous works [292].

Total blood volume was reported to be in the range of 75 to 80 ml/kg body weight for a normal male subject [83, 72]. Stressed volume is usually approximately 30–40% of total volume [176, 106]. The unstressed volume is the volume in a compartment when the transmural pressure is equal to zero. In previous version of the model [201, 202, 292], only the stressed component of the total blood volume was considered in lumped-parameters models of the microcirculation, heart, and pulmonary circulation. We added here the unstressed part in order to have complete control on total blood volume.

Using assigned compliances as in Table 5.1 and pressures as in previous works [292], we set for each vascular territories the amount of unstressed volume such that the total blood volume distribution among different vascular compartments follows those reported in the literature. For the heart circulation, we fixed 50 ml of unstressed volume (one sixth of the cardiac blood volume), 20 ml for each atrium, and 5 ml in each ventricle, as suggested in [304, 70]. In the pulmonary circulation, we set 70 ml of unstressed volume, divided between arteries and capillaries, and 490 ml of unstressed volume in venous compartment [70]. Concerning the systemic circulation, we considered 715 ml of arterial unstressed volume, distributed between 1D arteries and arterioles, and 2500 ml of venous unstressed blood that was assigned to capillaries, venules, and 1D veins [70]. In the arterial part, we evaluated the unstressed volume of 1D arteries as the volume in each vessel at zero-transmural pressure according to tube law in Equation (5.3), and then subtracted it to the total amount of arterial unstressed volume; the remaining part was distributed between arterioles compartments of vascular beds according to flow distribution in venous capacitors (C_{vn}, see Figure 5.2). The same was done for the venous circulation; after subtracting 1D venous unstressed volume from total venous unstressed volume, the remaining part was distributed between capillaries (15%) and venules (85%) following the flow distribution in venous capacitors. Table 5.1 summarizes the assigned compliances and unstressed volume distribution.

5.2.3 Nonlinear venous resistances and compliances

In order to take into account the distension of the vasculature during the infusion test, we modified the resistances that characterize the venous vascular beds in a nonlinear manner according to blood volume variation. The resistances that are located between capillaries and venules compartments and the characteristic impedances that couple 1D veins to venules compartment (R_{cp} and R_{vn}, see Figure 5.2) in the

FIGURE 5.2: Example of a generic complex vascular bed connecting three 1D arteries to multiple 1D veins [292]. Each connecting artery can be linked to one or both venous capacitors C_{vn}, while each venous capacitor can be connected to any number of terminal veins. Each 1D artery is connected to arterioles compartments (R_{al}, C_{al}), that in turn is connected to either one or two capillaries compartments (R_{cp}, C_{cp}). The pressure drop between 1D arteries and the vascular beds is regulated by R_{da} while on the venous side by R_{vn}.

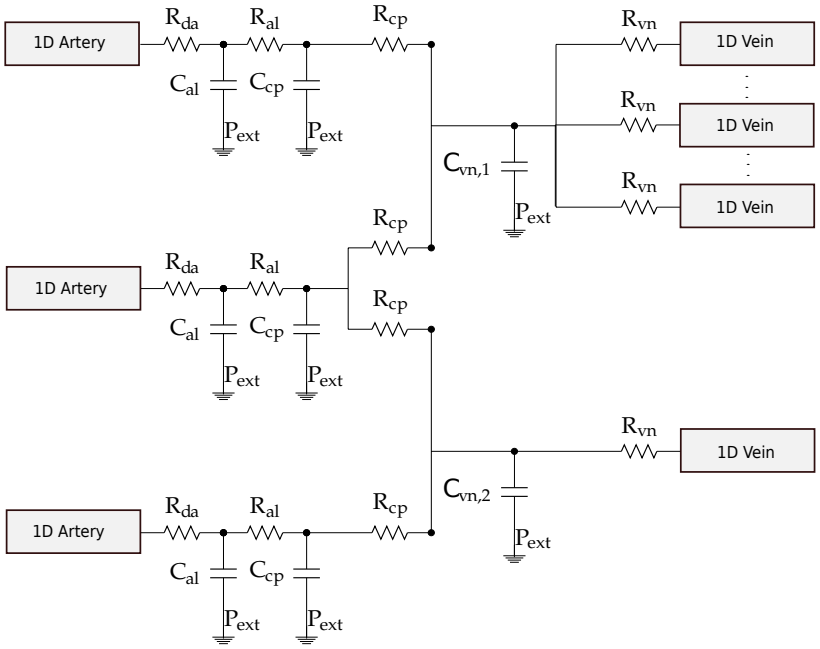

vascular beds were modified at each time step according to the following relationship:

$$R(t) = R_{ref}\left(\frac{V_{ref}}{V(t)}\right)^2, \tag{5.7}$$

where $R(t)$ stands for R_{cp} or R_{vn} at time t, R_{ref} is the corresponding reference resistance in the baseline condition, $V(t)$ is the current volume in the capacitor, and V_{ref} is the reference volume of the venous capacitor at the baseline condition.

In order to account for the nonlinear pressure–volume relation of the venous system during the blood infusion test, we applied a nonlinear pressure–volume relation to zero-dimensional venules compartments. The equation describing this behaviour is the following:

$$P(t) = K\left(\left(\frac{V(t)}{V_{ref}}\right)^m - \left(\frac{V(t)}{V_{ref}}\right)^n\right) + P_{ref} + P_{ext}\,, \tag{5.8}$$

where m and n are set to be 10 and $-3/2$, respectively, as it is usually done for 1D veins. P_{ref} and V_{ref} constitute the basal point of the pressure-volume relationship with the basal value of compliance C_{ref} as in the linear case. The value of the parameter K is assigned by imposing the passage of the curve through P_{ref} and V_{ref}, that is, $\left(\frac{dV}{dP}\right)_{V=V_{ref}} = C_{ref}$. Given this nonlinear pressure–volume relationship, the unstressed volume V_{un} in the venules compartments was modified imposing zero transmural pressure in Equation (5.8). Figure 5.3 compares the linear and nonlinear pressure-volume relation of one venule compartment of the right forearm. As a result of this parametrization procedure we recover the linear compliance case if we set $m = 1$ and $n = 0$.

5.2.4 The baroreflex regulation

The baroreflex model adopted in this work is based on [69, 32, 306]. It includes the activity of high- and low-pressure receptors. The set of parameters undergoing regulation is $\epsilon = \{\ \mathrm{H}, \mathrm{E}_{max}, \mathrm{R}_a, \mathrm{C}_v, \mathrm{V}_u\ \}$, where

FIGURE 5.3: Comparison between linear and nonlinear pressure–volume relationship in one venule/vein compartment of the right forearm. (V_{ref}, P_{ref}) is the basal point of the pressure-volume relationship with linear basal value of compliance C_{ref} and reference unstressed volume V_{un}^{ref}. Following the nonlinear pressure–volume relationship, the unstressed volume V_{un} was calculated imposing zero transmural pressure.

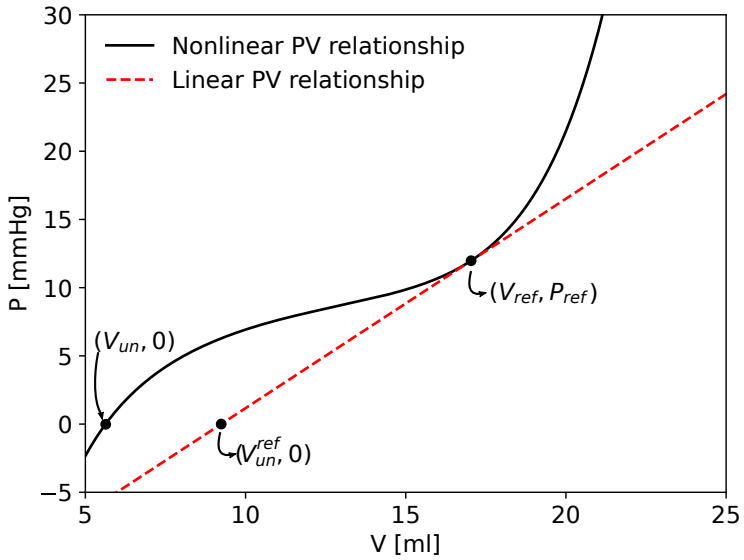

H is the heart rate, E_{max} is the maximum value of elastance of the four cardiac chambers, R_a is the arterial resistance, and C_v and V_u are the venous compliance and unstressed volume (i.e., the venous tone). In our closed-loop model, R_a refers to the proximal resistance of 1D terminal arteries and to the resistance of arteriolar compartment of vascular beds for all vascular districts, except for the brain, which is directly regulated by cerebral autoregulation with the model presented in [292]. C_v and V_u refers to compliance and unstressed volume of venules compartment of non-intracranial vascular beds and 1D veins; changes in compliance and unstressed volume of 1D veins are reflected in variation of reference area A_0 and stiffness K of these vessels, as explained later at the end of this section.

The arterial baroreflex is activated by the mean arterial pressure (over a cardiac cycle) in the aortic arch and in both carotid arteries. We assumed that the receptors located in all these arteries behave in the same manner [32]. The low-pressure baroreceptors are activated by the right atrial pressure. The level of activation of the afferent nervous system is evaluated as

$$\bar{P}_a = \frac{1}{3}(\bar{P}_{rc} + \bar{P}_{lc} + \bar{P}_{aa}) \,, \tag{5.9}$$

$$\bar{P}_v = \bar{P}_{ra} \,, \tag{5.10}$$

where $\bar{P}_{rc}$, $\bar{P}_{lc}$, $\bar{P}_{aa}$, and $\bar{P}_{ra}$ are the mean pressure over the previous cardiac cycle of right carotid artery, left carotid artery, aortic arch, and right atrium, respectively.

Alterations in the arterial pressure $\bar{P}_a$ and/or in the venous pressure $\bar{P}_v$ affect the firing rates of afferent fibers. These fibers reach the central nervous system which in turn generates efferent sympathetic and parasympathetic nerve activity. An enhanced firing rate results in an enhanced parasympathetic response and a reduced sympathetic activity. It was experimentally proved in vagotomized animals that the efferent responses in heart rate and arterial resistances follow a sigmoid relationship. For this reason, the sympathetic and parasympathetic firing rates are modelled via sigmoid functions that depend on arterial and venous pressure changes [69, 32, 306]. The sympathetic and parasympathetic activity are described by the following expressions:

$$n_{s,i} = \frac{1}{1 + e^{y_i/k_i}} \,, \tag{5.11}$$

$$n_{p,i} = \frac{1}{1 + e^{-y_i/k_i}} \,, \tag{5.12}$$

where y_i is a linear combination of pressure changes

$$y_i = g_{a,i}(\bar{P}_a - \mu) + g_{v,i}(\bar{P}_v - \delta) \,, \tag{5.13}$$

and the index i ranges the set ϵ. μ and δ are the baseline arterial and venous activation, respectively. The values of the sympathetic and parasympathetic responses range between 0 and 1; when y_i is equal to 0, i.e., when the model is operating in the baseline setting with $\bar{P}_a = \mu$ and $\bar{P}_v = \delta$, both n_s and n_p assume the value 0.5. n_s approaches 1 when y_i is less than 0 while it tends to 0 when y_i is larger than 1; this implies that the sympathetic nerve activity is reduced when the relative change of arterial and/or venous pressure from the baseline values increases. By contrast, the parasympathetic response n_p assumes its maximum value 1 when y_i tends to infinity. g_a and g_v are the maximum open loop gains of the arterial and cardiopulmonary baroreceptor mechanisms, each evaluated when the other mechanism is not operating. g_v is set equal to zero for all variables in ϵ, expect for R_a and V_u, on which both arterial and low-pressure baroreceptors work in synergism; in this case, the total open loop gain results from a nonlinear superimposition of the action of the two classes of receptors [306]. Finally, k_i is a parameter which determines the slope of the sigmoidal characteristic at its central point, chosen to be equal to -1 as in [306]. The efferent responses are governed by first order ordinary differential equations. These equations read as

$$\frac{dx_i}{dt} = \frac{1}{\tau_i}\left(-x_i + \sigma_i\right) \,, \tag{5.14}$$

where

$$\sigma_i = \alpha_i n_{s,i} - \beta_i n_{p,i} + \gamma_i \,, \quad i \in \epsilon \,. \tag{5.15}$$

τ_i is the characteristic time constant, while α_i, β_i, and γ_i are defined using physiologically admissible threshold values. Table 5.2 reports parameters for the baroreflex model, which were taken from [69, 32, 306]. Following the works in [69, 32], a symmetric response to deviations was assumed by setting minimum and maximum threshold values at equal distance from the central point of the sigmoid function.

The baroreflex regulation changes venous compliance and unstressed volume; in order to maintain constant total blood volume, we reset the venous pressure in 0D venules compartments modifying the reference pressure P_{ref} in Equation (5.8), according to the modified compliance and unstressed volume given by the baroreflex model. The same is done in one-dimensional veins. The venous pressure is reset by changing reference area and stiffness of 1D veins. In each computational cell of a vein, given $\hat{A}_{us}$ and $\hat{C}$ the unstressed area and compliance determined by the baroreflex regulation, the modified reference area $\hat{A}_0$ and vessel stiffness $\hat{K}$ are evaluated solving the following nonlinear system:

$$\begin{cases} \hat{\Psi}(\hat{A}_{us}) + P_0 = 0 \\ \int_0^L \left(\frac{\partial \hat{\Psi}(A)}{\partial A}|_{A=\hat{A}_0} \right)^{-1} dx = \hat{C} \,, \end{cases} \tag{5.16}$$

where

$$\hat{\Psi}(A) = \hat{K}\left(\left(\frac{A}{\hat{A}_0} \right)^m - \left(\frac{A}{\hat{A}_0} \right)^n \right). \tag{5.17}$$

The first equation of system (5.16) is derived from the definition of unstressed area, that is, the area for which the transmural pressure is equal to zero; the second equation relies upon the definition of compliance in a one-dimensional vessel, that is the integral average over the length of the domain of the inverse of the pressure changes with respect to area variation, when area is the reference area of the vessel.

TABLE 5.2: Parameters for the efferent pathways of the baroreceptors and for the arterial and venous gain in Equation (5.15) for all $i \in \epsilon$.

Actuator	τ_i [s]	α_i	β_i	γ_i	$g_{a,i}$ [mmHg^{-1}]	$g_{v,i}$ [mmHg^{-1}]
H	4	1.15	0.34	0.595	0.02	0
E_{max}	10	0.4	0	0.8	0.02	0
R_a	15	0.8	0	0.6	0.02	0.7
C_v	30	−0.2	0	1.1	0.02	0
V_u	60	−0.2	0	1.1	10.8	417

5.2.5 Determination of total effective compliance

The TEVC of the above-described computational model was computed by reproducing in silico the experiment reported in [171]. A 500 ml blood infusion in four minutes was simulated adding a flow source at the level of the left atrium, starting from a periodic solution in the baseline setting. In all the simulations, the infusion started at 80 s and ended at 320 s; after the expansion, the new periodic state was reached in 40 s and the simulations were stopped at 400 s. Main cardiovascular indexes were recorded after completion of the infusion's generated transient, i.e., after a periodic state was reached for the new situation with increased blood volume. During the simulated infusion test, the mean central venous pressure (right atrial pressure) over a cardiac cycle was plotted against changes in total blood volume. The effective compliance was evaluated in the following three scenarios:

(1) Linear case: linear resistances and compliances in 0D venous compartments were applied. The use of linear resistances implies that $R(t) = R_{ref}$ in Equation (5.7) during the entire simulation. With linear compliance, pressure in 0D venules compartments is evaluated with $m = 1$ and $n = 0$ in Equation (5.8); this is equivalent to

$$P(t) = \frac{V(t) - V_{un}^{ref}(t)}{C_{ref}} + P_{ext} \,, \tag{5.18}$$

where V_{un}^{ref} is the unstressed volume of the linear pressure–volume relationship (see Figure 5.3) and C_{ref} is the basal value of compliance in Equation (5.8).

(2) Nonlinear case: in case of nonlinear resistances and compliances in 0D venous compartments, Equation (5.7) was applied for the evaluation of nonlinear resistances, while (5.8) was used for nonlinear compliances.

(3) Baroreflex case: in this case, the model presented in Section 5.2.4 was applied with parameters of Table 5.2 in conjunction with nonlinear resistances and compliances in venules/distal veins compartments.

The numerical results were compared to experimental results reported in [171].

5.3 Results & Discussion

5.3.1 Control of vascular blood volume

The mathematical model adopted in this work departs from the Müller–Toro mathematical model [201, 202, 292] for the systemic and pulmonary circulations in the entire human body. In previous versions of the model, the unstressed component of blood volume was included only in vessels described by one-dimensional models according to the nonlinear relationship between area and pressure described by the

FIGURE 5.4: Total blood volume distribution. In the left pie chart, distribution among different vascular compartments, while in the right frame distribution between stressed and unstressed volume. In square brackets, reference blood volume distribution [113]. Total blood volume is set to be 5520 ml. Arterial blood: 1D arteries and arterioles; Venous Blood: 1D veins and venules; Heart: sum of volume of the four cardiac chambers; Pulmonary circulation: arterial, capillaries and venous blood of pulmonary compartments.

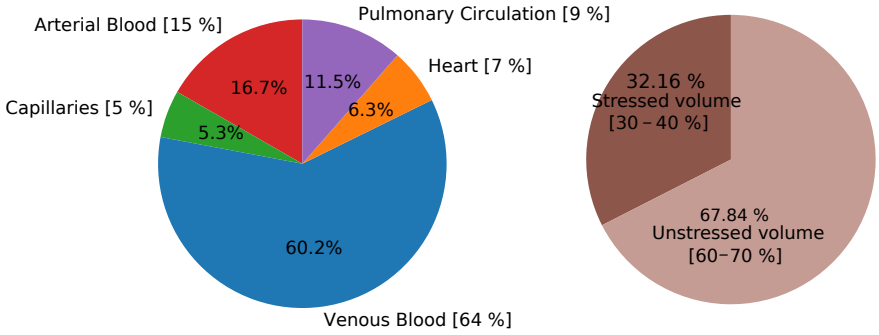

tube law in Equation (5.3). By contrast, in the models for heart, pulmonary circulation, and microvasculature, only the stressed component (that determines flow in the circulation) of blood volume was considered. While this modelling assumption was sufficient in previous applications of the model, in this case a complete control of the total blood volume in the circulation became necessary as we were interested in the total capacitance of the vascular system and the short-term cardiovascular homeostasis. The introduction of the unstressed volumes was generally adopted in fully lumped-parameters models of the circulation [304, 308, 161, 159]. This is the first global model with one-dimensional representation of major arteries and veins with total control of blood volume. The presence of the unstressed volumes in the venous part of the circulation is of primary importance when the baroreflex control of the arterial pressure is considered.

Vascular compliance (for the evaluation of the stressed volumes) and unstressed volume for each vascular territory had to be assigned for the determination of the capacitance of the vascular system. The mathematical model proposed here was parametrized with values of compliances and unstressed volumes based on literature data for humans and animals, as described in Section 5.2.2. Total blood volume was set to 5520 ml, of which about 70% is unstressed blood volume (3745 ml). Figure 5.4 shows the total blood volume distribution in different vascular territories; this distribution agrees with literature observations [152, 113]. The same happens for the main cardiovascular indexes and the pressures of different vascular compartments. Table 5.3 reports main cardiovascular indexes computed on model results and general literature data, as well as London et al. [171]. The first part of the table refers to variables of the systemic circulation, mean arterial pressure, pulse pressure, cardiac output, and central venous pressure. Arterial compliance was evaluated as the ratio between stroke volume and brachial pulse pressure, as routinely performed in clinical practice [9]. We can observe that even if the arterial compliance parameter is assigned to be 4 ml/mmHg (Table 5.1), the effective value of the arterial compliance evaluated as proposed in [9] is in the physiological range. The second part of Table 5.3 shows the main cardiac indexes, heart rate, arterial elastance, left ventricle elastance, arterial–ventricular coupling index, maximum left ventricular volume, and minimum pressure rate of left ventricle. The computed values are in line with literature observations and the model is able to represent a normal functioning heart.

Figure 5.5 shows the relationship between changes in blood volume and changes in central venous pressure for the three scenarios considered here, as well as experimental results reported by London et al. [171]. As in the literature, this relationship is practically linear. The value of TEVC is expressed in brackets in ml/mmHg and then normalized to the body weight, considered to be 75 kg. Even if the physical parametrization of the model concerning compliance distribution and total blood volume was assigned following physiological measurements based on the literature, the TEVC of the computational model is not

TABLE 5.3: Cardiovascular indexes. Current Value: computed numerical value; Ref. Value: literature reference value with mean and standard deviation. (S/D)BP: systolic/diastolic aortic blood pressure; MBP: mean blood pressure; PP: pulse pressure in aortic root and in brachial artery; $PP_{Amplitude}$: ratio between pulse pressure in brachial artery and aortic root; CO: cardiac output; C_a: arterial compliance evaluated as the ratio between stroke volume and brachial pulse pressure [9]; CVP: central venous pressure; H: heart rate; E_a: arterial elastance; E_{es}: left ventricle elastance; E_a/E_{es}: arterial-ventricular coupling index; LV_{max}: maximum left ventricle volume; LV_{EF}: averaged left ventricle volume; max. $\frac{dP_{LV}}{dt}$: maximum pressure rate of left ventricle; min. $\frac{dP_{LV}}{dt}$: minimum pressure rate of left ventricle.

Index	**Current Value**	**Ref. Value**	**Ref.**
SBP [mmHg]	107.48	$105 \pm 8, 129 \pm 3$	[191, 171]
DBP [mmHg]	76.18	$71 \pm 7, 76 \pm 2$	[191, 171]
MBP [mmHg]	91.19	$89 \pm 8, 97 \pm 2$	[191, 171]
PP_{Aorta} [mmHg]	31.31	30 ± 6	[191]
$PP_{Brachial}$ [mmHg]	38.01	49 ± 9	[191]
$PP_{Amplitude}$ [mmHg]	1.21	1.7 ± 0.14	[191]
CO [ml/s]	88.64		
C_a [ml/mmHg]	1.91	1.7	[9]
CVP [mmHg]	4.21	4.2 ± 0.8	[171]
H [beats/min]	75	76 ± 4	[171]
E_{es} [mmHg/ml]	4.61	4.5	[218]
E_a [mmHg/ml]	2.80	2.3	[218]
E_a/E_{es}	0.60	0.58	[218]
LV_{max}	116.66	150 ± 67	[215]
LV_{EF}	0.62	0.68 ± 0.12	[215]
max. $\frac{dP_{LV}}{dt}$	1511.27	1915 ± 410	[215]
min. $\frac{dP_{LV}}{dt}$	-2632.04	-2296 ± 530	[215]

FIGURE 5.5: Computed TEVC by means of an infusion test of 500 ml of blood in 4 min. Changes in mean central venous pressure are plotted against changes in total blood volume and the inverse of the slope of their linear relationship is the value of the effective compliance. C_{Linear}: linear relationship for resistances and compliances in venules compartments; $C_{Nonlinear}$: nonlinear resistances and compliances in venules compartments; $C_{Baroreflex}$: nonlinear resistances and compliances and baroreflex control; $C_{Literature}$: London et al. [171] experimental results on 9 controls subjects (mean value of the group and $\pm$ 1 standard deviation).

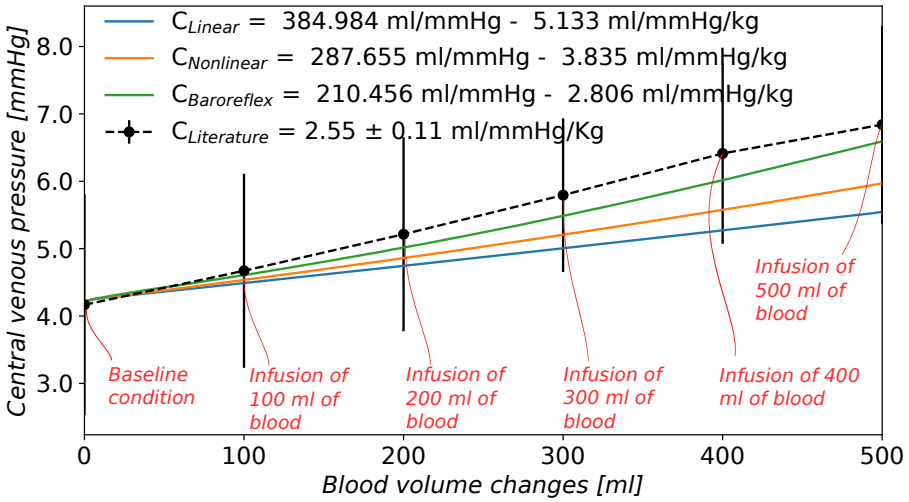

comparable to literature data if one considers the model setup with linear venule resistance and compliance and no baroreflex (Figure 5.5): 5.13 ml/mmHg compared to 2.55 ± 0.11 ml/mmHg in [171], 2.7 in [99], and 2.3 in [82]. A reasonable value of TEVC can be reached changing the physical parameter for the venous compliance. According to sensitivity analysis not reported here, venous compliance and unstressed volume are the main determinants of the TEVC of the global model in case of linear resistances and compliances and without regulation; variations in these parameters could improve the effective behaviour of the mathematical model. Reducing the compliance of the systemic venous circulation from $C_v = 111$ ml/mmHg to $C_v = 36$ ml/mmHg and the total blood volume to 4800 ml, the resulting TEVC was 2.7 ml/mmHg when we considered linear resistances and compliances in the venous lumped parameters compartments and we neglected the autonomic nervous system control by the baroreceptors. In this case, the capacitance of the vascular system was changed by modified venous compliance, i.e., stressed volume, without changes in unstressed volume. With this setting, the unstressed volume was 78% of total blood volume, while the blood distribution between vascular compartments was the following: 19.3% of arterial blood, 6.1% of blood in capillaries, 53.7% of venous blood, 7.3% of blood in cardiac circulation, and 13.2% in lungs. In the baseline condition, the mean arterial pressure and cardiac output were 92.53 mmHg and 90.87 ml/s, respectively, while the baseline central venous pressure was 4.28 mmHg. We observed that this parametrization led to a physiological status of the mathematical model in the baseline setting, and the numerical effective compliance was comparable to the literature. However, the changes in main cardiovascular indexes during the infusion were unreasonable: the mean arterial pressure and the cardiac output increased by more than 35% and the cardiopulmonary blood volume changed by 25%. Even if the baroreflex control was activated, the authors did not find physiological parameters for the baroreflex model that were able to control the main cardiovascular indexes as in [171]. These observations highlight the importance of including both, realistic physical parameters, appropriate mathematical models for physical processes and relevant physiological processes regarding the adaptation of the cardiovascular system to deviations from baseline conditions. These elements are essential in order to reproduce experimental observations that imply large deviations of

the model with respect to the baseline condition for which the model was parametrized (and/or conceived).

5.3.2 Nonlinearities in venous compartments

Another modelling improvement of this work regards the introduction of nonlinear equations for the determination of venous resistances and compliances. As shown in Figure 5.5, when linear venous compliances and constant resistances were considered, the computed TEVC was higher with respect to experimentally measured compliance. During the infusion test, the central venous pressure evaluated in the right atrium increased by 1.3 mmHg, while in terminal veins and venules compartments, the change in venous pressure was twice the one observed in central veins. Echt et al. [82] evaluated changes in central and peripheral venous pressures during infusion of 500 ml of 6% dextran solution within 3 min. The central venous pressure was recorded in the right atrium while the peripheral pressure was measured in a vein in the distal third of the left forearm. The central venous pressure rose from 6.6 mmHg to 9.8 mmHg after infusion of 500 ml of blood while the peripheral venous pressure increased from 10.2 mmHg to 12.9 mmHg. A comparable increase in pressure was measured in both vascular locations. During the infusion test, the increased blood volume distends the blood vessels, thus reducing their resistance and the resistance to venous return. Guyton et al. [111] studied the effect of blood transfusion or hemorrhage on the venous return curve. The slope of the curve which relates venous return and right atrial pressure is a measure of the resistance to venous return; the more vertical the slope, the less is the resistance to the return of blood to the heart. In dogs, it was observed that blood transfusion modified the slope of the venous return-right atrial pressure relation: increased blood volume distended the blood vessels and hence it decreased the resistance to blood flow. These considerations lead to the introduction of a nonlinear relationship between compartment volume and resistance of the post-capillary compartments. Vessel resistance is proportional to the inverse of radius to the power four and volume is proportional to the radius squared; thus, for a given vessel length, volume behaves as the inverse square root of the resistance; according to Equation (5.7), if the volume increases with respect to the reference volume, the resistance will decrease. This kind of relation was previously used by [234] to describe the biomechanics of the arterial–arteriolar cerebrovascular bed, while in [60] it was used also for the venous cerebral compartments. In [292], this relation was adopted to describe changes in cerebral arterial vasculature caused by an autoregulation model. In this work, we applied this nonlinear relation between resistance and volume to all venous compartments. The use of nonlinear resistances in venous compartments decreased the effective compliance of the mathematical model of the human circulation by 18.8% (from 5.133 ml/mmHg/kg to 4.168 ml/mmHg/kg).

According to the work in [244], the relationship between total contained volume in the vasculature and the transmural pressure is nonlinear. As most of the total blood volume is contained in the venous circulation, a good approximation of the behaviour of the venous compartments is essential for obtaining reasonable results in the determination of TEVC. The 1D venous network adopted in this work contains all the main large veins. However, most of the venous blood volume and the larger portion of venous compliance were assigned to the 0D compartments which represent venules/distal veins. For this reason, a nonlinear relationship between volume and pressure based on 1D veins tube law was applied to 0D venous compartments. The law that represents venous compliance (Equation (5.8)) is such that the actual compliance is similar to the reference linear compliance in baseline volume condition. If the volume in the compartment is higher than the reference volume, the transmural pressure evaluated according to the nonlinear pressure–volume relationship will be higher with respect to linear compliance case. Ursino et al. [304] showed how the nonlinear behaviour of the relationship between pressure and volume influenced the computational results on the hemorrhage test; the use of linear pressure–volume curves is acceptable provided that moderate blood volume changes are simulated. As pointed out by Drees and Rothe [75], the use of linear compliances is probably adequate in the physiological pressure range, but in the context of highest blood volume changes the extrapolation of the results may produce unacceptable errors. The

FIGURE 5.6: Comparison between linear and nonlinear resistances and compliances of venule compartments. C_{Linear}: linear relationship for resistances and compliances in venules compartments; $C_{NonlinearR}$: nonlinear resistances in venule compartments (Equation (5.7)); $C_{NonlinearC}$: nonlinear compliances in venule compartments (Equation (5.3)); $C_{Nonlinear}$: nonlinear resistances and compliances in venules compartments; $C_{Literature}$: London et al. [171] experimental results on 9 controls subjects (mean value of the group and $\pm$ 1 standard deviation).

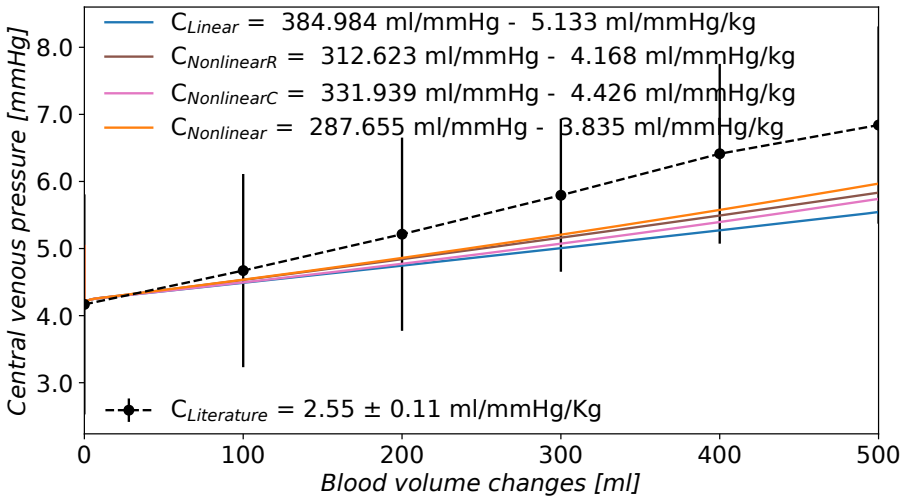

presence of nonlinear compliances in venous compartments improved the computational effective compliance by 13.78% (from 5.133 ml/mmHg/kg in linear case (1) to 4.426 ml/mmHg/kg). Compared to the case of nonlinear resistances, the sensitivity of the effective compliance to nonlinear compliances is lower than to nonlinear resistances. When both resistances and compliances are nonlinear, the effective compliance improved from 5.133 ml/mmHg/kg in scenario (1) to 3.835 ml/mmHg/kg in scenario (2). Figure 5.6 compares the computed effective compliance in case of: linear resistances and compliances of venule compartments (scenario (1)), variable resistances according to volume variation and linear compliances, constant resistances and nonlinear compliances, nonlinear resistances and compliances (scenario (2)). It can be observed that when both resistances and compliances are nonlinear, the computed effective compliance is closer to the literature value of TEVC.

5.3.3 Baroreflex

London et al. [171] performed the infusion test of 500 ml of 6% dextran within 4 min in 9 control patient in supine position. They found that an increase in total blood volume changes the mean arterial pressure by 3%. Even if the study was carried out in the shortest possible time, short-term cardiovascular regulation is considered to play a role in maintaining arterial blood pressure. Figure 5.7 shows the variation in main cardiovascular indexes during the expansion compared to London's data (mean error and standard deviations) [171]. The variables under consideration are mean arterial pressure (MAP), cardiac output (CO), heart rate (HR), and cardiopulmonary blood volume. Heart rate is evaluated as the inverse of the duration of the cardiac cycle while cardiopulmonary blood volume is the sum of blood in heart and lungs. Mean arterial pressure and cardiac output increased by more than 20% (23.20% and 22.72%, respectively) in case of linear venules resistances and compliances. The increment in these quantities was even higher in the case of nonlinear venules resistances and compliances. The cardiopulmonary blood volume increased by 16.07% during the infusion test. Computational results revealed the need for baroreflex control to limit the changes in mean arterial pressure. The baroreflex represents the main neural mechanism involved in short-term regulation of arterial pressure. Two categories of baroreceptors can be distinguished according to their location: high-pressure arterial baroreceptors and low-pressure baroreceptors (also known as

FIGURE 5.7: Changes in haemodynamic parameters before and after expansion. Comparison between computational results for scenario (1) with linear resistances and compliances, scenario (2) with nonlinear relationship in venous compartments, and scenario (3) with nonlinearities and baroreflex control. Computed results are compared to literature data from [171]. Parameters under consideration are MAP, mean arterial pressure; CO, cardiac output; H, heart rate; CPBV, cardiopulmonary blood volume.

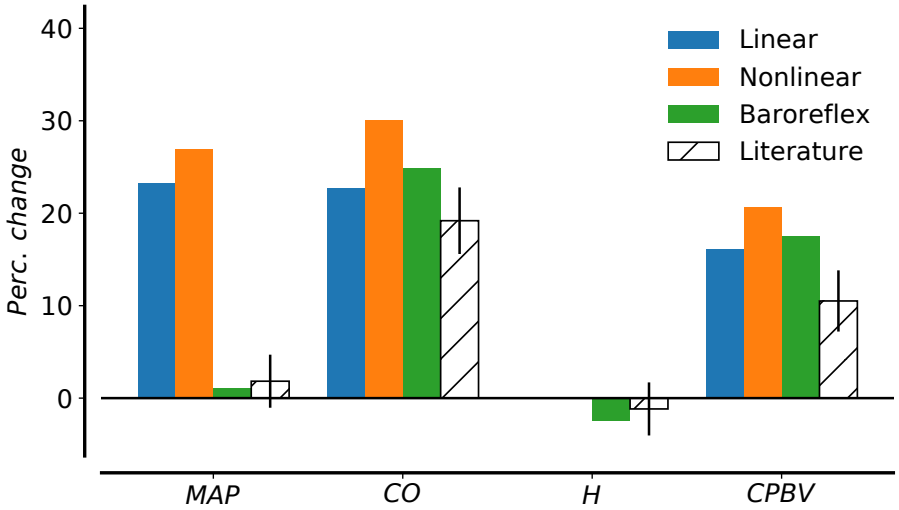

cardiopulmonary or volume receptors). The first group of baroreceptors is located in the carotid arteries and the aortic arch, and they are activated by a variation in systemic blood pressure. Afferent signals will then be processed; the response to deviations from a nominal state will be conveyed by efferent fibers and ultimately result in changes in vascular resistance, heart rate and cardiac contractility and venous tone. Cardiopulmonary receptors compose an heterogeneous group of sensors [237]. Despite their heteromorphism, cardiopulmonary receptors tonically inhibit the vasomotor center in analogy to arterial baroreceptors. Low-pressure baroreceptors are located in large systemic veins and the atria of the heart (at the junction of the venae cavae and the pulmonary veins). They act on arterial resistance, venous tone, and heart rate [180]. These low-pressure receptors minimize arterial pressure changes when the blood volume variation is too small to be detected by high-pressure receptors; they activate reflexes parallel to the arterial baroreflexes to ensure a stronger control of arterial pressure. Moreover, they participate in the control of renin release and vasopressin secretion, with effects on salt and water retention, production of urine and long-term control of arterial pressure. However, as the goal of this chapter was to simulate an infusion of blood in four minutes, only the short-term pressure regulation by high- and low-pressure baroreceptors was considered.

In this work, the mathematical function representing the nervous responses for both high- and low receptors was a sigmoid function, which ranges between the low and high saturation values symmetrically with respect to the baseline central point. It was experimentally proved in anesthetized dogs [62] that the firing rate of high-pressure receptors acted in an asymmetrical way in response to increasing or decreasing carotid pressure, like in an hysteresis loop. Moreover, this asymmetry was more evident in the parasympathetic activity than in the sympathetic one [237]: the parasympathetic firing rate response is faster when the blood pressure increases than in response to a decrease in pressure. For simplicity, the asymmetrical behaviour of the firing rate was neglected in this work; however, other mathematical models of the baroreflex activity considered the asymmetry of the firing rates, in particular in the control of the heart rate, where the parasympathetic nerve activity plays a role [229, 242].

The control of heart rate by atrial receptors is called the Bainbridge reflex. In 1915, Bainbridge [18] reported that if 200 to 400 ml of blood or saline was injected into a 10 kg dog over a period of 1.5 to 4 min then its heart rate increased; this increase did not seem to be tied to arterial blood pressure because the

heart rate rose regardless of whether arterial blood pressure changed, but it increased whenever central venous pressure increased sufficiently to increase ventricular end-diastolic pressure and cause ventricular dilation. The Bainbridge reflex occurs especially if the initial heart rate is low [244]; on the other hand, with more rapid heart rate, the infusion ordinarily slows the heart. Several studies have failed to demonstrate a Bainbridge effect in humans [281]. This reflex might be poorly developed or less sensitive in humans than in dogs, thus species-dependent. Moreover, a 10% volume expansion stimulates also the aortic receptors; it has been shown that the reflex generated by aortic receptors was able to reverse the tachycardic Bainbridge reflex into a bradycardic response [244]. The resulting effect could maintain constant heart rate. In view of these considerations, we applied the effects of cardiopulmonary receptors to arterial resistance and venous unstressed volume, neglecting the Brainbidge reflex on the heart rate, in agreement with work done in [306]. According to the sigmoid function, which describes the heart rate variation by means of the sympathetic and parasympathetic activity from arterial baroreceptors, the assumption of omitting the low-pressure receptors control of heart rate may lead to insignificant changes in heart rate if the changes in arterial pressure are small.

Mathematical models of human cardiovascular system [32, 303, 69] were applied to study the effects of short-term regulation of arterial pressure during hemorrhage. These works included only the high-pressure baroreceptors which were sufficient to appropriately control the arterial pressure. We performed an hemorrhage test for the validation of the parameters of the arterial baroreflex model, obtaining reasonable results in comparison with animals and humans data [123, 143], as well as other mathematical models [69]. There is literature evidence on the activation of cardiopulmonary receptors when there are variations in total blood volume. Gupta et al. [108] demonstrated in dogs that the firing rate from the low-pressure receptors decreased in proportion to the loss of blood volume, concluding that the low-pressure receptors are primarily responsible for the reflex maintenance of arterial pressure. Abboud et al. [1] stressed that both arterial pressure and cardiac filling pressure increase with expansion of blood volume and activate the arterial baroreceptors as well as cardiopulmonary baroreceptors with vagal afferents. The mathematical model presented in Section 5.2.4 was first validated for a hemorrhage test; even if the underlying model with high-pressure receptors alone was able to reproduce physiological variation in mean arterial pressure during hemorrhage test, this was not the case for the infusion test. According to a sensitivity analysis study, arterial resistance is positively correlated to arterial pressure while negatively correlated to right atrial pressure. This means that a decrease in arterial resistance might decrease the arterial pressure and increase the central venous pressure. Therefore, the effect of the baroreflex control on arterial resistance is twofold: it helps controlling the arterial pressure during the infusion and it increases the central venous pressure, decreasing the total effective compliance. As reported in [171], the infusion test did not significantly change the arterial pressure, so the variation in arterial resistance might be due to the action of the low-pressure receptors. Figure 5.8 compares the percentage change in mean arterial pressure and other cardiovascular indexes during the infusion test under the action of either high-pressure baroreceptors ($g_{v,i} = 0$ for all $i \in \epsilon$) or low-pressure receptors alone ($g_{a,i} = 0$ for all $i \in \epsilon$). In the first case, the mean arterial pressure increases by 9%, leading to 20% variation in heart rate. On the contrary, under the action of the low-pressure receptors alone, the value of the mean arterial pressure is almost equal to the pre-infusion one due to the variation in arterial resistance and venous unstressed volume. When the two types of receptors work together, the mean arterial pressure increases only by 1.03% after the volume expansion; the cardiac output and the cardiopulmonary blood volume increase by 24.11% and 16.98%, respectively, while the heart rate decreases by 2.44% (as shown in Figure 5.7). As blood volume is infused in the circulation, the pressure in carotid arteries and aortic arch increases and activates the sympathetic control of the high-pressure baroreceptors; the low-pressure receptors are in turn activated by changes in right atrial pressure. The variation in arterial resistance and the unstressed volume was modified mainly by the receptors in the low-pressure

FIGURE 5.8: Changes in haemodynamic parameters before and after expansion. Comparison between simulation with high-baroreceptors alone ($g_{v,i} = 0$ for all $i \in \epsilon$) and simulation with complete baroreflex control with both high- and low-pressure receptors. Computed results are compared to literature data from [171]. Parameters under consideration are MAP, mean arterial pressure; CO, cardiac output; H, heart rate; CPBV, cardiopulmonary blood volume.

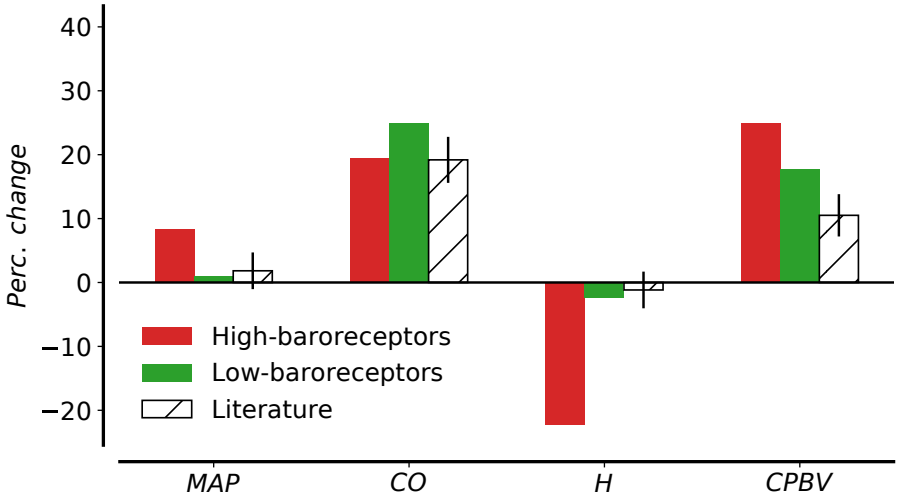

system while the other variables undergoing regulation remain almost constant during the infusion, as we see in the efferent responses (Figure 5.9). The 39% variation in arterial resistance increased the right atrial pressure up to 6.3 mmHg, decreasing the TEVC to 2.806 ml/mmHg/kg. This change in arterial resistance is such that the variation in total systemic vascular resistance evaluated as ratio between mean arterial pressure and cardiac output reflects the one observed in [171].

Concerning the unstressed volume, few data are available about the entity of changes in venous tone during infusion or hemorrhagic events. Even if there are several techniques for the determination of body venous tone, all of them present technical limitations; in whole animals, information on body venous tone or capacitance cannot be obtained with intact cardiovascular reflex system. The MCFP method was used for the evaluation of whole body venous tone or venoconstrictor influence; however, this method is unable to obtain reliable readings of compliance and unstressed volume. First, the amount of unstressed volume was linearly extrapolated from the blood volume/MCFP relationship; however, this relies on the assumption that there is a linear volume–pressure relationship, but this is not generally valid. Moreover, changes in blood volume activate cardiovascular reflexes that modify the unstressed volume, which in turn initiate other regulatory mechanisms. The volume/MCFP relationship has been obtained in animals with suppressed autonomic reflex [299] and even then the effects of vasoactive agents, such as angiotensin II, vasopressin or endothelium-derived relaxing and contracting factors modified the volume of blood, leading to over- or underestimation of changes in compliance and/or unstressed volume. There is evidence that a change in blood volume induced a larger change in unstressed volume than compliance [75]. Echt et al. [82] measured venous tone in the arm during blood volume changes by means of venous occlusion plethysmography in the left forearm. Using forearm volume and pressure, the volume elasticity coefficient at an intravenous pressure of 15 mmHg was used as measure of venous tone. Their observations failed to reveal changes in venous tone with moderate ($\pm$10%) changes in central blood volume; they did not excluded the possibility of venous tone variation, probably these changes took place in other parts of the capacitance system. Figure 5.9 shows the percentage alteration of the parameters controlled by the baroreflex model during blood infusion. The venous compliance remained almost constant during the infusion, while the unstressed volume varied by less that 10%, according to venous pressure changes and the threshold and saturation points given by previous works [306]. From literature evidence, it is difficult to establish the real

FIGURE 5.9: Efferent response of the baroreflex model during the volume expansion evaluated at the beginning of the cardiac output by a first order differential Equation (5.14). Infusion starts at 80 s and it ends at 320 s. The parameters undergoing regulation are H, heart rate, E_{max}, maximum elastance of cardiac chambers, R_a, arterial resistance in terminal arteries and arterioles' compartments, C_v, venous compliance, V_u, venous unstressed volume.

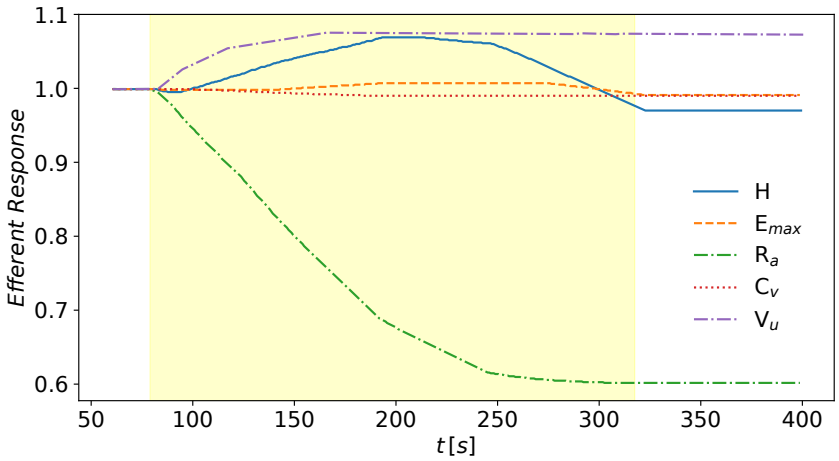

variation of unstressed volume or compliance per se, without combining the baroreceptors activity with other reflex control mechanisms. However, we are aware that such variation in unstressed volume is necessary to control the mean arterial pressure and cardiac output as in the physiological experiment, especially when other cardiovascular regulatory system are not taken in consideration. The local sensitivity analysis (not reported here) of the principal parameters of the global mathematical model with linear relationship for resistances and compliances and without baroreflex control revealed that the venous unstressed volume is one of the major determinants of computed mean arterial pressure and mean central venous pressure. Both arterial and venous pressures were negatively correlated to venous unstressed volume; an increase of 20% in venous unstressed volume caused a decrease of 10.11% in mean arterial pressure and 13.32% in mean central venous pressure.

5.4 Conclusions

A mathematical model of the human circulation was used to estimate the TEVC of a mathematical model for human circulation, evaluating the changes in central venous pressure with respect to changes in blood volume during an infusion test. In order to perform this experiment the original model was modified. The main changes regarded (i) the introduction of total blood volume, including both stressed and unstressed volume, (ii) the parametrization of vascular compliance and its distribution between different vascular compartments, (iii) the use of nonlinear pressure-volume relations for venule compartments, and (iv) the use of resistances for capillaries and venules featuring a nonlinear dependence from compartment volume. We showed that a physiological parametrization of the mathematical model, in particular the assignment of physical compliance and unstressed volume in different vascular compartments, is necessary but not sufficient for obtaining a TEVC in agreement with experimental data. In fact, major physiological mechanisms must be considered, such as, for example, the short-term control of arterial pressure by baroreceptors which is crucial for obtaining modelling results that are in agreement with observed variations in mean arterial pressure, cardiac output, heart rate, and cardiopulmonary blood volume during the infusion test.

As we pointed out previously, other reflex mechanisms are activated to control volume homeostasis and to re-establish baseline cardiovascular variables after blood volume changes. Increased blood volume leads to increased cardiac output, which in turn increases the capillary pressure; due to the capillary fluid shift mechanism, fluid starts to flow out of the circulation through the tissue capillary walls to readjust the blood volume. Moreover, increased venous pressure gradually distend the veins by the reflex called stress-relaxation; the venous blood reservoirs (the unstressed volume in the liver and spleen) distend or contract, modifying the mean systemic pressure. Finally, excess blood flow in the peripheral tissues activates autoregulatory mechanisms of blood flow control. This kind of local control occurs within seconds to minutes and provide rapid regulation of tissue blood flow by means of local vasodilation or vasoconstriction of small terminal vessels (arterioles and pre-capillaries), thus modifying the peripheral vascular resistance and resistance to venous return. Drees and Rothe [75] measured variation in mean circulatory pressure at 0.5, 2, and 5 min after randomized changes in blood volume in dogs; they showed the reflexogenic control of vascular capacity evaluating the changes in effective compliance with time. They concluded that the compensation after about 30 s was mostly from passive viscoelastic creep and fluid shifts; less than half of the compensation for hemorrhage during the first 5 min came from the stress-relaxation venoconstriction. Even if the infusion considered in this work was performed in the shortest possible time, four minutes are long enough to start reflex mechanisms other than the baroreflex control. This is one of the main limitations of the present work. In future work, all these mentioned mechanisms should be taken into account to better represent the physiology of this infusion test. This will imply the introduction of a model for solute transport that permits to study the transcapillary fluid shift during the infusion experiment.

London et al. [169, 248] showed the strong positive relationships between compliance and cardiopulmonary, interstitial and extracellular fluid volumes. As demonstrated by animal experiments and by immersion in man, the filling pressure of the heart is monitored through cardiac mechanoreceptors controlling renal function, extracellular fluid volume and thirst via the autonomic nervous system. Thus, even if the effective compliance was evaluated by an infusion within four minutes, a complete control of the volume in the circulation should be obtained only if other body fluid compartments are added to the mathematical model and the main regulatory mechanisms that participate in the long-term regulation of arterial pressure are included. This link with other body fluids was stressed in the evaluation of effective compliance in arterial hypertensive patients. It has been shown [248, 249, 169, 170] that hypertensive patients are characterized by decreased TEVC, mainly in the venous compartment, due to complex haemodynamic abnormalities with alterations in main fluid volume control mechanisms. A decreased venous compliance could increase the cardiac output, causing the activation of regulatory mechanisms that modify the total peripheral resistance; this could be an initiating factor in hypertension. Future work will focus on the estimation of the effective compliance in the context of remodelling that is cause/consequence of arterial hypertension.

A further aspect that leaves room for improvement is that of local autoregulation. Previous versions of this model included the myogenic response of cerebral autoregulation. In this work, we did not consider the local control, but a global regulation of venous resistances. One should differentiate regulation with local mechanisms to brain and heart and global control to the remaining vascular territories, as proposed in [8]. Finally, note that even if the short-term control of arterial pressure by baroreceptors adopted in this work produced results in agreement with experimental observations available in the literature, an aspect that could be addressed in future developments is to consider a more refined baroreflex model that would account for the asymmetrical response of receptors and that would be able to generate an hysteresis loop for the nervous receptors activity, first of all in the cardiac regulation.

While the parametrization of the mathematical model provided in this work and the consequent adaptation of the cardiovascular system to the infusion test might not be totally accurate, especially because of

lack of experimental data available for model parametrization, we believe that the results presented here should contribute to raise awareness about the difference of effective and physical parameters, as well as about the need to enrich the set of physiological processes that models like the one considered here need to incorporate, especially if large deviations from the baseline model state are to be described.

Chapter 6

Major determinants of essential hypertension: a computational study based on a closed-loop model for the human circulation

6.1 Introduction

Arterial hypertension is by far one of the most important sources of morbidity and mortality in the world [226]. It affects approximately 40-45% of the world population aged >25 years (1.13 billion in 2015 [179]) with a global age-standardized prevalence of 24 and 20% in men and women, respectively [179]. Moreover, hypertension becomes progressively more common with advancing age, with a prevalence > 60% in people aged > 60 years. As populations age and adopt more sedentary lifestyles, prevalence of hypertension continues to rise and is expected to affect more than 1.5 billion people by 2025 [179]. It has been estimated that complications of hypertension account for 9.4 million deaths worldwide every year [226]; examples of hypertension-related diseases are ischaemic heart disease, heart failure, atrial fibrillation, chronic kidney disease, peripheral artery disease, stroke and cognitive decline, to name but a few. The recent COVID-19 pandemic has posed particular attention on possible risks associated to hypertension. The available evidence is consistent overall in suggesting that hypertension increases the risk of acquiring SARS CoV-2 infection, admission to intensive care units, severe disease and mortality. Whether these increased risks were independent of other risk factors, however, has not been fully elucidated [227].

Essential, or primary, or idiopathic hypertension is historically defined as a rise in blood pressure; according to the guidelines of the European Society of Hypertension [179], hypertension is defined as an office systolic blood pressure > 140 and/or diastolic blood pressure > 90 mmHg, which is equivalent to a 24 h ambulatory blood pressure monitoring average of > 130/80 mmHg or a home blood pressure monitoring average of > 135/85 mmHg. Blood pressure can be highly variable, hence the diagnosis of hypertension should not be based on a single office measurement (unless blood pressure is substantially increased), but on repeated office blood pressure measurements during a number of visits and/or out-of-office blood pressure measurement using 24 h ambulatory or home blood pressure monitoring. Moreover, depending on the severity of blood pressure elevation, the assessment of the presence of other cardiovascular risk factors (such as dyslipidaemia and metabolic syndrome) or hypertension-mediated organ damage (such as left ventricle hypertrophy, chronic kidney disease or advanced retinopathy) are necessary to establish the severity in the progression of arterial hypertension. Multiple risk factors for high blood pressure have been identified, including genetic variations, obesity, insulin resistance, high alcohol intake, and stress. When a

potential cause of high blood pressure is identified (especially in people with young onset of hypertension), it is referred as secondary hypertension. However, hypertension is a highly heterogeneous disorder with a multifactorial aetiology and its cause remains enigmatic in 95% of cases [39]. While precise causes of increased arterial blood pressure are rarely determined, it was demonstrated that lowering blood pressure can substantially reduce premature morbidity and mortality [179]. There are two well-established strategies to reach this goal: lifestyle interventions and antihypertensive drugs. Lifestyle modifications include increased physical activity, weight control, sodium restriction, alcohol moderation, healthy eating, and smoking cessation; all these factors delay the onset of drug therapy. Two general classes of drugs are used to treat hypertension: vasodilator drugs that relax the smooth muscle cells to reduce systemic vascular resistance and natriuretic or diuretic drugs that decrease tubular reabsorption of salt and water to reduce blood volume; ACE inhibitors, ARBs, calcium channel blockers, and thiazide or thiazide-like diuretics are usually recommended as drug treatment. Despite the evidence of treatment benefit, fewer than half of all hypertensive patients have adequately controlled blood pressure. Poor patient adherence to treatment (especially when based on multiple pills) is now recognised as the major factor contributing to poor blood pressure control [179].

The body is endowed with many interrelated arterial pressure regulating mechanisms. Each one of them performs a specific function to provide both short-term and long-term arterial pressure regulation [113, 112]. The first line of reaction against acute changes in arterial pressure is the nervous control system; this class of regulatory mechanisms that respond in seconds to pressure changes includes the baroreceptor feedback mechanism, the central nervous system ischaemic mechanism and the chemoreceptor mechanism. The nervous mechanisms act on constriction/dilation of most peripheral arterioles, on contractility of the heart and on vein reservoir properties to almost instantly reset arterial pressure into a normal range. After few minutes following acute arterial pressure changes, other mechanisms are activated: the renin-angiotensin vasoconstrictor mechanism, stress-relaxation of the vasculature, and shift of fluid through the tissue capillary walls in and out of the circulation to readjust the blood volume as needed. The long-term (over days, months, and years) pressure regulation is achieved mainly by kidney's mechanisms through renal-body fluids pressure-volume control and its interaction with other factors, such as the renin-angiotensin system with the aldosterone mechanism. How these regulatory mechanisms contribute in the development and progression of the hypertensive disease remains subject of debate [112, 233].

In this unclear and board scenario, computational models can be a practical approach to better quantifying the haemodynamic effects of cardiovascular properties in this medical condition. An early, seminal contribution in this field is due to Guyton in the early 70s [112], which was concerned with the system analysis of arterial pressure regulation and hypertension. The model presented in [112] consists of several hundred algebraic and ordinary differential equations that incorporate the main ingredients of the vascular system, their interaction with extracellular fluid volume and detailed regulatory mechanisms. The original Guyton's model includes many simplifications, that were mandatory to accommodate a large number of cardiovascular relationships and to create a model that requires a reasonable computational cost. From the pioneering Guyton's contributions, other mathematical models have been developed to provide a more comprehensive representation of the entire circulation and its control by other influences, including the central nervous system [137, 136, 3]. Other approaches in mathematical modelling of arterial hypertension focused on particular districts of the cardiovascular system. An example was proposed by Segers et al. [261], who studied heart-arterial interaction in hypertension-induced left ventricular hypertrophy using a left ventricle time-varying elastance model coupled to a 4-element lumped parameter model of the systemic arterial system. One-dimensional models of the arterial system have been widely employed to study arterial haemodynamics under various pathophysiological conditions; this kind of models are suitable for

studying wave propagation phenomena under ageing and hypertensive conditions. Two exemplary papers along these lines are [157] and [53]. In the first one, the hypothesis that increased pulse wave reflection and altered backward waveform morphology contribute to increased pulse pressure in subjects with higher pulse pressure was tested with the help of numerical modelling (55-segment 1D arterial network model) to confirm the interpretation of the experimental results. In the second paper, one-dimensional computational modelling was used to provide a database of arterial pulse waves to span a range of cardiovascular conditions, representative of a population of healthy adults. Another example was due to Blanco et al. [30]. In that work, an Anatomically Detailed Arterial Network (ADAN) model was used to study the role of hypertension in cerebral small vessel disease; model parameters were modified to consider structural changes in arterial vessels in the hypertensive scenario. All these 1D models are open-loop and do not consider the closed-loop case. A first step in this direction was proposed by Liang [158]; as pointed out by the authors of that work [158], mechanical, structural and functional changes may occur in the entire cardiovascular system as a cause or consequence of hypertension, hence traditional 1D models are not sufficient to well describe the remodelling due to hypertension. In this framework, Liang et al. [158] proposed a multiscale model which integrates the main cardiovascular components prone to alterations in hypertension (such as the heart, large arteries, distal arteries and arterioles) into a unique computational framework that enables to explore the determinant cardiovascular factors for haemodynamic variables of concern in the treatment of hypertension. The model provided by Liang et al. includes a one-dimensional network for major arteries, structured-tree models for small arteries and arterioles while other cardiovascular components are described by zero-dimensional models, included the venous circulation, which is represented by two compartments, one for the upper-body and another one for the lower-body. The role played by venous system changes was not explored.

In the present work, we use a global closed-loop mathematical model for the entire human circulation to investigate the hypertensive condition. Such a model departs from the original Müller-Toro model, firstly proposed in 2014 [201, 202] and then improved in 2021 [292]. It is a geometric multiscale type model which includes one-dimensional models for blood flow in major vessels and zero-dimensional lumped-parameters models describing blood flow in the remaining compartments. It includes 323 vessels, comprising arteries and veins; four heart chambers and cardiac valves; 3 compartments for the pulmonary circulation; 31 compartmental models describing the connections between terminal arteries and veins through the microcirculation; 17 venous valves; 21 Starling resistors. Moreover, it is coupled to a simple model based on [307] which describes the intracranial pressure as function of the cerebral blood volume; this intracranial pressure serves as external pressure of all the intracranial districts. Concerning physiological control systems, this global mathematical model incorporates a cerebral autoregulation model, which aims at maintaining adequate and stable cerebral blood flow during changes in blood pressure working on dilatation or contraction of arterioles and capillaries [305, 234], and a model for short-term regulation of pressure, which considers the activity of high- and low-pressure baroreceptors [32, 51]. Figure 6.1 summarizes schematically the structure of the work. Based on clinical studies, we reproduce computationally the structural changes that are causes and/or consequences of high-blood pressure. There is clinical evidence showing that the hypertensive setting does not affect only large arteries, but also the microcirculation, the heart, the pulmonary circulation and the 'low-pressure' system (the venous circulation). This requires to change our model parameters to reflect how the cardiovascular system adapts to this new state. Using a global closed-loop model allows us to establish the interplay between different blood compartments and to have a more complete description of the role played by different hypertension-induced/inducing alterations of the baseline setting in the determination of arterial pulse pressure.

FIGURE 6.1: Schematic representation of the global model of the circulation and its adaptation in hypertensive condition. 1D model refers to networks of major arteries and veins, which are modelled using evolutionary partial differential equations, providing space- and time-resolved blood pressure and flow. Rectangles represent lumped-parameter models, which are used to describe the heart chambers, the pulmonary circulation, the microcirculation, as well as valves, Starling resistors and intracranial pressure dynamics. Two regulatory systems are also incorporated: cerebral autoregulation and baroreflex control. Such compartments and regulatory processes are modelled using ordinary differential equations (0D model), which provide time-resolved haemodynamic variables.

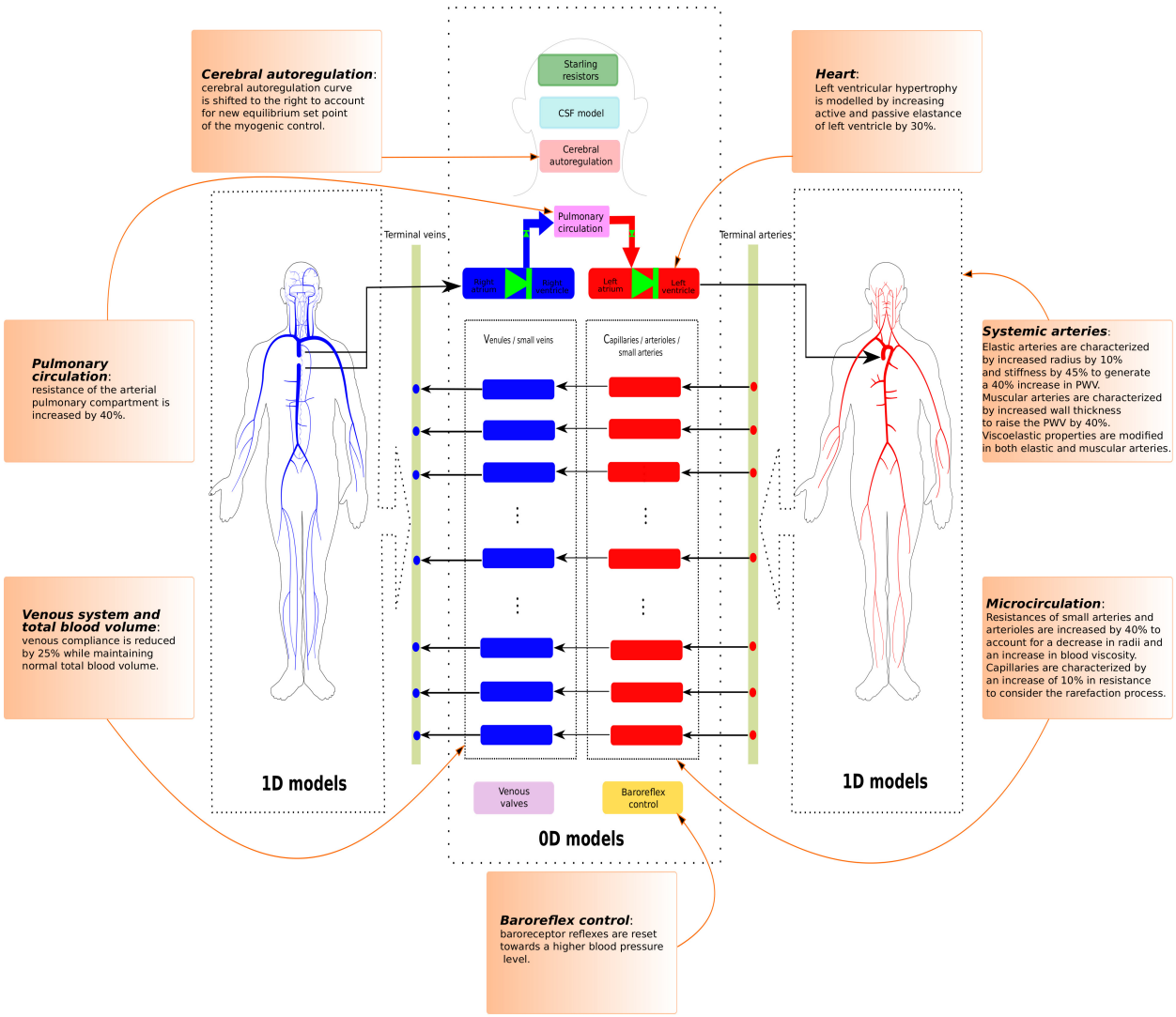

The rest of the chapter is structured as follows. Section 6.2 summarizes the main features of the cardiovascular model on which this work is based and then it describes the modifications on the model parameters to simulate the hypertensive condition. Section 6.3 presents main computational results on normotensive and hypertensive conditions. Computed data are validated and discussed with respect to clinical measurements reported in the literature; moreover, an assessment of the effects of remodelling in different cardiovascular districts is performed to better quantify their role in the progression of the disease. Finally, Section 6.4 includes concluding remarks with comments on limitations and possible future works.

6.2 Methods

In this section, we present the global closed-loop mathematical model of the entire human circulation and its adaptation to arterial hypertension remodelling. All the main ingredients of the global model were described in detail in previous works and are here briefly summarized. We refer the reader to [201, 202, 292, 51]. Concerning the remodelling due to hypertension, we describe how the model parameters are changed based on clinical measurements reported in the literature.

6.2.1 Mathematical model of the cardiovascular system

We model blood flow in the entire human circulation by means of a geometric multiscale type model which includes one-dimensional averaged models for major vessels and compartmental models for the remaining components.

Arteries and veins Blood flow in major vessels, arteries and veins, is modelled using a 1D system of partial differential equations based on averaging the incompressible Navier-Stokes equations over the vessel's cross-sectional area. The resulting system expressing conservation of mass and balance of momentum is given by

$$\begin{cases} \partial_t A + \partial_x q = 0\,, \\ \partial_t q + \partial_x \left(\hat{\alpha} \frac{q^2}{A} \right) + \frac{A}{\rho} \partial_x p = -f\,. \end{cases} \tag{6.1}$$

The three unknowns are $A(x,t)$, the cross-section's area of the vessel's lumen, $q(x,t)$, the blood flow rate and $p(x,t)$, the cross-sectionally averaged internal pressure. $\hat{\alpha}$ is the Coriolis coefficient linked to the velocity profile, here taken equal to 1, ρ is the blood density and f is the friction force per unit length of the tube. To close the system, we adopt a pressure-area relation which aims the viscoelastic nature of vessels wall

$$p(x,t) = p_{ext}(x,t) + \underbrace{K(x)\left(\left(\frac{A(x,t)}{A_0(x)}\right)^m - \left(\frac{A(x,t)}{A_0(x)}\right)^n\right) + P_0}_{\textit{Elastic term}} + \underbrace{\frac{\Gamma}{A_0\sqrt{A}}\partial_t A}_{\textit{Viscoelastic term}}\,, \tag{6.2}$$

where $A_0(x)$ is the vessel cross-sectional area at equilibrium, $K(x)$ the vessel stiffness, P_0 the reference pressure, p_{ext} the external pressure. Γ is a constant related to the viscoelastic properties of the vessel wall and it is chosen following [7], as

$$\Gamma = \frac{2}{3}\sqrt{\pi}\gamma h_0(x)\,, \tag{6.3}$$

where γ is the wall viscosity and $h_0(x)$ is the wall thickness. The value of these parameters are chosen such that the hysteresis of pressure-area plots in peripheral arteries and veins reproduces physiological observations. We refer the reader to [292] for more details about the chosen parameters of the viscoelastic term in the tube law. The vessel stiffness accounts for mechanical and geometrical properties of the vessel and it is obtained from the reference wave speed c_0 assumed for each vessel, distinguishing arteries, veins,

and dural sinuses [292]. For arteries, this wave speed is computed as proposed by Olufsen et al. [225], namely,

$$c_0^2 = \frac{2}{3\rho}(k_1 \exp(k_2 r_0) + k_3) \ , \tag{6.4}$$

where r_0 is the artery's radius at the reference configuration, k_1, k_2 and k_3 are empirical constants and are taken to achieve normal wave speeds in the large vessels for a young adult human and a reasonable increase in smaller vessels. We set $k_1 = 3 \times 10^6 \ g/s^2/cm$, $k_2 = -7 \ cm^{-1}$ and $k_3 = 40 \times 10^4 \ g/s^2/cm$. The parameters m and n are two real numbers that can be derived from experimental measurements; throughout this work, we assume $m = 10$ and $n = -1.5$ for both arteries and veins. In previous versions of this mathematical work [201, 292, 51], we usually assumed $m = 0.5$ and $n = 0$ for arteries; generally one needs to choose $m > 0$ and n in $[-2, 0]$ in order to preserve desirable mathematical properties of the PDE system [289]. However, in [63], direct estimation of m and n in ovine and human arteries revealed that values of m greater than 4 and values of n smaller than -0.4 are more appropriate for the representation of the hyperelastic nature of the vessels wall and their collapsing behaviour; real vessels tend to become stiffer as deformations grow, which is not satisfied if the value $m = 0.5$ is adopted. Since we are interested in hypertension remodelling and hence vessels' deformations over a wide blood pressure range, we believe that more realistic values of these constants need to be used.

When the vessel wall viscoelasticity is incorporated in the model, a second-order spatial derivative of the flow variable in the momentum balance equation arises, turning the problem into an advection-diffusion-reaction problem. Using a relaxation technique, firstly proposed by Cattaneo [49], we obtain a non-linear hyperbolic PDE system that is solved using a high-order well-balanced non-linear numerical scheme in space and time based on the ADER (Arbitrary high-order DERivatives) [294] finite volume scheme [197, 199, 295, 205, 206] and a local time stepping (LTS) approach [207, 78], which is implemented so that the local time step is defined at the level of the vessels. We refer the reader to the works in [294, 288] for an up-to-date review on ADER schemes, to the works in [205, 206] for full details about the high-order well-balanced scheme in the framework of path-conservative schemes, to the works in [295, 197, 199] for clarification about the hyperbolic reformulation of the parabolic system incorporating the viscoelastic nature of the vessel wall mechanics, and finally to the works in [207, 78] for the local time-stepping procedure.

Microcirculation Lumped-parameter models for the microcirculation describe the connection between arteries and veins through arterioles, capillaries and venules; the generic vascular bed model used for all microvasculature beds is based on the three-element Windkessel model. This model is characterized by

- characteristic impedances that couple any number of connecting 1D arteries/veins to lumped-parameter models for the microvasculature (R_{da} or R_{vn}) and regulate the pressure drop between 1D domains and vascular beds;
- peripheral resistance and compliance divided between arterioles (R_{al}, C_{al}) and capillaries (R_{cp}, C_{cp});
- venous compartment characterized by a nonlinear pressure-volume relation with related compliance (C_{vn}) at its basal point [51].

Moreover, the resistances that are located between capillaries and venules' compartments and the characteristic impedances that couple 1D veins to venules' compartment (R_{cp} and R_{vn}) are nonlinearly related to blood volume variation as described in [51].

Heart and pulmonary circulation The heart model uses the 'time-varying elastance' model [160, 276] to describe the dynamics of relaxation/contraction of the four cardiac chambers, while cardiac valves are modelled as in [216]. For each heart chamber, the time-varying elastance $E(t)$ is defined by

$$E(t) = E_A e(t) + E_B \,, \tag{6.5}$$

where E_A and E_B are respectively the maximal contractility at systole and the baseline elastance, while $e(t)$ is the normalized time-varying elastance taken as in [276].

The pulmonary circulation is divided into arteries, capillaries and veins; each compartment is characterized by a pulmonary resistance and a pulmonary inertance that are used for the evolution of the fluid exchange between compartments.

Venous valves and Starling resistors Venous circulation is equipped with venous valves. Starling resistor models are placed at the confluence of cortical veins in the dural sinuses and they prevent the vein collapse maintaining the blood pressure upstream the collapsed segment higher than the intracranial pressure. Both venous valve and Starling resistor are represented by ideal diodes using the model presented in [216].

Total blood volume Since total blood volume is of primary importance in the determination of arterial pressure, it is crucial to include a total blood volume control in the global model. To this end, we consider both the stressed and unstressed component of blood volume in both 1D vascular networks and lumped-parameters models for the microcirculation, heart and pulmonary circulation. The unstressed volume is the volume in a compartment when the transmural pressure is equal to zero, while the stressed volume creates an elastic recoil pressure that is an important factor in the generation of blood flow and depends on the vascular compliance of a specific compartment. The reader is referred to [51] for a comprehensive description of the blood volume distribution between different vascular districts, which includes assignment of compliances and unstressed volume.

Cerebrospinal fluid model The blood circulation model is coupled to a simple cerebrospinal fluid model. This model, based on [307, 202], is characterized by a single compartment representing the cranial and spinal cavity with elastic behaviour allowing for volume changes. Variations in cerebral blood volume produce fluctuations in intracranial pressure.

Cerebral autoregulation Cerebral autoregulation is a mechanism which aims to maintain stable cerebral blood flow despite changes in arterial pressure. Three key mechanisms, the myogenic, metabolic and neurogenic, play a role in the cerebral autoregulation. The myogenic process refers to the active behaviour of the vasculature in response to changes in arterial blood pressure; changes in strain of the walls of the small arteries results in vasoconstriction or vasodilatation, hence modifications in the resistance to blood flow. The metabolic response results from any local mismatch between supply and demand for oxygen while the neurogenic response is the least well understood since sympathetic activity has been proved to be the hardest both to interpret and to measure [235]. In this work, cerebral arterial circulation is controlled by a cerebral autoregulation model which works on resistances and compliances of terminal arteries, arterioles and capillaries compartments in response to changes in cerebral blood flow. The action of myogenic regulation includes a static gain and first-order low-pass dynamics. An increase in cerebral blood flow causes vasoconstriction, with consequently decrease in compliance and increase in resistance of cerebral arterioles/capillaries. The regulatory response is modelled by a sigmoidal static relationship with upper and lower levels which account for limited vasodilatation and vasoconstriction capacities [292, 305, 234].

Baroreflex control The baroreceptor system is one of the major short-term pressure regulation mechanisms. Baroreceptors in carotid arteries in the neck and in the arch of the aorta are stimulated by stretch of the arterial wall due to alterations in arterial blood pressure, while low-pressure baroreceptors are activated by the right atrial pressure. Alterations in the arterial pressure and/or in the venous pressure affect the firing rates of afferent fibers; such rates are modelled via sigmoid functions that depend on arterial and venous pressure changes [69, 32, 306]. The averaged responses mediated by the sympathetic and parasympathetic systems are a combination of pressure changes. Baroreflex acts on heart rate, maximum value of elastance of the four cardiac chambers, arterial resistance (which comprises proximal resistance of 1D terminal arteries and resistance of arteriolar compartment of vascular beds for all vascular districts, except for the brain), and venous compliance and unstressed volume (i.e., the venous tone) of venules compartment of non-intracranial vascular beds and 1D veins. A detailed description of the model and how it is incorporated in the present global model can be found in [69, 32, 51].

Parametrization of the model The parameters needed for the implementation of the global closed-loop model are defined in order to simulate a young healthy subject. Unless specified otherwise in this work, the parametrization is the same as the one reported in [292] and [51]. We refer the reader to the works in [201, 202, 292, 51] for more details about the model description, parameter selection, and validation of the baseline state.

6.2.2 Hypertensive scenario

Pathophysiological studies have extensively investigated the remodelling and functional changes in hypertension. Here, we modify our model in order to reproduce main changes experienced by the cardiovascular system for the hypertensive condition. As previously said, this medical condition is more prevalent in middle-aged and old patients; during 2015-2016 in United-States [97], the prevalence of hypertension was 29.0% and increased with age: age group 18-39, 7.5%, 40-59, 33.2% and 60 and over, 63.1 %. Therefore, we focused on middle-aged untreated subject with mild to moderate hypertension (systolic pressure 130-159 mmHg, diastolic pressure 85-99 mmHg) and we adjusted the model parameters according to observations reported in the literature. Main modifications involve large arteries stiffness, peripheral resistance of small arteries and arterioles, decrease in capillary density, left ventricular hypertrophy of the heart and distensibility of the venous system.

Large arteries remodelling Large arteries alterations associated with hypertension may involve both structural and mechanical properties of arterial wall. Moreover, ageing mainly affects large arteries by the arteriosclerosis process [191, 189]. The remodelling due to ageing and hypertension is not homogeneous along the aortic tree. Arteries can be subdivided into two types: elastic and muscular; the first group has relatively large diameters and are located close to the heart (thoracic aorta, common carotid artery, aortic root), while muscular arteries are located at the periphery (femoral, brachial, and radial arteries). It has been observed that elastic arteries of hypertensive subjects are characterized by an increase in intima-media thickness and lumen enlargement [43, 148, 85]. On the other hand, muscular arteries are characterized by increased thickness but no change in lumen diameter; moreover, the elastic response is maintained despite hypertrophy of the arterial wall [150]. In view of this evidence, we divide the network of arteries into elastic (along the aortic branch) and muscular vessels. According to [150], the ratio between wall thickness and internal radius increases by 40 % in muscular peripheral arteries while it is not significantly changed in elastic arteries [43]. On the contrary, the elastic modulus increases by 45% in elastic arteries and remains unchanged in the other group. Radius of elastic arteries increases by 10% since it was proved that aortic root size increases with ageing [84]; in order to maintain normal ratio between wall thickness and

internal radius, the wall thickness increases proportionally. These modifications do not affect the stiffness $K(x)$. However, since we are interested in middle-aged hypertensive subjects, the intrinsic stiffness of elastic arteries is augmented due to the ageing process. This physiological behaviour is translated into the mathematical model in order to generate a 40% increase in pulse wave velocity. For muscular arteries we consider an augmented wall thickness for the evaluation of the stiffness $K(x)$ to match the carotid-femoral pulse wave velocity increase by 40%.

In this work, we are considering a viscoelastic behaviour of the vessels wall, which depends on Γ; this parameter describes the viscoelastic properties of the wall and it is proportional to the vessel wall thickness, as described in Eq. (6.3). Therefore, in the hypertensive scenario, we increase Γ for both elastic and muscular arteries proportionally to the increase in wall thickness.

Microcirculation Vasoconstriction, eutrophic remodelling with increased media-to-lumen ratio, decreased vasodilation reserve, and rarefaction characterize small resistance arteries in patients with essential hypertension [148]. According to the literature, the main site for structural elevation of resistance is the proximal part of the microcirculation; for this reason, R_{da} and R_{al} increase by 40 % to account for a decrease in small vessel radii of about 7-8 % and an increase in blood viscosity [153, 148, 187, 243]. On the other hand, the capillaries, that are crucially important for local flow distribution, are partly protected from pressure elevation by a raised resistance upstream. Resistance vessels ensure that the mean intra-capillary pressure remains within a tightly controlled range well below the arterial level for preservation of the structural integrity of the fragile capillary wall. Therefore, R_{cp} increases by only 10 % in order to consider the reduction of capillary density that characterizes the ageing process [153, 129].

Heart and pulmonary circulation Elevated systemic load induced by hypertension lead to left ventricular hypertrophy in the heart. Enlargement and thickening of the heart muscle of the left ventricle maintain the systolic wall stress at normal values despite increased load. Both active and passive elastance increases by 30 % to match literature data [261].

Concerning the heart rate, there is no appreciable difference between the normo- and hypertensive patients. McEniery et al. [190] reported an heart rate of 69 $\pm$ 12 beats/minute in an healthy group of 5648 patients and 70 $\pm$ 12 beats/minute in an hypertensive group of 3420 subjects. Abdelhammed at el. [2] found that normal subjects (19 people) have an heart rate of 68 $\pm$ 12 beats/minutes while hypertensive patients at stage I of the disease (systolic blood pressure 140-159 mmHg, diastolic blood pressure 90-99 mmHg) with uncontrolled blood pressure (44 subjects) have an heart rate of 70.6 $\pm$ 10.6 beats/minutes. They also observed that heart rate tended to be higher in the pre-hypertensive group, but this difference was not statistically significant. For this reason, the same cardiac cycle duration (0.8 s) has been adopted for simulations of both the normotensive and hypertensive subjects.

As in the systemic circulation, the arterial pulmonary pressure and resistance increase in hypertension. Hence, the resistance of the arterial compartment of the pulmonary circulation increases by 40% [224, 175]. On the other hand, pulmonary compliance remains unchanged since it was observed that intrathoracic vascular compliance is comparable between normotensive and hypertensive patients [170, 249].

Total blood volume and vascular compliance It has been observed that total intravascular volume is normal or decreased in hypertension [175]. In contrast, human and animal studies revealed that vascular compliance is reduced [171, 169, 170, 168, 247, 248, 251]. In view of these considerations, we set up the same total blood volume in both normotensive and hypertensive subjects while venous compliance is reduced by 25 %. Increased stiffness in 1D arteries leads to decreased total arterial compliance. Hence, the parameter for total arterial compliance, which includes both 1D arteries compliance and arterial miscovasculature

compliance, is modified such that the arterial part of the vascular beds is characterized by the same compliance of the normotensive case. For the assessment of the total effective vascular compliance, we perform a blood infusion test of 500 ml in four minutes in normotensive and hypertensive context, following the experimental procedure proposed in [82, 171]. We refer the reader to [51] for a complete discussion on how to perform this test, the mathematical modelling implications and a comparison with the existing literature in normotensive case.

Regulatory systems Hypertension results in chronic adaptation of the cerebral circulation to higher levels of blood pressure, such that the autoregulated curve of cerebral blood flow is shifted to the right with respect to the setting point used for normotensive individuals [58]. This implies that, if blood pressure is lowered to a level that would be safe in nonhypertensive individuals, the brain would be more susceptible to hypoperfusion. This right shifting of the autoregulation curve, first described in animals model and then verified in a limited number of hypertensive individuals, has been attributed to the increase in vascular resistance induced by remodelling in cerebral resistance vessels [58]. In our model, we reproduce the shift of this curve resetting the baseline values of arterial resistances and volumes to the hypertensive status determined by means of a simulation in the hypertensive scenario without the action of regulatory mechanisms.

The same happens with the baroreceptors regulation. According to literature data [212], the baroreceptor reflexes are reset towards a higher blood pressure level. Therefore, the baseline levels of activation for both high- and low-pressure baroreceptors are reset to the new hypertensive states, evaluated by means of a simulation in the hypertensive scenario without the action of regulatory mechanisms. Moreover, the baroreflex seems to operate with reduced sensitivity in hypertension; there is evidence that this occurs in sustained hypertensive patients and it is secondary to elevated blood pressure rather than playing a role in early stage of the disease [212]. Since we are considering a mild to moderate class of hypertensive subjects, we do not consider this aspect.

6.3 Results & Discussion

In this section, we report and discuss the main computational results comparing normotensive and hypertensive states. The discussion focuses on large and small arteries remodelling, the heart in hypertension, total blood volume, effective vascular compliance and the venous system in hypertension. Computational results, as well as the modelling assumptions to obtain them, are compared and discussed with respect to existing literature. The final part of this discussion compares the effects of the remodelling in different compartments of the cardiovascular system, one by one; this analysis could be helpful in understanding which cardiovascular elements are more significant in the determination of arterial pressure.

6.3.1 Large and small arteries remodelling

The first part of this discussion assesses the arterial circulation, which comprises 1D arteries and 0D arterioles and capillaries. Table 6.1 shows main cardiovascular indexes linked to arterial circulation; we refer to systolic, diastolic, mean and pulse pressure in brachial, carotid and aortic arteries, as well to pulse pressure indexes (augmentation index and pulse pressure amplification), pulse wave velocities and arterial compliance index. Computed values in normotensive and hypertensive subjects are compared with literature data. In the hypertensive scenario, systolic, diastolic and mean blood pressures values in brachial, carotid and aortic arteries well reproduce the pressure rise that was clinically observed in patients at stage I of the disease. Figure 6.2 compares the computed waveforms over a cardiac cycle along the aorta and major arteries of the lower limb in normotensive and hypertensive subjects. Cardiac-cycle averaged pressure

values are reported for each analysed arteries above the corresponding plot in Figure 6.2; a comparable increase in mean arterial pressure can be observed along the aortic tree.

TABLE 6.1: Cardiovascular indexes: comparison between normo- and hypertensive subject. (S/D)BP: systolic/diastolic blood pressure; MBP: mean blood pressure; PP: pulse pressure; cf-PWV: carotid-femoral pulse wave velocity; baPWV: brachial-ankle pulse wave velocity; Augmented P: augmented pressure; C_a index: total arterial compliance index [2]. Details on how to evaluate these indexes can be found in the Appendix B.

Index	**Normotensive**		**Hypertensive**		**Ref.**
	Value	**Ref. Value**	**Value**	**Ref.Value**	
Brachial SBP [mmHg]	111.52	115 ± 11	162.98	153 ± 22	[43]
Brachial DBP [mmHg]	73.14	71 ± 7	90.41	99 ± 10	[43]
Brachial MBP [mmHg]	89.74	86 ± 8	124.28	119 ± 12	[43]
Brachial PP [mmHg]	38.38	38 ± 2.8	71.24	49 ± 1.7	[232]
Carotid SBP [mmHg]	109.46	118 ± 14	162.84	166 ± 24	[43]
Carotid DBP [mmHg]	73.59	70 ± 7	91.14	95 ± 12	[43]
Carotid PP [mmHg]	35.96	48 ± 15	71.70	71 ± 24	[43]
Aortic SBP [mmHg]	108.15	108 ± 12	161.72	140 ± 17	[190]
Aortic DBP [mmHg]	74.05	75 ± 8	91.61	88 ± 11	[190]
Aortic PP [mmHg]	34.10	33 ± 10	70.10	52 ± 17	[190]
Augmented P [mmHg]	3.72	7 ± 7	12.56	16 ± 10	[190]
Augmentation Index [%]	10.91	18 ± 18	17.91	28 ± 14	[190]
$PP_{Amplification}$	1.12	1.44 ± 0.25	1.03	1.30 ± 0.2	[190]
cfPWV [m/s]	9.27	8.5 ± 1.5	14.21	11.8 ± 2.7	[15]
baPWV [m/s]	11.46	14.84 ± 3.4	16.05	16.7 ± 3.6	[282] [135]
C_a index [ml/mmHg/m^2]	0.97	1.08 ± 0.25	0.55	0.61 ± 0.19	[2]

A brief review on large arteries remodelling Over the last decades noninvasive and invasive techniques allowed a better quantification of vascular changes in hypertensive humans and experimental animals. Large arteries undergo outward hypertrophic remodelling (increase wall thickness with limited changes in vessel's radius) and increased stiffness with aging and hypertension. In elderly patients, stiffening of central large (thoracic aorta, carotid) arteries is associated with increased aortic diameter and wall thickness, elastic fragmentation and calcification, as well as elevated collagen content. Even if age and hypertension both alter the structure of arterial wall and stiffness, the anatomical and functional changes are not the same; structural modifications in hypertension are accelerated with respect to age-related changes. Increased stiffness in hypertension is associated to hypertrophy of arterial wall and changes in the extracellular matrix, mainly an increase in collagen [25]. However, the major determinant of arterial stiffness remains the increase in blood pressure [247, 249, 25].

High blood pressure increases circumferential wall stress unless the change in pressure is matched by a proportional decrease in vessel's radius or thickness. According to the Laplace's equation, the circumferential wall stress σ is proportional to radius r, pressure p, and inversely proportional to thickness h:

$$\sigma = \frac{pr}{h}. \tag{6.6}$$

The elevated circumferential stress is the fundamental trigger for the adaptive response of the vessel wall. Wall thickening results from both cellular growth and synthesis of new extracellular material. All these

FIGURE 6.2: Computed blood pressure p in the aortic tree at different locations a) to g) in normotensive (blue line) and in hypertensive (orange line) state. Cardiac-cycle averaged values are denoted by $\bar{p}_N$ (normotensive) and $\bar{p}_H$ (hypertensive).

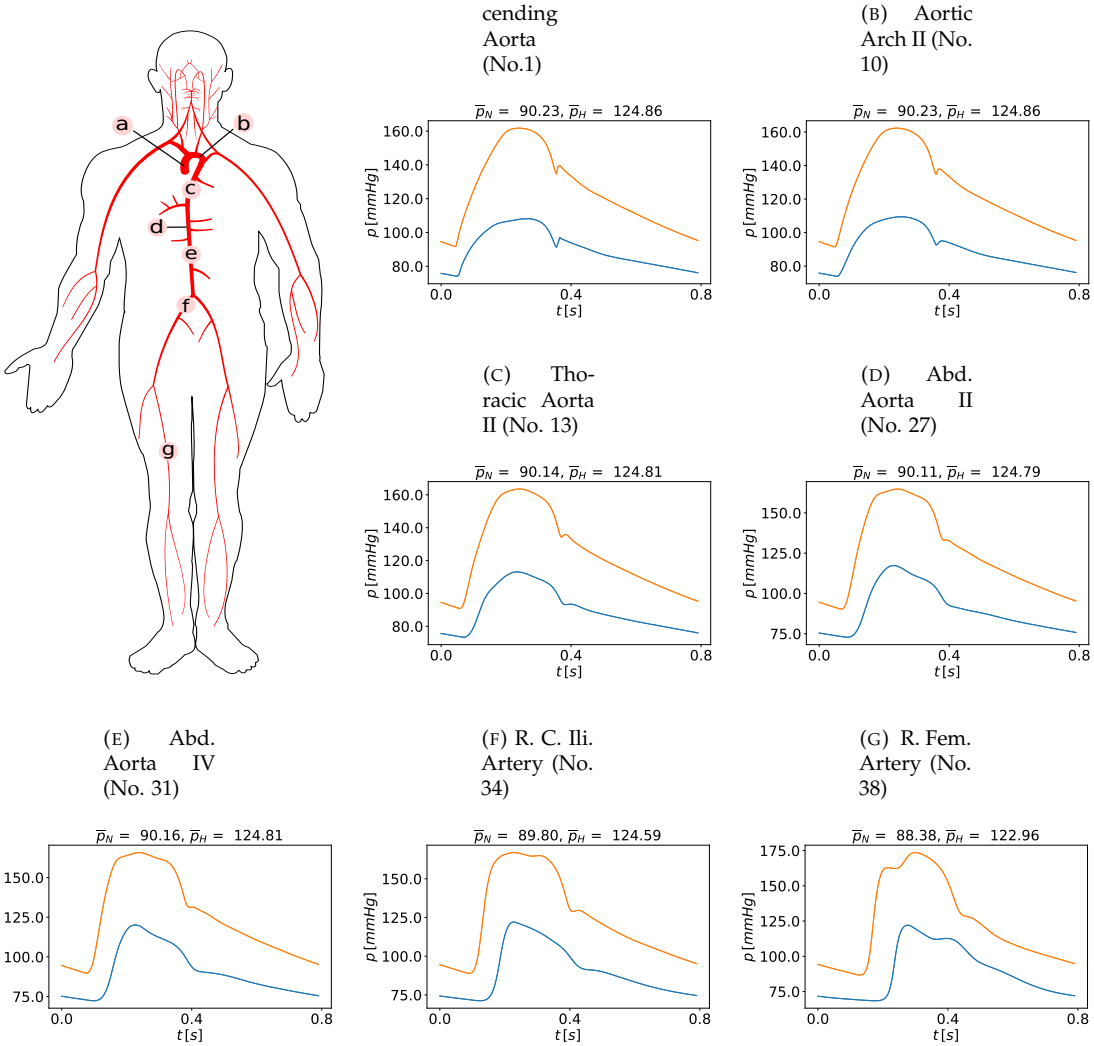

changes alter the biomechanical properties of the arterial wall, and therefore wall-material stiffness, a parameter usually evaluated from the determination of incremental elastic modulus. For the evaluation of arterial structural changes in subjects with clinical hypertension, two different arteries have been widely studied: the common carotid and the radial artery. The latter is composed almost exclusively of vascular smooth muscle and serves as a model of a peripheral muscular artery, while the first one represents a central musculo-elastic artery. Laurent et al. [150] performed the first non-invasive study for the determination of the elastic characteristics of radial artery wall material in hypertensive patients. It was observed that the intima-media thickening compensates for the rise in blood pressure (lumen diameter is not enlarged), and circumferential wall stress is maintained within normal ranges [148]. Moreover, elastic response of the radial artery is maintained despite hypertrophy of the arterial wall. The authors concluded that at the site of distal, muscular, medium-size arteries, thanks to their hypertrophy, normal compliance is maintained despite the increase in intravascular pressure through the normalization of the Young's elastic modulus (the slope of the stress-strain relationship of vascular wall). This means that in these arteries any increase in stiffness in hypertensive subjects always returns to the normal range when pressure is reduced to the normal range. Furthermore, muscular arteries dilate in hypertensive subjects such that their compliance (absolute volume change with change in pressure) may appear to be normal or even increased [250, 267, 150, 219]. At the site of hypertensive proximal elastic arteries, the intima-media thickening is insufficient to compensate for both the enlargement of internal diameter and the rise in blood pressure: circumferential wall stress is significantly increased compared to the one observed in normotensive subjects. The evaluation of the Young's elastic modulus of the common carotid artery [43] revealed that it is increased only in younger hypertensive patients, while in middle-aged and older patients, the mechanical properties of the carotid arterial wall material are unchanged. In [149], the distensibility of the carotid artery was determined in hypertensive patients and compared to age and sex-matched normotensive subjects. It was shown that distensibility decreases as blood pressure increases; moreover, evaluation of distensibility at the same blood pressure level revealed that it is not significantly different between hyper- and normotensive patients after adjustment for age, but it decreases with ageing. This suggested that the decreased distensibility in large elastic arteries in hypertensive subjects is due primarily to the increased distending pressure and that age-independent structural modifications of the arterial wall play only a minor role [149]. In this case, the stiffness results in increased pulse-wave velocity and alterations of amplitude and timing of wave reflections and thus causes a disproportionate increase in systolic and pulse pressure [252].

Computational pressure-area relationship of large arteries

Keeping in mind these physiological and experimental evidence on large arteries remodelling, we now focus on computational results. Figure 6.3 compares the pressure-diameter curves of these exemplary arteries with respect to literature data [149, 150]. In case of common carotid artery, we are considering a 10 % enlargement of vessel's diameter, according to data in [43]. Comparing the computed pressure-diameter curve with respect to [149], computational results for the hypertensive subject are at the limit of the physiological range; this is probably due to the fact that in [149] middle-aged matched normotensive and hypertensive patients (50 ± 5 and 51 ± 3 years old, respectively) were compared. As stressed by Farasat et al. [84], age accounts for dilation of large arteries, rather than hypertension; for adjustment with age, differences between aortic diameter of normotensive and hypertensive patients were not observed. In view of these considerations, since we are considering two groups of normotensive and hypertensive patients at different age, we believe that it is reasonable to observe an higher increase in diameter with respect to [149]. Anyway, we can notice that the lumen enlargement is more pronounced in the elastic artery, while in the muscular artery the area is slightly increased, as observed in the experimental data. Moreover, the modelling pressure-area relationship, the so called tube law in Eq. (6.2), is able to satisfactorily reproduce

FIGURE 6.3: Computed diameter-pressure curve in right common carotid artery and in right radial artery in normotensive (N) and hypertensive (H) subjects. Computational results are compared to literature data in [149, 150] (mean ± SEM) for both normotensive (N_{Lit}) and hypertensive (H_{Lit}) states. Diameter is normalized with respect to the average value over a cardiac cycle.

(A) Elastic artery: common carotid artery [149]

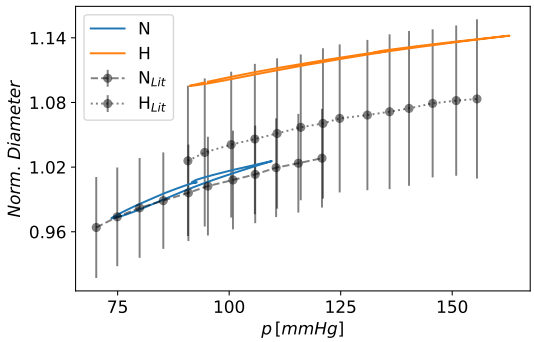

(B) Muscular artery: radial artery [150]

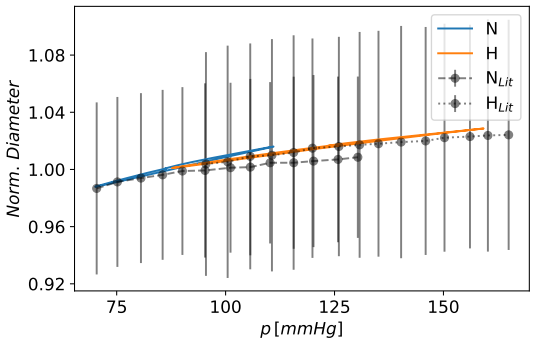

the physiological behaviour of the vessel's wall deformation. As previously said, Eq. (6.2) depends on m and n, two experimental parameters that are usually taken $m > 0$ and n in the range $[-2, 0]$. The choice of $m = 1/2$ and $n = 0$ results in a tube law that does not reproduce the stiffening in the high blood pressure range; therefore, in this work we imposed $m = 10$, $n = -3/2$ in order to simulate a more realistic and physiological behaviour. To stress the effect of this choice, we compare in Figure 6.4 the computed pressure-area curve (A, B) and the computed pressure waveforms (C,D) when $m = 1/2$, $n = 0$ (classical choice) and when $m = 10$, $n = -3/2$ obtained from simulations in normotensive and hypertensive conditions. In the normotensive case, both choices give comparable results; the differences are more evident in the hypertensive results. For $m = 10$, $n = -3/2$ one can see how the stiffening behaviour results in higher pulse amplitude. In Figure 6.4 (C,D), arterial pressure curves over a cardiac cycle obtained with the two parametrizations of the tube law are displayed. The mean arterial pressure values are not significantly different: in hypertensive cases, radial artery mean pressure is 90.1 mmHg when $m = 1/2$, $n = 0$, while it is 93.9 mmHg when $m = 10$, $n = -3/2$ (percentage difference of 4 %). On the other hand, pulse pressure is significantly affected: from 55.27 mmHg to 71.52 mmHg in the radial artery of hypertensive scenario (percentage difference of 29.4 %). If we consider the hypertensive scenario without imposing the stiffening of large arteries changing $K(x)$ in Eq. (6.2), but simply a stiffer pressure-area relation given by $m = 10$, $n = -3/2$, the results reveal that this would be enough to match what observed in hypertension. In fact, mean aortic pressure is 121.16 mmHg, while systolic and diastolic pressures are 150.43 mmHg and 93.24 mmHg, respectively. Pulse pressure at the aortic level is 57.19 mmHg while at the brachial level it is 60.58 mmHg.

Assessment of arterial stiffening by means of pulse wave velocity, augmentation and arterial compliance indexes

Large artery stiffening is the most important pathophysiological determinant of hypertension and age-dependent increase in pulse pressure. As the wave travels away from the heart towards the periphery, the systolic peak pressure increases according to physiological patterns. $PP_{Amplification}$ is an index representing the disparity between central and peripheral pressure and is calculated as the ratio between brachial and aortic pulse pressure. As reported in the literature [190], this index is reduced in the hypertensive scenario (Table 6.1); one of the most determining factors of the central-to-peripheral pressure gradient is ageing

FIGURE 6.4: Pressure-area curves and pressure waveforms for two exemplary arteries: the right radial artery and the right common carotid artery. Normotensive state (N) is compared to the hypertensive one (H), with two different values for the parameters m and n in the tube law Eq. (6.2). $m = 1/2$, $n = 0$ refer to the classical tube law usually adopted in previous work [201, 202, 292], while $m = 10$, $n = -3/2$ are chosen based on experimental evidences [63].

(A) Pressure-area curve of the right common carotid artery

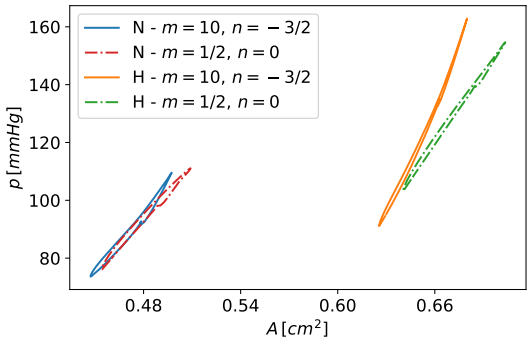

(B) Pressure-area curve of the right radial artery

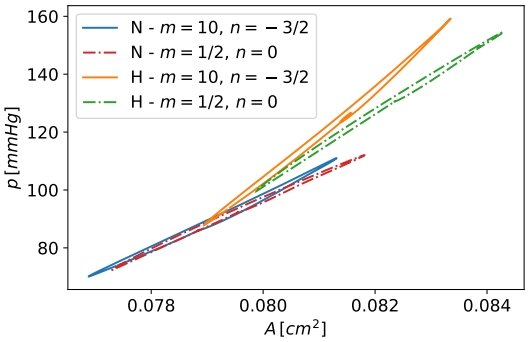

(C) Blood pressure in the right common carotid artery

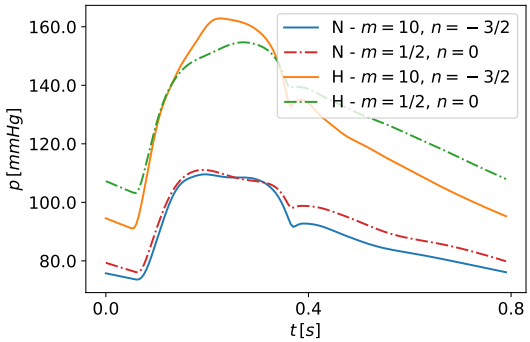

(D) Blood pressure in the right radial artery

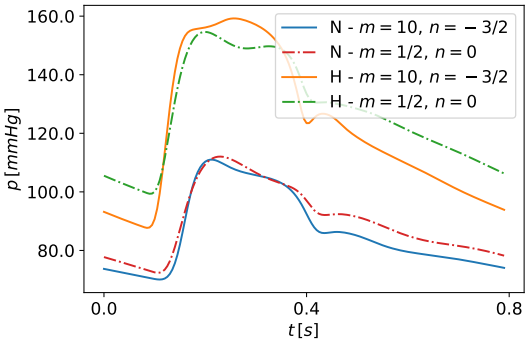

process. The measurement of pulse wave velocity is generally accepted as the most simple, noninvasive, robust, and reproducible method with which to determine regional arterial stiffness [148]. Pulse wave velocity (PWV) is a measure of the speed at which the pressure waveform propagates along a segment of the arterial tree; the stiffer the vessel, the faster the wave travels. Carotid-femoral PWV (cfPWV) is evaluated as the distance between carotid and femoral artery divided by the transit time of the wave (evaluated with the foot-to-foot method). A cfPWV $>$10 m/s is considered a conservative estimate of significant alterations of aortic function in middle-aged hypertensive patients [179]. The pulse wave velocity can be measured also at the brachial-ankle level, considering the brachial and the tibial arteries [210, 282]. Both computed PWV are in line with literature data about young normotensive patients and elderly hypertensive subjects (Table 6.1). Augmentation pressure (Augmented P) is calculated as the difference between the second and first systolic peaks of aortic pressure, and augmentation index is calculated as augmentation pressure expressed as a percentage of the pulse pressure [190]. Augmentation index has been proposed as a measure of wave reflection; arterial stiffening increases the pulse wave velocity and hence causes an early return of the reflected wave [263]; computed augmentation index goes from 10.91 % in normotensive subject to 17.91 % in hypertension (Table 6.1). As a consequence of increased arterial stiffness, arterial compliance is reduced. Total arterial compliance index is evaluated as the ratio between stroke index and pulse pressure, as suggested in [9, 2], and compared to clinical data from [2]. Hypertensive subject has a significantly lower total arterial compliance index (0.55 ml/m^2/mmHg *vs* 0.97 ml/m^2/mmHg in healthy condition, see Table 6.1). Abdelhammed et al. [2] found that total arterial compliance index is lower in hypertensive patients at stage I and II of the disease, in both controlled and uncontrolled subjects; moreover, they stressed the correlation between this index and age.

The arterioles and capillaries compartments

The increase in pulse pressure that characterizes the 1D arterial vessels is reflected also in the arterioles compartments but it is attenuated in the capillaries compartments. Figure 6.5 shows the pressure waveforms along the vascular system of right arm: from radial artery to capillary beds. It can be observed that the main sites of elevation of blood pressure are 1D arteries and arterioles. We consider all the vascular beds of the model and evaluate the pressure variations in the arterial compartments between healthy and pathological case; data about mean pressure over a cardiac cycle are presented as mean $\pm$ standard deviation of all vascular beds. Terminal arteries pressure rises from 88 $\pm$ 1.44 in normotensive to 122.78 $\pm$ 5.32 mmHg in hypertension, while mean arterioles pressure is increased from 74.77 $\pm$ 6.66 to 99.40 $\pm$ 11.35 mmHg. Structural changes of small resistance arteries in patients with essential hypertension are usually a consequence of inward eutrophic remodelling [148], that is a greater media thickness, a reduced lumen and external diameter with increased media-to-lumen ratio, without any significant change of the total amount of wall tissue. Eutrophic remodelling is accompanied by structural elevation of resistance; the main site for vasoconstriction are the proximal resistance arteries, while the most distal resistance artery sites are partly protected from pressure elevation by a raised resistance upstream. The computed capillary pressure increases from 29.99 $\pm$ 2.62 to 34.23 $\pm$ 3.42 mmHg from normotensive to hypertensive case; its pulse rises from 5.24 $\pm$ 2.48 mmHg in normotensive to 6.47 $\pm$ 2.82 mmHg in hypertension with a good agreement with the literature range [129]. The term rarefaction indicates the reduction in the number of interconnected small arteries and capillaries [153, 14]; increased number of non perfused microvessels can progress in anatomic absence of microvessels [148]. Capillary rarefaction could represent an early structural abnormality in borderline hypertension and in offspring from hypertensive parents. Antonios et al. [14] studied capillaries of the skin of the dorsum of the fingers by intravital capillary microscopy in people with borderline hypertension and proved that rarefaction may precede high blood pressure and it could be an early abnormality in the progression of hypertension.

FIGURE 6.5: Computed pressure variations along the vascular system of the right arm. N: normotensive subject; H: hypertensive subject. Cardiac-cycle averaged values are reported in brackets.

(A) Radial artery pressure

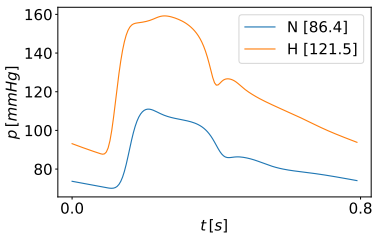

(B) Arterioles' pressure

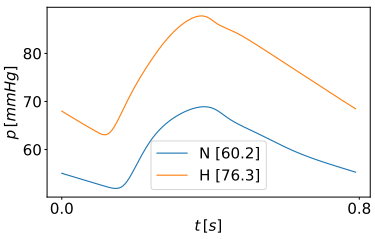

(C) Capillaries' pressure

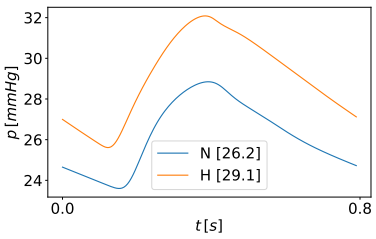

Pulsatility and resistive indexes

A close relationship was established between microvascular damage in brain and kidney and indices of age and hypertension [228]. Exposure of small vessels to highly pulsatile pressure and flow explains microvascular damage and resulting renal insufficiency and intellectual deterioration. Pulsatility index (PI) is defined as the difference between the peak systolic and minimum diastolic flow rate, divided by the mean flow rate over a cardiac cycle, or equivalently, as the difference between the peak systolic and minimum diastolic flow velocity, divided by the mean velocity over a cardiac cycle. It can be measured with non-invasive methods and it is widely used for the assessment of vascular resistance as well as for the determination of end-organ damage. Chuang et al. [56] observed a strong association between the PI in the common carotid artery and the possibility of future stroke. Cho et al. [55] measured flow velocities and PI of the middle cerebral and internal carotid arteries in 94 hypertensive patients; they observed decreased flow velocity with increased flow pulsatility in patients with a longer duration of hypertension, while no significant differences were found in patients with < 5 years of hypertension. PI was also studied in the renal circulation; Petersen et al. [238] observed an association between renal artery PI and renal function parameters, such as creatinine clearance, in patients with renal failure and hypertension. In light of the role played by the PI, we focused on its evaluation along the circulation in computational simulations of normotensive and hypertensive subjects. In the 1D arterial network, PI ranges between 0.71 and 7.3 and in general it is lower in the hypertensive scenario with respect to the normotensive one. The percentage difference is -4.64 $\pm$ 16.9, evaluated as mean and standard deviation over the complete arterial 1D network. However, some 1D arteries present higher pulsatility indexes: these includes mainly arteries of the abdominal region, such as abdominal, gastric, hepatic arteries, as well as cerebral arteries.

Regarding the kidney's circulation, we compared the pulsatility index of the renal artery to literature measurements from [238, 223]. Petersen et al. [238] measured PI and resistive index (RI) from blood flow velocities of renal arteries in normotensive and hypertensive patients; RI was calculated as the difference of peak systolic velocity and peak diastolic velocity over peak systolic velocity. They reported an increase in PI from 1.19 (0.93-1.25) to 1.65 (1.31-1.86) in hypertensive patients compared to normotensive controls; the RI increased from 0.67 (0.64-0.70) to 0.76 (0.69-0.81). Okura et al. [223] measured PI and RI from blood flow velocity in interlobar arteries; they found PI equal to 1.30 $\pm$ 0.29 and RI equal to 0.65 $\pm$ 0.08 in a cohort of patients with essential hypertension. In our computational results, there are no significant changes between computed PI in normotensive and hypertensive subjects: the renal arteries PI is 1.52 and 1.53 while the RI is 0.70 and 0.75, respectively, in normotensive subject and in hypertensive scenario. In the vascular bed of the splanchnic circulation, computed PI from the flow waveform of the arterioles' and capillaries' compartments increases by about 13 % while in the vascular bed of the renal circulation PI increases by about 6.3

%. Computed indexes are in line with values reported in the literature; however, computational results do not reproduce the significant rise in PI of renal arteries observed in clinical measurements. This is probably due to the fact that we do not differentiate the hypertension remodelling of the renal circulation from other vascular territories. Nevertheless, the kidneys play an inextricable role in hypertension; abnormalities in kidneys' function and sequential changes in renal hemodynamics were observed in hypertensive patients [61]. Moreover, the kidney, as the brain, are characterized by a pronounced blood flow regulation based on two mechanisms, the myogenic response and the tubuloglomerular feedback [133]. These kidney-specific changes in renal circulation were not included in our model and could be the cause for observed discrepancies between our computational results and clinical observations.

Concerning the cerebral circulation, previous works mainly focused on carotid and middle cerebral arteries to study the haemodynamic changes associated with hypertension. Ferrara et al. [87] used ultrasound images for the evaluation of PI and a RI in the proximal segment of the internal carotid arteries and the middle cerebral arteries. Comparing normotensive and hypertensive patients, they found a PI equal to 0.84 ± 0.11 and 0.88 ± 0.19 and RI equal to 0.79 ± 0.12 and 0.81 ± 0.12, respectively, in internal carotid arteries; in middle cerebral arteries, they measured PI to be 0.54 ± 0.05 and 0.55 ± 0.07 and RI equal to 0.52 ± 0.05 and 0.52 ± 0.05 in normotensive and hypertensive patients, respectively. No significant differences were found between the healthy and the pathological groups of patients. From our computational model, computed PI and RI in internal carotid arteries are 1.02 and 0.58 in normotensive condition, while 0.84 and 0.54 in hypertension; concerning the middle cerebral artery, PI and RI are 0.74 and 0.48 in healthy subject, while 0.69 and 0.49 in hypertensive scenario. In these arteries PI tends to decrease from normotensive condition to hypertension, even if their values are comparable to literature measurements. A different behaviour can be observed at the level of 0D arterioles/small arteries and capillaries. In cerebral vascular beds, PI computed on flow rate waveforms increases by about 25-29 % in both arterioles and capillaries from normotensive to hypertensive condition.

6.3.2 The heart in hypertension

Left ventricle hypertrophy and its effect on elastance

Chronically increased left ventricular workload due to arterial stiffness in hypertensive patients can result in left ventricular hypertrophy, impaired relaxation, left atrial enlargement, an increased risk of arrhythmias, especially atrial fibrillation, and an increased risk of heart failure with preserved ejection fraction and heart failure with reduced ejection fraction. Structural changes of left ventricle in hypertension can be classified as concentric hypertrophy (increase in left ventricular mass and relative wall thickness), concentric remodelling (normal left ventricular mass, abnormal relative wall thickness), or eccentric hypertrophy (increased mass with normal relative wall thickness) [187, 98]. Remodelling usually characterizes normal aging without hypertension and it is probably an adaptation to preserve ejection fraction [187]. In case of concentric hypertrophy, the cardiac muscle cells increase in thickness by building more contractile proteins in parallel. According to the Laplace's law (6.6), the thicker wall with normal lumen normalizes peak systolic wall stress despite higher blood pressure. Cardiac hypertrophy acts to maintain a normal stroke volume and cardiac output through increased intraventricular pressure. Table 6.2 presents some of the main cardiac indexes in normotensive and hypertensive scenarios compared to literature measurements; assigned heart rate and then computed values of cardiac index, stroke index are reported. The cardiac index (the ratio between cardiac output and body surface area) is comparable between normotensive and hypertensive state, as well as the stroke index, evaluated as stroke volume over body surface area. We stress that the same body surface area of 1.92 m^2 has been adopted in the healthy and patholocigal subjects for the

evaluation of cardiac and stroke indexes; Abdelhammed at el. [2] reported 1.93 $\pm$ 0.25 m^2 in an healthy group while 1.91 $\pm$ 0.20 m^2 in an hypertensive group at stage I of the disease.

Figure 6.6 (A) shows the pressure-volume relationship evaluated during a cardiac cycle in the left ventricle for normotensive and hypertensive subjects; compared to the normotensive pressure-volume loop, the hypertensive one is traslated to the right as effect of left ventricle hypertrophy. Considering arterial elastance, E_a, and left ventricle elastance, E_{es}, Table 6.2 shows that they increase by the same ratio in the hypertensive group compared to the normotensive one, meaning that left ventricular-arterial coupling (E_a/E_{es}) is similar in both groups. Borlaug et al. [36], in a large cohort of hypertensive patients, concluded that arterial stiffening is matched with left ventricle systolic stiffening, with a concordant increase in E_a and E_{es}; moreover, they observed that left ventricle hypertrophy is associated with enhanced myocardial contractility. Antihypertensive therapies could improve the ventricular-arterial coupling, by reducing both E_a and E_{es}, as pointed out by Lam et al. [146].

The right heart and the pulmonary circulation

The right heart and the pulmonary circulation are not immune to the effects of systemic hypertension. Table 6.2 reports maximum volume, ejection fraction, maximum and minimum pressure rate, systolic and end-duiastolic pressures of right ventricle, as well as pulmonary arterial pressure (systolic, diastolic and mean). Computational results show that the right-heart pressures among the hypertensive patients increase significantly with respect to the values in the normotensive controls. In the same way, pulmonary arterial pressure increases in hypertensive patients with respect to values observed in the normotensive scenario. Olivari et al. [224] presented the first comprehensive study on the pulmonary circulation and right ventricular function in uncomplicated hypertensive patients, comparing 16 hypertensives with left ventricle hypertrophy and 17 without it. They observed that pulmonary vascular resistance is increased compared to controls; this is unrelated to left ventricle filling pressures and it could be due to the fact that pulmonary vessels experience similar structural changes as those observed in systemic vessels. The same conclusion has been reported by Guazzi et al. [107]. Moreover, Olivari et al. [224] showed decreased stroke volume as a function of right atrial pressure in patients without left ventricle hypertrophy while a preserved relation between stroke volume and right atrial pressure in patients with hypertrophy. Established cardiac hypertrophy could lead to a reduction in stroke volume in the absence of effective compensation; such compensation can be found in the form of increased cardiac filling pressure. In a previous mathematical model of arterial hypertension, Liang et al. [158] reproduced ventricular hypertrophy increasing the elastance of left ventricle without considering modifications of the pulmonary or venous systems. This leads to decreased cardiac index and stroke volume, as observed in Ganau et al. [98] in case of concentric remodelling of left ventricle in hypertensive patients. However, observing patients with concentric hypertrophy, Ganau et al. [98] found slightly increased stroke volume and cardiac index. As shown in [261] by means of a simple mathematical model of the heart-arterial coupling, in case of concentric hypertrophy, the increased venous filling pressure normalizes the end-diastolic wall stress, still while normalizing the systolic wall stress; as a consequence, stroke volume and cardiac output are preserved in hypertension. Computed central venous pressure, evaluated as mean right atrial pressure, increases from 4.16 mmHg in normotensive subject to 5.15 mmHg in hypertension, in line with the increase observed by Safar et al. [251] (from 4.4 $\pm$ 0.6 mmHg in normotensive controls to 5.0 $\pm$ 0.6 mmHg in hypertensive patients). Changes in venous filling pressure could be caused by reduced venous compliance in order to produce an adequate driving pressure for the hypertrophied heart. This theory was supported by Safar and London [247]. In a more recent review on right heart and pulmonary circulation in hypertension [312], the authors concluded that right ventricle function may be altered at an early stage of hypertension when left ventricle hypertrophy is still not evident. However, as the left ventricle remodelling progresses and pulmonary arterial

FIGURE 6.6: Computed volume-pressure relationship of the left and right cardiac ventricles. Comparison between normotensive subject (N) and hypertensive patient (H).

(A) Left ventricle

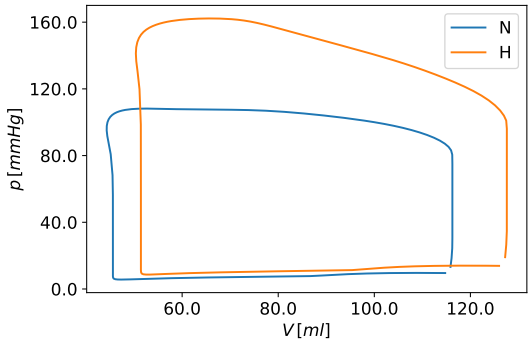

(B) Right ventricle

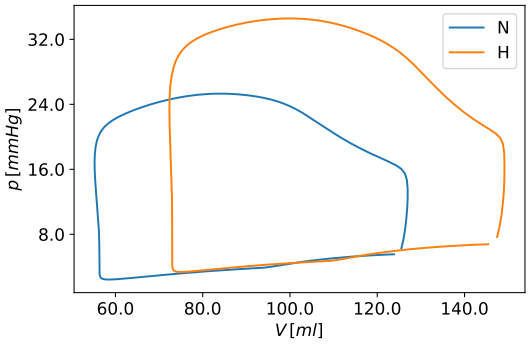

pressure increases, the right ventricle becomes hypertrophic in a parallel way than those of the left ventricle. Figure 6.6 shows the computed volume-pressure relationship of the right ventricle in normotensive and hypertensive subjects, displaying a translation on the right of the curve in hypertensive. Even if the parameters that characterize the model of the right ventricle are not modified in the hypertensive scenario, our computational results display an hypertrophic behaviour as a consequence of left ventricle hypertrophy and increased pulmonary arterial resistance.

6.3.3 Total blood volume and vascular compliance

As discussed in the previous section, cardiac hypertrophy leads to a reduction in stroke volume in the absence of normalization of diastolic wall stress. This normalization is due to increased venous filling pressure, that could be the result of decreased venous compliance.

The vascular compliance of the circulatory system is defined as the slope of the relationship between intravascular volume and circulatory filling pressure; this property reflects the inherent elasticity of the vascular system. In animals, total vascular compliance can be obtained by determining mean circulatory filling pressure-blood volume curves. Mean circulatory filling pressure can be extrapoled by stopping the heart and waiting for blood to redistribute in the vascular system according to the capacity of the different districts. To avoid this methodological limitation, a different index of capacitance was introduced as a measure of total vascular compliance. This method was first presented in [82]; it involves simultaneous recording of right atrial pressure and volume changes induced by transfusion, bleeding, or rapid iso-oncotic dextran infusion. London et al. [171] determined the total effective vascular compliance (TEVC) using an infusion of 500 ml of 6% dextran carried out within four minutes in a large forearm vein in control and hypertensive patients in supine position. The slope of the relationship between central venous pressure (CVP) and blood volume was called TEVC in order to differentiate it from the compliance obtained from mean circulatory filling pressure measurements. Several studies have shown that effective total vascular compliance in normal man has the character of a biological constant with values ranging from 2.1 to 2.7 ml/mmHg/kg [82, 171, 249]. Total effective vascular compliance is the sum of compliances of the arterial system, which is very low in man (1-3% of the total compliance), and the venous system, which accounts for 97-98% of the total compliance. In patients with uncomplicated sustained essential hypertension, it was proved that total effective compliance is significantly reduced by 25% in comparison with normal subjects of the same age and sex [171, 169, 251]. For the same volume expansion as in normotensive controls, central venous pressure is significantly higher in hypertensive subjects. On the other hand, effective cardiopulmonary vascular

TABLE 6.2: Cardiac and pulmonary indexes: comparison between normo- and hypertensive subject. HR: heart rate; CI: cardiac index; SI: stroke index; E_a: arterial elastance; E_{es}: left ventricle elastance; E_a/E_{es}: arterial-ventricular coupling index; LV/RV_{max}: maximum volume of ventricle; LV/RV_{EF}: ejection fraction of ventricle; max/min $\frac{dP}{dt}$: maximum/minimum pressure rate; RV-SP: right ventricle systolic pressure; RV-EDP: right ventricle end-diastolic pressure; M/S/D PAP: mean/systolic/diastolic pulmonary artery pressure. Details on how to evaluate these indexes can be found in the Appendix B.

Index	**Normotensive**		**Hypertensive**		**Ref..**
	Value	**Ref. Value**	**Value**	**Ref.Value**	
HR [beats/min]	75	75 ± 12	75	77 ± 9	[86]
CI [L/min/m^2]	2.76	2.9 ± 0.8	2.97	3.1 ± 0.8	[98]
SI [ml/m^2]	37.48	43 ± 9	40.22	45 ± 11	[98]
E_a [mmHg/ml]	1.32	1.52 ± 0.1	1.83	1.8 ± 0.17	[34]
E_{es} [mmHg/ml]	2.14	2.03 ± 0.2	2.80	2.43 ± 0.2	[34]
E_a/E_{es}	0.61	0.77 ± 0.04	0.65	0.73 ± 0.06	[34]
LV_{max} [ml]	116.25	150 ± 67	127.59		[215]
LV_{EF}	0.62	0.68 ± 0.12	0.61		[215]
RV_{max} [ml]	126.96	173 ± 95	149.15		[215]
RV_{EF}	0.56	0.57 ± 0.10	0.51	0.59 ± 7	[215] [86]
max. $\frac{dP_{LV}}{dt}$ [mmHg/s]	1505.59	1915 ± 410	2139.55		[215]
min. $\frac{dP_{LV}}{dt}$ [mmHg/s]	-2505.36	-2296 ± 530	-4253.05		[215]
max. $\frac{dP_{RV}}{dt}$ [mmHg/s]	262.08	248 ± 25	322.60		[215]
min. $\frac{dP_{RV}}{dt}$ [mmHg/s]	-306.79	-232	-459.90		[215]
RV-SP [mmHg]	25.31	22 ± 6	34.57	27 ± 5	[86]
RV-EDP [mmHg]	2.42	3 ± 2	3.36	5 ± 2	[86]
MPAP [mmHg]	16.14	12 ± 3	21.97	17 ± 5	[86]
SPAP [mmHg]	24.68	20 ± 6	33.87	26 ± 6	[86]
DPAP [mmHg]	10.61	8 ± 2	14.22	11 ± 5	[86]

compliance (evaluated as the ratio between changes in cardiopulmonary blood volume and central venous pressure during infusion) is comparable between normotensive and hypertensive patients [170]. As observed in animals [82], these findings reflect a reduced distensibility in the systemic vessels of hypertensive humans [171] and not in the cardiopulmonary circulation. The venous function can be modified by structural or functional changes, or both [248]. In animal models of hypertension [104], venous wall hypertrophy was found in the portal vein which creates a stiffer framework on which the active contractile process is able to develop greater tension. These observations are translated into our mathematical model of arterial hypertension by reducing the venous compliance value. We observe that this modelling assumption affects only the compliance of small veins and venules, without modifying the structural properties of larger caliber veins. However, the major part of total venous compliance is distributed in the venules compartments and hence modifications of 1D veins compliance will have slight effects on total vascular compliance. Moreover, in this mathematical framework, venous compliance is reduced in hypertensive scenario without considering venous unstressed volume that is maintained equal to that of the normotensive case. Venous tone is determined by the interaction between venous compliance and unstressed volume, hence changes in unstressed volume could influence the total effective compliance determination. We chose to reduce venous compliance instead of changing unstressed volume because there is evidence of stiffening in rats'

veins [104]. Total effective vascular compliance was computationally estimated in our model by means of an infusion of 500 ml of blood, as described in [51]. Figure 6.7 (left) shows the computed linear relation between volume and right atrial pressure modifications due to the rapid infusion of blood. The value of TEVC is expressed in mL/mmHg and then normalized to the body weight, considered to be 75 kg in the normotensive state and 85 kg in the hypertensive subject. We consider the same percentage increase in body weight between normo- and hypertensive groups reported by London et al. [171]. Computational results show that TEVC is significantly reduced in hypertensive subjects (2.02 vs 2.82 ml/mmHg/kg in normotensive scenario).

The role of the veins in modelling hypertension had received little attention. However, since approximately two-thirds of the systemic blood is normally contained in venous circulation, this variation in vascular compliance has important consequences on the venous vasculature, as well as on the overall circulation. The decreased venous distensibility produces a redistribution of blood volume; since total blood volume is normal or reduced and there is no decrease in the compliance of the cardiopulmonary circulation [247, 170, 82], this results in a shift of blood to the central circulation (heart and lungs). Figure 6.8 shows the blood volume distribution in the main districts of the circulation: arterial blood (1D arteries, small arteries and arterioles), capillaries, venous blood (venules, small veins and 1D veins), heart and pulmonary circulation. It can be observed that in the hypertensive case, the arterial and capillaries percentages of blood volume are comparable to the normotensive state, but there is a slight increase in heart and pulmonary circulation amount of blood (+3 %), matched by a small decrease in venous blood. London et al. [169] reported that the percentage of cardiopulmonary blood volume with respect to total blood volume was 23 $\pm$ 1 in normotensive group while 25 $\pm$ 1 in hypertensive group; in another study by the same leading author [170], the cardiopulmonary blood volume was increased by about 7% in hypertesive subjects with respect to the healthy controls. The shift to central blood volume is caused by the reduced venous compliance, which decreases the capacity of the venous system to accomodate enough blood volume. As a consequence of the shift of blood to the central circulation, filling pressure and cardiac output slightly increases. Ulrych et al. [300] showed that the increase in cardiac output following an intravenous volume load was exaggerated in hypertensive patients, suggesting a reduction in peripheral vascular capacity. Moreover, there is an inverse correlation between cardiac output and vascular compliance in hypertensive subjects: the greater the reduction in the compliance, the higher the cardiac output.

Figure 6.7 (right) shows the percentage variation in main haemodynamic parameters (mean arterial pressure, cardiac output, heart rate, cardiopulmonary blood volume) before and after expansion. Computed results are compared to [171]. We can observe that cardiac output and cardiopulmonary blood volume increases with a similar percentage between normotensive and hypertensive patients, proving that the cardiopulmonary capacity of accommodating blood volume remains comparable between normo- and hypertensive subjects. Heart rate decreases in normotensive case, while it increases in hypertension; however, changes in heart rate are not significantly. The variation in mean arterial pressure during volume expansion is controlled by the baroreceptors located in the high- and low-pressure systems. Baroreflex control plays an essential role in the short-term regulation of arterial pressure. In this mathematical model of hypertension, the set points of the level of activation of the high- and low- baroreceptors are shifted to higher values to account for increased arterial and venous pressures. The abnormalities of the baroreflex function have been discussed in numerous studies; there is evidence that dysfunctions of baroreceptors could precede the onset of arterial hypertension and influence its pathogenesis. When arterial pressure increases after manipulation of baroreceptor afferent nerve signaling, it is referred to as neurogenic hypertension; this term includes both the case wherein the true origin of the hypertension is neural (i.e., the primary underlying issue is in the brain or in afferent or efferent nerves) or the case whose origin is non-neural but results in neurally mediated increase in blood pressure [273]. Dysfunction in sympathetic activity could affect heart

FIGURE 6.7: Left frame: computed total effective vascular compliance by means of an infusion test of 500 ml of blood in 4 minutes. Changes in mean central venous pressure are plotted against changes in total blood volume and the inverse of the slope of their linear relationship is the value of the effective compliance. Computed results are compared to literature data reported in [171].
Right frame: Changes in haemodynamic parameters before and after expansion. Computed results are compared to literature data from [171]. Parameters under consideration are MAP, mean arterial pressure; CO, cardiac output; H, heart rate; CPBV, cardiopulmonary blood volume.

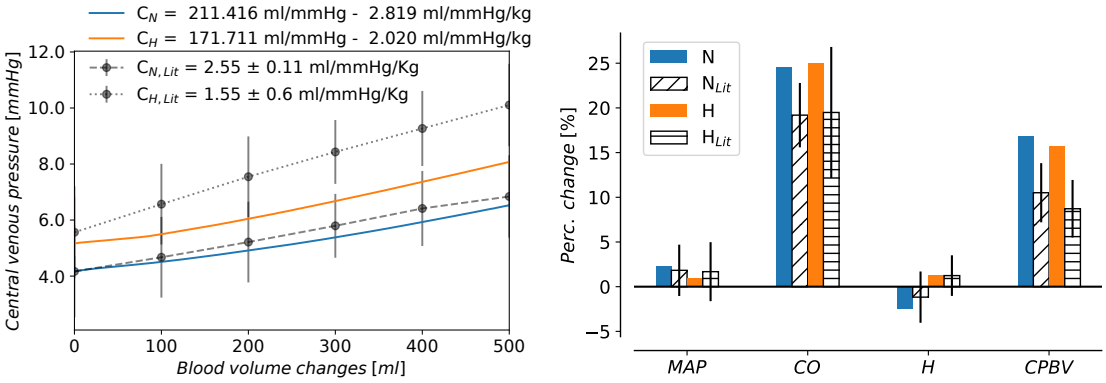

rate, cardiac output, peripheral resistance, venous tone, as well as plasma and urinary levels.

6.3.4 The venous system in hypertension

For years, it was thought that the main role of the venous circulation was returning blood to the heart; it is now recognized that systemic veins perform other important functions. As stressed in the previous section, the venous system serves as a blood reservoir for the entire circulation; it is able to store a highly variable amount of blood and to make it available when required for several reasons, such as cardiac output regulation.

Beyond the role played by the decreased venous distensibility, the behaviour of the venous system in essential hypertension has not been often considered in clinical studies on arterial hypertension. Novo et al. [221] showed that the arm venous pressure in hypertensive patients and in elderly patients with systolic hypertension is higher compared to that measured in healthy controls; the authors concluded that in essential hypertension, both the arterial and the venous circulatory systems are characterized by increased pressure. In a recent study on chronic venous insufficiency [240], the authors supported the thesis of an interdependence of venous and arterial hypertension. Rubira et al. [245] showed that endothelial dysfunction that usually characterized arteries was also present in the venous system of hypertensive patients. Moreover, a recent review [195] stressed the importance of cellular and molecular mechanisms of aging processes of veins and their similarities with those of the arterial system.

In this section, we present computational results about the venous circulation. Pressure, flow and PIs of some one-dimensional veins are compared between hypertensive and normotensive scenarios. Figure 6.9 shows the computed pressure waveforms over a cardiac cycle in selected veins at different locations. One can observe that venous pressure increases by about 20 % in all selected veins. The venous pulse pressure increases in the hypertensive scenario with respect to that obtained the normotensive state. In the inferior vena cava, it is 2.15 mmHg in the normotensive case while 2.94 mmHg in hypertension (percentage difference of 36.13 %). In dural sinuses, the change is more significant: in the superior sagittal sinus, venous pulse pressure increases from 2.10 mmHg in normotensive subject to 3.35 mmHg in hypertensive condition (percentage difference of 59.03%). Accordingly to the pressure-area relationship of large veins, higher venous

FIGURE 6.8: Computational blood volume distribution in normotensive and hypertensive subject. Arterial blood: 1D arteries and arterioles' compartments. Venous blood: 1D veins and venules' compartments. Value in brackets refers to literature blood volume distribution in [113].

(A) Normotensive case

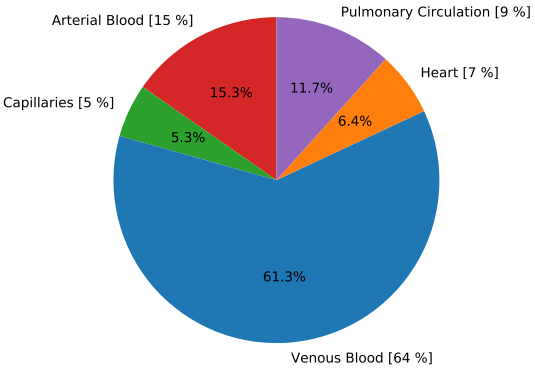

(B) Hypertensive case

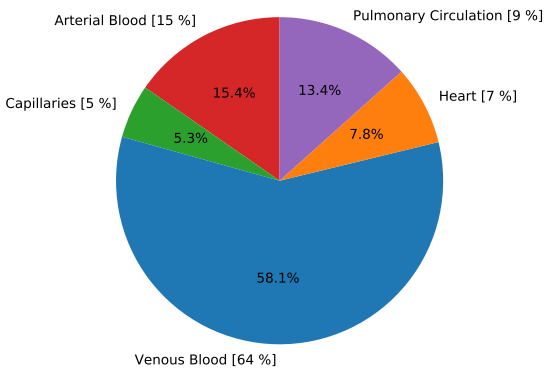

pressure range results in higher pulse amplitude. However, this holds if we model reduced venous compliance without considering unstressed volume changes; indeed, unstressed volume modification would translate the pressure-area curve, resulting in higher venous pressure without significant changes in pulsatility. Taking in mind our modelling assumption, computational results reveal that arterial hypertension leads to venous hypertension and increased venous pulse pressure, both in systemic and cerebral venous circulation. Chung et al. [57] hypothesized that chronic elevated cerebral venous pressure might cause cerebral venule hypertension, resulting in reduce cerebral blood flow, altered microvessel structures, impair cerebral autoregulation; these consequences would lead to chronic cerebral ischemia and leukoaraiosis pathology. Moreover, increased cerebral venous pressure may impair the cerebrospinal fluid system dynamics [23].

Concerning flow rate, Figure 6.10 shows the computed mean flow rate in selected systemic veins and in some head and neck veins. Computational results obtained in the hypertensive scenario are compared with computational results of the normotensive case, as well as with literature data or MRI flow quantification data of normotensive patients. In systemic veins, average flow rate is slightly increased (up to 10 %) in hypertension with respect to values obtained in the normotensive subject. The same can be observed in head and neck veins, wherein average flow rate increases by 10-13 % with respect to what measured in veins of normotensive subject. The PI, evaluated from the flow waveform, also increases by about 30 % along the entire venous network.

Despite little evidence on the characteristics of the venous circulation in essential hypertension, our computational results show that this vascular district is also affected, displaying venous hypertension, increased flow rate and increased pulsatility of both pressure and flow waveforms. Chung et al. [57] stressed that only a compliant vein can accommodate the increased venous pressure by effective distension to maintain a normal venous pressure; decreased venous compliance and distensibility was found in normotensive men with positive family histories of hypertension and in borderline hypertension. This might indicate that reduced venous compliance is present before hypertension is developed, contributing to the pathogenesis of hypertension.

FIGURE 6.9: Computed blood pressure p in selected veins at different locations a) to g) in normotensive (blue line) and in hypertensive (orange line) state. Cardiac-cycle averaged values are denoted by $\bar{p}_N$ (normotensive) and $\bar{p}_H$ (hypertensive).

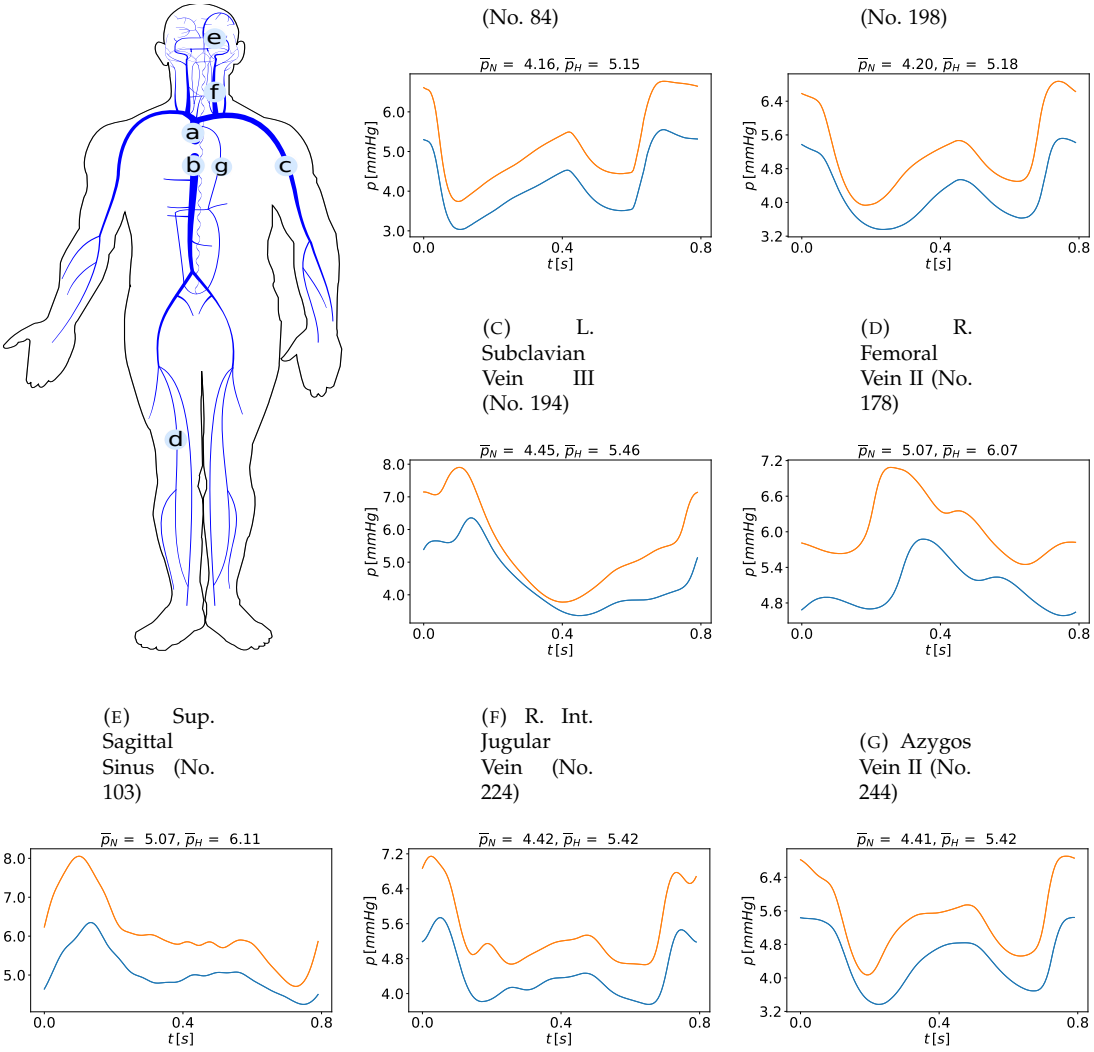

(A) Sup. Vena Cava I (No. 84)

(B) Inf. Vena Cava I (No. 198)

(C) L. Subclavian Vein III (No. 194)

(D) R. Femoral Vein II (No. 178)

(E) Sup. Sagittal Sinus (No. 103)

(F) R. Int. Jugular Vein (No. 224)

(G) Azygos Vein II (No. 244)

FIGURE 6.10: Blood flow distribution in selected systemic veins (left frame) and in head and neck veins. Computational results obtained in the hypertensive scenario are compared with computational data of the healthy subject and with literature data (average and standard deviation) or MRI flow quantification data [201].
Left frame: Mean flow rate in systemic veins. SVC: Superior Vena Cava; IVC: Inferior Vena Cava; AzG V.: Azygos Vein; SCV: Subclavian Vein. Literature: [a]Murgo *et al.* [211]; [b]Wolf *et al.* [322]; [c]Zitnik *et al.* [325]; [d]Cheng *et al.* [54].
Right frame: Mean flow rate in head and neck veins. SSS: Superior sagittal Sinus; StS: Straight Sinus; TS: Transverse Sinus; IJV: Internal Jugular Vein.

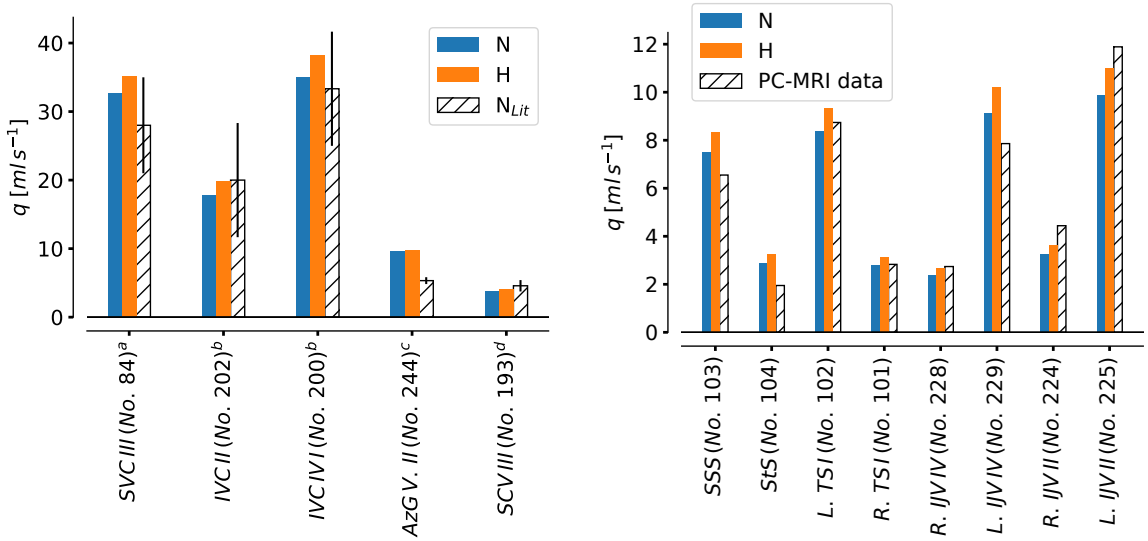

6.3.5 Analysis of distinctive effects of remodelling

Up to now, computational results, as well as modelling construction of the hypertensive setup, have been validated and discussed through comparison with literature observations. The hypertensive scenario well represents the main characteristics of an hypertensive patient at stage I of the disease. In this section, our goal is to determine what is the impact of changes in single model districts/parameters on the arterial pulse wave. We ran nine simulations, each one with only one modified parameter/compartment as in the hypertensive scenario. We considered: 1) Active elastance of left ventricle (E_A), 2) Passive elastance of left ventricle (E_B), 3) Pulmonary arterial resistance ($R_{pul,A}$), 4) Venous compliance (C_{vn}), 5) Arterial characteristic impedance (R_{da}), 6) Arteriolar resistance (R_{al}), 7) Capillaries resistance (R_{cp}), 8) Remodelling of muscular arteries (increased stiffness by means of increased pulse wave velocity), 9) Stiffness of elastic arteries (enlarged radius and increased pulse wave velocity). Figure 6.11 shows the percentage change with respect to the normotensive subject in mean arterial pressure (MBP), systolic (SBP) and diastolic (DBP) pressures evaluated in the aortic root and pulse pressure (PP) of brachial artery. Figure 6.15 compares the percentage change in cardiac index (CI), arterial elastance (E_a), left ventricular elastance (E_{es}) and the ratio E_a/E_{es}. In both pictures, the last bar of each analysed variable refers to the complete hypertensive scenario.

Effects on arterial pressure

Mean aortic pressure is mainly affected by arterial stiffening of both elastic and muscular arteries, venous compliance and arteriolar resistance. The same trend can be observed in systolic and diastolic pressures. The larger contribution to pulse pressure is given by arterial stiffening and to a comparable degree by venous compliance. In a previous mathematical work of arterial hypertension [158], Liang et al. performed a sensitivity analysis on the parameters representing the major cardiovascular properties involved in the development of hypertension. They observed that stiffness of central elastic arteries has a remarkable

influence on pulse pressure, a moderate influence on systolic pressure and a negligible influence on mean pressure and cardiac index; on the contrary, stiffening of peripheral arteries resulted in mild haemodynamic changes. Our computational results show that stiffening of both, elastic and muscular, arteries contributes in a similar way to the elevation of arterial pressure. Moreover, Liang et al. observed that arteriolar radius and heart period mainly affect mean pressure, while pulse pressure is mainly determined by central arteries stiffness and heart period.

Differences between observations made in [158] and results presented here can be interpreted as follows. Firstly, we did not considered heart rate since it is comparable between the class of hypertensive patients under study and normotensive controls, as previously stated. Secondly, Liang et al. performed a sensitivity analysis wherein all the analysed parameters are modified by ± 20 %; in our results, each parameter is modified in the same way as in the hypertensive scenario, hence different percentage variations are applied depending on the parameter (for example, arteriolar resistance increases by 40% while venous compliance decreases by 25%) since the aim of this work is to establish the contribution of each cardiovascular change to the complete hypertensive scenario. Results shown in Figure 6.11 reveal that cardiac hypertrophy, increased pulmonary resistance, as well as capillaries resistance do not affect significantly the change in arterial pressure. These results suggest that cardiac hypertrophy is a consequence of high blood pressure which chronically increases left ventricle workload. Changes in passive elastance of the left ventricle and pulmonary arterial resistance result in a reduced brachial pulse pressure. Comparing the increase in pressure obtained with the modification of one haemodynamic variable and that obtained in the complete hypertensive scenario, it can be observed that the combined action of all alterations results in a larger effect compared to what observed for individual changes. This means that established high blood pressure is the result of the interplay between various modifications; after the initial rise in blood pressure in the pre-hypertensive state, the advance in cardiovascular remodelling worsens the hypertensive state. In order to delve into the relative importance of different remodelling aspects, we studied the impact of all the possible combinations of the four main alterations: stiffening of either elastic or muscular arteries, arterial resistance and venous compliance. Figures 6.12 and 6.13 display pressure variables obtained combining two changes of the hypertensive scenario. Upper triangular part of Figure 6.12 refers to systolic pressure while lower part reports diastolic pressure at the aortic level; in Figure 6.13, the upper triangular part displays mean pressure evaluated in the aortic root and the lower part shows brachial pulse pressure. Computed values are compared to the complete hypertensive setup and percentage differences are reported. It can be observed that the combined effect of increased arterial resistance and reduced venous compliance rises systolic blood pressure in a comparable way as the complete hypertensive setup, while diastolic pressure is higher when only arterial resistance and venous compliance are modified compared to the fully hypertensive scenario. Stiffening of elastic or muscular arteries combined to either arterial resistance or venous compliance results in a lower effect on systolic and diastolic pressures. Compared to the complete scenario, systolic pressure is about 15 % lower in all these cases while diastolic pressure is about 6 % lower when stiffening of either elastic or muscular arteries is combined to arterial resistance and 12 % lower when stiffening is applied in combination with reduced venous compliance. Similar observations can be drawn for mean arterial pressure and pulse pressure: the combined effect of increased arterial resistance and reduced venous compliance leads to a mean pressure comparable to the complete hypertensive scenario, while pulse pressure is 6% lower. Other combinations modify mean arterial pressure to a lower degree; the same holds for pulse pressure. One can observe that stiffening of elastic and muscular arteries together has the lowest effect on pulse pressure if not combined with venous compliance. Figure 6.14 displays systolic, diastolic, mean and pulse pressures obtained when three of the most relevant modifications of the hypertension scenario are combined. These scenarios are compared to the computational normotensive and hypertensive conditions and to normotensive, pre-hypertensive and hypertensive data from the

FIGURE 6.11: Percentage change in mean arterial pressure (MBP), systolic (SBP) and diastolic (DBP) pressures evaluated in the aortic root and pulse pressure (PP) of brachial artery with respect to the healthy control. Nine scenarios are considered, each one refers to the adaptation of only one parameter/compartment of the hypertensive scenario.

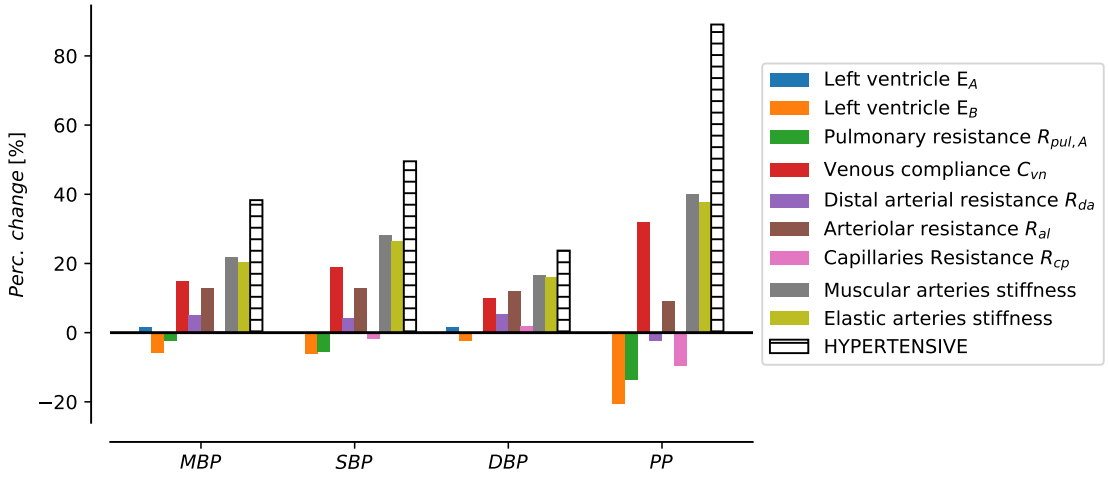

literature [2]. It can be observed that all combinations result in increased pressure, which results to be higher than the one observed in the pre-hypertensive state; scenarios that include elevation of arteriolar resistance and reduced venous compliance produce the highest elevation in blood pressure compared to the normotensive case. Combining stiffness of elastic and muscular arteries with increased arteriolar resistance, computed values of pressure are placed at the lower limit of the literature range for hypertension at stage I. Stiffening of elastic and muscular arteries combined with reduced venous compliance results in the lowest increase in systolic, diastolic and mean blood pressure compared to the other analysed scenarios, it mainly affects the pulse pressure. We can conclude that the most relevant parameters for elevation of arterial pressure is stiffening of both elastic and muscular arteries if considered alone, but when combined with other parameters its effect is attenuated. The major role in the hypertensive setup is played by the combination of modified arteriolar resistance and venous compliance, which returns pressure values similar to those of the complete hypertensive scenario.

Effects on arterial elastance and left ventricle elastance

Arterial elastance (E_a), evaluated as the ratio between end systolic pressure of left ventricle and stroke volume, is mainly increased by arterial stiffening and arteriolar resistance, followed by distal arterial resistance, venous compliance and capillaries resistance (Figure 6.15). Figure 6.16 shows arterial elastance (lower triangular part) and cardiac index (upper triangular part) obtained from simulations wherein two of the most relevant parameters of the hypertension scenario are combined together. From Figure 6.16 it can be observed that arterial elastance is mainly affected by arterial resistance: the values of E_a obtained with simulations wherein increased arterial resistance is combined with arterial stiffening of elastic or muscular arteries, or reduced venous compliance are modified to a similar degree of the simulation wherein the complete hypertension scenario is applied. Left ventricle elastance (E_{es}) increases when parameters E_A and E_B of left ventricle are changed, with the former giving the larger contribution. If remodelling due to hypertension causes disproportionate changes in E_a and E_{es}, then their ratio would be affected. It decreases when cardiac and pulmonary circulation are involved while it increases in other cases; the highest increase is caused by arterial stiffening which impairs arterial elastance without significantly modifying the ventricular elastance.

FIGURE 6.12: Systolic and diastolic blood pressures (SBP and DBP) at the aortic level obtained from simulations wherein two of the most relevant parameters of the hypertensive scenario are combined together. Computed value and percentage difference with respect to the complete hypertensive setup are reported for each studied case. In the main diagonal, values for the adaptation of only one parameter/compartment of the hypertensive scenario are reported.

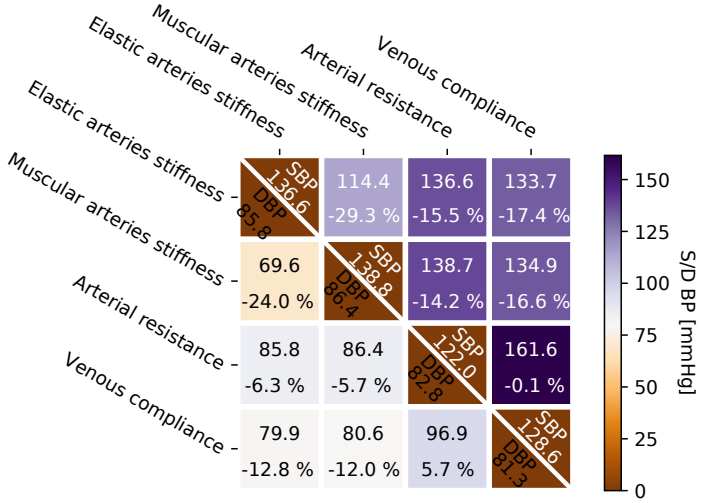

FIGURE 6.13: Mean blood pressure (MBP) and pulse pressure (PP) at the aortic level obtained from simulations wherein two of the most relevant parameters of the hypertension scenario are combined together. Computed value and percentage difference with respect to the complete hypertensive setup are reported for each studied case. In the main diagonal, values for the adaptation of only one parameter/compartment of the hypertensive scenario are reported.

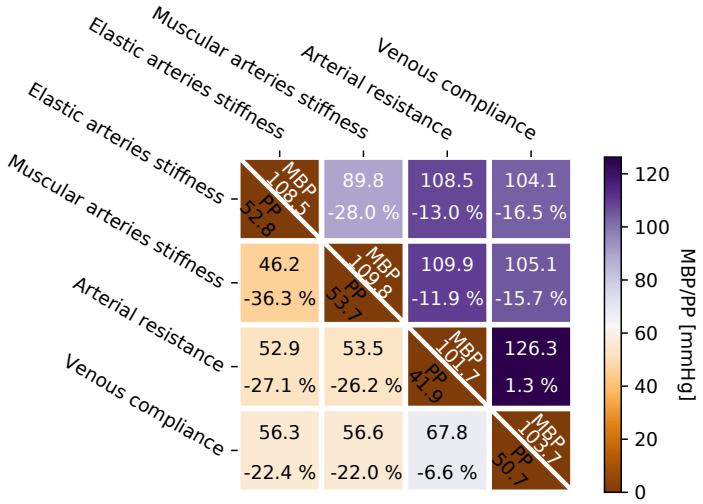

FIGURE 6.14: Systolic, diastolic, mean and pulse pressure at the aortic level. Normotensive condition is compared with complete hypertensive setup and four different scenarios wherein most relevant modifications are combined into three by three: stiffness of elastic arteries (SE), stiffness of muscular arteries (SM), increased arterioles resistance (R_{al}), reduced venous compliance (C_{vn}). Computational results are compared to literature data about normotensive group (N_{Lit}), pre-hypertensive (Pre-H_{Lit}) and stage I hypertensive patients (H_{Lit}) patients from [2].

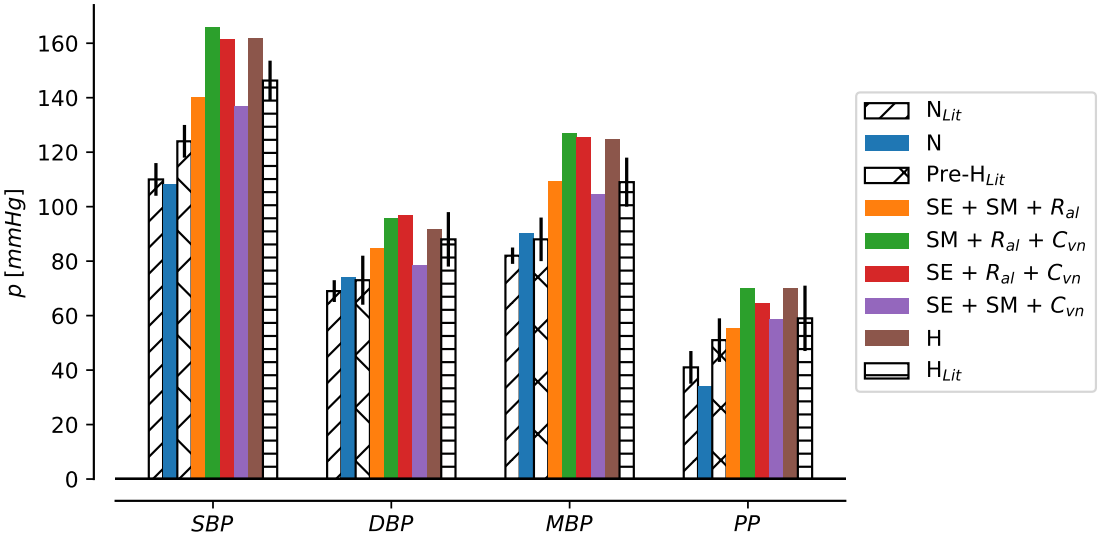

Effects on cardiac index: the role of reduced venous compliance

Concerning cardiac index, it is decreased in all configurations, except for reduced venous compliance, which causes a significant increase in cardiac output, and for variation of active elastance of the heart, which slightly modifies it. Considering two changes applied together (Figure 6.16), we can observe that cardiac index is higher than in the complete hypertensive scenario when reduced venous compliance is combined with other changes. Stiffening of elastic or muscular arteries combined with arterial resistance results in lower cardiac index. As already pointed out, the scenarios which include increased arterial resistance and reduced venous compliance return values of pressure similar to the complete hypertensive scenario. This consideration holds also for the cardiac index. When stiffening of elastic and muscular arteries is combined with increased arteriolar resistance the cardiac index is reduced by 5.5% with respect to the normotensive case; on the other hand, when it is combined with reduced venous compliance the cardiac index increases by 16.0%. Liang et al. [158] observed that cardiac index was dominated by heart period and moderately influenced by arteriolar radius; in that analysis, the venous compliance was not considered but our results poses attention on its role. The negative correlation between cardiac output and venous compliance is in line with [300]. Mean arterial pressure is the product between cardiac output and systemic vascular resistance; hence, high blood pressure is the result of an increase in cardiac output, or in systemic resistance, or both. Following the theoretical observations by Folkow [92], that in turn are based on Guyton's system-analysis [112], the initial elevation of resistance can ensue from either an initial increase of smooth muscle activity in the resistance vessels, followed by structural autoregulation or by an initial structural alteration. On the other side, increased cardiac output as hypothetical hypertension precursor could ensue from selective chronotropic-inotropic cardiac stimulation, but more likely it follows from elevated venous return, which in turn could be caused by increased filling of the system and/or reduced capacitance/compliance of the system. The increased cardiac output is then followed by an overall resistance elevation, according to the "whole-body autoregulation" mechanisms proposed by Guyton. Schmieder [258] analysed haemodynamic, volume and cardiac structural differences between a normotensive control group and patients

FIGURE 6.15: Percentage change in cardiac index (CI), arterial elastance (E_a), left ventricular elastance (E_{es}) and the ratio E_a/E_{es}. Nine scenarios are considered, each one refers to the adaptation of only one parameter/compartment of the hypertensive scenario.

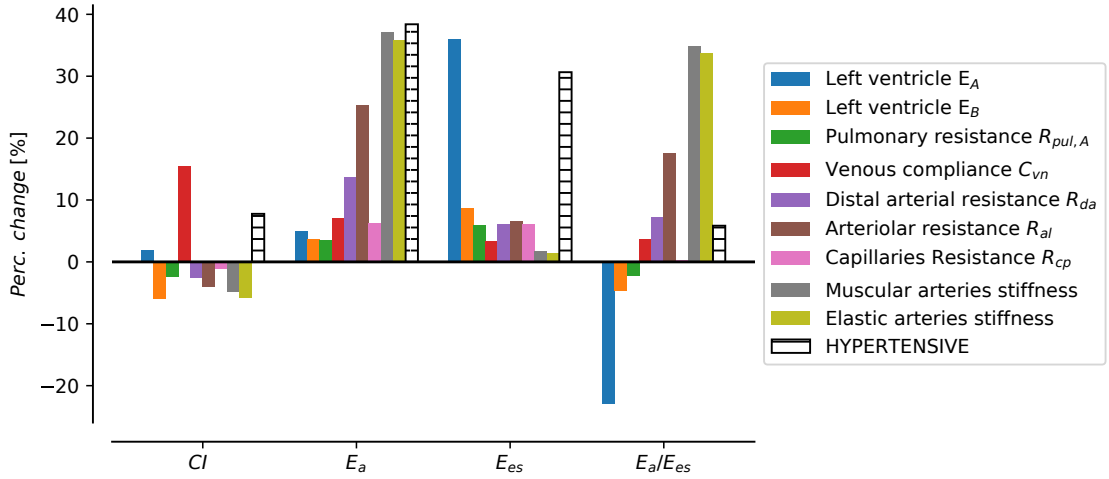

with different degrees of arterial hypertension. He found that borderline hypertensive patients were characterized by increased central blood volume, stroke volume and cardiac output without significant changes in vascular resistance. On the other hand, in established hypertension, total peripheral resistance was significantly increased while cardiac output is normal compared to the normotensive control group. From our computational results, we can conclude that decreased venous compliance contributes in increasing cardiac output and hence it could play a role in the early phase of hypertension, but also in established hypertension, to compensate the decrease caused by increased vascular resistance. There is evidence in the literature about the role of venous tone in the development of hypertension. Martin et al. [184] studied the initial stages of spontaneously hypertensive rats and compared them to normotensive Wistar-Kyoto rats in order to test the hypothesis that venous tone is elevated in the early stage of hypertension. They observed that mean circulatory filling pressure was elevated in hypertensive rats at an early stage; moreover, impairment of autonomic function by ganglionic blockade abolished the elevated venous tone, suggesting that these differences were neurally mediated. Delaney et al. [74] observed that limb venous compliance was similar between hypertensive humans and healthy controls; however, venous capacitance was reduced in pathological subjects. In addition, in order to examine venous tone and its responsiveness in hypertensive humans, they found that venous compliance was not acutely altered by endothelium-independent venodilation or non-baroreflex-mediated sympatho-excitation in the hypertensive group, while forearm volume was significantly increased in response to nitroglycerin, which may suggest chronically increased venous tone. Decreased vascular capacitance is most marked in the veins outside the central compartment, and is particularly notable in the splanchnic circulation [222]. Small veins and venules in this body region represent the major part of peripheral venous circulation and exhibit the highest degree of active venoconstriction [105]. Therefore, factors regulating venomotor tone in the entire circulation, and in particular sympathetic venoconstrictor activity in these vessels, are critical in determining active changes in capacitance. Venous smooth muscle tone and vascular capacitance contribute to long-term blood pressure regulation [89]; moderately increased sympathetic nervous system activity could contribute to the development of hypertension by reducing vascular capacitance. This hypothesis has been supported both in humans [132] and animals studies [184].

FIGURE 6.16: Arterial elastance (E_a) and cardiac index (CI) obtained from simulations wherein two of the most relevant parameters of the hypertensive scenario are combined together. Computed value and percentage difference with respect to the complete hypertensive setup are reported for each studied case. In the main diagonal, values for the adaptation of only one parameter/compartment of the hypertensive scenario are reported.

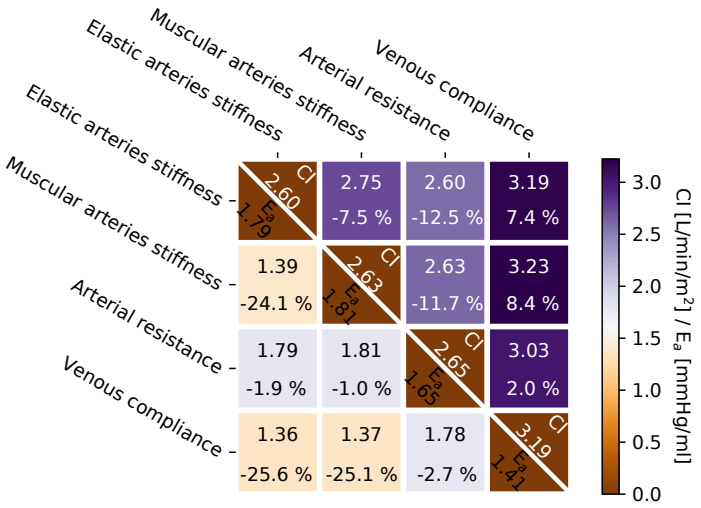

6.4 Conclusions

We have introduced the functional and structural changes that are cause/consequence of arterial hypertension into a global multiscale closed-loop model of the entire circulation in order to theoretically establish the interplay between different vascular compartments in the pathological state. To the best of our knowledge, this is the first time that this disease is studied in a global closed-loop context by means of a model which comprises both one-dimensional representation of main large to medium size arteries and other major compartments of the blood circulation, in particular the venous system, that is represented by means of one-dimensional sytems of equations for major veins and zero-dimensional models for small veins and venules. In a previous mathematical work [158], the authors focused on one-dimensional network of arteries to assess the wave propagation and the increase in wave velocity that is usually observed in hypertensive patients; even if they used a closed-loop model, they did not considered the effect of reduced venous compliance. Another completely lumped-parameter approach was adopted in global models for system analysis of arterial pressure, such as the work by Guyton [112]. The work presented in this chapter permits to study both the wave propagation in the arterial system and the function of the venous circulation in developing high blood pressure and controlling cardiac output. To this end, we have assessed the contribution of individual modifications to the cardiovascular system on the arterial pressure; computational results sustain experimental evidences on the influence of reduced total effective vascular compliance in the early stage of the disease. Moreover, the assessment of combined modifications in the hypertensive scenario revealed that increased arterial resistance combined with reduced venous compliance leads to the highest increase in arterial pressure with slightly increased cardiac index. Regarding cardiac index in hypertension, we observed that it slightly increases when both the systolic and end-diastolic wall stresses of left ventricle are normalized; this happens when cardiac remodelling is combined with reduced venous compliance which increases venous filling pressure. An important aspect of this work is the introduction of total blood volume, which comprises both stressed and unstressed components, that together with vascular capacitance, play a role in the determination of arterial pressure. The short-term regulation of pressure due

to baroreflex has been introduced in the global model and reset to high blood pressure levels in the hypertensive scenario. The leading role of the baroreflex in short-term regulation of arterial pressure is well established in the literature; more recent studies have raised doubts about its complex and long-term role in hypertension. Its introduction in the global model of circulation represents an added value for the study of hypertension. In fact, its role is crucial for estimating total effective vascular compliance. As pointed out in a previous work [51], the physiological parametrization of the mathematical model, in particular the assignment of physical compliance and unstressed volume in different vascular compartments, is necessary but not sufficient for the determination of total effective vascular compliance in agreement with experimental data [171]; major physiological mechanisms, in particular the short-term control of arterial pressure, are needed to obtain modelling results that are in agreement with observed variations in mean arterial pressure, cardiac output, heart rate, and cardiopulmonary blood volume during the infusion test. A major limitation of this work is that haemodynamic changes on the global model due to hypertension were calibrated to population-averaged data or previous mathematical studies. However, haemodynamic conditions largely differ among patients, due to age, weight, to name but a few; patient-specific characteristics and remodelling could improve the model-based theoretical insights on specific hypertensive status. To be viable, large data support from *i*n vivo studies would be required. A step forward could be done considering different hypertensive scenarios, at different ages and stages of the disease. Another aspect which deserves attention is the role played by other regulatory systems of arterial pressure, in particular the body fluids control in long-term regulation and its implication in the hypertension of renal origin. Future works could address the interaction between blood volume and extracellular fluids, as well as their regulation. The role played by the microcirculation in hypertension, as well as in ageing, is a popular topic in the clinical literature [257, 239, 232, 209, 156, 129]. In this work, the microcirculation was simplified as lumped resistor-capacitor compartments. Remodelling in the microcirculation due to hypertension involves structural modifications and rarefaction processes that are simply translated into an increase in vascular resistance. However, a more realistic microvascular networks model would better capture the consequence of the remodelling. In the clinic, an open question remains about the microcirculation: is it affected in the same way in all vascular sites? Especially for capillaries, it can be possible to measure their pressure only in the skin. Mathematical models could help in elucidating this issue. Furthermore, little attention has been given to the cerebral circulation in this work; even if we are including the cerebral autoregulation and the shift on the right of the its curve, we did not focus on a detailed analysis on the effects of hypertension in this crucial region of the circulation. Future work will address this topic.

Chapter 7

Conclusions

In this chapter we will discuss the achievements reached through the results presented in this thesis. Furthermore, we will suggest several aspects that could be improved motivated by the encountered limitations of the current works, as well as possible topics to be considered in future development.

7.1 Achievements

The discussion in this section is divided in three parts: the first one focuses on computational modelling of global haemodynamics, the second part stresses the achievements about mathematical modelling for the interaction between blood and cerebrospinal fluid dynamics, while the last part is centred on arterial hypertension modelling.

7.1.1 Computational modelling of global haemodynamics

The work developed during this PhD project is based on a global closed-loop multiscale mathematical model of human circulation. This model departs from the Müller-Toro mathematical model [201, 202] for the global systemic and pulmonary circulations in the entire human body. It includes a one-dimensional representation of large to medium arteries and veins and lumped-parameter description of other districts of the circulation (microvasculature, heart and pulmonary circulation). With respect to the original Müller-Toro model, several improvements were introduced, both on physiological aspects of the circulatory system as well as on numerical strategies to solve the governing equations. Concerning the physiological processes considered in the present thesis, the improvements regard the application of viscoelastic tube laws for both the arterial and venous circulations, a more complete heart model, the parametrization of the vascular beds with the introduction of nonlinear behaviour of resistances and compliances in the venous microvasculature, the physiological parametrization of vascular compliances and total distribution of blood volume and the introduction of short-term mechanisms of pressure and flow regulation.

When the arterial and venous networks are equipped with viscoelastic tube laws, rather than the elastic ones, computational results of pressure and flow waveforms are more realistic. The heart model was improved by the introduction of new cardiac valves models, based on [216]. The parametrization of vascular beds was made more general, based on total resistance and compliance distribution along different vascular territories; in this way, other vascular beds can be easily added to the network. Moreover, the introduction of the nonlinear behaviour of the pressure-volume curve of the venous 0D compartments, as well as the nonlinear characterization of the resistances according to blood volume, enables to better reproduce the physiological deviations of the venous system from the baseline situation, as in the case of a blood infusion test. In order to have a physiological quantification of the amount of blood in the vasculature, we introduced the unstressed components of blood volume in all vascular compartments together with a physiological distribution of vascular compliances; to the best of the author's knowledge, this is the first

multiscale model of the human cardiovascular system that poses attention on the total amount of blood volume and its distribution. Two regulatory mechanisms were introduced in this thesis: the cerebral autoregulation and the high- and low-pressure baroreceptors for the short-term regulation of arterial pressure. The cerebral autoregulation model is relevant when studying anatomical malformations of the cerebral circulation while the effects of the baroreflex in controlling main cardiovascular indexes, such as mean arterial pressure and cardiac output, are evident when hemorrhage or blood infusion tests are simulated.

Regarding the numerical methodology adopted in this work, the physiological introduction of the viscoelastic nature of all major blood vessels implies dealing with parabolic systems of equations, that are approximated by hyperbolic systems with stiff source terms. A numerical improvement regards the involvement of the local time stepping technique; as shown in [207], the local time step selection in a vessel-wise fashion with respect to a global time step reduces the computational cost of a simulation. The benefit of using this strategy is of particular importance when coupling the blood circulation to the CSF and brain dynamics, as the computational time needed to reach periodicity of the solution is large due to different time scales of the coupled systems.

In light of the physiological aspects considered in this thesis and of the computational results, some general considerations on cardiovascular modelling in the global context can be done. Our global multiscale model of the entire human circulation is characterized by a large number of parameters that aim to reproduce the circulatory physiology; generally these parameters are based on the effective behaviour of the cardiovascular system. However, good estimation of physical parameters is necessary but not sufficient to obtain computational results in agreement with medical evidence, especially when considering medical experiments or pathological conditions that introduce large deviations from the baseline healthy condition. In these situations, it becomes necessary to reproduce the nonlinear behaviour of the physiological processes to avoid a wrong response of the model with respect to the actual sensitivity of physiological processes to the modelled situation. Moreover, the human body is endowed with several regulatory mechanisms that act at different temporal scales and locations to maintain the normal physiological equilibrium. Major physiological mechanisms must be considered in the mathematical framework to well capture the physiology of our body. Our mathematical model represents a step forward in the understanding of the global haemodynamics and it represents a useful tool to address many pathophysiological conditions associated with the circulatory system, involving both the arterial and the venous systems. In this thesis, we focused on the effects of abnormalities in the venous circulation on the cerebral dynamics and arterial hypertension; in the following, we discuss each one of these fields.

7.1.2 Mathematical modelling of the cerebrospinal fluid system and its interaction with the blood circulation

One of the main novelties of this thesis is the coupling of the blood circulation to refined mathematical models of the cerebrospinal fluid dynamics in the craniospinal cavities. The CSF model comprises the cerebral ventricles, the aqueduct of Sylvius, the cranial subarachnoid space and the brain parenchyma, represented by means of lumped-parameter models. Concerning the spinal column, we considered two models with different mathematical complexity: the first one comprises a single lumped-parameter compartment while the second version includes a coaxial one-dimensional model representing the spinal cord surrounded with the subarachnoid space. The Monro-Kellie hypothesis, which states that the intracranial volume inside the cranial cavity is constant, was considered in its classical form and also in a relaxed version which admits small variations in time and reproduces the exponential-like behaviour of intracranial pressure with respect to volume changes. Moreover, the nonlinearity of the pressure-volume relationships was introduced also at the level of the spinal subarachnoid space.

Our mathematical model helps in providing useful insight into the cerebrospinal fluid dynamics and its interaction with the cerebral circulation. We simulated healthy and pathological scenarios to understand the main determinants of intracranial pressure waveform, as well as the temporal coupling and dynamics of variables of interest of arterial, venous and CSF compartments. Computational results confirm that intracranial pressure is the result of a dynamic interaction between the CSF production, the arterial pulsation, the venous reabsorption of CSF and the ability of the spinal subarachnoid space in accommodating the displaced CSF from the cranial spaces. This interaction is reflected in the intracranial pressure waveform with its physiological landmark peaks, both in healthy and pathological conditions. Particular emphasis was placed on the consequences of abnormalities in the head and neck venous network which impair the normal venous drainage from the brain back to the heart. Due to venous hypertension, CSF absorption into the venous system is hampered, leading to intracranial hypertension in order to maintain the balance between CSF generation and absorption. The severity of the consequences of venous outflow obstructions depends on the balance between CSF generation and absorption, the compliance of the craniospinal CSF systems and the ability of the venous network in developing collateral routes.

The mathematical model presented in this thesis provides the basis for a more general holistic, multiscale closed-loop mathematical model which includes networks of arteries, veins, the cerebrospinal fluid system and the representation of all other extracellular body fluids.

7.1.3 Mathematical modelling of arterial hypertension

Hypertension remains a major and growing global public health issue; it is a silent, invisible killer, one of the key risk factors for cardiovascular diseases, stroke, kidney failure and premature mortality and disability. Despite the wide range of available pharmacological approaches and/or device-based and procedural interventions to blood pressure lowering, the high variability in response to these therapies indicates that the pathophysiology is still not completely understood.

One of the goals of this thesis was that of contributing to a better understanding of the pathophysiological mechanisms in hypertension. To this end, we adapted the global closed-loop model of the entire circulation to an hypertensive scenario which includes the main hypertension-induced/inducing alterations in the cardiovascular system. The main novelty of this work with respect to previous published mathematical models of hypertension is the global approach to the study of the disease. This implied dealing with the contribution of the venous system, the introduction of total blood volume and the determination of total effective vascular compliance. Moreover, we also considered how the cerebral autoregulation and baroreflex control are reset in hypertensive condition. Computational results showed the predominant role of arterial resistance and vascular compliance in determining blood pressure increase, with the venous compliance contributing in the normalisation of cardiac index in hypertension. The computational study presented in this thesis is an initial step to deepen our knowledge on the pathophysiology of essential hypertension through mathematical models; other improvements need to be considered to enhance the predictive character of this tool. To this end, a big issue is the lack of large data support from in vivo studies; more detailed physiological experiments would be required to better parametrize the model and/or include additional physiological aspects.

7.2 Future works

Mathematical models are useful tools to improve the understanding of the interactive dynamics between body fluid systems. During this PhD project, we focused on the cardiovascular and the cerebrospinal fluid systems, in healthy and pathological states, and we explored the arterial hypertension condition; both topics were treated in the context of a global multiscale modelling approach. Although the adopted

model offers a wide range of applications as it is, several aspects can be improved or introduced to enlarge the number of physiological processes included in the model, as well as the possibility of studying the pathophysiology of several medical conditions. A first improvement would be the modelling of postural changes. Viscoelastic properties in the venous circulation represent an added component for the project of simulating transient phases during postural changes. Indeed, when standing from supine position, the veins below the right atrium are exposed to positive hydrostatic pressure and are distended by the pressure within them while veins above heart level experience negative transmural pressure and will collapse; under this condition, the wave speed for veins in the collapse region will lead to transcritical flows. The algorithm used to treat junctions in case of elastic vessels [201] is unable to deal with Riemann problems for trans/supercritical flow regime. As a work-around, one can exploit the introduction of viscoelasticity. Indeed, the wave speed associated to the viscoelastic tube law depends on the relaxation parameter and it tends to infinity as such parameter tends to zero. Therefore, sufficiently small relaxation parameter should avoid to fall into situations of regime changes. Adopting viscoelastic properties in the venous circulation, as well as considering the short-term regulation of arterial pressure, poses the basis for future investigations about the cardiovascular system and its interaction with the cerebrospinal fluid in upright position. The second aspect to be introduced in the model is the modelling of temporal variation of intrathoracic and abdominal pressures; the fluctuations caused by the respiration affect the pulsatility of the venous blood flow and the cerebrospinal fluid pressure. Another aspect that would deserve attention is to provide nutrients, oxygen, carbon dioxide and solutes to the body; to this end, a model for solute transport and exchange, as well as metabolism model, should be incorporated in a global multiscale framework. Some topics that could be deepened in this context are brain waste clearance and how it is disrupted by impaired venous drainage, as well as the metabolic mechanism of cerebral autoregulation which depends on the concentration of cerebral carbon dioxide. Of particular interest for a more complete analysis of arterial hypertension would be the introduction of different regulatory mechanisms, such as the long-term control of arterial pressure (the renal-body fluid system) and the interaction between blood volume and extracellular fluid. The kidneys have a primary role in long-term control of arterial pressure and abnormal kidney function is a key feature of all forms of chronic hypertension; therefore, a first step towards this direction would be including a refined description of the kidney's vasculature with its blood flow regulation based on two mechanisms, the myogenic response and the tubuloglomerular feedback. A last but not least point regards the brain in hypertension; in this thesis, little care was given to this particular region of the circulation. However, the brain is known to be an early target for organ damage due to hypertension: small vessel disease, white matter lesions, lacunar infarcts, cognitive impairment, accelerated atrophy are some of the effects on brain functioning caused by hypertension. Moreover, recent medical breakthrough [314] showed that congenital cerebral vascular variations, such as decreased vertebral artery diameters and variants in the posterior circle of Willis, are tightly coupled to the development of arterial hypertension and may play an important role in triggering high blood pressure. The mathematical model presented in this thesis offers a practical tool to quantify the cause/consequences of arterial hypertension on cerebral circulation.

Appendix A

Geometry of 1D vessels' networks

Tables A.1 and A.2 report geometrical data for arteries and veins networks. The first columns refer to number, name, length and radii of each vessel while the last one show the location of the vessel in the human body (using the same location codes of [201], 1=Dural sinuses, 2=Extracranial, 3=Neck, 4=Thorax, 5=Abdomen, 6=Upper limbs, 7=Lower limbs, 8=Pelvis, 9=Intracranial). Geometrical data are the same of [201, 202, 297] while, for vessels added or changed in this work, the geometry is estimated from literature data [29, 186].

TABLE A.1: Geometrical and mechanical parameters of the arterial network. R^T is given in mmHg s/ml while C_{art} in ml(s mmHg)$^{-1}$.

No	Vessel name	L (cm)	r_0 (cm)	r_1 (cm)	R^T	C_{art}	Loc
1	Ascending aorta	2	1.525	1.42	-	-	4
2	Aortic arch	3	1.42	1.342	-	-	4
3	Brachiocephalic a.	3.5	0.65	0.62	-	-	4
4	R. subclavian a.	3.5	0.425	0.407	-	-	6
5	R. carotid a.	17.7	0.4	0.37	-	-	3
6	R. vertebral a.	13.5	0.15	0.136	-	-	3
7	R. subclavian a.	39.8	0.407	0.23	-	-	6
8	R. radius	22	0.175	0.14	40.3876	0.0059	6
9	R. ulnar a.	6.7	0.215	0.215	-	-	6
10	Aortic arch	4	1.342	1.246	-	-	4
11	L. carotid a.	20.8	0.4	0.37	-	-	3
12	Thoracic aorta	5.5	1.246	1.124	-	-	4
13	Thoracic aorta	10.5	1.124	0.924	-	-	4
14	Intercostal a.	7.3	0.3	0.3	10.7761	0.0586	4
15	L. subclavian a.	3.5	0.425	0.407	-	-	6
16	L. vertebral a.	13.5	0.15	0.136	-	-	3
17	L. subclavian a.	39.8	0.407	0.23	-	-	6
18	L. ulnar a.	6.7	0.215	0.215	-	-	6
19	L. radius	22	0.175	0.14	40.8837	0.0059	6
20	Celiac a.	2	0.35	0.3	-	-	5
21	Celiac a.	2	0.3	0.25	-	-	5
22	Hepatic a.	6.5	0.275	0.25	27.8243	0.0089	5
23	Splenic a.	5.8	0.175	0.15	41.2558	0.0059	5
24	Gastric a.	5.5	0.2	0.2	18.0678	0.0139	5
25	Abdominal aorta	5.3	0.924	0.838	-	-	5
26	Sup. mesenteric a.	5	0.4	0.35	7.1584	0.0342	5

27	Abdominal aorta	1.5	0.838	0.814	-	-	5
28	R. renal a.	3	0.275	0.275	8.8134	0.0287	5
29	Abdominal aorta	1.5	0.814	0.792	-	-	5
30	L. renal a.	3	0.275	0.275	8.8134	0.0287	5
31	Abdominal aorta	12.5	0.792	0.627	-	-	5
32	Inf. mesenteric a.	3.8	0.2	0.175	52.3507	0.0075	5
33	Abdominal aorta	8	0.627	0.55	-	-	5
34	R. com. iliac a.	5.8	0.4	0.37	-	-	8
35	R. ext. iliac a.	14.5	0.37	0.314	-	-	8
36	R. int. iliac a.	4.5	0.2	0.2	42.8843	0.0077	8
37	R. deep femoral a.	11.3	0.2	0.2	25.902	0.0485	7
38	R. femoral a.	44.3	0.314	0.275	-	-	7
39	R. ext. carotid a.	4.1	0.2	0.15	-	-	2
40	L. int. carotid a.	17.6	0.25	0.2	-	-	3
41	R. post. tibial a.	34.4	0.175	0.175	57.3809	0.0211	7
42	R. ant. tibial a.	32.2	0.25	0.25	25.7857	0.0485	7
43	R. interosseous a.	7	0.1	0.1	644.368	0.0018	6
44	R. ulnar a.	17	0.203	0.18	40.9859	0.0059	6
45	L. ulnar a.	17	0.203	0.18	40.9859	0.0059	6
46	L. interosseous a.	7	0.1	0.1	644.368	0.0018	6
47	R. int. carotid a.	17.6	0.25	0.2	-	-	3
48	L. ext. carotid a.	4.1	0.2	0.15	-	-	3
49	L. com. iliac a.	5.8	0.4	0.37	-	-	8
50	L. ext. iliac a.	14.5	0.37	0.314	-	-	8
51	L. int. iliac a.	4.5	0.2	0.2	42.8843	0.0077	8
52	L. deep femoral a.	11.3	0.2	0.2	25.902	0.0485	7
53	L. femoral a.	44.3	0.314	0.275	-	-	7
54	L. post. tibial a.	34.4	0.175	0.175	57.3809	0.0211	7
55	L. ant. tibial a.	32.2	0.25	0.25	25.7857	0.0485	7
56	Basilar a.	0.96	0.162	0.162	-	-	1
57	R. post. cerebral. a.	0.5	0.107	0.107	-	-	1
58	R. post. cerebral. a.	8.6	0.105	0.105	46.3595	0.0029	1
59	R. post. communicating a.	1.5	0.073	0.073	-	-	1
60	R. int. carotid a.	0.5	0.2	0.2	-	-	1
61	R. mid. cerebral a.	11.9	0.143	0.143	22.5727	0.0059	1
62	R. ant. cerebral a.	1.2	0.117	0.117	-	-	1
63	R. ant. cererbal a.	10.3	0.12	0.12	45.0952	0.0029	1
64	Ant. communicating a.	0.3	0.1	0.1	-	-	1
65	L. ant. cerebral a.	10.3	0.12	0.12	45.0952	0.0029	1
66	L. ant. cerebral a.	1.2	0.117	0.117	-	-	1
67	L. mid. cerebral a.	11.9	0.143	0.143	22.5727	0.0059	1
68	L. int. carotid a.	0.5	0.2	0.2	-	-	1
69	L. post. communicating a.	1.5	0.073	0.073	-	-	1
70	L. post. cerebral a.	8.6	0.105	0.105	46.3595	0.0029	1
71	L. post. cerebral a.	0.5	0.107	0.107	-	-	1
72	L. ext. carotid a.	6.1	0.2	0.2	-	-	3

73	R. ext. carotid a.	6.1	0.2	0.2	-	-	3
74	L. sup. thyroid a.	10.1	0.1	0.1	228.82	0.0016	3
75	R. sup. thyroid a.	10.1	0.1	0.1	228.82	0.0016	3
76	L. superf. temporal a.	6.1	0.16	0.16	-	-	2
77	R. superf. temporal a.	6.1	0.16	0.16	-	-	2
78	L. maxillary a.	9.1	0.11	0.11	190.278	0.0016	2
79	R. maxillary a.	9.1	0.11	0.11	190.278	0.0016	2
80	L. superf. temp. fron. bran.	10	0.11	0.11	11379.1	0.0016	2
81	R. superf. temp. fron. bran.	10	0.11	0.11	190.278	0.0016	2
82	L. superf. temp. pari. bran.	10.1	0.11	0.11	190.278	0.0016	2
83	R. superf. temp. pari. bran	10.1	0.11	0.11	11379.1	0.0016	2
169	R. facial a.	11.6	0.13	0.13	207.502	0.0063	2
170	L. facial a.	11.6	0.13	0.13	207.502	0.0063	2
274	Basilar a. II	0.386	0.162	0.162	-	-	1
275	R. Labyrinthine artery	1	0.01	0.01	377411	0.0006	1
278	L. Labyrinthine artery	1	0.01	0.01	377421	0.0006	1
285	R. PICA I	1	0.0433	0.0433	-	-	1
286	L. PICA I	1	0.0433	0.0433	-	-	1
287	R. SCA	1	0.0558	0.0558	111.364	0.0006	1
288	L. SCA	1	0.0558	0.0558	111.368	0.0006	1
293	L. Vertebral artery II	0.75	0.15	0.136	-	-	3
294	R. Vertebral artery II	0.75	0.15	0.136	-	-	3
304	R. AICA I	1.4	0.0366	0.05	-	-	1
305	L. AICA I	1.4	0.0366	0.05	-	-	1
306	R. AICA II	2.35	0.0366	0.05	468.13	0.0006	1
307	L. AICA II	2.35	0.0366	0.05	468.23	0.0006	1
308	R. PICA MB	1	0.0216	0.0216	17099.13	0.0006	1
309	L. PICA MB	1	0.0216	0.0216	17099.13	0.0006	1
310	R. PICA II	1	0.0433	0.0433	646.13	0.0006	1
311	L. PICA II	1	0.0433	0.0433	646.13	0.0006	1
312	R. ASA	1	0.048	0.048	1509.03	0.0006	1
313	L. ASA	1	0.048	0.048	1509.03	0.0006	1
314	R. VA III	0.75	0.15	0.136	-	-	3
315	L. VA III	0.75	0.15	0.136	-	-	3
316	R. pontine a. I	1	0.012	0.012	91716.93	0.0006	1
317	R. pontine artery II	1	0.012	0.012	91596.94	0.0006	1
318	L. pontine a. I	1	0.012	0.012	91716.93	0.0006	1
319	L. pontine artery II	1	0.012	0.012	91596.94	0.0006	1
320	BA III	0.386	0.162	0.162	-	-	1
321	BA IV	0.386	0.162	0.162	-	-	1
322	BA V	0.386	0.162	0.162	-	-	1
323	BA VI	0.386	0.162	0.162	-	-	1

TABLE A.2: Geometrical and mechanical parameters of the venous network. R_{vn} is given in mmHg s/ml while C_{vn} in ml(s mmHg)$^{-1}$.

No	Vessel name	L (cm)	r_0 (cm)	r_1 (cm)	R_{vn}	C_{vn}	Loc
84	Sup. vena cava	1.5	0.8	0.8	-	-	4
85	Sup. vena cava	2	0.8	0.8	-	-	4
86	R. brachiocephalic v.	4	0.564	0.564	-	-	4
87	L. brachiocephalic v.	7.5	0.535	0.535	-	-	4
88	L. subclavian v. I	3	0.564	0.564	-	-	6
89	R. subclavian v. I	3	0.564	0.564	-	-	6
90	R. ext. jugular v.	10	0.252	0.252	-	-	3
91	L. ext. jugular v.	10	0.252	0.304	-	-	3
92	R. int. jugular v.	2.5	0.399	0.399	-	-	3
93	L. int. jugular v.	2.5	0.564	0.618	-	-	3
94	L. vertebral v.	11	0.138	0.16	-	-	3
95	R. vertebral v.	11	0.138	0.16	-	-	3
96	R. deep cervical v.	13	0.16	0.16	-	-	3
97	L. deep cervical v.	13	0.16	0.16	-	-	3
98	Vertebral venous plexus	71	0.368	0.368	-	-	3
99	R. sigmoid sinus	3.5	0.252	0.252	-	-	1
100	L. sigmoid sinus	3.5	0.357	0.378	-	-	1
101	R. trans. sinus	3.5	0.178	0.252	-	-	1
102	L. trans. sinus	3.5	0.309	0.357	-	-	1
103	Sup. sagittal sinus	2.5	0.35	0.367	-	-	1
104	Straight sinus	4	0.25	0.25	-	-	1
105	Inf. sagittal sinus	3.67	0.16	0.16	-	-	1
106	Vein of Galen	0.6	0.366	0.4	-	-	9
107	L. int. cerebral v.	5	0.126	0.126	5.369	0.0539	9
108	R. int. cerebral v.	5	0.126	0.126	5.369	0.0539	9
109	L. basal v. of Rosenthal	1	0.126	0.126	5.369	0.0539	9
110	R. basal v. of Rosenthal	1	0.126	0.126	5.369	0.0539	9
111	R. sup. petrosal sinus	3.7	0.149	0.149	-	-	1
112	L. sup. petrosal sinus	3.7	0.149	0.149	-	-	1
113	R. inf. petrosal sinus	3.2	0.08	0.16	-	-	1
114	L. inf. petrosal sinus	3.2	0.08	0.16	-	-	1
115	R. post. auricular v.	5	0.08	0.08	15.817	0.0119	2
116	L. post. auricular v.	5	0.08	0.08	15.817	0.0119	2
117	R. post. retromandibular v.	3.52	0.25	0.25	-	-	2
118	L. post. retromandibular v.	3.52	0.25	0.25	-	-	2
119	R. ant. retromandibular v.	3.15	0.235	0.235	-	-	2
120	L. ant. retromandibular v.	3.15	0.235	0.235	-	-	2
121	R. retromandibular v.	4.5	0.26	0.26	-	-	2
122	L. retromandibular v.	4.5	0.26	0.26	-	-	2
123	R. facial v.	6	0.132	0.178	-	-	2
124	L. facial v.	6	0.132	0.178	-	-	2
125	R. com. facial v.	0.9	0.18	0.18	-	-	2

126	L. com. facial v.	0.9	0.18	0.18	-	-	2
127	R. superf. temp. v.	5	0.19	0.19	2.119	0.5042	2
128	L. superf. temp. v.	5	0.19	0.19	2.119	0.5042	2
129	R. maxillary v.	1	0.175	0.175	-	-	2
130	L. maxillary v.	1	0.175	0.175	-	-	2
131	R. deep facial v.	0.9	0.25	0.25	-	-	2
132	L. deep facial v.	0.9	0.25	0.25	-	-	2
133	R. emissary v.	3	0.1	0.1	-	-	2
134	L. emissary v.	3	0.1	0.1	-	-	2
135	R. pterygoid plexus	0.9	0.15	0.15	-	-	2
136	L. pterygoid plexus	0.9	0.15	0.15	-	-	2
137	R. marginal sinus	4	0.1	0.1	-	-	1
138	L. marginal sinus	4	0.1	0.1	-	-	1
139	Occipittal sinus	3.5	0.235	0.235	-	-	1
140	R. ext. jugular v.	10	0.252	0.252	-	-	3
141	R. mastoid emissary v.	7.2	0.175	0.175	-	-	2
142	L. mastoid emissary v.	7.2	0.175	0.175	-	-	2
143	R. post. condylar v.	3	0.315	0.315	-	-	2
144	L. post. condylar v.	3	0.315	0.315	-	-	2
145	R. subocc. sinus	1	0.45	0.45	-	-	2
146	R. lat. ant. condylar v.	3	0.315	0.315	-	-	2
147	L. lat. ant. condylar v.	3	0.315	0.315	-	-	2
148	L. ext. jugular v.	10	0.304	0.357	-	-	3
149	Sup. sagittal sinus	4.33	0.229	0.258	-	-	1
150	R. Labbe v.	5	0.15	0.15	3.622	0.0539	9
151	L. Labbe v.	5	0.15	0.15	3.622	0.0539	9
152	Sup. sagittal sinus	4.33	0.258	0.287	-	-	1
153	Sup. sagittal sinus	2.5	0.334	0.35	-	-	1
154	L. cavernous sinus	1.5	0.1	0.1	-	-	1
155	R. cavernous sinus	1.5	0.1	0.1	-	-	1
156	Occipittal v.	5	0.126	0.126	-	-	2
157	Sup. sagittal sinus	5	0.3	0.334	-	-	1
158	Cerebral vein	5	0.15	0.15	3.622	0.0207	9
159	Cerebral vein	5	0.15	0.15	3.622	0.0207	9
160	Azygos v.	2	0.425	0.425	-	-	4
161	Cerebral vein	5	0.15	0.15	3.622	0.0207	9
162	Cerebral vein	5	0.15	0.15	3.622	0.0207	9
163	R. vertebral v.	5	0.16	0.16	-	-	3
164	L. vertebral v.	5	0.16	0.16	-	-	3
165	Sup. sagittal sinus	4.33	0.2	0.229	-	-	1
166	L. subocc. sinus	1	0.45	0.45	-	-	2
167	R. anastomotic v.	2	0.1	0.1	-	-	3
168	L. anastomotic v.	2	0.1	0.1	-	-	3
171	R. great saphenous v.	7.5	0.2215	0.23	-	-	7
172	L. great saphenous v.	7.5	0.2215	0.23	-	-	7
173	L. post. tibial v.	17.3	0.15	0.15	-	-	7

174	L. ant. tibial v.	16	0.15	0.15	-	-	7
175	R. popliteal v.	19	0.34	0.34	-	-	7
176	L. popliteal v.	19	0.34	0.34	-	-	7
177	L. femoral v.	25.4	0.35	0.35	-	-	7
178	R. femoral v.	25.4	0.35	0.35	-	-	7
179	R. deep femoral v.	12.6	0.35	0.35	0.51	2.8741	7
180	L. deep femoral v.	12.6	0.35	0.35	0.51	2.8741	7
181	R. ext. iliac v.	14.4	0.5	0.5	-	-	8
182	L. ext. iliac v.	14.4	0.5	0.5	-	-	8
183	L. int. iliac v.	5	0.15	0.15	3.622	3.5692	8
184	R. int. iliac v.	5	0.15	0.15	3.622	3.5692	8
185	R. com. iliac v.	2	0.575	0.575	-	-	8
186	L. com. iliac v.	2	0.575	0.575	-	-	8
187	R. radial v.	40.6	0.2	0.2	1.885	0.651448	6
188	L. interosseous v.	7	0.1	0.1	9.069	0.0372	6
189	R. ulnar v.	30.6	0.2	0.2	1.885	0.6514	6
190	L. ulnar v.	30.6	0.2	0.2	1.885	0.6514	6
191	L. interosseous v.	7	0.1	0.1	9.069	0.0372	6
192	L. radial v.	40.6	0.2	0.2	1.885	0.6514	6
193	L. subclavian v.	27	0.52	0.52	-	-	6
194	R. subclavian v.	27	0.52	0.52	-	-	6
195	L. subclavian v.	3	0.52	0.52	-	-	6
196	R. subclavian v.	3	0.52	0.52	-	-	6
197	L. ulnar v.	10	0.2	0.2	-	-	6
198	Inf. vena cava	15.3	0.7625	0.7625	-	-	5
199	Hepatic v.	6.8	0.485	0.485	0.229	82.3232	5
200	Inf. vena cava	1.5	0.7625	0.7625	-	-	5
201	inf. vena cava	1.5	0.7625	0.7625	-	-	5
202	Inf. vena cava	12.5	0.7625	0.7625	-	-	5
203	Inf. vena cava	8	0.7625	0.7625	-	-	5
204	R. com. iliac v.	3.8	0.575	0.575	-	-	8
205	L. com. iliac v.	3.8	0.575	0.575	-	-	8
206	R. ulnar v.	10	0.2	0.2	-	-	6
207	L. renal v.	3.2	0.25	0.25	1.128	11.6388	5
208	R. renal v.	3.2	0.25	0.25	1.128	11.6388	5
209	Ascending lumbar v.	23	0.2	0.2	-	-	5
210	hemiazygos v.	23	0.28	0.28	-	-	5
211	Inf. mesenteric v.	6	0.45	0.45	0.276	4.5795	5
212	R. post. tibial v.	17.3	0.15	0.15	-	-	7
213	R. ant. tibial v.	16	0.15	0.15	-	-	7
214	R. ant. tibial v.	2	0.6	0.6	0.132	0.5787	7
215	L. ant. tibial v.	2	0.6	0.6	0.132	0.5787	7
216	R. lumbar v.	3.8	0.1	0.1	-	-	5
217	L. lumbar v.	3.8	0.1	0.1	-	-	5
218	R. sup. thyroid v.	4	0.15	0.15	-	-	3
219	L. sup. thyroid v.	4	0.15	0.15	-	-	3

220	R. mid. thyroid v.	3	0.1	0.1	-	-	3
221	L. mid. thyroid v.	3	0.1	0.1	-	-	3
222	Inf. thyroid v.	7	0.126	0.126	-	-	3
223	Thyroid connection	2	0.16	0.16	3.131	0.2585	3
224	R. int. jugular v.	3	0.357	0.357	-	-	3
225	L. int. jugular v.	3	0.564	0.564	-	-	3
226	R. int. jugular v.	2.7	0.252	0.357	-	-	3
227	L. int. jugular v.	2.7	0.564	0.564	-	-	3
228	R. int. jugular v.	6.8	0.252	0.252	-	-	3
229	L. int. jugular v.	6.8	0.399	0.564	-	-	3
230	R. sigmoid sinus	1.5	0.252	0.252	-	-	1
231	L. sigmoid sinus	1.5	0.378	0.399	-	-	1
232	R. trans. sinus	3.5	0.218	0.178	-	-	1
233	L. trans. sinus	3.5	0.437	0.309	-	-	1
234	R. facial v.	2	0.113	0.132	6.256	0.284	2
235	L. facial v.	2	0.113	0.132	6.256	0.284	2
236	Sup. sagittal sinus	2	0.287	0.3	-	-	1
237	Cerebral vein	5	0.15	0.15	3.622	0.1652	9
238	Cerebral vein	5	0.15	0.15	3.622	0.1652	9
239	Cerebral vein	5	0.15	0.15	3.622	0.1652	9
240	Intra-cavernous sinus	2	0.126	0.126	-	-	1
241	Inf. sagittal sinus	3.67	0.16	0.16	-	-	1
242	R. int. jugular v.	1	0.399	0.399	-	-	3
243	L. int. jugular v.	1	0.618	0.618	-	-	3
244	Azygos v.	28	0.425	0.425	-	-	4
245	Cerebral vein	3	0.15	0.15	3.622	0.1652	9
246	L. basal v. of Rosenthal	7	0.126	0.126	-	-	9
247	R. basal v. of Rosenthal	7	0.126	0.126	-	-	9
248	Inf. sagittal sinus	3.67	0.16	0.16	-	-	1
249	Cerebral vein	3	0.15	0.15	3.622	0.1652	9
250	Intercostal v.	2	0.4	0.4	0.369	1.395	4
251	R. post. tibial v.	17.3	0.15	0.15	3.622	0.6805	7
252	R. ant. tibial v.	16	0.15	0.15	-	-	7
253	R. great saphenous v.	37.5	0.145	0.1875	-	-	7
254	L. great saphenous v.	37.5	0.145	0.1875	-	-	7
255	L. ant. tibial v.	16	0.15	0.15	-	-	7
256	L. post. tibial v.	17.3	0.15	0.15	3.622	0.6805	7
257	R. great saphenous v.	30	0.1875	0.2215	-	-	7
258	L. great saphenous v.	30	0.1875	0.2215	-	-	7
259	Confluence of sinuses	1	0.1	0.1	-	-	1
260	Cerebral vein	3	0.15	0.15	3.622	0.1652	9
261	Terminal cerebral vein	1	0.15	0.15	-	-	1
262	Terminal cerebral vein	1	0.15	0.15	-	-	1
263	Terminal cerebral vein	1	0.15	0.15	-	-	1
264	Terminal cerebral vein	1	0.15	0.15	-	-	1
265	Terminal cerebral vein	1	0.15	0.15	-	-	1

266	Terminal cerebral vein	1	0.15	0.15	-	-	1
267	Terminal cerebral vein	1	0.15	0.15	-	-	1
268	Terminal cerebral vein	1	0.15	0.15	-	-	1
269	Terminal cerebral vein	1	0.15	0.15	-	-	1
270	Terminal cerebral vein	1	0.15	0.15	-	-	1
271	Terminal cerebral vein	1	0.309	0.366	-	-	9
272	Terminal cerebral vein	1	0.15	0.15	-	-	1
273	Terminal cerebral vein	1	0.15	0.15	-	-	1
276	R. v. of cochlear aq. I	0.65	0.01	0.01	253.077	2.33E-05	9
277	R. labyrinthine v. I	0.43	0.037	0.037	71.986	2.33E-05	9
279	L. v. of cochlear aq. I	0.65	0.01	0.01	253.077	2.33E-05	9
280	L. labyrinthine v. I	0.43	0.037	0.037	17.997	2.33E-05	9
281	R. v. of cochlear aq. II	0.65	0.01	0.01	-	-	1
282	R. labyrinthine v. II	0.43	0.037	0.037	-	-	1
283	L. v. of cochlear aq. II	0.65	0.01	0.01	-	-	1
284	L. labyrinthine v. II	0.43	0.037	0.037	-	-	1
289	R. Sup. Vermian vein	1	0.08	0.08	15.817	0.006	9
290	L. Sup. Vermian vein	1	0.08	0.08	15.817	0.006	9
291	R. Inf. Vermian vein	1	0.09	0.09	11.577	0.008	9
292	L. Inf. Vermian vein	1	0.09	0.09	11.577	0.008	9
295	R. Inf. Vermian vein II	1	0.09	0.09	-	-	1
296	L. Inf. Vermian vein II	1	0.09	0.09	-	-	1
297	Cerebral vein	1	0.309	0.36	-	-	9
298	R. Sup. Petrosal vein	1	0.08	0.08	15.817	0.008	9
299	L. Sup. Petrosal vein	1	0.08	0.08	15.817	0.008	9
300	R. Sup. Petrosal vein II	1	0.08	0.08	-	-	1
301	L. Sup. Petrosal vein II	1	0.08	0.08	-	-	1
302	R. Sup. Petrosal sinus II	2	0.149	0.149	-	-	1
303	L. Sup. Petrosal sinus II	2	0.149	0.149	-	-	1

Appendix B

Cardiovascular indexes

In this appendix, we summarize the main cardiovascular indexes adopted throughout this work, how they are defined and calculated. All the indexes were evaluated from the numerical solution in the last cardiac cycle of a simulation that was converged to periodic solution. Therefore, in the following list we refer to maximum, minimum and mean values over a cardiac cycle. For one-dimensional vessels computed values are extracted from pressure, flow or velocity waveforms evaluated at the middle-point of the vessel's length.

- SBP: systolic blood pressure; maximum blood pressure.
- DBP: diastolic blood pressure; minimum blood pressure.
- MBP: mean blood pressure; average blood pressure.
- PP: pulse pressure; difference between maximum and minimum blood pressures.
- $\mathrm{PP}_{Amplification}$: pulse pressure amplification; it is evaluated as ratio between pulse pressure in brachial artery and aortic root.
- cfPWV: carotid-femoral pulse wave velocity; it is evaluated with the 'foot-to-foot' method as

  $$cfPWV = \frac{\Delta L}{\Delta t},$$

  where Δt is the time delay between the arrival of pulse at the right common carotid artery and at the right femoral artery and ΔL is the distance between the two measurement points.
- baPWV: brachial-ankle pulse wave velocity; it is evaluated with the 'foot-to-foot' method as

  $$baPWV = \frac{\Delta L}{\Delta t},$$

  where Δt is the time interval between the arrival of pulse at the right brachial artery and at the right tibial artery and ΔL is the distance between the two measurement points.
- Augmented P: augmented pressure; it is calculated as the difference between the second and first systolic peaks of aortic pressure.
- Augmentation index; it is calculated as the ratio between augmentation pressure and pulse pressure of aortic root.
- C_a: total arterial compliance index; arterial compliance index is evaluated as the ratio between stroke volume and brachial pulse pressure.

- C_a index: total arterial compliance index; arterial compliance index is evaluated as the ratio between stroke volume and brachial pulse pressure, divided by body surface area, taken as 1.92 m^2 for both normotensive and hypertensive subjects.
- HR: heart rate.
- CO: cardiac output.
- CI: cardiac index; it is calculated as cardiac output divided by body surface area, taken as 1.92 m^2 for both normotensive and hypertensive subjects.
- SI: stroke index; it is evaluated as stroke volume (end-diastolic volume - end-systolic volume of left ventricle) divided by body surface area.
- E_a: arterial elastance; it is calculated as the ratio between left ventricle end-systolic pressure and stroke volume. In Chapter 3, it was normalized by body surface area.
- E_{es}: left ventricle elastance; it is evaluated as left ventricle end-systolic pressure divided by left ventricle end-systolic volume. In Chapter 3, it was normalized by body surface area.
- E_a/E_{es}: arterial-ventricular coupling index.
- LV/RV_{max}: maximum volume of left/right ventricle.
- LV/RV_{EF}: ejection fraction of left/right ventricle; it is calculated as the ratio between stroke volume and end-diastolic volume.
- $\max/\min \frac{dP}{dt}$: maximum/minimum pressure rate.
- RV-SP: right ventricle systolic pressure.
- RV-EDP: right ventricle end-diastolic pressure.
- M/S/D PAP: mean/systolic/diastolic pulmonary artery pressure, evaluated in the zero-dimensional compartment of the arteries in the pulmonary circulation.
- PI: pulsatility index. It is evaluated from flow waveform or velocity waveform as the difference between the peak systolic and minimum diastolic value, divided by the mean value.
- RI: resistive index. It is calculated from velocity waveform as the difference between peak systolic and peak diastolic velocities divided by peak systolic velocity.

Bibliography

[1] F. M. Abboud and F. C. Thames. "Interaction of Cardiovascular Reflexes in Circulatory Control." In: *Comprehensive Physiology*. American Cancer Society, 2011, pp. 675–753.

[2] A. Abdelhammed et al. "Noninvasive Hemodynamic Profiles in Hypertensive Subjects". In: *American Journal of Hypertension* 18.2 (Feb. 2005), pp. 51–59.

[3] S. R. Abram et al. "Quantitative Circulatory Physiology: An Integrative Mathematical Model of Human Physiology for Medical Education". In: *Teaching With Technology* 31 (2007), p. 9.

[4] N. Agarwal et al. "Intracranial Fluid Dynamics Changes in Idiopathic Intracranial Hypertension: Pre and Post Therapy". In: *Current Neurovascular Research* 15.2 (July 2018), pp. 164–172.

[5] G. Aktas et al. "Spinal CSF Flow in Response to Forced Thoracic and Abdominal Respiration". In: *Fluids and Barriers of the CNS* 16.1 (Dec. 2019), p. 10.

[6] J. Alastruey et al. "Lumped Parameter Outflow Models for 1-D Blood Flow Simulations: Effect on Pulse Waves and Parameter Estimation". In: *Communications in Computational Physics* 4 (2008), pp. 317–336.

[7] J. Alastruey et al. "Pulse Wave Propagation in a Model Human Arterial Network: Assessment of 1-D Visco-Elastic Simulations against in Vitro Measurements". In: *Journal of Biomechanics* 44.12 (2011), pp. 2250–2258.

[8] A. Albanese et al. "An Integrated Mathematical Model of the Human Cardiopulmonary System: Model Development." In: *American Journal of Physiology-Heart and Circulatory Physiology* 310 (2016), H899–H921.

[9] J. Alfie et al. "Contribution of Stroke Volume to the Change in Pulse Pressure Pattern With Age". In: *Hypertension* 34.4 (Oct. 1999), pp. 808–812.

[10] M. R. Alfonso et al. "A Novel Interpretation for Arterial Pulse Pressure Amplification in Health and Disease". In: *Journal of Healthcare Engineering* 2018 (2018), pp. 1–9.

[11] N. Alperin. "Does the Brain Have Mechanical Compliance?" In: *Magnetic Resonance Materials in Physics, Biology and Medicine* 33.6 (Dec. 2020), pp. 753–756.

[12] N. Alperin et al. "Quantifying the Effect of Posture on Intracranial Physiology in Humans by MRI Flow Studies". In: *Journal of Magnetic Resonance Imaging* 22 (2005), pp. 591–596.

[13] D. C. Alpini et al. "Chronic Cerebrospinal Venous Insufficiency (CCSVI) in Ménière's Disease, Case or Cause?" In: *ScienceMed* 4 (2013), pp. 9–15.

[14] T. F. T. Antonios. "Rarefaction of Skin Capillaries in Normotensive Offspring of Individuals with Essential Hypertension". In: *Heart* 89.2 (Feb. 2003), pp. 175–178.

[15] R. G. Asmar et al. "Aortic Distensibility in Normotensive, Untreated and Treated Hypertensive Patients." In: *Blood Pressure* 4.1 (1995), pp. 48–54.

[16] A. Aspelund et al. "A Dural Lymphatic Vascular System That Drains Brain Interstitial Fluid and Macromolecules". In: *Journal of Experimental Medicine* 212.7 (June 2015), pp. 991–999.

[17] C. Avezaat and J. H. van Eijndhoven. "Cerebrospinal Fluid Pulse Pressure and Craniospinal Dynamics : A Theoretical, Clinical and Experimental Study". PhD thesis. Erasmus MC: University Medical Center Rotterdam, Feb. 1984.

[18] F. A. Bainbridge. "The Influence of Venous Filling upon the Rate of the Heart". In: *The Journal of Physiology* 50.2 (Dec. 1915), pp. 65–84.

[19] A.C. L. Barnard et al. "A Theory of Fluid Flow in Compliant Tubes". In: *Biophysical Journal* 6.6 (1966), pp. 717–724.

[20] G. A. Bateman. "Arterial Inflow and Venous Outflow in Idiopathic Intracranial Hypertension Associated with Venous Outflow Stenoses". In: *Journal of Clinical Neuroscience* 15.4 (Apr. 2008), pp. 402–408.

[21] J. Beck et al. "Cerebrospinal Fluid Outflow Resistance as a Diagnostic Marker of Spontaneous Cerebrospinal Fluid Leakage". In: *Journal of Neurosurgery: Spine* 27.2 (Aug. 2017), pp. 227–234.

[22] E. Beeri et al. "In Vivo Evaluation of Fontan Pathway Flow Dynamics by Multidimensional Phase-Velocity Magnetic Resonance Imaging". In: *Circulation* 98 (1998), pp. 2873–2882.

[23] C. B. Beggs. "Venous Hemodynamics in Neurological Disorders: An Analytical Review with Hydrodynamic Analysis". In: *BMC Medicine* 11 (2013), p. 142.

[24] C.B. Beggs et al. "Aqueductal Cerebrospinal Fluid Pulsatility in Healthy Individuals Is Affected by Impaired Cerebral Venous Outflow". In: *Journal of Magnetic Resonance Imaging* 40 (2014), pp. 1215–1222.

[25] A. Benetos et al. "Large Artery Stiffness in Hypertension." In: *Journal of Hypertension. Supplement: Official Journal of the International Society of Hypertension* 15.2 (1997), S89–S97.

[26] K. Berkouk, P. W. Carpenter, and A. D. Lucey. "Pressure Wave Propagation in Fluid-Filled Co-Axial Elastic Tubes Part 1: Basic Theory". In: *Journal of Biomechanical Engineering* 125.6 (Dec. 2003), pp. 852–856.

[27] C. D. Bertram, A. R. Brodbelt, and M. A. Stoodley. "The Origins of Syringomyelia: Numerical Models of Fluid/Structure Interactions in the Spinal Cord". In: *Journal of Biomechanical Engineering* 127.7 (Dec. 2005), pp. 1099–1109.

[28] C.D. Bertram. "A Numerical Investigation of Waves Propagating in the Spinal Cord and Subarachnoid Space in the Presence of a Syrinx". In: *Journal of Fluids and Structures* 25.7 (Oct. 2009), pp. 1189–1205.

[29] P. J. Blanco and R. A. Feijóo. "A 3D-1D-0D Computational Model for the Entire Cardiovascular System". In: *Computational Mechanics, eds. E. Dvorking, M. Goldschmit, M. Storti* 29 (2010), pp. 5887–5911.

[30] P. J. Blanco, L. O. Müller, and J. D. Spence. "Blood Pressure Gradients in Cerebral Arteries: A Clue to Pathogenesis of Cerebral Small Vessel Disease". In: *Stroke and Vascular Neurology* 2.3 (Sept. 2017), pp. 108–117.

[31] P.J. Blanco et al. "An Anatomically Detailed Arterial Network Model for One-Dimensional Computational Hemodynamics". In: *IEEE transactions on bio-medical engineering* 62 (2015), pp. 736–53.

[32] P.J. Blanco et al. "On the Integration of the Baroreflex Control Mechanism in a Heterogeneous Model of the Cardiovascular System: MODELING THE BAROREFLEX MECHANISM IN THE CARDIOVASCULAR SYSTEM". In: *International Journal for Numerical Methods in Biomedical Engineering* 28.4 (Apr. 2012), pp. 412–433.

[33] P.J. Blanco et al. "On the Potentialities of 3D-1D Coupled Models in Hemodynamics Simulations". In: *Journal of biomechanics* 42.7 (2009), pp. 919–930.

[34] B. Bonnet et al. "Noninvasive Evaluation of Left Ventricular Elastance According to Pressure-Volume Curves Modeling in Arterial Hypertension". In: *American Journal of Physiology-Heart and Circulatory Physiology* 313.2 (Aug. 2017), H237–H243.

[35] M.J. Boorder, J. Hendrikse, and J. ven der Grond. "Phase-Contrast Magnetic Resonance Imaging Measurements of Cerebral Autoregulation with a Breath-Hold Challenge: A Feasibility Study". In: *Stroke* 35 (2004), pp. 1350–1354.

[36] B. A. Borlaug et al. "Contractility and Ventricular Systolic Stiffening in Hypertensive Heart Disease". In: *Journal of the American College of Cardiology* 54.5 (July 2009), pp. 410–418.

[37] T. Brinker et al. "A New Look at Cerebrospinal Fluid Circulation". In: *Fluids and Barriers of the CNS* 11.1 (2014), p. 10.

[38] B. S. Brook, S. A. E. G. Falle, and T. J. Pedley. "Numerical Solutions for Unsteady Gravity-Driven Flows in Collapsible Tubes: Evolution and Roll-Wave Instability of a Steady State". In: *Journal of Fluid Mechanics* 396 (Oct. 1999), pp. 223–256.

[39] S. Brouwers et al. "Arterial Hypertension". In: *The Lancet* 398.10296 (July 2021), pp. 249–261.

[40] A. Bruno et al. "The Prevalence of Chronic Cerebrospinal Venous Insufficiency in Meniere Disease: 24-Month Follow-up after Angioplasty". In: *Journal of Vascular and Interventional Radiology* 28.3 (Mar. 2017), pp. 388–391.

[41] J. Buishas, I. G. Gould, and A. A. Linninger. "A Computational Model of Cerebrospinal Fluid Production and Reabsorption Driven by Starling Forces". In: *Croatian Medical Journal* 55.5 (2014), pp. 481–97.

[42] R. Burman et al. "Patient-Specific Cranio-Spinal Compliance Distribution Using Lumped-Parameter Model: Its Relation with ICP over a Wide Age Range". In: *Fluids Barriers (CNS)* 15.29 (2018).

[43] C. Bussy et al. "Intrinsic Stiffness of the Carotid Arterial Wall Material in Essential Hypertensives". In: *Hypertension* 35.5 (May 2000), pp. 1049–1054.

[44] J. Cai et al. "Evaluation of Thoracic Spinal Cord Motion Using Dynamic MRI". In: *Radiotherapy and Oncology* 84.3 (Sept. 2007), pp. 279–282. ISSN: 01678140.

[45] E. R. Cardoso, J. O. Rowan, and S. Galbraith. "Analysis of the Cerebrospinal Fluid Pulse Wave in Intracranial Pressure". In: *Journal of Neurosurgery* 59.5 (Nov. 1983), pp. 817–821.

[46] B.I.R. Carlborg and J.C. Farmer. "Transmission of Cerebrospinal Fluid Pressure via the Cochlear Aqueduct and Endolymphatic Sac". In: *American Journal of Otolaryngology* 4 (1983), pp. 273–282.

[47] P. W. Carpenter, K. Berkouk, and A. D. Lucey. "Pressure Wave Propagation in Fluid-Filled Co-Axial Elastic Tubes Part 2: Mechanisms for the Pathogenesis of Syringomyelia". In: *Journal of Biomechanical Engineering* 125.6 (Dec. 2003), pp. 857–863.

[48] E. Carrera et al. "What Shapes Pulse Amplitude of Intracranial Pressure?" In: *Journal of Neurotrauma* 27 (2010), pp. 317–324.

[49] C. Cattaneo. "A Form of Heat-Conduction Equations Which Eliminates the Paradox of Instantaneous Propagation". In: *Comptes Rendus Mathématique de l'Academie des Sciences* 247 (1958), pp. 431–433.

[50] M. Celant, E. F. Toro, and L. O. Müller. "A Multi-Scale Model for the Dynamic of the Cerebrospinal Fluid Coupled to the Systemic Circulation." In: *Fluids and Barriers of the CNS* To be submitted (2022).

[51] M. Celant, E. F. Toro, and L. O. Müller. "Total Effective Vascular Compliance of a Global Mathematical Model for the Cardiovascular System". In: *Symmetry* 13.10 (Oct. 2021), p. 1858.

[52] M. Celant et al. "Major Determinants of Essential Hypertension: A Computational Study Based on a Closed-Loop Model for the Human Circulation". In: *To be submitted* (2022).

[53] P. H. Charlton et al. "Modeling Arterial Pulse Waves in Healthy Aging: A Database for in Silico Evaluation of Hemodynamics and Pulse Wave Indexes". In: *American Journal of Physiology-Heart and Circulatory Physiology* 317.5 (Nov. 2019), H1062–H1085.

[54] C.P. Cheng, R.J. Herfkens, and C.A. Taylor. "Inferior Vena Caval Hemodynamics Quantified in Vivo at Rest and during Cycling Exercise Using Magnetic Resonance Imaging". In: *American Journal of Physiology: Heart and Circulatory Physiology* 284 (2002), H1161–H1167.

[55] S. J. Cho et al. "Blood Flow Velocity Changes in the Middle Cerebral Artery as an Index of the Chronicity of Hypertension". In: *Journal of the Neurological Sciences* 150.1 (Sept. 1997), pp. 77–80.

[56] S. Chuang et al. "Blood Pressure, Carotid Flow Pulsatility, and the Risk of Stroke: A Community-Based Study". In: *Stroke* 47.9 (Sept. 2016), pp. 2262–2268.

[57] C. Chung and H. Hu. "Pathogenesis of Leukoaraiosis: Role of Jugular Venous Reflux". In: *Medical Hypotheses* 75.1 (July 2010), pp. 85–90.

[58] M. J. Cipolla, D. S. Liebeskind, and S. Chan. "The Importance of Comorbidities in Ischemic Stroke: Impact of Hypertension on the Cerebral Circulation". In: *Journal of Cerebral Blood Flow & Metabolism* 38.12 (Dec. 2018), pp. 2129–2149.

[59] S. Cirovic. "A Coaxial Tube Model of the Cerebrospinal Fluid Pulse Propagation in the Spinal Column". In: *Journal of Biomechanical Engineering* 131.2 (Feb. 2009), p. 021008.

[60] S. Cirovic, C. Walsh, and W. D. Fraser. "Mathematical Study of the Role of Non-Linear Venous Compliance in the Cranial Volume-Pressure Test". In: *Medical & Biological Engineering & Computing* 41.5 (Sept. 2003), pp. 579–588.

[61] T. M. Coffman. "The Inextricable Role of the Kidney in Hypertension". In: *Journal of Clinical Investigation* 124.6 (June 2014), pp. 2341–2347.

[62] H. M. Coleridge et al. "Operational Sensitivity and Acute Resetting of Aortic Baroreceptors in Dogs." In: *Circulation Research* 48.5 (May 1981), pp. 676–684.

[63] C. Colombo. "Mathematical Properties-Preserving Parameter Estimation for a Blood Flow Model Using Ovine and Human in Vitro Data." MA thesis. Trento: University of Trento, Department of Mathematics, 2020.

[64] C. Contarino. "A Holistic Multi-Scale Mathematical Model of the Murine Extracellular Fluid Systems and Study of the Brain Interactive Dynamics". PhD thesis. Trento: University of Trento, Department of Mathematics, 2018.

[65] A. Cyrous, B. O'Neal, and W. D. Freeman. "New Approaches to Bedside Monitoring in Stroke". In: *Expert Review of Neurotherapeutics* 12.8 (Aug. 2012), pp. 915–928.

[66] M. Czosnyka. "Monitoring and Interpretation of Intracranial Pressure". In: *Journal of Neurology, Neurosurgery & Psychiatry* 75.6 (June 2004), pp. 813–821.

[67] M. Czosnyka and Z. Czosnyka. "Origin of Intracranial Pressure Pulse Waveform". In: *Acta Neurochirurgica* 162 (2020), pp. 1815–1817.

[68] M. Czosnyka et al. "Cerebrospinal Fluid Dynamics". In: *Physiological Measurement* 25.5 (Oct. 2004), R51–R76.

[69] M. Danielsen. "Modeling of Feedback Mechanisms Which Control the Heart Function in a View to an Implementation in Cardiovascular Models". PhD thesis. Roskilde, Denmark: Roskilde University Center.

[70] T. L. Davis. "Teaching Physiology through Interactive Simulation of Hemodynamics." PhD thesis. Cambridge, MA, USA: Massachusetts Institute of Technology, 1991.

[71] H. Davson and M. B. Segal. *Physiology of the CSF and Blood-Brain Barriers*. CRC press, 1996.

[72] K. P. Davy and D. R. Seals. "Total Blood Volume in Healthy Young and Older Men". In: *Journal of Applied Physiology* 76.5 (May 1994), pp. 2059–2062.

[73] C. De Ciuceis et al. "Cerebral Small-Resistance Artery Structure and Cerebral Blood Flow in Normotensive Subjects and Hypertensive Patients". In: *Neuroradiology* 56 (2014), pp. 1103–1111.

[74] E. P. Delaney et al. "Limb Venous Tone and Responsiveness in Hypertensive Humans". In: *Journal of Applied Physiology* 105.3 (Sept. 2008), pp. 894–901.

[75] J. A. Drees and C. F. Rothe. "Reflex Venoconstriction and Capacity Vessel Pressure-Volume Relationships in Dogs". In: *Circulation Research* 34.3 (Mar. 1974), pp. 360–373.

[76] M. Dumbser, C. Enaux, and E.F. Toro. "Finite Volume Schemes of Very High Order of Accuracy for Stiff Hyperbolic Balance Laws". In: *Journal of Computational Physics* 227 (2008), pp. 3971–4001.

[77] M. Dumbser and M. Käser. "Arbitrary High Order Non-Oscillatory Finite Volume Schemes on Unstructured Meshes for Linear Hyperbolic Systems". In: *Journal of Computational Physics* 221 (2007), pp. 692–723.

[78] M. Dumbser, M. Käser, and E. F. Toro. "An Arbitrary High Order Discontinuous Galerkin Method for Elastic Waves on Unstructured Meshes v: Local Time Stepping and p–Adaptivity". In: *Geophysical Journal International* 171 (2007), pp. 695–717.

[79] M. Dumbser and E.F. Toro. "A Simple Extension of the Osher Riemann Solver to Non-Conservative Hyperbolic Systems". In: *Journal of Scientific Computing* 48 (2011), pp. 70–88.

[80] M. Dumbser et al. "ADER Schemes on Unstructured Meshes for Non-Conservative Hyperbolic Systems: Applications to Geophysical Flows". In: *Computers and Fluids* 38 (2009), pp. 1731–1748.

[81] M. Dumbser et al. "FORCE Schemes on Unstructured Meshes II: Non Conservative Hyperbolic Systems with Source Terms". In: *Computational Methods in Applied Mechanics and Engineering* 199 (2010), pp. 625–647.

[82] M. Echt et al. "Effective Compliance of the Total Vascular Bed and the Intrathoracic Compartment Derived from Changes in Central Venous Pressure Induced by Volume Changes in Man". In: *Circulation Research* (1974), p. 8.

[83] R. Falz et al. "Normal Values of Hemoglobin Mass and Blood Volume in Young, Active Women and Men". In: *International Journal of Sports Medicine* 40.04 (Apr. 2019), pp. 236–244.

[84] S. M. Farasat et al. "Do Hypertensive Individuals Have Enlarged Aortic Root Diameters? Insights From Studying the Various Subtypes of Hypertension". In: *American Journal of Hypertension* 21.5 (May 2008), pp. 558–563.

[85] F. Feihl, L. Liaudet, and B. Waeber. "The Macrocirculation and Microcirculation of Hypertension". In: *Current Hypertension Reports* 11.3 (June 2009), pp. 182–189.

[86] J. Ferlinz. "Right Ventricular Performance in Essential Hypertension." In: *Circulation* 61.1 (Jan. 1980), pp. 156–162.

[87] L. A. Ferrara et al. "Carotid Diameter and Blood Flow Velocities in Cerebral Circulation in Hypertensive Patients." In: *Stroke* 26.3 (1995), pp. 418–421.

[88] C.R. Figley and P.W. Stroman. "Investigation of Human Cervical and Upper Thoracic Spinal Cord Motion: Implications for Imaging Spinal Cord Structure and Function". In: *Magnetic Resonance in Medicine* 58.1 (July 2007), pp. 185–189.

[89] G. D. Fink. "Sympathetic Activity, Vascular Capacitance, and Long-Term Regulation of Arterial Pressure". In: *Hypertension* 53.2 (Feb. 2009), pp. 307–312.

[90] J. E. Flaherty, J. B. Keller, and S. I. Rubinow. "Post Buckling Behavior of Elastic Tubes and Rings with Opposite Sides in Contact". In: *SIAM Journal on Applied Mathematics* 23.4 (Dec. 1972), pp. 446–455.

[91] J. Flores Gerónimo et al. "Estimating Central Pulse Pressure From Blood Flow by Identifying the Main Physical Determinants of Pulse Pressure Amplification". In: *Frontiers in Physiology* 12 (Feb. 2021), p. 608098.

[92] B. Folkow. "Physiological Aspects of Primary Hypertension." In: *Physiological Reviews* 62.2 (Apr. 1982), pp. 347–504.

[93] L. Formaggia, D. Lamponi, and A. Quarteroni. "One-Dimensional Models for Blood Flow in Arteries". In: *Journal of Engineering Mathematics* 47.3/4 (2003), pp. 251–276.

[94] L. Formaggia, A. Quarteroni, and A. Veneziani, eds. *Cardiovascular Mathematics: Modeling and Simulation of the Circulatory System*. MS & A : Modeling, Simulation & Applications 1. Milano: Springer, 2009.

[95] J.B. Fortune and P. Feustel. "Effect of Patient Position on Size and Location of the Subclavian Vein for Percutaneous Puncture". In: *Archives of Surgery* 138 (2003), pp. 996–1000.

[96] U. Friberg and H. Rask-Andersen. "Vascular Occlusion in the Endolymphatic Sac in Meniere's Disease". In: *Annals of Otology, Rhinology and Laryngology* 111.3 (Mar. 2002), pp. 237–245.

[97] C. D. Fryar and G. Zhang. "Hypertension Prevalence and Control Among Adults: United States, 2015–2016". In: 289 (2017), p. 8.

[98] A. Ganau et al. "Patterns of Left Ventricular Hypertrophy and Geometric Remodeling in Essential Hypertension". In: *Journal of the American College of Cardiology* 19.7 (June 1992), pp. 1550–1558.

[99] O. H. Gauer, J. P. Henry, and H. O. Sieker. "Changes in Central Venous Pressure after Moderate Hemorrhage and Transfusion in Man". In: *Circulation Research* 4.1 (Jan. 1956), pp. 79–84.

[100] L. Geregele et al. "Dynamics of Cerebrospinal Fluid: From Theoretical Models to Clinical Applications". In: Aug. 2019, pp. 181–214.

[101] J. Ghajar. "Traumatic Brain Injury". In: *Lancet* 356 (2000), pp. 923–929.

[102] I. G. Gould and A. A. Linninger. "Hematocrit Distribution and Tissue Oxygenation in Large Microcirculatory Networks". In: *Microcirculation* 22.1 (2015), pp. 1–18.

[103] I. G. Gould et al. "The Capillary Bed Offers the Largest Hemodynamic Resistance to the Cortical Blood Supply". In: *Journal of Cerebral Blood Flow & Metabolism* 37.1 (2017), pp. 52–68.

[104] S. Greenberg and D.F. Bohr. "Venous Smooth Muscle in Hypertension: Enhanced Contractility of Portal Veins from Spontaneously Hypertensive Rats." In: *Circulation Research* 36 (1975), pp. 208–215.

[105] C. V. Greenway. "Role of Splanchnic Venous System in Overall Cardiovascular Homeostasis." In: *Federation proceedings* 42.6 (Apr. 1983), pp. 1678–1684.

[106] C. V. Greenway and W. W. Lautt. "Blood Volume, the Venous System, Preload, and Cardiac Output". In: *Canadian Journal of Physiology and Pharmacology* 64.4 (Apr. 1986), pp. 383–387.

[107] M. D. Guazzi et al. "Evidence of a Shared Mechanism of Vasoconstriction in Pulmonary and Systemic Circulation in Hypertension: A Possible Role of Intracellular Calcium." In: *Circulation* 66.4 (Oct. 1982), pp. 881–886.

[108] P. Gupta et al. "Responses of Atrial and Aortic Baroreceptors to Nonhypotensive Hemorrhage and to Tranfusion". In: *American Journal of Physiology-Legacy Content* 211.6 (Dec. 1966), pp. 1429–1437.

[109] S. Gupta et al. "Three-Dimensional Computational Modeling of Subject-Specific Cerebrospinal Fluid Flow in the Subarachnoid Space". In: *Journal of Biomechanical Engineering* 131.2 (Feb. 2009), p. 021010.

[110] A. C. Guyton, D. Polizo, and G. G. Armstrong. "Mean Circulatory Filling Pressure Measured Immediately After Cessation of Heart Pumping". In: *American Journal of Physiology-Legacy Content* 179.2 (Oct. 1954), pp. 261–267.

[111] A. C. Guyton et al. "Effect of Blood Transfusion and Hemorrhage on Cardiac Output and on the Venous Return Curve". In: *American Journal of Physiology-Legacy Content* 194.2 (Aug. 1958), pp. 263–267.

[112] A. C. Guyton et al. "Systems Analysis of Arterial Pressure Regulation and Hypertension". In: *Annals of biomedical engineering* 1.2 (1972), pp. 254–281.

[113] J. E. Hall and A. C. Guyton. *Guyton and Hall Textbook of Medical Physiology. Twelve Edition.* 12th ed. Saunders/Elsevier, 2011.

[114] M. Harary, R. G. Dolmans, and W. Gormley. "Intracranial Pressure Monitoring—Review and Avenues for Development". In: *Sensors* 18.2 (Feb. 2018), p. 465.

[115] A. Harten and S. Osher. "Uniformly High–Order Accurate Nonoscillatory Schemes. I". In: *SIAM Journal on Numerical Analysis* 24.2 (1987), pp. 279–309.

[116] A. Harten et al. "Uniformly High Order Accuracy Essentially Non–Oscillatory Schemes, III". In: *Journal of Computational Physics* 71 (1987), pp. 231–303.

[117] G. Hartung et al. "Mathematical Synthesis of the Cortical Circulation for the Whole Mouse Brain-part II: Microcirculatory Closure". In: *Microcirculation* (Feb. 2021).

[118] G. Hartung et al. "Simulations of Blood as a Suspension Predicts a Depth Dependent Hematocrit in the Circulation throughout the Cerebral Cortex". In: *PLOS Computational Biology* 14.11 (Nov. 2018). Ed. by Christopher Gerald Ellis, e1006549.

[119] A. Hatt et al. "MR Elastography Can Be Used to Measure Brain Stiffness Changes as a Result of Altered Cranial Venous Drainage During Jugular Compression". In: *American Journal of Neuroradiology* 36.10 (Oct. 2015), pp. 1971–1977.

[120] J. P. Henry, O. H. Gauer, and H. O. Sieker. "The Effect of Moderate Changes in Blood Volume on Left and Right Atrial Pressures". In: *Circulation Research* 4.1 (Jan. 1956), pp. 91–94.

[121] S. B. Hladky and M. A. Barrand. "Mechanisms of Fluid Movement into, through and out of the Brain: Evaluation of the Evidence". In: *Fluids and Barriers of the CNS* 11.1 (2014), p. 26.

[122] J. Holtz et al. "Increased Effective Vascular Compliance and Venous Pooling of Intravascular Volume during Sustained Venodilation in Conscious Dogs". In: *Basic Research in Cardiology* 76.6 (Nov. 1981), pp. 657–669.

[123] H. Hosomi and K. Sagawa. "Sinovagal Interaction in Arterial Pressure Restoration after 10% Hemorrhage". In: *American Journal of Physiology-Regulatory, Integrative and Comparative Physiology* 237.3 (Sept. 1979), R203–R209.

[124] J. Hua et al. "MRI Techniques to Measure Arterial and Venous Cerebral Blood Volume". In: *NeuroImage* 187 (2019), pp. 17–31.

[125] T. J.R. Hughes and J. Lubliner. "On the One-Dimensional Theory of Blood Flow in the Larger Vessels". In: *Mathematical Biosciences* 18.1-2 (1973), pp. 161–170.

[126] M. Hupp et al. "Segmental Differences of Cervical Spinal Cord Motion: Advancing from Confounders to a Diagnostic Tool". In: *Scientific Reports* 9.1 (Dec. 2019), p. 7415.

[127] J. J. Iliff et al. "A Paravascular Pathway Facilitates CSF Flow Through the Brain Parenchyma and the Clearance of Interstitial Solutes, Including Amyloid β". In: *Science translational medicine* 4.147 (2012), 147ra111.

[128] Y. Itzchak et al. "External Iliac Artery Blood Flow in Patients with Arteriosclerosis Obliterans". In: *American Journal of Roentgenology* 125 (1975), pp. 437–441.

[129] M. A. James et al. "Effects of Aging and Hypertension on the Microcirculation". In: *Hypertension* 47.5 (May 2006), pp. 968–974.

[130] O. C. Jones and J. C. M. Leung. "An Improvement in the Calculation of Turbulent Friction in Smooth Concentric Annuli". In: *Journal of Fluids Engineering* 103.4 (Dec. 1981), pp. 615–623.

[131] O. Juge et al. "Critical Appraisal of Cerebral Blood Flow Measured from Brain Stem and Cerebellar Regions after Xe Inhalation in Humans". In: *Stroke* 10 (1979), pp. 428–437.

[132] S. Julius. "Interaction between Renin and the Autonomic Nervous System in Hypertension". In: *American Heart Journal* 116.2 (Aug. 1988), pp. 611–616.

[133] A. Just. "Mechanisms of Renal Blood Flow Autoregulation: Dynamics and Contributions". In: *American Journal of Physiology-Regulatory, Integrative and Comparative Physiology* 292.1 (Jan. 2007), R1–R17.

[134] M. Kaczmarek, R.P. Subramaniam, and S.R. Neff. "The Hydromechanics of Hydrocephalus: Steady-state Solutions for Cylindrical Geometry". In: *Bulletin of Mathematical Biology* 59 (1997), pp. 295–323.

[135] M. Kaibe et al. "Arterial Stiffness Index: A New Evaluation for Arterial Stiffness in Elderly Patients with Essential Hypertension: ASI in Elderly Hypertensive Patients". In: *Geriatrics & Gerontology International* 2.4 (Dec. 2002), pp. 199–205.

[136] F. Karaaslan, Y. Denizhan, and R. Hester. "A Mathematical Model of Long-Term Renal Sympathetic Nerve Activity Inhibition during an Increase in Sodium Intake". In: *American Journal of Physiology-Regulatory, Integrative and Comparative Physiology* 306.4 (Feb. 2014), R234–R247.

[137] F. Karaaslan et al. "Long-Term Mathematical Model Involving Renal Sympathetic Nerve Activity, Arterial Pressure, and Sodium Excretion". In: *Annals of Biomedical Engineering* 33.11 (Nov. 2005), pp. 1607–1630.

[138] A. Khasawneh, R. Garling, and C. Harris. "Cerebrospinal Fluid Circulation: What Do We Know and How Do We Know It?" In: *Brain Circulation* 4.1 (2018), p. 14.

[139] M. Kim and S. Cirovic. "A Computational Model of the Cerebrospinal Fluid System Incorporating Lumped-Parameter Cranial Compartment and One-Dimensional Distributed Spinal Compartment". In: *Journal of Biorheology* 25.1-2 (Dec. 2011), pp. 78–87.

[140] C. Kirkness et al. "Intracranial Pressure Waveform Analysis: Clinical and Research Implications". In: *Journal of Neuroscience Nursing* 32.5 (2000), pp. 271–7.

[141] M. Kosteljanetz. "Pressure-Volume Conditions in Patients with Subarachnoid and/or Intraventricular Hemorrhage". In: *Journal of Neurosurgery* 63.3 (Sept. 1985), pp. 398–403.

[142] H. Koubenec, W. D. Risch, and O. H. Gauer. "Effective Compliance of the Circulation in the Upright Sitting Posture". In: *Pflügers Archiv European Journal of Physiology* 374.2 (May 1978), pp. 121–124.

[143] M. Kumada and K. Sagawa. "Aortic Nerve Activity during Blood Volume Changes". In: *American Journal of Physiology-Legacy Content* 218.4 (Apr. 1970), pp. 961–965.

[144] V. Kurtcuoglu. "Computational Fluid Dynamics for the Assessment of Cerebrospinal Fluid Flow and Its Coupling with Cerebral Blood Flow". In: *Biomechanics of the Brain*. Ed. by Karol Miller. New York, NY: Springer New York, 2011, pp. 169–188.

[145] V. Kurtcuoglu et al. "Computational Investigation of Subject-Specific Cerebrospinal Fluid Flow in the Third Ventricle and Aqueduct of Sylvius". In: *Journal of Biomechanics* 40.6 (Jan. 2007), pp. 1235–1245.

[146] C. S. P. Lam et al. "Effect of Antihypertensive Therapy on Ventricular-Arterial Mechanics, Coupling, and Efficiency". In: *European Heart Journal* 34.9 (Mar. 2013), pp. 676–683.

[147] N.A. Lassen. "Cerebral Blood Flow and Oxygen Consumption in Man". In: *Phisiological reviews* 39 (1959), pp. 183–238.

[148] S. Laurent and P. Boutouyrie. "The Structural Factor of Hypertension: Large and Small Artery Alterations". In: *Circulation Research* 116.6 (Mar. 2015), pp. 1007–1021.

[149] S. Laurent et al. "Carotid Artery Distensibility and Distending Pressure in Hypertensive Humans." In: *Hypertension* 23.6_pt_2 (June 1994), pp. 878–883.

[150] S. Laurent et al. "Elastic Modulus of the Radial Artery Wall Material Is Not Increased in Patients with Essential Hypertension." In: *Arteriosclerosis and Thrombosis: A Journal of Vascular Biology* 14.7 (July 1994), pp. 1223–1231.

[151] A. Lavinio et al. "The Relationship between the Intracranial Pressure–Volume Index and Cerebral Autoregulation". In: *Intensive Care Medicine* 35.3 (Mar. 2009), pp. 546–549.

[152] J. R. Levick. *An Introduction to Cardiovascular Physiology. Fifth Edition*. London: Hodder Arnold, 2010.

[153] B.I. Levy et al. "Microcirculation in Hypertension: A New Target for Treatment?" In: *Circulation* 104.6 (Aug. 2001), pp. 735–740.

[154] M.N. Levy, B.A. Stanton, and B.M. Koeppen. *Berne & Levy, Physiology*. Ed. by Mosby. 6th ed. 2009.

[155] P. Lewis et al. "Measurement of Volume Flow in the Human Common Femoral Artery Using a Duplex Ultrasound System". In: *Ultrasound in Medicine and Biology* 10 (1986), pp. 777–784.

[156] L. Li et al. "Age-Related Changes in Skin Topography and Microcirculation". In: *Archives of Dermatological Research* 297.9 (Mar. 2006), pp. 412–416.

[157] Y. Li et al. "Forward and Backward Pressure Waveform Morphology in Hypertension". In: *Hypertension* 69.2 (Feb. 2017), pp. 375–381.

[158] F. Liang, D. Guan, and J. Alastruey. "Determinant Factors for Arterial Hemodynamics in Hypertension: Theoretical Insights From a Computational Model-Based Study". In: *Journal of Biomechanical Engineering* 140.3 (Mar. 2018), p. 031006.

[159] F. Liang and H. Liu. "Simulation of Hemodynamic Responses to the Valsalva Maneuver: An Integrative Computational Model of the Cardiovascular System and the Autonomic Nervous System". In: *The Journal of Physiological Sciences* 56.1 (2006), pp. 45–65.

[160] F.Y. Liang et al. "Biomechanical Characterization of Ventricular–Arterial Coupling during Aging: A Multi-Scale Model Study". In: *Journal of Biomechanics* 42.6 (Apr. 2009), pp. 692–704.

[161] E. Lim et al. "A Cardiovascular Mathematical Model of Graded Head-Up Tilt". In: *PLoS ONE* 8.10 (Oct. 2013). Ed. by Mathias Baumert, e77357.

[162] A. A. Linninger et al. "A Mathematical Model of Blood, Cerebrospinal Fluid and Brain Dynamics". In: *Journal of Mathematical Biology* 59.6 (Dec. 2009), pp. 729–759.

[163] A. A. Linninger et al. "Cerebral Microcirculation and Oxygen Tension in the Human Secondary Cortex". In: *Annals of Biomedical Engineering* 41.11 (2013), pp. 2264–84.

[164] A. A. Linninger et al. "Cerebrospinal Fluid Flow in the Normal and Hydrocephalic Human Brain". In: *IEEE Transactions on Biomedical Engineering* 54.2 (Feb. 2007), pp. 291–302.

[165] A. A. Linninger et al. "Cerebrospinal Fluid Mechanics and Its Coupling to Cerebrovascular Dynamics". In: *Annual Review of Fluid Mechanics* 48.1 (Jan. 2016), pp. 219–257.

[166] A. A. Linninger et al. "Starling Forces Drive Intracranial Water Exchange during Normal and Pathological States". In: *Croatian Medical Journal* 58.6 (Dec. 2017), pp. 384–394.

[167] A.A. Linninger et al. "Pulsatile Cerebrospinal Fluid Dynamics in the Human Brain". In: *IEEE Transactions on Biomedical Engineering* 52.4 (Apr. 2005), pp. 557–565.

[168] G. M. London et al. "Cardiac and Arterial Interactions in End-Stage Renal Disease." In: *Kidney International* 50.2 (Aug. 1996), pp. 600–608.

[169] G. M. London et al. "Total Effective Compliance, Cardiac Output and Fluid Volumes in Essential Hypertension." In: *Circulation* 57.5 (May 1978), pp. 995–1000.

[170] G. M. London et al. "Total, Peripheral and Intrathoracic Effective Compliances of the Vascular Bed in Normotensive and Hypertensive Patients". In: *Contributions to Nephrology*. Ed. by J. Bahlmann and H. Liebau. Vol. 30. S. Karger AG, July 1982, pp. 144–153.

[171] G.M. London et al. "Total Effective Compliance of the Vascular Bed in Essential Hypertension". In: *American Heart Journal* 95.3 (Mar. 1978), pp. 325–330.

[172] F. Loth, M. A. Yardimci, and N. Alperin. "Hydrodynamic Modeling of Cerebrospinal Fluid Motion Within the Spinal Cavity". In: *Journal of Biomechanical Engineering* 123.1 (Feb. 2001), pp. 71–79.

[173] A. Louveau et al. "Structural and Functional Features of Central Nervous System Lymphatic Vessels". In: *Nature* 523.7560 (July 2015), pp. 337–341.

[174] J. Ludbrook and W. F. Graham. "The Role of Cardiac Receptor and Arterial Baroreceptor Reflexes in Control of the Circulation during Acute Change of Blood Volume in the Conscious Rabbit." In: *Circulation Research* 54.4 (Apr. 1984), pp. 424–435.

[175] P. Lund-Johansen. "Haemodynamics in Essential Hypertension". In: *Clinical Science* 59.s6 (Dec. 1980), 343s–354s.

[176] S. Magder. "Volume and Its Relationship to Cardiac Output and Venous Return". In: *Critical Care* 20.1 (Dec. 2016), p. 271.

[177] C. Magnano et al. "Cine Cerebrospinal Fluid Imaging in Multiple Sclerosis". In: *Journal of Magnetic Resonance Imaging* 36.4 (Oct. 2012), pp. 825–834.

[178] A.C.I. Malossi, P.J. Blanco, and S. Deparis. "A Two-Level Time Step Technique for the Partitioned Solution of One-Dimensional Arterial Networks". In: *Computer Methods in Applied Mechanics and Engineering* 237 (2012), pp. 212–226.

[179] G. Mancia et al. "2018 ESC/ESH Guidelines for the Management of Arterial Hypertension". In: *European Heart Journal* 39 (2018), pp. 3021–3104.

[180] A. L. Mark and G. Mancia. "Cardiopulmonary Baroreflexes in Humans". In: *Comprehensive Physiology*. Ed. by Ronald Terjung. Hoboken, NJ, USA: John Wiley & Sons, Inc., Jan. 2011, cp020321.

[181] A. Marmarou, K. Shulman, and J. LaMorgese. "Compartmental Analysis of Compliance and Outflow Resistance of the Cerebrospinal Fluid System". In: *Journal of Neurosurgery* 43.5 (Nov. 1975), pp. 523–534.

[182] A. Marmarou, K. Shulman, and R. M. Rosende. "A Nonlinear Analysis of the Cerebrospinal Fluid System and Intracranial Pressure Dynamics". In: *Journal of Neurosurgery* 48.3 (Mar. 1978), pp. 332–344.

[183] B. A. Martin et al. "A Coupled Hydrodynamic Model of the Cardiovascular and Cerebrospinal Fluid System". In: *American Journal of Physiology-Heart and Circulatory Physiology* 302.7 (Apr. 2012), H1492–H1509.

[184] D. S. Martin, M. C. Rodrigo, and C. W. Appelt. "Venous Tone in the Developmental Stages of Spontaneous Hypertension". In: *Hypertension* 31.1 (Jan. 1998), pp. 139–144.

[185] A. L. Maset et al. "Pressure-Volume Index in Head Injury". In: *Journal of Neurosurgery* 67.6 (Dec. 1987), pp. 832–840.

[186] T. Matsushima et al. "Microsurgical Anatomy of the Veins of the Posterior Fossa". In: *Journal of Neurosurgery* 59 (1983), pp. 63–105.

[187] J. Mayet. "Cardiac and Vascular Pathophysiology in Hypertension". In: *Heart* 89.9 (Sept. 2003), pp. 1104–1109.

[188] A. Mazzoni and C.C. Hansen. "Surgical Anatomy of the Arteries of the Internal Auditory Canal". In: *Archives of Otolaryngology* 91 (1970), pp. 128–135.

[189] C. M. McEniery, I. B. Wilkinson, and A. P. Avolio. "AGE, HYPERTENSION AND ARTERIAL FUNCTION". In: *Clinical and Experimental Pharmacology and Physiology* 34.7 (July 2007), pp. 665–671.

[190] C. M. McEniery et al. "Central Pressure: Variability and Impact of Cardiovascular Risk Factors: The Anglo-Cardiff Collaborative Trial II". In: *Hypertension* 51.6 (June 2008), pp. 1476–1482.

[191] C. M. McEniery et al. "Normal Vascular Aging: Differential Effects on Wave Reflection and Aortic Pulse Wave Velocity". In: *Journal of the American College of Cardiology* 46.9 (Nov. 2005), pp. 1753–1760.

[192] D. J. Mikulis et al. "Oscillatory Motion of the Normal Cervical Spinal Cord." In: *Radiology* 192.1 (1994), pp. 117–121.

[193] R.C. Millington, V.A. Titarev, and E.F. Toro. "ADER: Arbitrary-order Non-Oscillatory". In: *International Series of Numerical Mathematics* 141 (2001), pp. 723–732.

[194] S. P. Mollan et al. "Evolving Evidence in Adult Idiopathic Intracranial Hypertension: Pathophysiology and Management". In: *Journal of Neurology, Neurosurgery & Psychiatry* 87.9 (2016), pp. 982–992.

[195] A. Á. Molnár et al. "The Aging Venous System: From Varicosities to Vascular Cognitive Impairment". In: *GeroScience* 43.6 (Dec. 2021), pp. 2761–2784.

[196] JP. Montani and B. N. Van Vliet. "Understanding the Contribution of Guyton's Large Circulatory Model to Long-Term Control of Arterial Pressure: Contribution of Guyton's Model". In: *Experimental Physiology* 94.4 (Apr. 2009), pp. 382–388.

[197] G. I Montecinos and E. F Toro. "Reformulations for General Advection-Diffusion-Reaction Equations and Locally Implicit ADER Schemes." In: *Journal of Computational Physics* 275 (2014), pp. 415–442.

[198] G. I Montecinos et al. "ADER Scheme with a Simplified Solver for the Generalized Riemann Problem and an Average ENO Reconstruction Procedure. Application to Blood Flow". In: *Submitted to Computers and Fluids* (2022).

[199] G.I. Montecinos, L.O. Müller, and E.F. Toro. "Hyperbolic Reformulation of a 1D Viscoelastic Blood Flow Model and ADER Finite Volume Schemes". In: *Journal of Computational Physics* 266 (2014), pp. 101–123.

[200] P.P. Morris et al. "Transverse Sinus Stenosis Is the Most Sensitive MR Imaging Correlate of Idiopathic Intracranial Hypertension". In: *American Journal of Neuroradiology* 38 (2017), pp. 471–477.

[201] L. O. Müller and E. F. Toro. "A Global Multiscale Mathematical Model for the Human Circulation with Emphasis on the Venous System". In: *International Journal for Numerical Methods in Biomedical Engineering* 30.7 (2014), pp. 681–725.

[202] L. O. Müller and E. F. Toro. "Enhanced Global Mathematical Model for Studying Cerebral Venous Blood Flow". In: *Journal of Biomechanics* 47.13 (Oct. 2014), pp. 3361–3372.

[203] L.O. Müller and P.J. Blanco. "A High Order Approximation of Hyperbolic Conservation Laws in Networks: Application to One-Dimensional Blood Flow". In: *Journal of Computational Physics* 300 (2015), pp. 423–437.

[204] L.O. Müller, G. Leugering, and P.J. Blanco. "Consistent Treatment of Viscoelastic Effects at Junctions in One-Dimensional Blood Flow Models". In: *Journal of Computational Physics* 314 (2016), pp. 167–193.

[205] L.O. Müller, C. Parés, and E.F. Toro. "Well-Balanced High-Order Numerical Schemes for One-Dimensional Blood Flow in Vessels with Varying Mechanical Properties". In: *Journal of Computational Physics* 242 (2013), pp. 53–85.

[206] L.O. Müller and E.F. Toro. "Well-Balanced High-Order Solver for Blood Flow in Networks of Vessels with Variable Properties". In: *International Journal for Numerical Methods in Biomedical Engineering* 29 (2013), pp. 1388–1411.

[207] L.O. Müller et al. "A High-Order Local Time Stepping Finite Volume Solver for One-Dimensional Blood Flow Simulations: Application to the ADAN Model." In: *International Journal for Numerical Methods in Biomedical Engineering* 32.10 (2015), n/a–n/a.

[208] L.O. Müller et al. "Impact of CCSVI on Cerebral Haemodynamics: A Mathematical Study Using MRI Angiographic and Flow Data". In: *Phlebology* 31 (2016), pp. 305–324.

[209] M. Mulvany. "Vascular Remodelling of Resistance Vessels: Can We Define This?" In: *Cardiovascular Research* 41.1 (Jan. 1999), pp. 9–13.

[210] M. Munakata. "Brachial-Ankle Pulse Wave Velocity in the Measurement of Arterial Stiffness: Recent Evidence and Clinical Applications". In: *Current Hypertension Reviews* 10.1 (Nov. 2014), pp. 49–57.

[211] J. P. Murgo et al. "Aortic Input Impedance in Normal Man: Relationship to Pressure Wave Forms." In: *Circulation* 62 (1980), pp. 105–116.

[212] H. Mussalo et al. "Baroreflex Sensitivity in Essential and Secondary Hypertension". In: *Clinical Autonomic Research* 12.6 (Dec. 2002), pp. 465–471.

[213] T. Mutsushima. *Microsurgical Anatomy and Surgery of the Posterior Cranial Fossa: Surgical Approches and Procedures Based on Anatomical Study*. 2015.

[214] J. P. Mynard and J. J. Smolich. "Influence of Anatomical Dominance and Hypertension on Coronary Conduit Arterial and Microcirculatory Flow Patterns: A Multiscale Modeling Study". In: *American Journal of Physiology-Heart and Circulatory Physiology* 311.1 (July 2016), H11–H23.

[215] J.P. Mynard and J.J. Smolich. "One-Dimensional Haemodynamic Modeling and Wave Dynamics in the Entire Adult Circulation". In: *Annals of Biomedical Engineering* 43 (2015), pp. 1443–1460.

[216] J.P. Mynard et al. "A Simple, Versatile Valve Model for Use in Lumped Parameter and One-Dimensional Cardiovascular Models". In: *International Journal for Numerical Methods in Biomedical Engineering* 28 (2012), pp. 626–641.

[217] M. Nabeshima et al. "Azygos Venous Blood Flow: Measurement with Direct Bolus Imaging". In: *Radiology* 195 (1995), pp. 467–470.

[218] S. S. Najjar et al. "Age and Gender Affect Ventricular-Vascular Coupling during Aerobic Exercise". In: *Journal of the American College of Cardiology* 44.3 (2004), pp. 611–617.

[219] W. W Nichols and D. A. MacDonald. *McDonald's Blood Flow in Arteries: Theoretical, Experimental and Clinical Principles (Sixth Edition)*. London: Hodder Arnold, 2011.

[220] N. H. Norager et al. "Changes in Intracranial Pressure and Pulse Wave Amplitude during Postural Shifts". In: *Acta Neurochirurgica* 162.12 (Dec. 2020), pp. 2983–2989.

[221] S. Novo et al. "Behaviour of Arm Venous Pressure in Patients with Systodiastolic Hypertension and in the Elderly with Isolated Systolic Hypertension in Comparison with Healthy Controls." In: *International Angiology : a journal of the International Union of Angiology* 16.2 (1997), pp. 129–133.

[222] R. Nyhof et al. "Splanchnic Circulation in Hypertension." In: *Federation proceedings* 42.6 (Apr. 1983), pp. 1690–1693.

[223] T. Okura. "Intrarenal and Carotid Hemodynamics in Patients with Essential Hypertension". In: *American Journal of Hypertension* 17.3 (Mar. 2004), pp. 240–244.

[224] M. T. Olivari et al. "Pulmonary Hemodynamics and Right Ventricular Function in Hypertension." In: *Circulation* 57.6 (June 1978), pp. 1185–1190.

[225] M.S. Olufsen. "Structured Tree Outflow Condition for Blood Flow in Larger Systemic Arteries". In: *American Journal of Physiology-Heart and Circulatory Physiology* 276 (1999), H257–H268.

[226] World Health Organization. *A Global Brief on Hypertension*. 2013.

[227] World Health Organization. *Hypertension and COVID-19 - Scientific Brief.* 2021.

[228] M. F. O'Rourke and M. E. Safar. "Relationship Between Aortic Stiffening and Microvascular Disease in Brain and Kidney: Cause and Logic of Therapy". In: *Hypertension* 46.1 (July 2005), pp. 200–204.

[229] J.T. Ottesen and M.S. Olufsen. "Functionality of the Baroreceptor Nerves in Heart Rate Regulation". In: *Computer Methods and Programs in Biomedicine* 101.2 (Feb. 2011), pp. 208–219.

[230] S. Pagoulatou and N. Stergiopulos. "Evolution of Aortic Pressure during Normal Ageing: A Model-Based Study". In: *PLOS ONE* 12.7 (July 2017). Ed. by Petter Bjornstad, e0182173.

[231] C. C. Y. Pang. "Measurement of Body Venous Tone." In: *Journal of Pharmacological and Toxicological Methods* 44 (2000), pp. 341–360.

[232] J. B. Park and E. L. Schiffrin. "Small Artery Remodeling Is the Most Prevalent (Earliest?) Form of Target Organ Damage in Mild Essential Hypertension:" in: *Journal of Hypertension* 19.5 (May 2001), pp. 921–930.

[233] R. J. Parmer, J. H. Cervenka, and R. A. Stone. "Baroreflex Sensitivity and Heredity in Essential Hypertension." In: *Circulation* 85.2 (Feb. 1992), pp. 497–503.

[234] S. Payne. "A Model of the Interaction between Autoregulation and Neural Activation in the Brain". In: *Mathematical Biosciences* 204 (2006), pp. 260–281.

[235] S. Payne. *Cerebral Autoregulation. Control of Blood Flow in the Brain*. 1st ed. Springer, 2016.

[236] R. D. Penn et al. "Pressure Gradients in the Brain in an Experimental Model of Hydrocephalus". In: *Journal of Neurosurgery* 102.6 (June 2005), pp. 1069–1075.

[237] P. B. Persson and H. R. Kirchheim, eds. *Baroreceptor Reflexes*. Berlin, Heidelberg: Springer Berlin Heidelberg, 1991.

[238] L. J. Petersen et al. "The Pulsatility Index and the Resistive Index in Renal Arteries in Patients with Hypertension and Chronic Renal Failure". In: *Nephrology Dialysis Transplantation* 10 (1995), pp. 2060–2064.

[239] D. C. Poole, B. J. Behnke, and T. I. Musch. "Capillary Hemodynamics and Oxygen Pressures in the Aging Microcirculation". In: *Microcirculation* 13.4 (Jan. 2006), pp. 289–299.

[240] J. H. Prochaska et al. "Chronic Venous Insufficiency, Cardiovascular Disease, and Mortality: A Population Study". In: *European Heart Journal* 42.40 (Oct. 2021), pp. 4157–4165.

[241] P. Reymond et al. "Validation of a One-Dimensional Model of the Systemic Arterial Tree". In: *American Journal of Physiology-Heart and Circulatory Physiology* 297.1 (2009), H208–H222.

[242] J. H. Ricketts and G. A. Head. "A Five-Parameter Logistic Equation for Investigating Asymmetry of Curvature in Baroreflex Studies". In: *American Journal of Physiology-Regulatory, Integrative and Comparative Physiology* 277.2 (Aug. 1999), R441–R454.

[243] D. Rizzoni and E. Agabiti-Rosei. "Structural Abnormalities of Small Resistance Arteries in Essential Hypertension". In: *Internal and Emergency Medicine* 7.3 (June 2012), pp. 205–212.

[244] C. F. Rothe. "Reflex Control of Veins and Vascular Capacitance". In: *Physiological Reviews* 63.4 (Oct. 1983), pp. 1281–1342.

[245] M. C. Rubira et al. "Venous or Arterial Endothelium Evaluation for Early Cardiovascular Dysfunction in Hypertensive Patients?" In: *The Journal of Clinical Hypertension* 9.11 (Nov. 2007), pp. 859–865.

[246] H.W. Ryder et al. "The Mechanism of the Change in Cerebrospinal Fluid Pressure Following an Induced Change in the Volume of the Fluid Space." In: *The Journal of laboratory and clinical medicine* 41.3 (1953), pp. 428–435.

[247] M. E. Safar and G. M. London. "Arterial and Venous Compliance in Sustained Essential Hypertension." In: *Hypertension* 10.2 (Aug. 1987), pp. 133–139.

[248] M. E. Safar and G. M. London. "Venous System in Essential Hypertension". In: *Clinical Science* 69.5 (Nov. 1985), pp. 497–504.

[249] M. E. Safar et al., eds. *Arterial and Venous Systems in Essential Hypertension*. Vol. 63. Developments in Cardiovascular Medicine. Dordrecht: Springer Netherlands, 1987.

[250] M. E. Safar et al. "Peripheral Large Arteries and the Response to Antihypertensive Treatment." In: *Hypertension* 5.5 (Sept. 1983).

[251] M. E. Safar et al. "Rapid Dextran Infusion in Essential Hypertension." In: *Hypertension* 1.6 (Nov. 1979), pp. 615–623.

[252] M. E. Safar et al. "Stiffness of Carotid Artery Wall Material and Blood Pressure in Humans: Application to Antihypertensive Therapy and Stroke Prevention". In: *Stroke* 31.3 (Mar. 2000), pp. 782–790.

[253] K. Sagawa, R. K. Lie, and J. Schaefer. "Translation of Otto Frank's Paper "Die Grundform Des Arteriellen Pulses" Zeitschrift Fur Biologie 37: 483–526 (1899)". In: *Journal of Molecular and Cellular Cardiology* 22.3 (Mar. 1990), pp. 253–277.

[254] J. Sahuquillo et al. "Reappraisal of the Intracranial Pressure and Cerebrospinal Fluid Dynamics in Patients with the So-Called ?Normal Pressure Hydrocephalus? Syndrome". In: *Acta Neurochirurgica* 112.1-2 (Mar. 1991), pp. 50–61.

[255] L. Sala, F. Salerni, and M. Szopos. "Mathematical Modeling of the Cerebrospinal Fluid Flow and Its Interactions". In: *Ocular Fluid Dynamics: Anatomy, Physiology, Imaging Techniques, and Mathematical Modeling*. Ed. by Giovanna Guidoboni, Alon Harris, and Riccardo Sacco. Cham: Springer International Publishing, 2019, pp. 497–540.

[256] R. E. Samar and T. G. Coleman. "Measurement of Mean Circulatory Filling Pressure and Vascular Capacitance in the Rat". In: *American Journal of Physiology-Heart and Circulatory Physiology* 234.1 (Jan. 1978), H94–H100.

[257] E. Schiffrin. "Remodeling of Resistance Arteries in Essential Hypertension and Effects of Antihypertensive Treatment". In: *American Journal of Hypertension* 17.12 (Dec. 2004), pp. 1192–1200.

[258] R. E. Schmieder, H. P. Schobel, and F. H. Messerli. "Central Blood Volume: A Determinant of Early Cardiac Adaptation in Arterial Hypertension?" In: *Journal of the American College of Cardiology* 26.7 (Dec. 1995), pp. 1692–1698.

[259] A. Scoz, L. Bertazzi, and E. F. Toro. "On Well-Posedness of a Mathematical Model for Cerebrospinal Fluid in the Optic Nerve Sheath and the Spinal Subarachnoid Space". In: *Applied Mathematics and Computation* 413 (Jan. 2022), p. 126625.

[260] M.B. Segal. "Transport of Nutriens across the Choroid Plexus". In: *Microscopy research and technique* 52 (2001), pp. 38–48.

[261] P. Segers et al. "Mathematical Model Analysis of Heart-Arterial Interaction in Hypertension". In: *2001 Conference Proceedings of the 23rd Annual International Conference of the IEEE Engineering in Medicine and Biology Society*. Vol. 1. Istanbul, Turkey: IEEE, 2001, pp. 192–195.

[262] K. Shapiro, A. Marmarou, and K. Shulman. "Characterization of Clinical CSF Dynamics and Neural Axis Compliance Using the Pressure-Volume Index: I. The Normal Pressure-Volume Index". In: *Annals of Neurology* 7.6 (June 1980), pp. 508–514.

[263] M. Shimizu and K. Kario. "Review: Role of the Augmentation Index in Hypertension". In: *Therapeutic Advances in Cardiovascular Disease* 2.1 (Feb. 2008), pp. 25–35.

[264] A. A. Shoukas and K. Sagawa. "Control of Total Systemic Vascular Capacity by the Carotid Sinus Baroreceptor Reflex". In: *Circulation Research* 33.1 (July 1973), pp. 22–33.

[265] A. A. Shoukas and K. Sagawa. "Total Systemic Vascular Compliance Measured as Incremental Volume-Pressure Ratio". In: *Circulation Research* 28.2 (Feb. 1971), pp. 277–289.

[266] A. C. Simon et al. "An Evaluation of Large Arteries Compliance in Man." In: *American Journal of Physiology-Heart and Circulatory Physiology* 237 (1979), H550–H554.

[267] A. C. Simon et al. "Estimation of Forearm Arterial Compliance in Normal and Hypertensive Men from Simultaneous Pressure and Flow Measurements in the Brachial Artery, Using a Pulsed Doppler Device and a First-Order Arterial Model during Diastole". In: *Cardiovascular Research* 17.6 (June 1983), pp. 331–338.

[268] M. J. Simon and J. J. Iliff. "Regulation of Cerebrospinal Fluid (CSF) Flow in Neurodegenerative, Neurovascular and Neuroinflammatory Disease". In: *Biochimica et Biophysica Acta (BBA) - Molecular Basis of Disease* 1862.3 (Mar. 2016), pp. 442–451.

[269] F. Smaltino, F.P. Bernini, and R. Elefante. "Normal and Pathological Findings of the Angiographic Examination of the Internal Auditory Artery". In: *Neuroradiology* 2 (1971), pp. 216–222.

[270] S. Sorek, J. Bear, and Z. Karni. "A Non-Steady Compartmental Flow Model of the Cerebrovascular System". In: *Journal of Biomechanics* 21 (1988), pp. 695–704.

[271] A. Spilimbergo, E. F. Toro, and L. O. Müller. "One-Dimensional Blood Flow with Discontinuous Properties and Transport: Mathematical Analysis and Numerical Schemes". In: *Communications in Computational Physics* 29.3 (2021), pp. 649–697.

[272] K. W. Stock et al. "Quantification of Blood Flow in the Middle Cerebral Artery with Phase-Contrast MR Imaging". In: *European Radiology* 10 (2000), pp. 1795–1800.

[273] S. D. Stocker, B. J. Kinsman, and A. F. Sved. "Recent Advances in Neurogenic Hypertension: Dietary Salt, Obesity, and Inflammation". In: *Hypertension* 70.3 (Sept. 2017), pp. 474–478.

[274] S. Stoquart-ElSankari et al. "A Phase-Contrast MRI Study of Physiologic Cerebral Venous Flow". In: *Journal of Cerebral Blood Flow & Metabolism* 29 (2009), pp. 1208–1215.

[275] M. Strocchi et al. "A Global Mathematical Model for the Simulation of Stenoses and Bypass Placement in the Human Arterial System". In: *Applied Mathematics and Computation* 300 (2017), pp. 21–39.

[276] Y. Sun et al. "A Comprehensive Model for Right–Left Heart Interaction under the Influence of Pericardium and Baroreflex". In: *American Journal of Physiology* 272 (1997), H1499–515.

[277] N. Sundström et al. "Comparison between 3 Infusion Methods to Measure Cerebrospinal Fluid Outflow Conductance: Clinical Article". In: *Journal of Neurosurgery* 113.6 (Dec. 2010), pp. 1294–1303.

[278] B. Sweetman and A. A. Linninger. "Cerebrospinal Fluid Flow Dynamics in the Central Nervous System". In: *Annals of Biomedical Engineering* 39.1 (Jan. 2011), pp. 484–496.

[279] R. Tain et al. "Determination of Cranio-Spinal Canal Compliance Distribution by MRI: Methodology and Early Application in Idiopathic Intracranial Hypertension". In: *Journal of Magnetic Resonance Imaging* 34.6 (Dec. 2011), pp. 1397–1404.

[280] H. Takatsu et al. "Quantitative Estimation of Compliance of Human Systemic Veins by Occlusion Plethysmography with Radionuclide–Methodology and the Effect of Nitroglycerin." In: *Japanese circulation journal* 53.3 (Mar. 1989), pp. 245–254.

[281] A. Takeshita et al. "Effect of Central Venous Pressure on Arterial Baroreflex Control of Heart Rate". In: *American Journal of Physiology-Heart and Circulatory Physiology* 236.1 (Jan. 1979), H42–H47.

[282] H. Tanaka et al. "Comparison between Carotid-Femoral and Brachial-Ankle Pulse Wave Velocity as Measures of Arterial Stiffness". In: *Journal of Hypertension* 27.10 (Oct. 2009), pp. 2022–2027.

[283] J. Th J. Tans and D.C.J. Poortvliet. "Intracranial Volume-Pressure Relationship in Man. Part I: Calculation of the pressure-volume index". In: *Journal of Neurosurgery* 56 (1982), pp. 524–528.

[284] J. Th J. Tans and D.C.J. Poortvliet. "Intracranial Volume-Pressure Relationship in Man. Part II: Clinical significance of the pressure-volume index". In: *Journal of Neurosurgery* 59 (1983), pp. 810–816.

[285] J. Th J. Tans and D.C.J. Poortvliet. "Relationship between Compliance and Resistance to Outflow of CSF in Adult Hydrocephalus". In: *Journal of Neurosurgery* 71 (1989), pp. 59–62.

[286] K.M. Thierfelder et al. "Vertebral Artery Hypoplasia: Frequency and Effect on Cerebellar Blood Flow Characteristics". In: *Stroke* 45 (2014), pp. 1363–1368.

[287] E. F. Toro. "Low-Dissipation Centred Schemes for Hyperbolic Equations in Conservative and Non-Conservative Form". In: *Journal of Computational Physics* 416 (2020), p. 109545.

[288] E. F. Toro. "The ADER Path to High-Order Godunov Methods." In: *Continuum Mechanics, Applied Mathematics and Scientific Computing: Godunov's Legacy- ALiber Amicorum to Professor Godunov.* Springer Verlag, 2020, pp. 359–366.

[289] E. F. Toro and A. Siviglia. "Flow in Collapsible Tubes with Discontinuous Mechanical Properties: Mathematical Model and Exact Solutions". In: *Communications in Computational Physics* 13.2 (Feb. 2013), pp. 361–385.

[290] E. F. Toro et al. "A Computational Model for the Dynamics of Cerebrospinal Fluid in the Spinal Subarachnoid Space". In: *Journal of Biomechanical Engineering* 141.1 (Jan. 2019), p. 011004.

[291] E. F. Toro et al. "AENO: A Novel Reconstruction Method in Conjunction with ADER Schemes for Hyperbolic Equations". In: *Communications on Applied Mathematics and Computation* (Sept. 2021).

[292] E. F. Toro et al. "Cerebrospinal Fluid Dynamics Coupled to the Global Circulation in Holistic Setting: Mathematical Models, Numerical Methods and Applications". In: *International Journal for Numerical Methods in Biomedical Engineering* (Oct. 2021), e3532.

[293] E. F. Toro et al. "Impact of Jugular Vein Valve Function on Cerebral Venous Haemodynamics". In: *Current Neurovascular Research* 12.4 (2015), pp. 384–397.

[294] E.F. Toro, R.C. Millington, and L.A.M. Nejad. "Towards Very High–Order Godunov Schemes". In: *Godunov Methods: Theory and Applications. Edited Review, E. F. Toro (Editor),* ed. by E.F. Toro. Kluwer Academic/Plenum Publishers, 2001, pp. 905–937.

[295] E.F. Toro and G.I. Montecinos. "Advection-Diffusion-Reaction Equations: Hyperbolisation and High-Order ADER Discretizations". In: *SIAM Journal of Scientific Computing* 36 (2014), A2423–A2457.

[296] E.F. Toro and V.A. Titarev. "Solution of the Generalized Riemann Problem for Advection–Reaction Equations". In: *Proceedings of the Royal Society A: Mathematical, Physical and Engineering Sciences* 458 (2002), pp. 271–281.

[297] E.F. Toro et al. "Inner-Ear Circulation in Humans Is Disrupted by Extracranial Venous Outflow Strictures: Implications for Ménière's Disease." In: *Veins and Lymphatics* 7.1 (2018).

[298] G. J. Tortora and B. Derrickson. *Principles of Anatomy and Physiology*. 12th ed. Hoboken, NJ: John Wiley & Sons, 2010.

[299] N. C. Trippodo. "Total Circulatory Capacity in the Rat. Effects of Epinephrine and Vasopressin on Compliance and Unstressed Volume." In: *Circulation Research* 49.4 (Oct. 1981), pp. 923–931.

[300] M. Ulrych et al. "Cardiac Output and Distribution of Blood Volume in Central and Peripheral Circulations in Hypertensive and Normotensive Man." In: *Heart* 31.5 (Sept. 1969), pp. 570–574.

[301] M. Ursino. "A Mathematical Study of Human Intracranial Hydrodynamics Part 1—The Cerebrospinal Fluid Pulse Pressure". In: *Annals of Biomedical Engineering* 16.4 (1988), pp. 379–401.

[302] M. Ursino. "A Mathematical Study of Human Intracranial Hydrodynamics Part 2 - Simulation of Clinical Tests". In: *Annals of Biomedical Engineering* 16.4 (1988), pp. 403–416.

[303] M. Ursino. "Interaction between Carotid Baroregulation and the Pulsating Heart: A Mathematical Model". In: *American Journal of Physiology-Heart and Circulatory Physiology* 275.5 (Nov. 1998), H1733–H1747.

[304] M. Ursino, M. Antonucci, and E. Belardinelli. "Role of Active Changes in Venous Capacity by the Carotid Baroreflex: Analysis with a Mathematical Model". In: *American Journal of Physiology-Heart and Circulatory Physiology* 267.6 (Dec. 1994), H2531–H2546.

[305] M. Ursino and M. Giannessi. "A Model of Cerebrovascular Reactivity Including the Circle of Willis and Cortical Anastomoses". In: *Annals of Biomedical Engineering* 38 (2010), pp. 955–974.

[306] M. Ursino and M. Innocenti. "Modeling Arterial Hypotension During Hemodialysis". In: *Artificial Organs* 21.8 (Nov. 2008), pp. 873–890.

[307] M. Ursino and C. A. Lodi. "A Simple Mathematical Model of the Interaction between Intracranial Pressure and Cerebral Hemodynamics". In: *Journal of Applied Physiology* 82.4 (Apr. 1997), pp. 1256–1269.

[308] M. Ursino and E. Magosso. "Acute Cardiovascular Response to Isocapnic Hypoxia. I. A Mathematical Model". In: *American Journal of Physiology-Heart and Circulatory Physiology* 279.1 (July 2000), H149–H165.

[309] A. Vallet et al. "Assessment of Pressure-Volume Index During Lumbar Infusion Study: What Is the Optimal Method?" In: *Intracranial Pressure and Neuromonitoring XVII*. Ed. by Bart Depreitere, Geert Meyfroidt, and Fabian Güiza. Vol. 131. Cham: Springer International Publishing, 2021, pp. 335–338.

[310] G. V. Varsos et al. "Intraspinal Pressure and Spinal Cord Perfusion Pressure after Spinal Cord Injury: An Observational Study". In: *Journal of Neurosurgery: Spine* 23.6 (Dec. 2015), pp. 763–771.

[311] Y. Vassilevski, V. Salamatova, and S. Simakov. "On the Elasticity of Blood Vessels in One-Dimensional Problems of Hemodynamics". In: *Computational Mathematics and Mathematical Physics* 55 (2015), pp. 1567–1578.

[312] O. Vriz et al. "The Right Heart-Pulmonary Circulation Unit in Systemic Hypertension". In: *Heart Failure Clinics* 14.3 (July 2018), pp. 247–253.

[313] A. Wåhlin et al. "Assessment of Craniospinal Pressure-Volume Indices". In: *American Journal of Neuroradiology* 31.9 (Oct. 2010), pp. 1645–1650.

[314] E.A. Warnert et al. "Is High Blood Pressure Self-protection for the Brain?" In: *Circulation Research* 119 (2016), e140–e151.

[315] V. Warren and E. S. Brannon. "Effect of Increasing the Blood Volume and Right Atria1 Pressure on the Circulation of Normal Subjects by Intravenous Infusions". In: *The American journal of medicine* 4.2 (1948), pp. 193–200.

[316] S. Wende, N. Nakayama, and P. Schwerdtfeger. "The Internal Auditory Artery". In: *Journal of Neurology* 210 (1975), pp. 21–31.

[317] N. Westerhof et al. "Analog Studies of the Human Systemic Arterial Tree". In: *Journal of Biomechanics* 2.2 (May 1969), pp. 121–143.

[318] F.M. White. *Fluid Mechanics*. McGraw-Hill International Editions. McGraw-Hill, 2003.

[319] C. K. Willie et al. "Integrative Regulation of Human Brain Blood Flow". In: *Journal of Physiology* 592 (2014), pp. 841–859.

[320] S. Winklhofer et al. "Spinal Cord Motion: Influence of Respiration and Cardiac Cycle". In: *RöFo - Fortschritte auf dem Gebiet der Röntgenstrahlen und der bildgebenden Verfahren* 186.11 (Apr. 2014), pp. 1016–1021.

[321] A. C. Witham, J. W. Fleming, and W. L. Bloom. "THE EFFECT OF THE INTRAVENOUS ADMINISTRATION OF DEXTRAN ON CARDIAC OUTPUT AND OTHER CIRCULATORY DYNAMICS 1". In: *Journal of Clinical Investigation* 30.9 (Sept. 1951), pp. 897–902.

[322] R.L. Wolf et al. "Measurement of Normal Renal Artery Blood Flow: Cine Phase-Contrast MR Imaging vs Clearance of p-Aminohippurate". In: *American Journal of Roentgenology* 161 (1993), pp. 995–1002.

[323] D. F. Young and Tsai, F.Y. "FLOW CHARACTERISTICS IN MODELS OF ARTERIAL STENOSES-I. STEADY FLOW". In: *Journal of Biomechanics* 6 (1973), pp. 395–410.

[324] P. Zamboni et al. "Chronic Cerebrospinal Venous Insufficiency in Patients with Multiple Sclerosis". In: *Journal of neurology, neurosurgery and psychiatry* 80 (2009), pp. 392–399.

[325] R.S. Zitnik et al. "Continuously Recorded Changes of Thoracic Aortic Blood Flow in Man in Response to Leg Exercise in Supine Position". In: *Circulation Research* 17 (1965), pp. 97–105.

[326] R. Zivadinov et al. "Changes of Cine Cerebrospinal Fluid Dynamics in Patients with Multiple Sclerosis Treated with Percutaneous Transluminal Angioplasty: A Case-control Study". In: *Journal of Vascular and Interventional Radiology* 24.6 (June 2013), pp. 829–838.

[327] Y. Zócalo et al. "Regional Differences in Veins Wall Viscosity, Compliance. Energetics and Damping: Analysis of the Pressure-Diameter Relationship during Cyclical Overloads". In: *Biological Research* 41.2 (2008).